

Scour holes in heterogeneous subsoil

A numerical study on hydrodynamic processes in the development of the scour holes

S. (Sam) Bom

November 2017

Delft University of Technology

Cover image: Scour hole in the Spui River near Nieuw-Beijerland, created by Dr. ir. C.J. Sloff
(available at <https://www.deltares.nl/nl/nieuws/erosiekuilen-oude-maas-en-dordtse-kil/>).

Scour holes in heterogeneous subsoil

A numerical study on hydrodynamic processes
in the development of the scour holes

by

S. (Sam) Bom

in partial fulfilment of the requirements to obtain the degree of

Master of Science
in Hydraulic Engineering

at the faculty of

Civil Engineering and Geosciences

at

Delft University of Technology

to be defended publicly on Wednesday November 8, 2017 at 11:00 AM.

Student number:	4227808
Project duration:	February 15, 2017 – November 8, 2017
Thesis committee:	Prof. dr. ir. W.S.J. Uijtewaal TU Delft
	Dr. ir. R.J. Labeur TU Delft
	Dr. Y. Huismans Deltares
	Dr. ir. N.G. Jacobsen Deltares
	Dr. ir. C.J. Sloff Deltares & TU Delft

An electronic version of this thesis is available at <http://repository.tudelft.nl/>.

Preface

The document you are reading is the final version of my master thesis on the case of scour holes in heterogeneous subsoil. It is the final product of my Master of Science in Hydraulic Engineering at Delft University of Technology, with the specialization Environmental Fluid Mechanics. The research is a collaboration between Delft University of Technology and Deltares. It was carried out at the office of Deltares in Delft.

This project is part of a large research project on scour holes in heterogeneous subsoil, consisting of multiple theses on the subject. The previous master students focused on analyzing the field data and performing laboratory experiments. I am the first student that completely focused on numerical modelling of the scour holes. In first instance, the aim is to obtain a better understanding of the formation and development of the scour holes. Ultimately we want to be able to predict the behaviour of the scour holes and overcome the problems that come with them. Hopefully, this will be achieved somewhere in the near-future.

In the first place, I would like to thank my graduation committee for their constructive criticism during the meetings. Wim Uijttewaal acted as chair of the committee, being responsible for the execution of the project. Even though he had a busy schedule, he always had full focus and interesting insights on the subject. Robert Jan Labeur made me aware of the importance of understanding the physical basis of the subject, before starting any model simulation. Kees Sloff supported me with a cheerful note and enthusiasm.

Special thanks goes out to my supervisors at Deltares, Ymkje Huisman and Niels Jacobsen. Ymkje and Niels were always available for questions and steered me in the right direction. Ymkje, thank you for your daily supervision and involvement in my project, even though the subject of numerical modelling is not completely your field of practice. I appreciate the spare time you spent on reading my documents a lot. Niels, the many hours we discussed my modelling issues and results were very informative and helped me reaching my goals. Your tips on writing a strong discussion made writing my own discussion easier. Your knowledge on numerical modelling in the field of hydraulic engineering is far-reaching, and I hope to approach that level myself once.

I also would like to thank Joost Stenfert, who performed his experimental study on scour holes in heterogeneous subsoil parallel to my research. Our brainstorm sessions on the subject were very fruitful and it was a lot of fun working with you.

Last but not least, thank you Jens for doing everything you could to support me during this project, even though you were 11340 km away during the final stage. Your checks on my writing improved my style and you kept me sharp when I needed it. The most important thing: you forced me to chill during the evenings and weekends and our amazing trip to Vietnam was the perfect break in this project.

*S. (Sam) Bom
Delft, October 2017*

Abstract

In the Rhine-Meuse Delta in the Netherlands, deep scour holes can develop very suddenly. The holes may form a potential risk for the stability of surrounding riverbanks, dikes, bridges, tunnels and buildings. In general, a scour hole can be the result of two conditions: local changes in hydrodynamical conditions or local changes in erosive capacity of the bed. In the Rhine-Meuse Delta, 40% of the scour holes are (partially) the result of the latter (Koopmans, 2017). The delta is characterized by a heterogeneous subsoil, consisting of alternating layers of peat, sand and clay being exposed to the forcing of the flow. When a patch of sand, which is highly erodible, is surrounded by clay or peat, which are poorly erodible, the sand will be eroded quickly.

Most of the research on scour holes is focusing on scour holes due to changes in hydrodynamical conditions. Predominantly empirical relations are found, with a limited physical foundation. In the past three years, analyses of field data and experimental research has been performed on scour holes in heterogeneous subsoil. However, a distinct method to predict the development of scour holes in heterogeneous subsoil has not been found yet. In this research a numerical model that simulates the hydrodynamics in a scour hole is used to gain more insight in the flow processes that are present in such a hole. The dependencies of the flow processes on the upstream water depth, upstream flow velocity and depth of the scour hole are investigated by changing these parameters systematically in the model simulations. Besides, a qualitative estimation of the expected erosion processes is made based on the hydrodynamics in the scour hole.

The numerical model that is used in this research is simulating a scour hole from the experimental study by Stenfert (2017). The model is set up in the open-source CFD toolbox OpenFOAM and uses the Generalized $k-\omega$ turbulence model by Wilcox (2006), logarithmic wall functions and a rigid lid at the surface boundary. At the upstream boundary a fully developed velocity profile is induced, whereas downstream the pressure is set to $0 \text{ m}^2/\text{s}^2$. The bed topography is approximated by a symmetrical bed in the model and the grid cell sizes in the vertical are based on the requirements for the wall functions.

The model is validated using three cases: a two-dimensional backward facing step, a two-dimensional scour hole measured by Van Zuylen (2015) and the three-dimensional scour hole measured by Stenfert (2017). The former two validation models give confidence that the model is able to simulate the flow inside the scour hole accurately, as the recirculation zone is captured nicely and the measured velocity profiles are calculated with a highest average relative error of 4.7 % for both the BFS cases and the two-dimensional scour hole. The results of the three-dimensional scour hole show the essential flow processes, which are the flow recirculation, contraction of flow and horseshoe vortex. However, a quantitative comparison with the flow measurements was not possible, as the quality of the flow velocity measurements in the three-dimensional scour hole is regarded as insufficient due to the large uncertainty in the recirculation zone.

In the parameter study, the effect of the water depth, flow velocity and depth of the scour hole on the flow processes is investigated. The processes that are included in the analysis are the flow separation and recirculation zone, the contraction of flow, the horseshoe vortex and the vortices downstream of the hole. Changes in water depth only have a significant influence on the flow contraction. A smaller upstream water depth results in a stronger contraction. A larger upstream flow velocity results in stronger vortices. The recirculation velocity is stronger, but the relative recirculation velocity is approximately constant.

Changes in the depth of the scour hole showed some interesting phenomena. It is found that three-dimensional processes suppress the formation of the recirculation zone, as flow separation happened for milder slopes and shallower holes in two-dimensional simulations. The contraction of flow is not necessarily stronger for larger holes, which was hypothesized. A deeper scour hole can have a relatively larger recirculation zone, resulting in a smaller 'active' area and a weaker flow contraction. The inflow component of the horseshoe vortex and the inner downstream vortices are related, and get stronger for deeper scour holes. For the outflow of the horseshoe vortex and the outer vortices the opposite holds.

The analysis of the bed shear stress in the model results shows a constant upstream slope angle, as the critical value for bed shear stress is not reached. In the downstream half of the hole, this value is reached and therefore erosion and sedimentation are expected. Both these findings confirm the observations in laboratory experiments, where the upstream slope angle stayed constant while the hole evolved in the downstream half. In coupling the calculated bed shear stresses to erosion, some major approximations are made. For calculation of the sediment transport, only the effects of the average bed shear stress and the bed slope are taken into account. Fluctuations in flow velocity, pressure and turbulent eddies are not included, while the contribution to sediment transport of these processes can be large. For example, in the measurements of the bed level, the area around the reattachment point is the deepest part of the hole, which cannot be derived from the bed shear stress profile in the model results. This is due to the fluctuating character of the impinging flow at the reattachment point. The average bed shear stress at that location is zero.

The bed shear stress in the model results shows strips of zero bed shear stress with large gradients at both sides of the hole. These strips have an angle of 1:8, which is also found in the laboratory experiments by [Koopmans \(2017\)](#), where the downstream expansion of the scour hole with a poorly erodible top layer had the same widening angle.

A larger upstream flow velocity results in larger values of the bed shear stress and thus more erosion. This is expected, as the hole will erode faster with a larger upstream velocity. The water depth hardly influences the bed shear stress in the hole. A shallower scour hole results in larger bed shear stresses, which is expected as the hole was eroding faster in earlier stages of the scour hole formation process.

The model can be used to get a better understanding of the presence and dependencies of the hydrodynamic processes in the scour hole. Coupling this to erosion gives insight in the erosion patterns and the influence of the hydrodynamics on them. A first rough estimation of the expected erosion in the scour hole can be made using the model results. The processes that are not included in the model simulation should be taken into account in a qualitative manner. Besides that, the model can function as a first step in the direction of a model that simulates both hydrodynamics and morphology.

It is recommended to perform additional flow velocity measurements with a lower uncertainty in the recirculation zone, in order to be able to validate the model results better. Besides, flow measurements from a scour hole in the field are needed to validate a model of such a case. A model of a scour hole in the field can give insight in the translation of the findings in this report to a prototype situation. Due to the many factors playing a role in a scour hole in the field, detailed validation data is needed.

Contents

Preface	iii
Abstract	v
List of Tables	ix
List of Figures	xi
Nomenclature	xix
1 Introduction	1
1.1 Background information	1
1.2 Research objective and research questions	2
1.3 Methodology	3
1.4 Outline of the report	3
2 Review of literature and previous studies	5
2.1 Formation of scour holes in heterogeneous subsoil	5
2.2 Hydrodynamic processes in scour holes in heterogeneous subsoil	6
2.2.1 Backward facing step.	6
2.2.2 Two-dimensional scour hole with non erodible edges	8
2.2.3 Three-dimensional scour hole	10
2.2.4 Analogy with flow around a circular object.	13
2.3 Erosion process and sediment transport	14
2.3.1 Stability of grains.	14
2.3.2 Sediment transport	15
2.3.3 Stability of the upstream slope in a scour hole in heterogeneous subsoil.	16
2.4 Conclusion	17
3 Model Setup	19
3.1 Reference case by Stenfert (2017)	19
3.2 Turbulence model	20
3.3 Near wall treatment	21
3.3.1 Bed treatment	21
3.3.2 Free surface treatment	22
3.4 Grid	22
3.4.1 Coordinate system	23
3.4.2 Bed topography	23
3.4.3 Grid generation	25
3.5 Boundary and initial conditions	27
3.6 Numerical process	28
4 Model Validation	29
4.1 Backward facing step	29
4.1.1 Reference cases	29
4.1.2 Validation results	30
4.1.3 Summary	32
4.2 Scour hole by Van Zuylen (2015)	32
4.2.1 Reference case	33
4.2.2 Validation results	33
4.2.3 Three-dimensional model	35
4.2.4 Summary	35

4.3	Scour hole by Stenfert (2017)	36
4.3.1	Data source	36
4.3.2	Validation results	36
4.4	Influence of the side walls and rigid lid approximation	39
4.5	Conclusion	39
5	Parameter study	41
5.1	Recirculation zone	42
5.1.1	Influence of the water depth	42
5.1.2	Influence of the flow velocity	43
5.1.3	Influence of the depth of the scour hole and upstream slope	43
5.2	Flow contraction	45
5.3	Vortices and coherent structures	49
5.3.1	Horseshoe vortex	49
5.3.2	Downstream flow structures	50
5.3.3	Influence of water depth, flow velocity and depth of the scour hole	52
5.3.4	Influence of the symmetrical scour hole	53
5.4	Bed shear stress and erosion	54
5.4.1	Coupling from bed shear stress to sediment transport and erosion	54
5.4.2	Bed shear stresses in the base cases	55
5.4.3	Influence of the water depth, flow velocity and depth of the scour hole	57
5.5	Conclusion	58
6	Discussion	61
6.1	Interpretation of the results	61
6.1.1	Calculation of sediment transport and erosion	61
6.1.2	Influence of the hydrodynamical processes on the morphodynamics	62
6.1.3	Interpretation of the estimated erosion	63
6.2	Comparison with numerical simulations by Van Zuylen (2015)	63
6.3	Relevance for scour holes in the field	63
6.3.1	Simplifications	63
6.3.2	Erosion process	66
7	Conclusions and recommendations	67
7.1	Conclusions	67
7.1.1	Research objective	67
7.1.2	Subquestions	67
7.1.3	Main question	68
7.2	Recommendations	69
	Bibliography	71
A	Additional literature	75
B	Numerical modelling of scour holes	95
C	Modelling software choice	99
D	OpenFOAM	101
E	Grid generation	109
F	Cyclic modelling	115
G	Additional information for Chapter 4	119
H	Errors in model validation	127
I	Additional figures for Chapter 5	131
J	Figures of the prototype scale simulations	141

List of Tables

3.1	Hydraulic conditions and dimensions of the scour hole for the experiments by Stenfert (2017). The parameters are: water depth (h), average flow velocity (\bar{u}), Reynolds number (Re), Froude number (Fr), bed shear velocity (u_\star), Nikuradse roughness of concrete and sand ($k_{n, \text{concrete}}$ and $k_{n, \text{sand}}$) and the length and width of the scour hole (L_{hole} and W_{hole}).	19
3.2	Cell sizes and expansion ratios in the different directions for the model of the scour hole from the experiments by Stenfert (2017).	26
3.3	Boundary conditions and initial conditions for the model of the scour hole from the experiments by Stenfert (2017).	27
4.1	Hydraulic conditions for the experiments in the reference cases for the BFS model validation. The parameters are: downstream depth (h_d), step height (dh), maximum flow velocity (u_{max}), downstream flow velocity (\bar{u}_d), Reynolds number (Re), Froude number (Fr) and relative reattachment point (x_R/dh).	30
4.2	Hydraulic conditions for the experiments by Van Zuylen (2015). The parameters are: water depth (h), average flow velocity (\bar{u}), Reynolds number (Re), Froude number (Fr), bed shear velocity (u_\star), Nikuradse roughness of steel and sand ($k_{n, \text{steel}}$ and $k_{n, \text{sand}}$) and the length of the scour hole (L_{hole}).	33
5.1	Overview of the model simulations that are performed for the parameter study. The average flow velocity (\bar{u}), water depth (h), maximum scour hole depth (h_s), upstream slope (β), bed shear velocity (u_\star), Froude number (Fr) and Reynolds number (Re) are given.	41
5.2	Recirculation parameters in the scour hole for simulations with different water depths. Some of the parameters from Table 5.1 are given, together with the recirculation velocity magnitude (u_r), the percentage of the average upstream flow velocity (u_r/\bar{u}), the length of the recirculation zone (L_r) and the ratio of the recirculation length over the depth of the scour hole (L_r/h_s).	42
5.3	Recirculation parameters in the scour hole for simulations with different water depths. The definition of the parameters is given in Table 5.2.	43
5.4	Recirculation parameters in the scour hole for simulations with different flow velocities. The definition of the parameters is given in Table 5.2.	43
5.5	Recirculation parameters in the scour hole for simulations with different depths of the scour hole. The definition of the parameters is given in Table 5.2, except for $\tan\beta$, which is the upstream slope. All runs have a water depth of $h = 0.14$ m and an average flow velocity of $\bar{u} = 0.360$ m/s.	44
5.6	Recirculation parameters in the scour hole for the two-dimensional simulations with different depths of the scour hole. The definition of the parameters is given in Table 5.2, except for $\tan\beta$, which is the upstream slope. All runs have a water depth of $h = 0.14$ m and an average flow velocity of $\bar{u} = 0.360$ m/s.	45
A.1	Different turbulence models with their advantages and disadvantages, based on Andersson et al. (2012).	80
A.2	Overview of the different sub-layers in the turbulent boundary layer (Andersson et al., 2012). For clarification of the velocity expressions see Section A.1.6.	82
A.3	Empirical relations for Ψ_c as a function of D_\star (Hoffmans and Verheij, 1997).	85
A.4	Results of different researches on the value of γ in Equation (A.36) (Hoffmans and Verheij, 1997).	89
A.5	The angle of repose for different soil types (Hoffmans and Verheij, 1997).	91
A.6	Angle of repose, critical slope angle and failure mechanism for different sand densities (Hoffmans and Verheij, 1997).	92
D.1	Listing of the different boundary types in OpenFOAM (OpenFOAM Foundation Ltd., 2016).	103

E.1	Hydraulic conditions for the experiments in the reference cases of the cyclic case.	115
E.2	Boundary conditions cyclic model	116
G.1	Boundary conditions of the BFS models.	120
G.2	Analytical validation of the different BFS cases.	121
G.3	Boundary conditions of the BFS model.	122
J.1	Overview of the model simulations that are performed with a prototype scale scour hole. The average flow velocity (\bar{u}), water depth (h), maximum scour hole depth (h_s), upstream slope (β), bed shear velocity (u_*), Froude number (Fr) and Reynolds number (Re) are given.	141

List of Figures

1.1	Scour holes in the Rhine-Meuse delta: overview and birdseye view of a scour hole in the Spui near Nieuw-Beijerland.	1
2.1	Schematical representation of the formation of scour holes in heterogeneous subsoil (Huisman et al., 2016).	5
2.2	Schematization of the flow regions in a scour hole, based on (Hoffmans and Booij, 1993a).	6
2.3	Schematization of the flow regions in a BFS situation (Bradshaw and Wong, 1972).	6
2.4	Upper: longitudinal component of the flow velocity at a backward facing step. Lower: turbulence intensity and turbulent shear stress at a backward facing step (Tani et al., 1961).	7
2.5	Schematization of the side view of the initial scouring stage of a scour hole between two steel plates (black rectangles). The gray profiles show the other scouring stages. The area with black dots indicates a sandy area.	8
2.6	Schematization of the side view of the developed scouring stage of a scour hole between two steel plates (black rectangles). The gray profiles show the other scouring stages. The area with black dots indicates a sandy area.	8
2.7	Schematization of the side view of the equilibrium stage of a scour hole between two steel plates (black rectangles). The gray profiles show the other scouring stages. The area with black dots indicates a sandy area.	9
2.8	Longitudinal recirculation in a scour hole. The black arrows represent the streamlines of the flow. Two close-up locations are shown: left the flow separation at the upstream edge and right the reattachment point. The + and - signs represent areas with respectively high and low pressure.	9
2.9	Mixing layer in a scour hole. The gray arrows represent the local velocity profile and the dotted black lines are the edges of the mixing layer.	10
2.10	Experiments by Koopmans (2017) and Uijttewaal et al. (2016).	10
2.11	Schematic representation of flow lines in the experiment by Stenfert (2017). The red arrows show flow lines in the red colored cross sections, the black arrows show flow lines in the gray part of the hole.	11
2.12	Lateral recirculation in a scour hole.	11
2.13	Flow contraction above a scour hole.	12
2.14	Flow regime around a circular object. S denotes the separation line (Baykal et al., 2017).	13
2.15	Shields diagram, adapted by Breusers (Hoffmans and Verheij, 1997).	14
2.16	Classification of sediment transport, based on Jansen et al. (1994).	15
2.17	Control volume for derivation of the sediment balance, based on Crosato (2015).	15
2.18	Forces on a grain at a slope.	16
3.1	Schematization of experimental set-up with a side view and a top view. The flume has a bed of concrete and a box from which sand can erode (Stenfert, 2017).	19
3.2	Coordinate systems for the two-dimensional and three-dimensional model simulations.	23
3.3	Generation of the non-symmetrical bed.	23
3.4	Plots showing the bed levels in the scour hole. The top view shows the oval edge and two dashed-lines representing the cross sections that are shown in the other two plots. The side view shows the cross section through the center axis in streamwise direction. The front view shows the cross section in lateral direction, with three points that are used to generate the symmetrical bed.	24
3.5	Symmetrical bed levels inside the scour hole.	24
3.6	Comparison of the symmetrical bed and the bed level measurements from the laboratory experiments. 9 cross sections in lateral direction are given.	25

3.7	Cross section of the central axis in streamwise direction of the computational grid for the model of the scour hole from the experiments by Stenfert (2017). Parts of the upstream and downstream reach of the domain are left out for plotting purposes. The boundaries are indicated with colors.	26
3.8	Velocity profile at the upstream boundary of the model, generated with the cyclic model (see Appendix F).	27
4.1	Model results and measurements of the ST1 case by Nakagawa and Nezu (1987). The plot includes velocity profiles at several locations in the model. The values are normalized with the maximum velocity, which is the streamwise velocity in the upstream region.	30
4.2	Visualization of the relative errors in the model validation using the BFS case ST1 by Nakagawa and Nezu (1987). For each location the normalized measured flow velocity is plotted against the normalized modelled flow velocity. Perfect agreement is indicated by the black solid line. All points that are between the dotted black lines have a difference of less than 10% between the model result and measurement.	31
4.3	Model results and measurements of the ST3 case by Nakagawa and Nezu (1987). The plot includes velocity profiles at several locations in the model. The values are normalized with the maximum velocity, which is the streamwise velocity in the upstream region.	31
4.4	Model results and measurements of the BFS case by Ampadu-Mintah and Tachie (2015). The plot includes velocity profiles at several locations in the model. The values are normalized with the maximum velocity, which is the streamwise velocity in the upstream region.	32
4.5	Schematical representation of the experiment <i>Run 17</i> by Van Zuylen (2015). The plate at the downstream edge of the hole has an angle of 45° and the length of the hole is 0.5 m. Image is based on Van Zuylen (2015).	33
4.6	Model results of the two-dimensional simulation and measurements of the Run 17 experiment by Van Zuylen (2015). The plot includes velocity profiles at several locations in the model. The values are normalized with the maximum velocity, which is the streamwise velocity at the surface in the upstream region.	33
4.7	Zoomed model results of the Run 17 experiment by Van Zuylen (2015). The plot includes velocity profiles at several locations in the model. The values are normalized with the maximum velocity, which is the streamwise velocity at the surface in the upstream region.	34
4.8	Model results of the three-dimensional simulation and measurements of the Run 17 experiment by Van Zuylen (2015). The plot includes turbulence intensity profiles at several locations in the model. The values are normalized with a value of $0.025 \text{ m}^2/\text{s}^2$	35
4.9	Schematization of the velocity measurements that were performed by Stenfert (2017). The oxygen bubbles are created using a wire mesh upstream of the measuring device. The bubbles tend to move upwards, as their density is much smaller than the density of water.	36
4.10	Model results of the simulation and measurements of the experiment by Stenfert (2017). The plot includes velocity profiles at several locations in the model. The values are normalized with the maximum velocity, which is the streamwise velocity at the surface in the upstream region.	37
4.11	Photos showing the visual observations during the scouring experiment. Small dye particles are placed on the bed, showing the local direction of flow. Figures based on (Stenfert, 2017).	37
4.12	Model results of the simulation and measurements of the experiment by Stenfert (2017). The plot includes velocity profiles at several locations in the model. The values are normalized with the maximum velocity, which is the streamwise velocity at the surface in the upstream region.	38
4.13	Model results of the simulation and measurements of the experiment by Stenfert (2017). The plot includes turbulence intensity profiles at several locations in the model. The values are normalized with a value of $k = 0.018 \text{ m}^2/\text{s}^2$	38
4.14	Plot showing the water level difference in the model simulation of the scour hole by Stenfert (2017). Above the hole ($x/L_{\text{hole}} = 0.0 - 1.0$) the water level increases.	39
5.1	Bed levels at two different points in time during the experiment. The reattachment point is indicated with a star.	41
5.2	Model result for run 1, with a bed topography after 30 hours of scouring. Streamlines in the central axis in streamwise direction are shown.	42

5.3	Plots showing the flow velocity profiles at the upstream boundary in the different model simulations.	42
5.4	Plot showing some of the bed topographies used in the runs to investigate the influence of the depth of the scour hole and the upstream slope. The point of reattachment is indicated with a star. Run 2 does not have a flow separation, so there is no star for that simulation. The green dashed line shows the definition of the upstream slope ($\tan \alpha$).	44
5.5	Visualization of the relation between the relative recirculation velocity and the upstream slope of the hole. The BFS range is based on Uijtewaal (2011), Tani et al. (1961) and Nakagawa and Nezu (1987).	45
5.6	Plot showing the flow contraction in the model domain. The colors show the flow velocity in lateral direction and the lines represent the flow lines in the cross section. The cross section is located at a height of $z = 0.01$ m. The streamwise component of the flow velocity in the flow lines is multiplied with a factor 0.5.	46
5.7	Plot showing the flow contraction in the model domain for runs with different depths. The lines represent the flow lines in the cross section at a height of $z = 0.05$ m. The streamwise component of the flow velocity is multiplied by a factor 0.1.	46
5.8	Graphs showing the relation between the relative maximum flow velocity in lateral direction at $z = 0.01$ m, the active scour area and the relative depth of the scour hole.	47
5.9	Graphs showing the relation between the relative maximum flow velocity in lateral direction at $z = 0.01$ and the relative depth of the scour hole. Runs with a varying flow velocity (run 11 and 12), water depth (run 13 and 14) and constant Froude number (run 16 and 17) are included.	47
5.10	Plot showing the difference in specific discharge in several cross sections in the model results. The difference with the upstream value is plotted. The values are scaled with a value of $0.014 \text{ m}^2/\text{s}$	48
5.11	Plot showing the difference in flow velocity in streamwise direction in several cross sections. The difference in flow velocity with the average upstream value is plotted. The values are scaled with a value of 0.1 m/s	48
5.12	Schematical representation of the horseshoe vortex and the vortices downstream of the scour hole. The dotted lines represent the centers of the vortices.	49
5.13	Cross section normal to the streamwise direction at $x/L_{\text{hole}} = 0.5$. The vectors are generated using the lateral and vertical flow velocity. The scale of the vectors is shown in the top left corner.	49
5.14	Top view of the domain showing surfaces of constant vorticity in streamwise direction. The surfaces are generated using values of $\omega_x = 2 \text{ s}^{-1}$ and $\omega_x = -2 \text{ s}^{-1}$. The areas that are indicated with a number are described in the text above the figure.	50
5.15	Top view of the domain showing surfaces of constant vorticity in streamwise direction. The surfaces are generated using values of $\omega_x = 0.15 \text{ s}^{-1}$ and $\omega_x = -0.15 \text{ s}^{-1}$. The areas that are indicated with a number are described in the text above the figure.	50
5.16	Cross section normal to the streamwise direction at $x/L_{\text{hole}} = 1.9$. The vectors are generated using the lateral and vertical flow velocity. The scale of the vectors is shown in the top left corner.	51
5.17	Picture from the laboratory experiment by Stenfert (2017). The sediment ridges behind the scour hole are indicated with the yellow areas.	51
5.18	Three-dimensional visualizations of the flow structures inside the scour hole and in the downstream region. Contours of vorticity are shown for several cross sections.	51
5.19	Graphs showing the magnitude of the flow structures. The values in the left plot are normalized with the values of run 10: inner vortex = 0.87 cm/s and inflow = 5.13 cm/s . The values in the right plot are normalized with the values of run 3: outer vortex = 0.60 m/s and outflow = 7.33 cm/s	52
5.20	Top view of the domain showing surfaces of constant vorticity in streamwise direction for the model simulation with an asymmetrical bed. The surfaces are created using values of $\omega_x = 1 \text{ s}^{-1}$ and $\omega_x = -1 \text{ s}^{-1}$. The yellow circle highlights the asymmetrical flow structures that are found.	53
5.21	Schematical visualization of the asymmetrical features in a lateral cross section of the measured bed topography.	53
5.22	Top view of the bed shear stress in streamwise direction in the scour hole and the surrounding area. Negative values have red colour, positive values are coloured in green.	54
5.23	Plots showing the bed shear stress (left) and sediment transport (right) in the central axis in streamwise direction. The critical value of the bed shear stress is calculated using Equation 2.3 and the adaptations for a slope in Section 2.3.2.	54

5.24	Top view of the bed shear stress in streamwise direction in the scour hole and the surrounding area. Negative values have red colour, positive values are coloured in green. The yellow ovals indicate the 1:8 slope in bed shear stress that is present inside the hole. The edge of the hole and the line with zero bed shear stress are indicated in black.	56
5.25	Top view of the bed shear stress in streamwise direction in the scour hole and the surrounding area. Negative values have red colour, positive values are coloured in green. The yellow ovals indicate the 1:8 slope in bed shear stress that is present outside the hole. The edge of the hole and the line with zero bed shear stress are indicated in black.	56
5.26	Pictures from the laboratory experiments by Koopmans (2017) and Stenfert (2017). The orange material in the left figure is used to mimic the poorly erodible top layer. The 1:8 slope is observed in the erosion of the poorly erodible layer. The right image shows the 1:8 slope in the sediment ridges that are formed at the edge of the hole.	56
5.27	Top view of the bed shear stress in lateral direction in the scour hole and the surrounding area. Negative values have red colour, positive values are coloured in green. Contours of several values are shown.	57
5.28	Top view of the bed shear stress in lateral direction in the scour hole and the surrounding area. Negative values have red colour, positive values are coloured in green. Contours of several values are shown.	57
5.29	Plot showing the sediment transport in the central axis in streamwise direction. The model results of runs 1 - 7 are shown. The critical value of the bed shear stress is calculated using Equation 2.3 and the adaptations for a slope in Section 2.3.2.	58
6.1	Schematization of the evolution of the bed, derived from the bed shear stress in the model results and the expected erosion near the reattachment point. The grey square indicates the area that is influenced by the bed shear stress.	62
6.2	Schematical representation of the effect of helical flow on the recirculation zone inside the scour hole. The grey lines in the hole indicate the edge of the recirculation zone for uniform flow conditions (solid line) and flow conditions behind a river bend (helical flow, dashed line).	64
6.3	Schematization showing the difference in velocity profile between the laboratory scale and the prototype scale.	65
A.1	Uniform flow in a sloping channel (Schierreck, 2012).	76
A.2	Influence of the pressure gradient on the velocity profile (Schierreck, 2012).	76
A.3	Velocity profiles in the boundary layer and inner region, based on Andersson et al. (2012).	81
A.4	Near-wall stresses in the inner region of the boundary layer (Andersson et al., 2012).	82
A.5	Wall functions in the inner region of the boundary layer (Andersson et al., 2012).	83
A.6	The forces on a grain in a flow, adapted from Schierreck (2012).	84
A.7	Scour depth as a function of time, based on (Hoffmans and Verheij, 1997).	86
A.8	Schematization of a local scour hole behind a bed protection and a sill, based on (Hoffmans and Verheij, 1997).	87
A.9	Schematization of a local scour hole behind a bed protection, showing the flow separation and recirculation in the scour hole, based on (Hoffmans and Verheij, 1997).	88
A.10	Four phases in the evolution of a scour hole by clear-water scour, based on (Hoffmans and Verheij, 1997).	88
A.11	Influence of the slope on stability (Schierreck, 2012).	91
A.12	Effect of shear on loose sand (Hoffmans and Verheij, 1997).	92
B.1	Time evolution of the maximum scour depth. The gray line is computed in Kim et al. (2014). The experimental data are retrieved from Khosronejad et al. (2012).	96
B.2	Visualisation of the streamwise phase-averaged velocity streamlines Baykal et al. (2015).	96
B.3	Comparison of different flow parameters, circles are measurements and solid lines are simulated profiles. Upper: time averaged streamwise flow velocity, Middle: nondimensional time-averaged Reynolds stress profiles of $-\overline{u'u'}$, Lower: nondimensional time-averaged Reynolds stress profiles of $-\overline{u'w'}$ (Nabi et al., 2012).	97
C.1	Difference between σ - (left) and Z-layers (right) (Deltares, 2014).	99

D.1	Directory structure of an OpenFOAM case (OpenFOAM Foundation Ltd., 2016).	101
D.2	Example of a <code>U</code> file in the <code>0</code> folder of an OpenFOAM case. The header of the file is left out.	102
D.3	Example of a <code>controlDict</code> file in the <code>system</code> folder of an OpenFOAM case. The header of the file is left out.	104
D.4	Example of a <code>fvSolution</code> file in the <code>system</code> folder of an OpenFOAM case. The header of the file is left out.	105
D.5	Example of a <code>fvSchemes</code> file in the <code>system</code> folder of an OpenFOAM case. The header of the file is left out.	106
D.6	Schematization of a loop of the PIMPLE algorithm in solving the equations (Aguerrea et al., 2013).	108
E.1	Example of a <code>blockMeshDict</code> file in the <code>polyMesh</code> folder of an OpenFOAM case. The header of the file is left out.	110
E.2	Initial grid after using the <code>blockMesh</code> utility. The boundaries are added to the figure.	111
E.3	Schematic representation of a part of the grid. The gray line is the actual bed level.	111
E.4	Deformed grid with $\alpha = 1$ and $\gamma = 0$. The boundaries are added in the figure.	112
E.5	Deformed grid with $\alpha = 4$ and $\gamma = 0$. The boundaries are added in the figure.	112
E.6	Deformed grid with $\alpha = 1$ and $\gamma = 5$. The boundaries are added in the figure.	113
E.7	Deformed grid with $\alpha = 1.2$ and $\gamma = 5$. The boundaries are added in the figure.	113
F.1	Example grid of the cyclic simulation with the different boundaries.	115
F.2	Principle of the cyclic case.	116
F.3	Comparison of measurements from Fuhrman et al. (2010) and model results for the smooth case. The error is calculated for each simulation with reference to the measurements.	117
F.4	Comparison of measurements from Fuhrman et al. (2010) and model results for the rough case. The error is calculated for each simulation with reference to the measurements.	118
G.1	Example grid of the BFS simulation with the different boundaries.	119
G.2	Schematization of the flow separation line and the recirculation zone in a BFS case. The gray lines are flow velocity profiles in streamwise direction.	120
G.3	Streamlines close to the step in the ST1 case, with a corner eddy clearly visible. The background colors indicate the streamwise component of the flow velocity.	120
G.4	Supporting images for the analytical model of the BFS cases.	121
G.5	Part of the grid for the simulation of run 17 by Van Zuylen (2015) with the different boundaries. In reality, the inlet and outlet boundaries are located further upstream and downstream.	122
G.6	Model results of the three-dimensional simulation and measurements of the Run 17 experiment by Van Zuylen (2015).	123
G.7	Plots showing the difference between the two-dimensional and three-dimensional model simulations at different locations over depth. The difference between the simulations is divided by the local value of the three-dimensional simulation.	124
G.8	Plot showing the three-dimensional effects in the model simulations. The flow velocity in lateral direction in a cross section at $x/L_{\text{hole}} = 0.1$ is shown.	124
G.9	Plot showing the three-dimensional effects in the model simulations. The vorticity in streamwise direction in a cross section at $z/h = 0.008$ is shown.	124
G.10	Schematization of Görtler vortices (De Souza et al., 2004).	125
H.1	Visualization of the relative errors in the model validation using the BFS case ST3 by Nakagawa and Nezu (1987). For each location the normalized measured flow velocity is plotted against the normalized modelled flow velocity. Perfect agreement is indicated by the black solid line. All points that are between the dotted black lines have a difference of less than 25% between the model result and measurement.	127
H.2	Visualization of the relative errors in the model validation using the BFS case by Ampadu-Mintah and Tachie (2015). For each location the normalized measured flow velocity is plotted against the normalized modelled flow velocity. Perfect agreement is indicated by the black solid line. All points that are between the dotted black lines have a difference of less than 10% between the model result and measurement.	127

H.3	Visualization of the relative errors in the model validation using the scouring case by Van Zuylen (2015). For each location the normalized measured flow velocity is plotted against the normalized modelled flow velocity. Perfect agreement is indicated by the black solid line. All points that are between the dotted black lines have a difference of less than 15% between the model result and measurement.	128
H.4	Visualization of the relative errors in the model validation using the scouring case by Van Zuylen (2015). For each location the normalized measured turbulence intensity is plotted against the normalized modelled turbulence intensity. Perfect agreement is indicated by the black solid line. All points that are between the dotted black lines have a difference of less than 25% between the model result and measurement.	128
H.5	Visualization of the relative errors in the model validation using the scouring case by Stenfert (2017). For each location the normalized measured flow velocity is plotted against the normalized modelled flow velocity. Perfect agreement is indicated by the black solid line. All points that are between the dotted black lines have a difference of less than 25% between the model result and measurement.	129
H.6	Visualization of the relative errors in the model validation using the scouring case of the larger hole by Stenfert (2017). For each location the normalized measured flow velocity is plotted against the normalized modelled flow velocity. Perfect agreement is indicated by the black solid line. All points that are between the dotted black lines have a difference of less than 25% between the model result and measurement.	129
H.7	Visualization of the relative errors in the model validation using the scouring case of the larger hole by Stenfert (2017). For each location the normalized measured turbulence intensity is plotted against the normalized modelled turbulence intensity. Perfect agreement is indicated by the black solid line. All points that are between the dotted black lines have a difference of less than 25% between the model result and measurement.	130
I.1	Plots showing the bed shear stress and sediment transport rate in the central axis in streamwise direction. The critical value of the bed shear stress is calculated using Equation (2.3) and the adaptations for a slope in Section 2.3.2.	131
I.2	Plots showing the bed shear stress and sediment transport rate in the central axis in streamwise direction. The critical value of the bed shear stress is calculated using Equation (2.3) and the adaptations for a slope in Section 2.3.2.	131
I.3	Plots showing the bed shear stress and sediment transport rate in the central axis in streamwise direction. The critical value of the bed shear stress is calculated using Equation (2.3) and the adaptations for a slope in Section 2.3.2.	132
I.4	Plots showing the bed shear stress and sediment transport rate in the central axis in streamwise direction. The critical value of the bed shear stress is calculated using Equation (2.3) and the adaptations for a slope in Section 2.3.2.	132
I.5	Plots showing the bed shear stress and sediment transport rate in the central axis in streamwise direction. The critical value of the bed shear stress is calculated using Equation (2.3) and the adaptations for a slope in Section 2.3.2.	132
I.6	Cross section normal to the streamwise direction at $x/L_{\text{hole}} = 0.0$. The vectors are generated using the lateral and vertical flow velocity. The scale of the vectors is shown in the top left corner.	133
I.7	Cross section normal to the streamwise direction at $x/L_{\text{hole}} = 0.1$. The vectors are generated using the lateral and vertical flow velocity. The scale of the vectors is shown in the top left corner.	133
I.8	Cross section normal to the streamwise direction at $x/L_{\text{hole}} = 0.2$. The vectors are generated using the lateral and vertical flow velocity. The scale of the vectors is shown in the top left corner.	133
I.9	Cross section normal to the streamwise direction at $x/L_{\text{hole}} = 0.3$. The vectors are generated using the lateral and vertical flow velocity. The scale of the vectors is shown in the top left corner.	134
I.10	Cross section normal to the streamwise direction at $x/L_{\text{hole}} = 0.4$. The vectors are generated using the lateral and vertical flow velocity. The scale of the vectors is shown in the top left corner.	134
I.11	Cross section normal to the streamwise direction at $x/L_{\text{hole}} = 0.5$. The vectors are generated using the lateral and vertical flow velocity. The scale of the vectors is shown in the top left corner.	134
I.12	Cross section normal to the streamwise direction at $x/L_{\text{hole}} = 0.6$. The vectors are generated using the lateral and vertical flow velocity. The scale of the vectors is shown in the top left corner.	135

Nomenclature

Abbreviations

Abbreviation	Full name
BFS	Backward Facing Step
CFD	Computational Fluid Dynamics
DNS	Direct Numerical Simulation
LES	Large Eddy Simulation
RANS	Reynolds-averaged Navier-Stokes equations
URANS	Unsteady Reynolds-averaged Navier-Stokes equations
VOF	Volume of Fluid

Latin symbols

Symbol	[Units]	Description
B	[-]	Coefficient in the logarithmic velocity profile ($B = 5.5$)
C	[m ^{1/2} /s]	Chézy roughness coefficient
C_0	[m ^{1/2} /s]	Maximum Chézy coefficient in f_c ($C_0 = 40$ m ^{1/2} /s)
C_c	[Pa]	Cohesion
C_f	[Pa]	Fatigue rupture strength of clay
C_{lim}	[m]	Stress-limiter strength
D	[m]	Height of the sill
D_\star	[-]	Dimensionless grain diameter
d	[m]	Grain diameter
d_{50}	[m]	Median grain diameter
d_a	[m]	Size of the detaching aggregates ($d_a = 0.004$ m)
d_n	[m]	Nominal grain diameter
dh	[m]	Step height in BFS case
F	[m ³ /s ²]	Momentum
F_1	[m ³ /s ²]	Momentum in cross section 1
F_2	[m ³ /s ²]	Momentum in cross section 2
F_D	[N]	Drag force on a grain

Symbol	[Units]	Description
F_F	[N]	Friction force on a grain
F_L	[N]	Lift force on a grain
F_S	[N]	Shear force on a grain
Fr	[-]	Froude number
f_c	[-]	Roughness function
f_{slope}	[-]	Slope factor
f_β	[-]	Vortex-stretching function
g	[m/s ²]	Gravitational acceleration, $g = 9.81 \text{ m/s}^2$
h	[m]	Water depth
h_0	[m]	Initial water depth
h_d	[m]	Downstream water depth
h_u	[m]	Upstream water depth
h_s	[m]	Maximum scour depth
$h_{s,e}$	[m]	Equilibrium scour depth
$h(\gamma_z)$	[-]	Correction factor in velocity profile of the outer layer
i_b	[-]	Bed slope
i_p	[m/s ²]	Pressure slope
K	[hours m ^{2.3} /s ^{4.3}]	Coefficient
$K_{\alpha_s/l}$	[-]	Reduction factor for slope strength
k	[m ² /s ²]	Turbulence intensity
k_n	[m]	Nikuradse roughness height
k_n^+	[m]	Dimensionless Nikuradse roughness height
$k_n, \text{concrete}$	[m]	Nikuradse roughness height of concrete
k_n, sand	[m]	Nikuradse roughness height of sand
k_n, steel	[m]	Nikuradse roughness height of steel
L	[m]	Length scale
L_{hole}	[m]	Length of the scour hole
L_p	[m]	Length of the bed protection
L_r	[m]	Length of the recirculation zone
ℓ	[m]	Turbulent length scale
l_\star	[m]	Characteristic length scale
M_s	[kg]	Mass of the grain
p	[Pa]	Pressure
q_s	[m ² /s]	Rate of transported bed material load including pores per unit width
R	[m]	Hydraulic radius
Re	[-]	Reynolds number
r_0	[-]	Relative turbulence intensity

Symbol	[Units]	Description
S_{ij}	[s ⁻¹]	Mean strain-rate tensor
T	[s]	Part of the tidal period where $\alpha\bar{u}_0 > \bar{u}_c$ ($T = t_2 - t_1$)
t	[s]	Time
t_1	[s]	Characteristic time scale
$t_{1,tide}$	[s]	Time at which $\alpha\bar{u}_0$ first exceeds \bar{u}_c during flood tide
$t_{1,u}$	[s]	Characteristic time scale in unsteady flow
$t_{2,tide}$	[s]	Time at which $\alpha\bar{u}_0$ drops below \bar{u}_c during ebb tide
U	[m/s]	Velocity scale
u	[m/s]	Flow velocity in streamwise direction
\bar{u}	[m/s]	Average flow velocity in streamwise direction
u'	[m/s]	Velocity fluctuations in streamwise direction
u_\star	[m/s]	Bed shear velocity
$u_{\star,c}$	[m/s]	Critical bed shear velocity
u^+	[-]	Dimensionless flow velocity in streamwise direction (wall coordinate)
u_0	[m/s]	Upstream flow velocity in streamwise direction
\bar{u}_c	[m/s]	Mean critical flow velocity
u_c	[m/s]	Critical velocity acting on the grain
\bar{u}_d	[m/s]	Downstream mean flow velocity
u_i	[m/s]	Flow velocity in i direction
u_j	[m/s]	Flow velocity in j direction
u_{L1}	[m/s]	Flow velocity in streamwise direction in layer 1
u_{L2}	[m/s]	Flow velocity in streamwise direction in layer 2
u_{max}	[m/s]	Maximum flow velocity in streamwise direction
u_r	[m/s]	Recirculating flow velocity
\bar{u}_u	[m/s]	Upstream mean flow velocity
V_s	[m ³]	Volume of the grain
v	[m/s]	Flow velocity in lateral direction
v'	[m/s]	Velocity fluctuations in lateral direction
W_{hole}	[m]	Width of the scour hole
W_s	[N]	Weight of a grain
w	[m/s]	Flow velocity in vertical direction
w'	[m/s]	Velocity fluctuations in vertical direction
y^+	[-]	Dimensionless coordinate in wall-normal direction (wall coordinate)
y_c^+	[-]	Dimensionless height of the first cell center (y_c/l_\star)
y_0	[m]	Integration constant in the logarithmic velocity profile
y_c	[m]	Height of the first cell center ($\Delta y/2$)
x	[m]	Coordinate in streamwise direction

Symbol	[Units]	Description
x_i	[m]	Coordinate in i direction
x_j	[m]	Coordinate in j direction
x_R	[m]	Location of the reattachment point in streamwise direction
y	[m]	Coordinate in lateral direction
z	[m]	Coordinate in vertical direction
z_b	[m]	Bed level elevation

Greek symbols

Symbol	[Units]	Description
α	[-]	Amplification factor for the flow velocity
$\alpha_{k-\omega}$	[-]	Closure coefficient in $k-\omega$ model
α_s	[°]	Slope angle
α_{δ_m}	[-]	Coefficient for thickness of the mixing layer, $\alpha \approx 0.085$
β	[°]	Angle of the slope
β_*	[-]	Closure coefficient in $k-\omega$ model
β_0	[-]	Closure coefficient in $k-\omega$ model
$\beta_{k-\omega}$	[-]	Closure coefficient in $k-\omega$ model
γ	[-]	Breusers' coefficient
γ_z	[-]	Normalized vertical coordinate ($\gamma_z = z/R$)
Δ	[-]	Relative density
Δh	[m]	Water level difference
Δp	[m ² /s ²]	Pressure difference
Δy	[m]	Near wall cell height
Δy^+	[-]	Dimensionless height of the first cell
δ	[m]	Thickness of the boundary layer
δ^+	[-]	Dimensionless thickness of the boundary layer
δ_m	[m]	Thickness of the mixing layer
ϵ	[m ² /s ³]	Turbulence dissipation
η	[m]	Kolmogorov length scale
θ	[°C]	Temperature
κ	[-]	Von Kármán coefficient, $\kappa = 0.4$
λ	[m]	Characteristic length scale
ν	[m ² /s]	Kinematic viscosity
ν_T	[m ² /s]	Kinematic eddy viscosity

Symbol	[Units]	Description
Π	[-]	Coles parameter ($\Pi = 0.2$)
ρ_s	[kg/m ³]	Density of sediment
ρ_w	[kg/m ³]	Density of water
ΣH	[N]	Sum of the forces in horizontal direction
ΣV	[N]	Sum of the forces in vertical direction
σ	[-]	Closure coefficient in k- ω model
σ^*	[-]	Closure coefficient in k- ω model
σ_d	[-]	Cross diffusion coefficient in k- ω model
σ_{do}	[-]	Cross diffusion coefficient in k- ω model
τ_b	[N/m ²]	Bed shear stress
τ_c	[N/m ²]	Critical shear stress
τ_{ij}	[m ² /s ²]	Specific Reynolds stress tensor
τ_η	[s]	Kolmogorov time scale
u_η	[m/s]	Kolmogorov velocity scale
Φ	[-]	Dimensionless bed load transport rate
Φ_β	[-]	Dimensionless bed load transport rate on a longitudinal slope
ϕ	[°]	Angle of repose of sediment
χ_ω	[-]	Cross diffusion coefficient in k- ω model
Ψ	[-]	Mobility parameter (Shields)
Ψ_c	[-]	Critical mobility parameter (Shields)
$\Psi_{c,\beta}$	[-]	Mobility parameter on a longitudinal slope (Shields)
Ω_{ij}	[s ⁻¹]	Mean rotation tensor
ω	[s ⁻¹]	Vorticity
ω_s	[-]	Turbulence coefficient, $\omega_s = 1 + 3r_0$ according to Dietz and Wittke (1969)
ω_T	[s ⁻¹]	Specific turbulence dissipation rate
$\tilde{\omega}_T$	[s ⁻¹]	Stress-limited specific turbulence dissipation rate
ω_x	[s ⁻¹]	Vorticity in streamwise direction
ω_y	[s ⁻¹]	Vorticity in lateral direction
ω_z	[s ⁻¹]	Vorticity in vertical direction
∇	[m ⁻¹]	Nabla operator (vector of partial derivatives)
∇_i	[m ⁻¹]	Nabla operator in i direction (vector of partial derivatives)

Chapter 1

Introduction

In this chapter an introduction to the research is given. First, background information on the topic of scour holes in heterogeneous subsoil in the Rhine-Meuse Delta is given. After that, the research objective and questions are posed, followed by the methodology of the research and the outline of the report.

1.1. Background information

In the Rhine-Meuse Delta, many scour holes have developed, as shown in Figure 1.1a. A scour hole is defined as a significant local deepening in the bed of a river (Hoffmans and Verheij, 1997). The scour holes in the delta may form a potential risk for the stability of riverbanks, dikes, bridges and tunnels. Because the hinterland of the delta is a densely populated area, the event of dike stability failure may have large consequences, such as fatalities and economic damage. A visualization of a typical scour hole is presented in Figure 1.1b. This scour hole in the Spui River near Nieuw-Beijerland is 20 meters deep and has slopes with angles larger than 45°.

The formation of scour holes in rivers can have a variety of causes. The most studied cause is the presence of hydraulic structures. Scour holes form close to structures due to changes in flow patterns. Huismans et al. (2016) investigated the causes for the scour holes in the Rhine-Meuse Delta. Part of the scour holes in the delta are present close to structures. However, approximately 40% of the scour holes in the delta are found to be (partially) caused by the composition of the subsoil (Koopmans, 2017). River deltas have large variations in the subsoil, reaching from poorly erodible clay and peat layers to highly erodible sand. The geological evolution in these areas created layers of different soil types in the lithology of the subsoil. The Rhine-Meuse Delta is an example of a river delta with these features. Local incision of sand between two poorly erodible clay layers causes scour holes to be formed very suddenly. This may lead to deep scour holes with steep slopes (Huismans et al., 2016; Sloff et al., 2013).

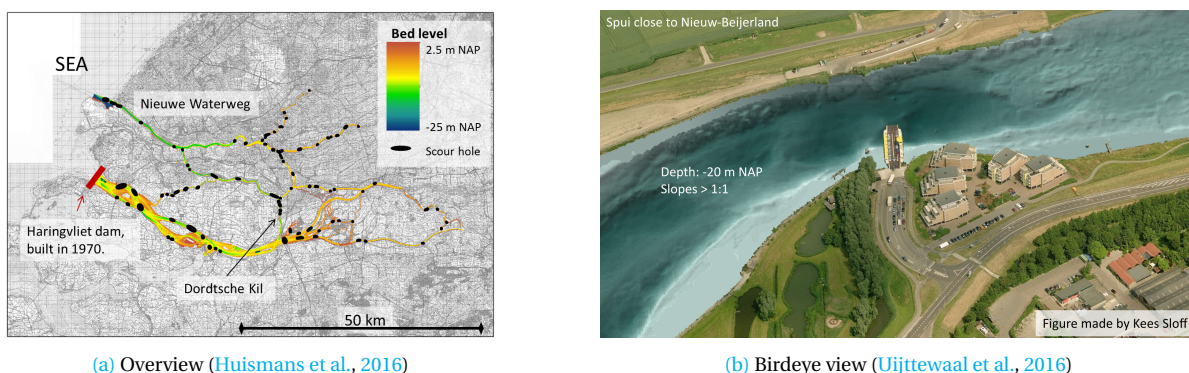


Figure 1.1: Scour holes in the Rhine-Meuse delta: overview and birdeye view of a scour hole in the Spui near Nieuw-Beijerland.

An overview of the research carried out on scour hole formation and development is given in the Scour Manual (Hoffmans and Verheij, 1997). Most of this research is performed between 1960 and 1990 and related to

scour near structures, such as weirs or bridges. The obtained formulas provide a useful basis for the first estimation of scour hole growth. However, as the parameters are fitted using data from experiments, the physical basis is limited, as well as the applicability to different types of scour hole formation, for example in the Rhine-Meuse Delta. The scour holes in the delta are three-dimensional in nature, because they usually cover only a part of the wetted cross section. Scouring processes in these holes develop in all directions with various complex flow patterns.

The specific situation of scour in heterogeneous subsoil in the Rhine-Meuse Delta is investigated by multiple researchers (Sloff et al., 2013; Van Zuylen, 2015; Huisman et al., 2016; Uijtewaal et al., 2016; Koopmans, 2017), but a distinct method to predict the development of a scour hole in this area is not yet developed.

This graduation thesis aims at a better understanding and prediction of this type of scour hole growth. It is part of multiple graduation theses on the subject of scour holes in heterogeneous subsoil, performed over the last couple of years. The research on scour holes in heterogeneous subsoil can generally be subdivided in three parts:

- **Analysis of field data in the Rhine-Meuse Delta**

This is done by Van Zuylen (2015) and Koopmans (2017). They have studied the formation and development of most of the scour holes in the delta. They concluded that the behaviour of the scour holes in the delta has a strong variance, due to the influence of the heterogeneous subsoil and changing hydrodynamic conditions.

- **Experimental research using laboratory experiments**

Laboratory experiments are performed by Van Zuylen (2015), Koopmans (2017) and Stenfert (2017). Van Zuylen (2015) investigated a two-dimensional scour situation. Koopmans (2017) and Stenfert (2017) performed three-dimensional laboratory tests. The work by Stenfert (2017) has been carried out parallel to this thesis research.

- **Numerical modelling**

Van Zuylen (2015) did some numerical model simulations with a 2DV model and simulated a scour situation in the Oude Maas and Spui. The models included only hydrodynamics and were set up in FINEL at Svasek Hydraulics.

1.2. Research objective and research questions

Research objective

In order to better judge and predict the potential risk that scour holes may form for the stability of the surrounding infrastructure, a better prediction of the formation and development of scour holes in heterogeneous subsoil is needed. In order to be able to make these predictions this more knowledge on the physical processes is needed. In this research an attempt will be made to create a numerical model which is able to reproduce the hydrodynamics in a scour hole in heterogeneous subsoil. The objective is formulated as follows:

Understanding of the formation and development of scour holes in heterogeneous subsoil by creating a three-dimensional numerical model that is able to simulate the hydrodynamics in the scour hole.

Research questions

The main research question for this research is based on knowledge that can be gained from the model:

Which processes are the most important for the erosion in scour holes in heterogeneous subsoil and where is the erosion most severe?

Subquestions

To be able to answer the main research question, several subquestions will be answered. These questions are more specific and are listed below:

- What are the important hydrodynamical processes that play a role in the development of a scour hole in heterogeneous subsoil?

- For each identified process: is it reproduced by the numerical model and how does it contribute to the morphodynamics inside the scour hole?
- What is the effect of the water depth, flow velocity and the depth of the scour hole on the processes?

Boundaries of the research

Many types of scour are occurring in the hydraulic environment. This research focuses on the local scour in heterogeneous subsoil. This scour happens when a highly erodible layer, for instance sand, is present between two poorly erodible layers, for example clay, in the horizontal direction. Other types of scour are only used to investigate the hydrodynamic processes, but are not modelled:

- Scour around objects and structures (for example monopiles, groynes and bridge piers)
- Jet scour (for example by a propeller of a ship)
- Scour by waves

The model that is created simulates the hydrodynamics only. An indication of the morphological developments in the scour hole is deduced from the flow field in the model results.

1.3. Methodology

Steps in the modelling process

A numerical model is used to get more insight in the processes that play a role in the formation and development of scour holes in heterogeneous subsoil. The creation of the model is done in several steps, which are described below:

1. Investigation of the hydrodynamic processes that play a role. Based on available literature as well as measurements.
2. Decision on the numerical software package to be used.
3. Determination of the turbulence closure model and wall function to be used.
4. Validation of the model based on laboratory measurements.

Parameter study

Once the model is working well, the influence of some parameters on the hydrodynamic processes in and around the scour hole is examined. The water depth, flow velocity and the depth of the scour hole are systematically changed in order to identify the differences in the processes.

The bed shear stress from the model is also investigated. From this, a rough estimate of the erosion and sedimentation pattern in the hole is made. The influence of the different parameters on the bed shear stress and erosion is also included in the investigation.

1.4. Outline of the report

In Chapter 2 a description of the available literature on development of scour holes in heterogeneous subsoil is given. This includes a part on formation of scour holes in heterogeneous subsoil, a description of the hydrodynamic processes in such scour holes and information on the erosion process and sediment transport. In Chapter 3 the setup of the numerical model of the scour hole is described. The validation of the model with measurements from several studies is shown in Chapter 4. The model is used to perform the parameter study, which is described in Chapter 5. A discussion on some of the aspects of this research is included in Chapter 6. Finally, the conclusions and recommendations for further research are written in Chapter 7.

The appendices are attached behind the bibliography. They include additional information from literature, a description of the choice of modelling software, an explanation of OpenFOAM and the grid generation, an elaboration of the cyclic model and additional information and figures for the model validation and parameter study.

Chapter 2

Review of literature and previous studies

In this chapter a review of the available literature on the formation and development of scour holes in heterogeneous subsoil and the hydrodynamical processes in the scour holes is given. Section 2.1 describes the basic principle of the formation of scour holes in heterogeneous subsoil. This section is followed by Section 2.2, which includes an elaboration of the hydrodynamic processes in scour holes in heterogeneous subsoil. Some important relations for calculation of the erosion process and scouring are described in Section 2.3. Section 2.4 concludes on the findings in this chapter and determines the questions that are unanswered yet. Appendix A contains complementary information on flow, erosion, sediment transport and a general description of the development of scour holes.

2.1. Formation of scour holes in heterogeneous subsoil

In general, scouring of a river bed happens when the local sediment transport exceeds the sediment supply from upstream. The difference between the two can be the result of a difference in flow velocity and turbulence (hydrodynamic conditions) or a difference in the river bed material (erosive capacity). Scour around structures is mostly caused by the former, as the structures influence the flow field (Schierreck, 2012).

The scour situation that is examined in this research focuses on the scouring in heterogeneous subsoil. Heterogeneous subsoil consists of different types of soil. The formation of scour holes in heterogeneous subsoil is the result of differences in river bed material. The river bed of the Rhine-Meuse Delta mostly consists of sand, clay and peat (Sloff et al., 2013). Sand is a material which is highly erodible, whereas clay and peat are poorly erodible. A local incision of a sand layer between two clay or peat layers, as illustrated in Figure 2.1, results in a difference between the local sediment transport and the supply from upstream. The sediment transport at the sand layer is high, as the sand is easily eroded by the flow. The sediment supply from upstream is low, as the clay or peat layer is poorly erodible and therefore stays mainly intact. This results in scouring of the sand layer, forming the large scour holes that are found all over the Rhine-Meuse Delta.

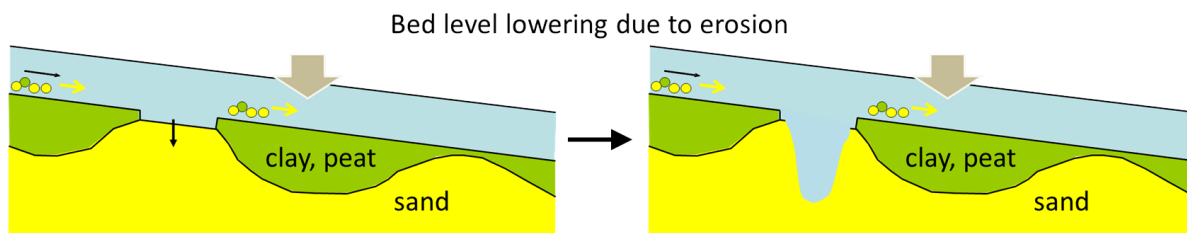


Figure 2.1: Schematical representation of the formation of scour holes in heterogeneous subsoil (Huisman et al., 2016).

2.2. Hydrodynamic processes in scour holes in heterogeneous subsoil

The available literature on the development of scour holes in general is described in Appendix A.3. At this moment, mostly empirical relations are available to describe the development of a scour hole. In order to gain more knowledge on the physics of scour hole development, the details of the hydrodynamics and flow patterns inside a scour hole have to be understood. In addition, the formation in heterogeneous subsoil adds extra complexity to the scour hole shape and growth, which has rarely been investigated. This section will give an overview of the available knowledge.

A schematization of the flow zones inside a two-dimensional scour hole is shown in Figure 2.2. These flow zones resemble the zones in a Backward Facing Step (BFS) case (Hoffmans and Verheij, 1997). This case is described first, as abundant research is carried out on BFS cases. After that, the research on flow in a two-dimensional scour hole with a non-erodible edges is described. Finally, knowledge on a three-dimensional scour hole with a poorly erodible top layer is presented.

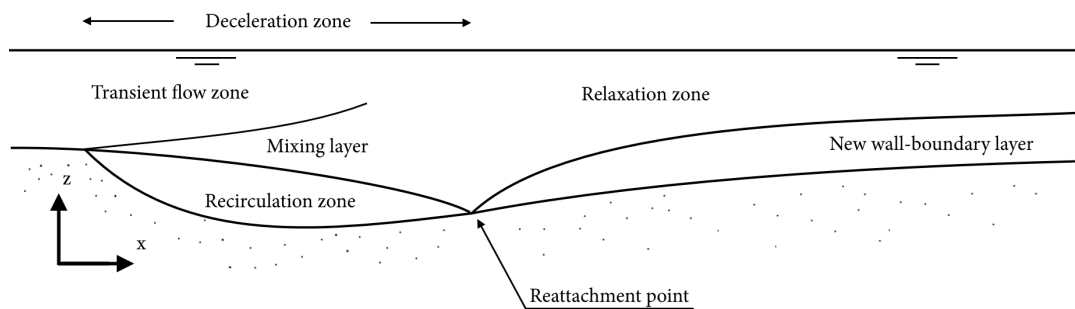


Figure 2.2: Schematization of the flow regions in a scour hole, based on (Hoffmans and Booij, 1993a).

2.2.1. Backward facing step

The flow patterns in a scour hole are similar to those in a BFS case. The latter is shown in Figure 2.3. This flow situation is studied extensively by many researchers. Some of these studies will be referenced, in order to be able to describe the important processes in a scour hole in heterogeneous subsoil more broadly.

Bradshaw and Wong (1972) describe the results of existing and new experiments with a BFS to demonstrate the complicated nature of the flow. In this study the flow behind a BFS is divided in five regions with different characteristics: the original shear layer, the new shear layer, the reattachment point, the recirculation region and the new sub-boundary layer. These regions will be described consecutively in this section.

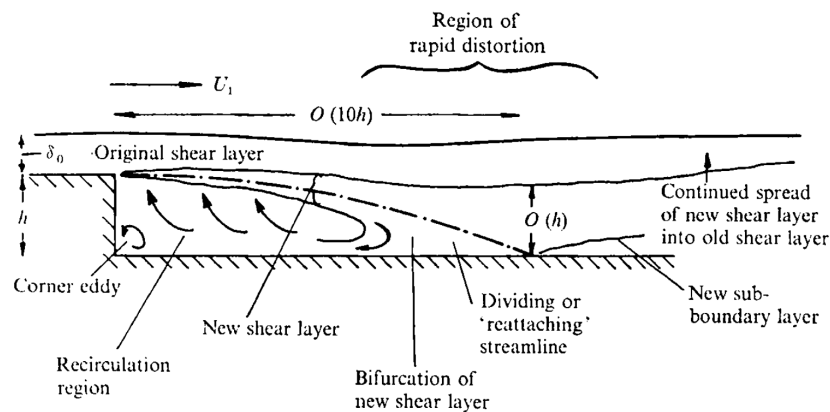


Figure 2.3: Schematization of the flow regions in a BFS situation (Bradshaw and Wong, 1972).

Original shear layer

The original shear layer has a fully developed velocity profile upstream of the step and is influenced by side effects of the flow separation, like curvature of the streamlines and the region of rapid distortion induced by the pressure field near reattachment.

New shear layer (mixing layer)

A shear layer is generated at about one step size downstream of the step. The new shear layer makes the velocity profile resemble more to a Gaussian profile, instead of the log-law profile upstream of the step. Separation eddies are formed in the shear layer. They grow due to the entrainment of surrounding fluid. This process is similar to processes in a ordinary turbulent mixing layer (Nakagawa and Nezu, 1987).

According to Tani et al. (1961), the turbulence intensity and shear stresses increase when moving further downstream in the mixing layer. The positions of maximum turbulence and shear stress roughly coincide with the mean dividing streamline, as can be seen in Figure 2.4 (lower part). The positions of maximum turbulence and shear stress deviate outwards from the streamline as the reattachment point is approached. Bradshaw and Wong (1972) state that the increase in turbulence intensity and shear stress is a result of the backflow in the recirculation region, as it increases the effective velocity difference across the shear layer. The recirculation and re-entrainment of the fluid also tend to increase the turbulent intensity and shear stress in this layer.

Reattachment point

At the reattachment point the new shear layer splits in two. Part of the flow moves upstream into the recirculation zone, and the other part flows downstream into the new sub-boundary layer. This bifurcation of the flow produces large and immediate changes in the portion of the flow that continues to flow downstream. As a result, the turbulent shear stresses and the turbulence length scales decrease rapidly in that direction. However, the flow in the area around the reattachment point has the highest attack on the bed. The reattachment point is located at a distance of 5-8 times the step size downstream of the step (Tani et al., 1961; Bradshaw and Wong, 1972; Nakagawa and Nezu, 1987).

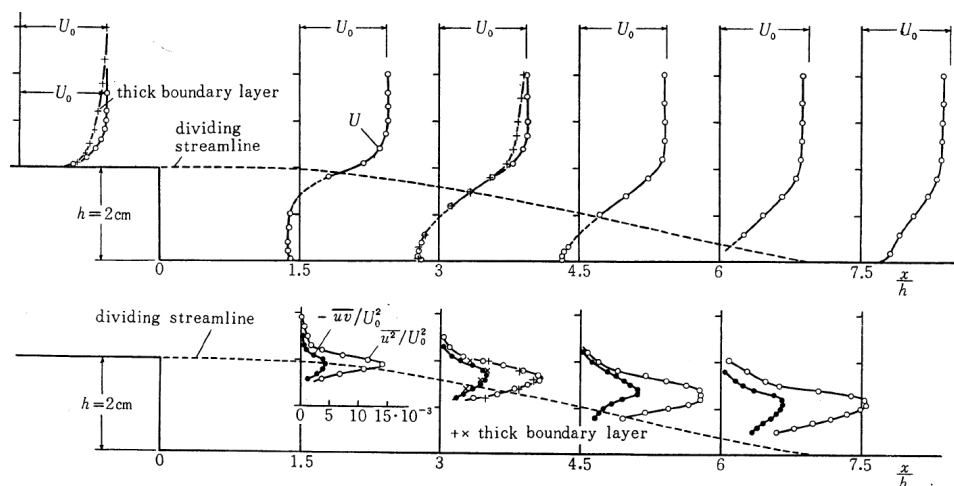


Figure 2.4: Upper: longitudinal component of the flow velocity at a backward facing step. Lower: turbulence intensity and turbulent shear stress at a backward facing step (Tani et al., 1961).

Recirculation zone

A portion of the flow at the reattachment point flows back upstream near the bed. This is visible in Figure 2.4 (upper part). According to Nakagawa and Nezu (1987) the turbulent energy is mostly dissipated in the recirculation zone. The fluctuations in horizontal velocity are nearly equal to the fluctuations in vertical velocity, making a non-hydrostatic approach necessary.

New sub-boundary layer

The zone downstream of the reattachment point is called the new sub-boundary layer. Tani et al. (1961) state that the turbulence intensity and shear stresses decrease in this zone. A new system of turbulence and shear stress develops in the new sub-boundary layer. According to Bradshaw and Wong (1972) the formation of a fully developed boundary layer is a slow process and takes approximately 30 times the step size in horizontal direction in a fairly simple case. In the fully developed case, the maximum shear stress is located at the water surface.

2.2.2. Two-dimensional scour hole with non erodible edges

The first experiments on scour hole growth in heterogeneous subsoil were carried out by [Van Zuylen \(2015\)](#). In a straight flume with a width of 0.4 m and a depth of 0.13 m, the sand was covered by two steel plates, representing the non erodible layer. In the opening between the plates a scour hole could form. As the flume and the steel plates were uniform in the lateral direction, the experiment is considered 2DV. The development of the scour hole and the processes inside the hole are described in this section.

Development stages

As described in Section [A.3.1](#), the formation and development of a scour hole can be divided in four stages ([Zanke, 1978](#)). For the description of the development of the scour hole in the experiments by [Van Zuylen \(2015\)](#), the two middle stages are combined. Three stages remain: the initial scouring stage (initiation), the developed scouring stage (development and stabilization) and the equilibrium stage. These three stages are described below.

Initial scouring stage

In the initial scouring stage a flat bed is present, see [Figure 2.5](#). The water is flowing over the bed with an equilibrium velocity profile. If the flow velocity is larger than the critical velocity of the sediment, the grains will start to move and form a small hole. For gentle upstream slopes of the hole, the flow is able to stay attached to the bed. This process will be present until the scour hole gets deeper and the upstream slope gets steeper. According to [Chandavari and Palekar \(2014\)](#), flow starts to separate at bed slopes of 7° . When the steeper slope causes the flow to separate, a recirculation zone and reattachment point are formed, in accordance with a BFS case. This is where the developed scouring stage starts and the initial scouring stage ends.

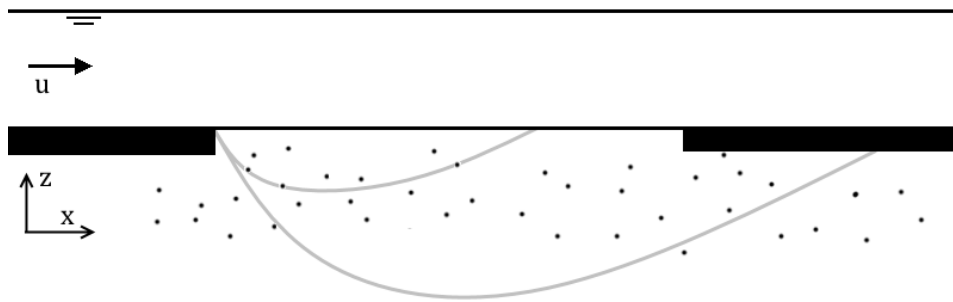


[Figure 2.5](#): Schematization of the side view of the initial scouring stage of a scour hole between two steel plates (black rectangles). The gray profiles show the other scouring stages. The area with black dots indicates a sandy area.

Developed scouring stage

In the developed scouring stage, the scour hole gets deeper and expands in downstream direction. The upstream slope remains attached to the steel plate and the angle of the slope is constant.

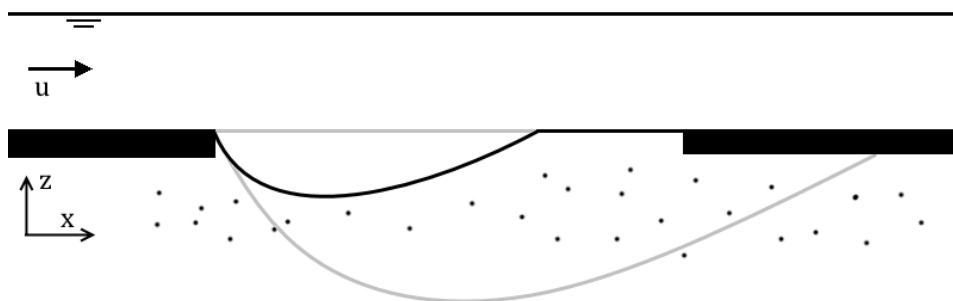


[Figure 2.6](#): Schematization of the side view of the developed scouring stage of a scour hole between two steel plates (black rectangles). The gray profiles show the other scouring stages. The area with black dots indicates a sandy area.

Equilibrium stage

The final stage is the equilibrium stage. This is shown in Figure 2.7. In this stage, the scouring process has come to an end and the scour hole does not change anymore. In order to reach this stage, all the processes have to reach an equilibrium. In the laboratory experiments by Van Zuylem (2015), the equilibrium stage was never reached. The experiments always included undermining at the downstream edge of the hole, which will be present in the equilibrium stage as well. In the experiments by Koopmans (2017) and Stenfert (2017), this was also observed.

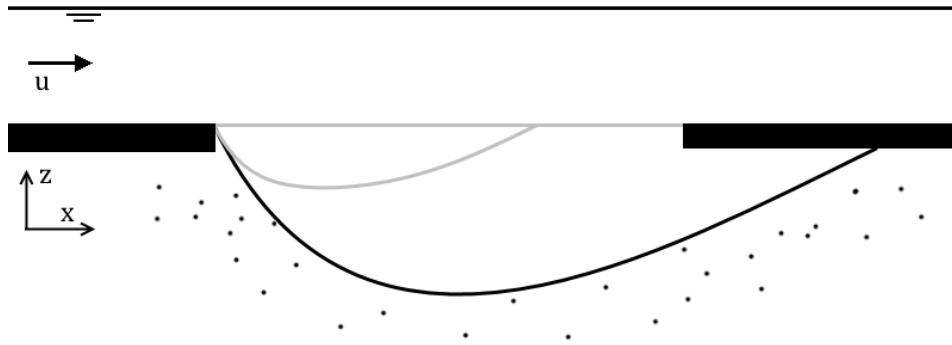


Figure 2.7: Schematization of the side view of the equilibrium stage of a scour hole between two steel plates (black rectangles). The gray profiles show the other scouring stages. The area with black dots indicates a sandy area.

Hydrodynamic processes in the developed scouring stage

In the developed scouring stage, a number of different hydrodynamic processes is present. Below an overview of the flow processes is given, together with the hypothesized main driving mechanisms.

- **Longitudinal recirculation**

The main flow characteristic in the developed scouring stage is the separation at the upstream edge and recirculation of the flow in longitudinal direction. This phenomenon is sketched in Figure 2.8. The driving mechanism for this process is the pressure distribution, see the insets in Figure 2.8. Just upstream of the edge, the pressure is lower than just downstream of the edge, because the flow velocity is higher just upstream. The pressure difference separates the streamlines from the bed. After the flow separation, the streamlines move down because of the mixing layer that is present and in this way the reattachment point is formed. According to Hoffmans and Booij (1993a), the reattachment point is located around 6 times the scour depth downstream of the upstream edge of the hole. At the reattachment point, a very high pressure is present because of the stagnation of flow. The local high pressure forces the flow to the sides. Part of the flow moves upstream, resulting in the flow recirculation.

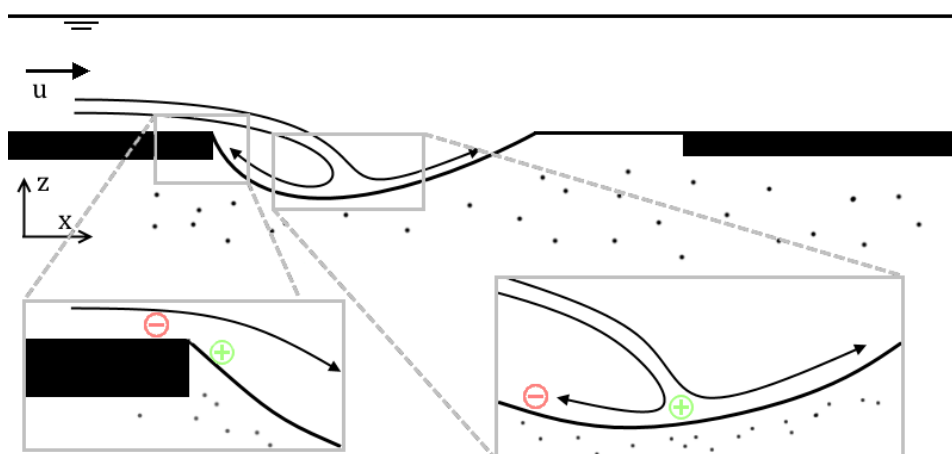


Figure 2.8: Longitudinal recirculation in a scour hole. The black arrows represent the streamlines of the flow. Two close-up locations are shown: left the flow separation at the upstream edge and right the reattachment point. The + and - signs represent areas with respectively high and low pressure.

- **Mixing layer**

Together with the flow separation, a mixing layer forms behind the edge of the scour hole, see Figure 2.9. The characteristics of this mixing layer resemble those of the new shear layer described in Section 2.2.1. The velocity difference between the flow in the scour hole and the flow above the scour hole results in a mixing layer that grows when moving downstream. According to Uijtewaal (2011), the width of the mixing layer grows according to Equation (2.1). The backflow near the bed has a magnitude of approximately 30% of the mean flow velocity, in case of a backward facing step. For now, this is assumed to be valid in the situation with a scour hole. From the equation and this statement follows that the shape of the mixing layer is the same for different values of the upstream velocity and the width grows linearly with distance. The mixing layer forces the flow lines to move downwards. Also, it influences the turbulence intensity near the reattachment point.

$$\frac{d\delta_m}{dx} = \alpha_{\delta_m} \frac{u_{L2} - u_{L1}}{\frac{1}{2}(u_{L1} + u_{L2})} \quad (2.1)$$

Where:	δ_m	[m]	Thickness of the mixing layer
	x	[m]	Coordinate in streamwise direction
	α_{δ_m}	[-]	Coefficient for thickness of the mixing layer, $\alpha \approx 0.085$
	u_{L1}	[m/s]	Flow velocity in streamwise direction in layer 1
	u_{L2}	[m/s]	Flow velocity in streamwise direction in layer 2

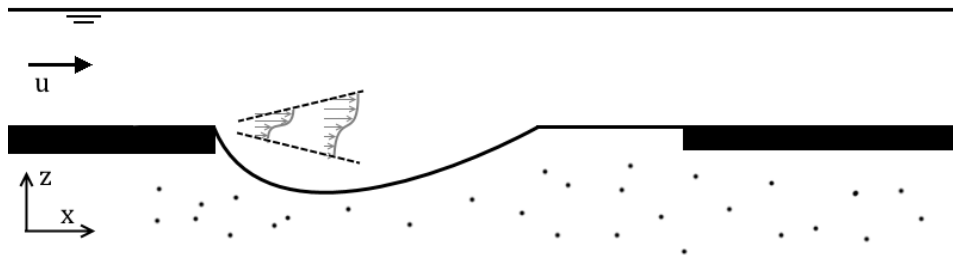
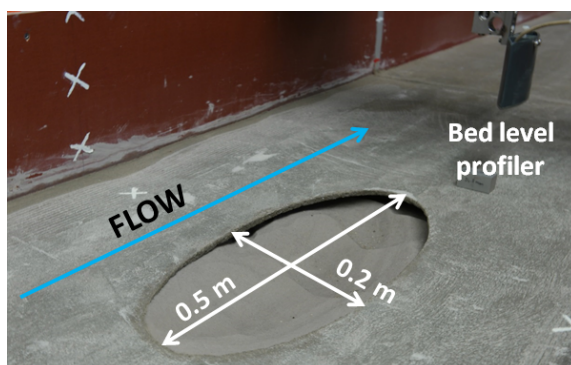


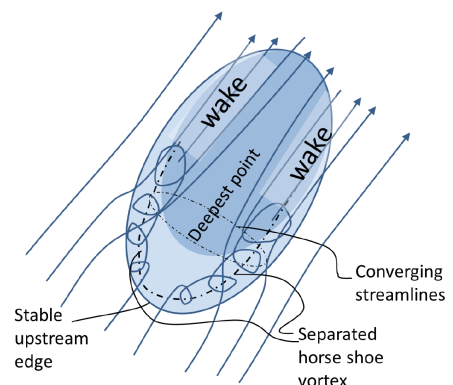
Figure 2.9: Mixing layer in a scour hole. The gray arrows represent the local velocity profile and the dotted black lines are the edges of the mixing layer.

2.2.3. Three-dimensional scour hole

A three-dimensional scouring case is examined by Uijtewaal et al. (2016), Koopmans (2017) and Stenfert (2017). In these experiments, the poorly erodible layer covering the sand is represented by a concrete layer. In the middle of the concrete layer, an oval hole is made and the underlying sand layer is exposed to the flow, see Figure 2.10a. In this way, the scour hole can be formed in the oval section. Schematic drawings of the resulting flow lines are given in Figures 2.10b and 2.11.



(a) Picture of the laboratory experiment by Koopmans (2017).



(b) Schematization of the three-dimensional flow in the experiment by Uijtewaal et al. (2016).

Figure 2.10: Experiments by Koopmans (2017) and Uijtewaal et al. (2016).

Uijttewaal et al. (2016) and Koopmans (2017) expected that the three-dimensional experiment would have a larger maximum scour depth when compared to the two-dimensional case by Van Zuylen (2015), because of the three-dimensional flow structures and the attraction of flow by the hole. On the other hand, the smoother upstream bed would give rise to a smaller maximum scour depth, as this causes a lower turbulence intensity and smaller length scales near the bed. The three-dimensional effects are expected to be the dominant factor, as the scouring in the three-dimensional situation is deeper.

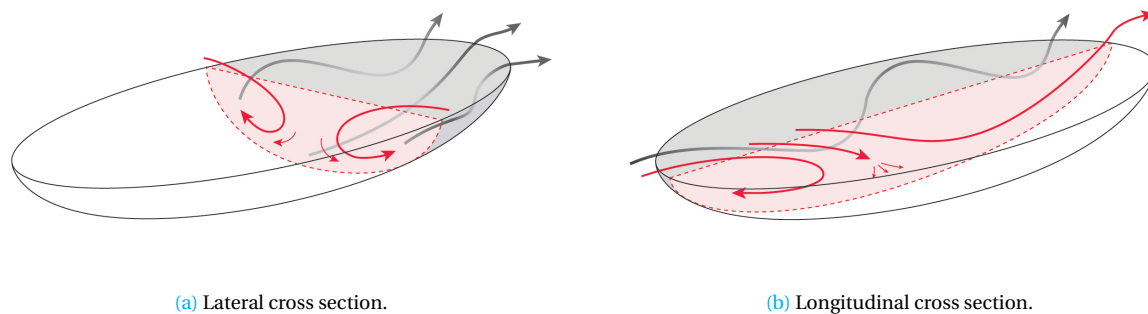


Figure 2.11: Schematic representation of flow lines in the experiment by Stenfert (2017). The red arrows show flow lines in the red colored cross sections, the black arrows show flow lines in the gray part of the hole.

Recirculation zone

In the three-dimensional scouring situation a recirculation zone emerges at the upstream edge. This recirculation zone has the same characteristics as the one described in Section 2.2.2. The only difference is the influence of the curvature of the upstream edge. This makes the recirculation zone being curved as well, when seen from the top.

Horseshoe vortex

At the upstream edge of the hole a horseshoe shaped vortex emerges. The vortex is curved with the edge, and is assumed to be a result of the flow separation at this location (Uijttewaal et al., 2016). At this side of the hole, a small lateral component of the flow takes the flow lines to the center of the hole. The converged flow is drawn to the bed, where the deepest scour is found. This is just downstream of the reattachment point. Further downstream inside the scour hole, the vortex breaks down in a less structured wake, with a slightly larger turbulence intensity. According to Uijttewaal et al. (2016) the erosion in this part of the hole is stronger. The wake widens with a 'natural' angle of 1:8. Due to this, the streamlines diverge and the turbulence intensity decreases, causing a slower scouring process at the downstream half of the hole.

In the three-dimensional scour hole a lateral recirculation is observed, see Figure 2.12. This recirculation can be explained using the pressure differences between a location inside the hole (1) and outside the hole (2). Due to the larger depth, the pressure is higher in the hole, which makes the flow close to the bed move out of the scour hole. Due to continuity, this effect drags the flow lines from higher in the water column into the scour hole. These flow lines come from upstream, as there is momentum in horizontal direction everywhere in the scour hole. The lateral recirculation is expected to feed the horseshoe vortex with momentum, as it has rotation in the same direction.

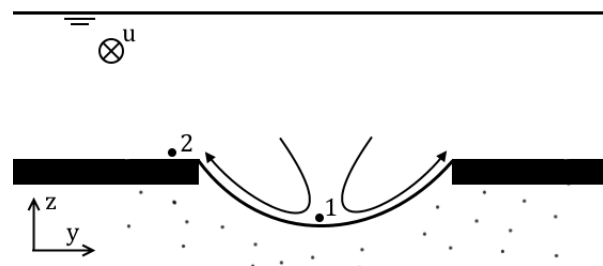


Figure 2.12: Lateral recirculation in a scour hole.

Flow contraction

When seen from above, the flow lines are contracting above the scour hole, see Figure 2.13a. This phenomenon could be caused by two effects. In the first place this could be the case due to the redistribution of momentum in the cross section at the location of the hole. This redistribution results in a different distribution of the discharge, as the discharge in the deeper section becomes larger. When comparing two cross sections, one more upstream from the hole (cross section 1) and one in the hole (cross section 2), relatively more discharge is flowing through the middle section in cross section 2. This discharge comes from the side sections, as the principle of continuity holds. Due to this fact, the flow lines from the side section contract to the middle section.

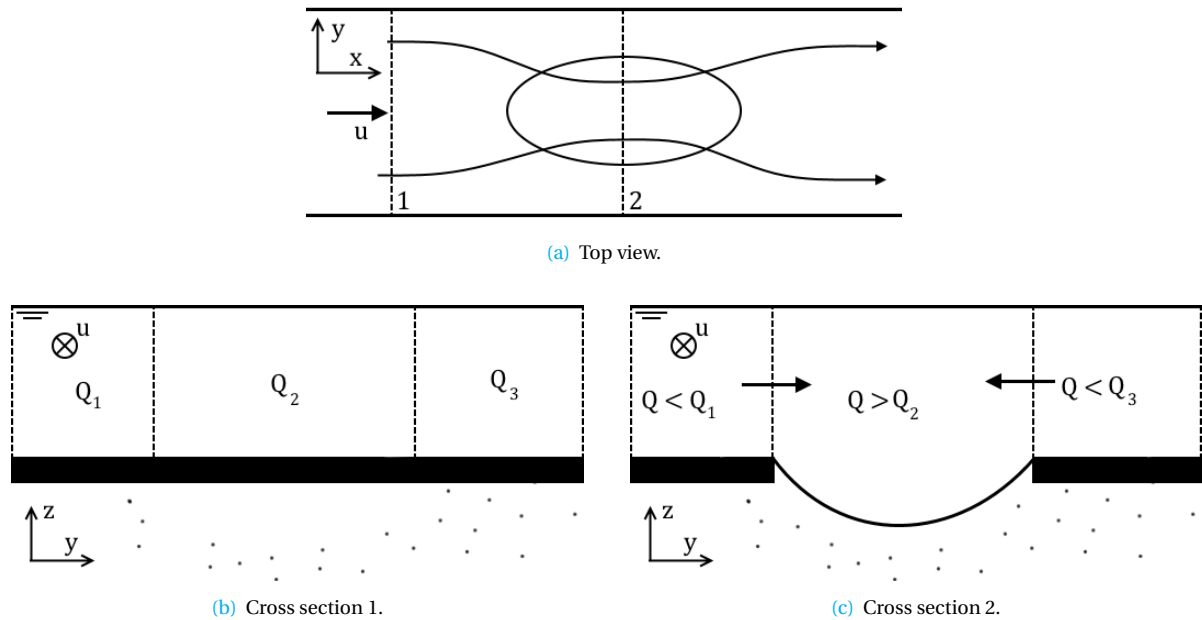


Figure 2.13: Flow contraction above a scour hole.

An additional process that enhances flow contraction is the principle of conservation of potential vorticity. This can only play a role in a three-dimensional scour hole, as it needs a velocity gradient in lateral direction. When this is present, the fluid tends to rotate, which is called vorticity. The potential vorticity of a fluid is considered to be constant in absence of vorticity inputs. The potential vorticity is given in Equation (2.2) (Pietrzak, 2015).

$$\frac{\omega}{h} = \text{constant} \quad (2.2)$$

Where: ω [s⁻¹] Vorticity
 h [m] Water depth

Upstream of the scour hole, the flow is in equilibrium and therefore, no gradients in lateral direction are present. Inside the scour hole, gradients are present, resulting in the presence of vorticity. At the downstream edge the depth gets smaller, and therefore the vorticity gets larger, according to Equation 2.2. A larger vorticity results in the diverging of streamlines downstream of the scour hole.

2.2.4. Analogy with flow around a circular object

The formation of a horseshoe vortex is a phenomenon that is also observed in situations of flow around a circular object. This flow situation is widely investigated and many experiments have been performed to understand the vortex system. In this section, some of these studies are described, in order to obtain the important processes in formation of the horseshoe vortex in the scour hole.

Dargahi (1989) carried out experiments with a circular cylinder mounted vertically on a flat wall. The obtained flow field around the object was essentially a three-dimensional separated boundary layer flow. The many different aspects of this type of flow interact in a complicated way.

A relatively large secondary flow region and skewed velocity distributions are the main characteristics of the flow. The pressure gradient normal to the main flow direction is causing the skewness. The boundary layer upstream of the cylinder has to withstand a strong pressure gradient, which is set up by the cylinder. As a result of this a flow separation region develops, where a vortex system is developed and stretched around the cylinder like a horseshoe (see Figure 2.14).

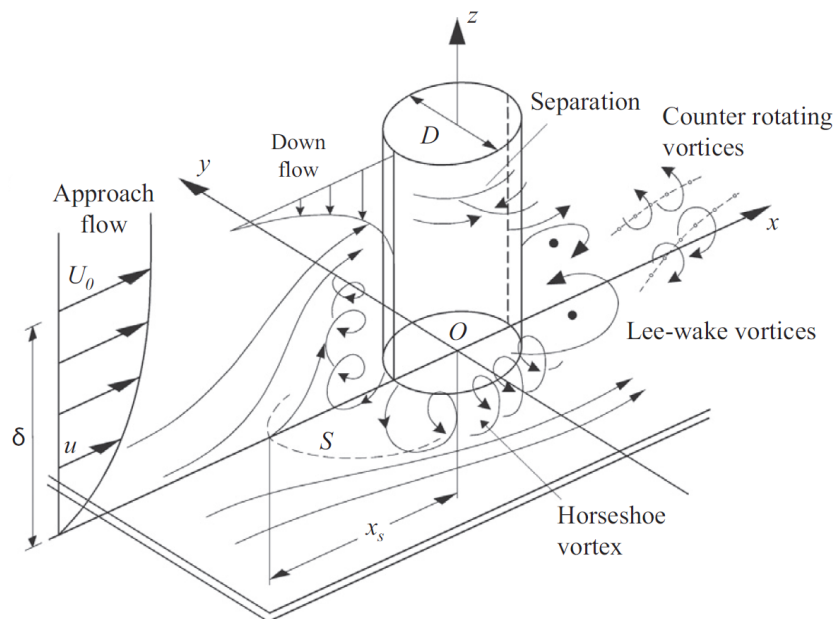


Figure 2.14: Flow regime around a circular object. S denotes the separation line (Baykal et al., 2017).

The horseshoe vortices have a periodical character. The characteristics of the vortex depend on the diameter of the cylinder, the mean flow depth, the flow velocity, the bed roughness and the boundary layer thickness. The horseshoe vortex is the most important phenomenon in the scouring process around a cylinder (Dargahi, 1989).

Muzzammil and Gangadhariah (2003) performed more experiments, in order to obtain time-averaged characteristics of the vortex. The study reveals that the mean size of the horseshoe vortex is approximately 20% of the diameter of the cylinder and the tangential velocity of the vortex is around 50% of the mean velocity. During the development of the scour hole around the cylinder the horseshoe vortex sinks into the hole and increases linearly in size with the depth of the scour.

The main cause for the presence of the horseshoe vortex in situations with a flow around a circular object is the geometry of the object. The curved surface makes the vortex move around the pile in a horseshoe shaped vortex. In the case of three-dimensional scour in the oval shaped hole, the upstream edge is also curved. This curve forces the vortex into the horseshoe shaped form.

2.3. Erosion process and sediment transport

Erosion of the subsoil is the basic principle in the scouring process. In the past, researchers investigated the erosion process in many different situations. In this section, the general erosion process is described, including the stability of the grains, sediment transport and the stability of a slope. Appendix A.2 gives additional information.

2.3.1. Stability of grains

In this section the stability of grains is described. Two researchers, Izbash and Shields, developed their own approach to calculate the stability of grains in a bed. The Izbash approach is described in Appendix A.2 and Shields' approach is elaborated on in this section.

Shields approach

According to Hoffmans and Verheij (1997) the first one to describe the initiation of motion of grains in a non-cohesive material was Shields. Assuming uniform flow and a channel with a much larger width than depth, he stated that the shear stress is the active force working on the sediment grains. Shields found a relation based on the characteristics of the flow and sediment in the bed. The mobility parameter of Shields is calculated with Equation (2.3) (Schiereck, 2012).

$$\Psi_c = \frac{\text{load}}{\text{strength}} = \frac{\tau_c d^2}{(\rho_s - \rho_w) g d^3} = \frac{u_{*,c}^2}{\Delta g d} = \frac{\bar{u}_c^2}{C^2 \Delta d} \quad (2.3)$$

Where:	Ψ_c	[-]	Critical mobility parameter (Shields)
	τ_c	[N/m ²]	Critical shear stress
	d	[m]	Grain diameter
	ρ_s	[kg/m ³]	Density of sediment
	ρ_w	[kg/m ³]	Density of water
	g	[m/s ²]	Gravitational acceleration, $g = 9.81 \text{ m/s}^2$
	$u_{*,c}$	[m/s]	Critical bed shear velocity
	Δ	[-]	Relative density
	\bar{u}_c	[m/s]	Mean critical flow velocity
	C	[m ^{1/2} /s]	Chézy roughness coefficient

Initially, Shields based his critical mobility parameter on the movement of uniform grains on a flat bed. However, in practice a bed never has a uniform distribution of grain size and placement and the flow velocity is never uniform (due to turbulence and other effects), so Shields drew a broad belt instead of a single curve. Breusers adapted the Shields curve and divided it into several stages. This graph is shown in Figure 2.15. The Rouse curve, which is the initial Shields curve, is close to stage 6, which includes 'permanent particle movement at all locations' (Hoffmans and Verheij, 1997).

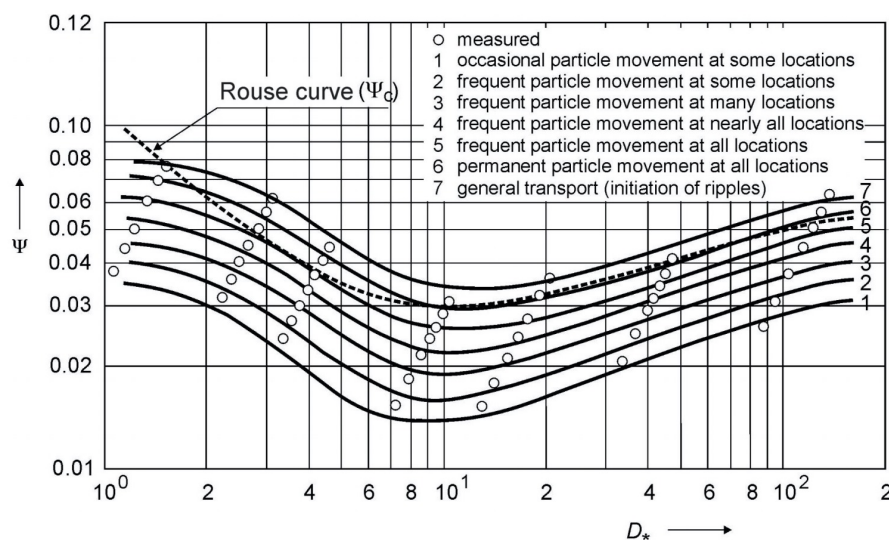


Figure 2.15: Shields diagram, adapted by Breusers (Hoffmans and Verheij, 1997).

The horizontal axis in Figure 2.15 shows values of D_* , which is calculated with Equation (2.4) (Hoffmans and Verheij, 1997).

$$D_* = d \left(\frac{\Delta g}{\nu^2} \right)^{1/3} \quad \text{with} \quad \nu = \frac{40 \cdot 10^{-6}}{20 + \theta} \quad (2.4)$$

Where: D_* [-] Dimensionless grain diameter
 ν [m^2/s] Kinematic viscosity
 θ [$^\circ\text{C}$] Temperature

2.3.2. Sediment transport

Flowing water is able to transport sediment. The flow velocity of the water and the sediment characteristics determine the amount of sediment that is transported. According to Jansen et al. (1994), sediment transport can be classified in two categories: bed load transport and suspended load transport. The rolling, sliding and jumping over the bed by sediment particles is part of the bed load transport. Sediment particles that are suspended in the fluid for a while are part of the suspended load transport. The origin of the sediment for both transport mechanisms is different. Bed load transport only moves bed material load, while suspended load transport moves both bed material load and wash load. Wash load consists of finer sediment than bed material. The transport of wash load is not related to the transport capacity of the flow. The transport mechanisms and origin of the sediment are shown in Figure 2.16.

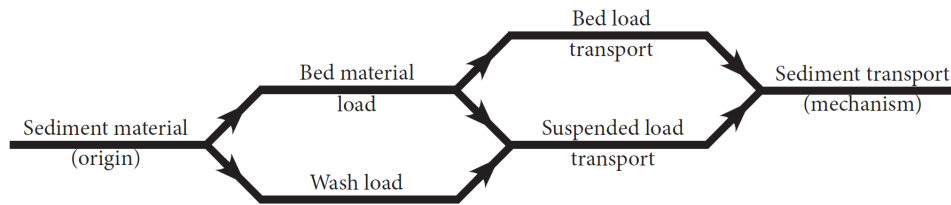


Figure 2.16: Classification of sediment transport, based on Jansen et al. (1994).

In the simplified situation of a uniform, flat bed with uniform flow, the sediment transport capacity is constant and no changes in the bed will be observed. As soon as there is a change in flow velocity, sediment characteristics or another parameter that influences the sediment transport capacity, a gradient in sediment transport will develop. This gradient causes the bed to degrade (positive gradient) or accrete (negative gradient). Therefore the Exner principle states: “erosion occurs in areas of accelerating flow whereas sedimentation occurs in areas of decelerating flow” (Crosato, 2015). The processes of bed changes over time are included in the Exner principle. It is based on the law of mass conservation for sediment. This is expressed in Equation (2.5) (see also Figure 2.17).

$$\frac{\partial z_b}{\partial t} + \frac{\partial q_s}{\partial x} = 0 \quad (2.5)$$

Where: z_b [m] Bed level elevation
 t [s] Time
 q_s [m^2/s] Rate of transported bed material load including pores per unit width

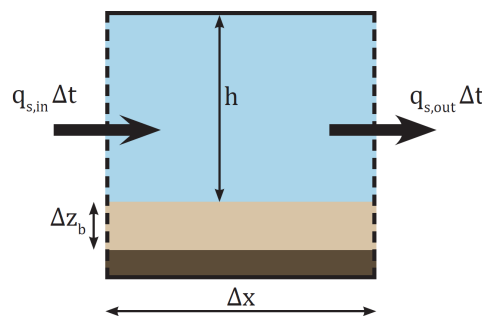


Figure 2.17: Control volume for derivation of the sediment balance, based on Crosato (2015).

Many transport formulas are available for the calculation of the bed load transport. A widely known relation is the semi empirical formula for the calculation of the bed load transport at a flat bed by Meyer-Peter and Müller (1948). Equation (2.6) shows the formula.

$$\Phi = 8 (\Psi - \Psi_c)^{3/2} \quad (2.6)$$

Where: Φ [-] Dimensionless bed load transport rate
 Ψ [-] Mobility parameter (Shields)

The bed load transport rate can be derived from the dimensionless parameter with Equation (2.7).

$$\Phi = \frac{q_s}{d\sqrt{\Delta g d}} \quad (2.7)$$

Sediment transport on a longitudinal slope

In a scour hole, sediment transport occurs not only at the flat bed, but also at the slopes of the hole. The effect of a non-horizontal bed cannot be neglected in the calculations. Therefore, an adaptation of the Shields parameter and the formula by Meyer-Peter and Müller (1948) is needed. Damgaard et al. (1997) describes the adaptation of the equations. The Shields parameter is multiplied by a factor that includes the bed slope and the angle of repose of the sediment. This can be seen in Equation (2.8).

$$\frac{\Psi_{c,\beta}}{\Psi_c} = \frac{\sin(\phi + \beta)}{\sin(\phi)} \quad (2.8)$$

Where: $\Psi_{c,\beta}$ [-] Mobility parameter on a longitudinal slope (Shields)
 ϕ [°] Angle of repose of sediment
 β [°] Angle of the slope

The bed load transport formula by Meyer-Peter and Müller (1948) is adapted by using the Shields parameter for transport on a longitudinal slope and by introducing a slope factor. This slope parameter is equal to 1 for positive values of the bed slope ($\frac{dz_b}{dx} > 0$) and has a higher value for negative values of the bed slope ($\frac{dz_b}{dx} < 0$). Equation (2.10) shows the calculation of the slope factor and Equation (2.9) shows the adapted formula by Meyer-Peter and Müller (1948).

$$\Phi_\beta = 8(\Psi - \Psi_{c,\beta})^{3/2} f_{\text{slope}} \quad (2.9)$$

$$f_{\text{slope}} = \begin{cases} 1 + 0.8 \left(\frac{\Psi_c}{\Psi}\right)^{0.2} \left(1 - \frac{\Psi_{c,\beta}}{\Psi_c}\right)^{\left(1.5 + \frac{\Psi}{\Psi_c}\right)} & \text{for } -\phi < \beta \leq 0 \\ 1 & \text{for } 0 < \beta < \phi \end{cases} \quad (2.10)$$

Where: Φ_β [-] Dimensionless bed load transport rate on a longitudinal slope
 f_{slope} [-] Slope factor

2.3.3. Stability of the upstream slope in a scour hole in heterogeneous subsoil

In the researches by Van Zuylen (2015), Koopmans (2017) and Stenfert (2017) the angle of the upstream slope turned out to be constant during the developed scouring stage. This phenomenon is probably the result of a balance in forces. The balance in forces on a horizontal bed is described in Appendix A.2. For the upstream slope, the situation changes slightly. The adapted situation is shown in Figure 2.18.

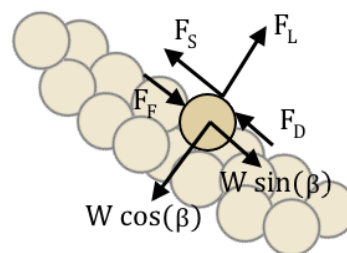


Figure 2.18: Forces on a grain at a slope.

The slope stays stable when the balances of the parallel forces and perpendicular forces hold. Equation (2.11) shows the balances and the result, based on the relations described in Appendix A.2.

$$\left. \begin{aligned} \Sigma H = 0: & \quad F_D + F_S = F_F + W_s \sin \beta \\ \Sigma V = 0: & \quad F_L = W_s \cos \beta \end{aligned} \right\} \beta \propto ud \quad (2.11)$$

Where:	ΣH	[N]	Sum of the forces in horizontal direction
	ΣV	[N]	Sum of the forces in vertical direction
	F_D	[N]	Drag force on a grain
	F_S	[N]	Shear force on a grain
	F_F	[N]	Friction force on a grain
	W_s	[N]	Weight of a grain
	F_L	[N]	Lift force on a grain
	u	[m/s]	Flow velocity in streamwise direction

According to this approach, the constant slope at the upstream edge in different laboratory experiments is a result of a constant balance between the flow velocity and the grain diameter. When the same sediment is used in different experiments, the local flow velocity at the upstream slope should be the same too. This local flow velocity is a combination of the mean flow velocity and turbulence influences. A constant slope means that the combination of those two is constant.

2.4. Conclusion

In this chapter, the basic principle of the formation of scour holes in heterogeneous subsoil is described, accompanied by findings in previous research on the hydrodynamic processes in the scour holes. Thoughts on the hydrodynamic processes in these scour holes are also described, and the chapter ends with a description of the erosion process and sediment transport.

The knowledge that is gained in this chapter is used to identify the hydrodynamical processes that are preferred to be reproduced by the numerical model. Some of these processes are schematically represented in Figure 2.11. The flow separation and the associated recirculation zone at the upstream slope of the hole are included in Figure 2.11b. The recirculating flow near the bed is expected to be the reason for the constant upstream slope during the scour hole development.

The horseshoe vortex emerges at the upstream edge and flows downstream along the side slopes. The rotating character of this vortex is assumed to be the result of a combination of the flow separation, contraction of flow and the geometry of the upstream edge. Water that flows in from outside the center axis gets diverted into the hole. When the flow line reaches the bed, it flows in upward direction along the side wall. This motion is visualized by the grey arrow in Figure 2.11b. The lateral recirculation that is associated with the horseshoe vortex is included by the red arrows in Figure 2.11a.

Another important process is the contraction of flow into the hole, dragging more momentum inside. Turbulence plays a role in the stirring up of sediment, making it possible to transport the sediment even when the average bed shear stress does not reach the critical value.

All the hydrodynamical processes and structures described above are desired to be reproduced by the numerical model. The influence of the flow and scour hole parameters on the processes is unknown. This will be investigated in this research using the numerical model of the three-dimensional scour hole as measured in the flume experiments by Stenfert (2017). By understanding the hydrodynamic processes, the development of the scour hole over time can be understood in more detail.

Chapter 3

Model Setup

The numerical model that is used for this research is the open-source CFD toolbox OpenFOAM (Open Field Operation And Manipulation), version 3.1-ext 2014. The choice for this model is based on the review of previous numerical studies on scouring situations in Appendix B and the argumentation in Appendix C. This chapter describes the choices that are made when setting up the model. The reference case by Stenfert (2017) is described in Section 3.1. After that, the different aspects of the numerical model are elaborated on. Sections 3.2 and 3.3 give explanations of the turbulence model and the near wall treatment, respectively. The generation of the grid is explained in Section 3.4 and the boundary and initial conditions are described in Section 3.5. Finally, the numerical process is explained briefly in Section 3.6.

3.1. Reference case by Stenfert (2017)

The model that is set up in this research simulates the hydrodynamics in a scour hole from the laboratory experiments by Stenfert (2017). The set-up of the experiments is shown schematically in Figure 3.1. A 12 meter long flume with a concrete bottom is filled with 14 cm of water. An oval shaped hole is made in the middle of the concrete. The hole has a length of 50.4 cm and a width of 22.4 cm. The hydraulic conditions and dimensions of the flume and the hole are listed in Table 3.1. When water is flowing over the hole, sand is eroded and the scour hole forms.

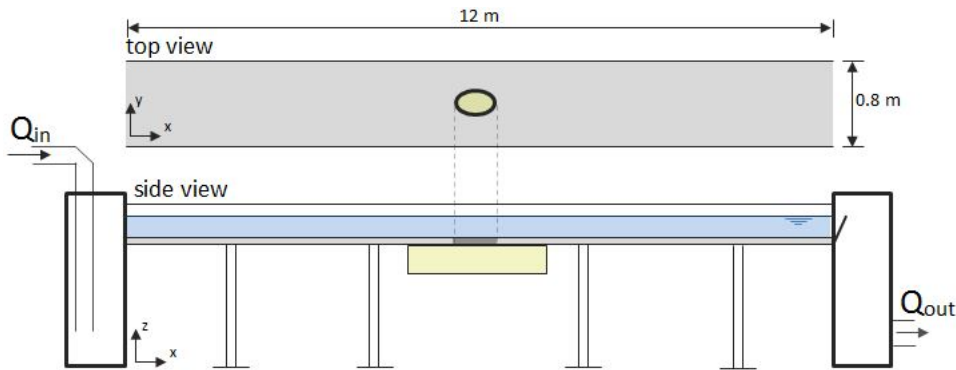


Figure 3.1: Schematization of experimental set-up with a side view and a top view. The flume has a bed of concrete and a box from which sand can erode (Stenfert, 2017).

Table 3.1: Hydraulic conditions and dimensions of the scour hole for the experiments by Stenfert (2017). The parameters are: water depth (h), average flow velocity (\bar{u}), Reynolds number (Re), Froude number (Fr), bed shear velocity (u_\star), Nikuradse roughness of concrete and sand ($k_{n, \text{concrete}}$ and $k_{n, \text{sand}}$) and the length and width of the scour hole (L_{hole} and W_{hole}).

h (cm)	\bar{u} (m/s)	Re (-)	Fr (-)	u_\star (m/s)	$k_{n, \text{concrete}}$ (mm)	$k_{n, \text{sand}}$ (mm)	L_{hole} (cm)	W_{hole} (cm)
14.0	0.36	$5.0 \cdot 10^4$	0.31	0.017	0.6	0.6	50.4	22.4

The hydrodynamics in the hole are modelled for a bed topography at a certain point in time. In this study, the bed topography after 10 hours and 30 hours of experiment are used in the parameter study in Chapter 5. These are taken from *Experiment 2* and *Experiment 3* from the study by Stenfert (2017) respectively. For the description of the bed topography in the model in Section 3.4.2 the values after 10 hours are used.

Many velocity measurements are performed after 15 hours of experiment with a larger hole ($W_{\text{hole}} = 33.6$ cm and $L_{\text{hole}} = 75.6$ cm). These measurements and the bed topography after 15 hours are used in a part of the model validation in Chapter 4.

3.2. Turbulence model

The wide range of possible turbulence closure models is described in Section A.1.5. The characteristics of the different models are shown in Table A.1. The model should be able to capture the hydrodynamic processes that are described in Section 2.2. Adverse pressure gradients and flow separation are playing an important role in the flow inside a scour hole. Therefore, a $k-\omega$ turbulence model is used. From the investigation of previous researches on numerical modelling of scour holes (see Appendix B) follows that the ‘Generalized $k-\omega$ model’ is used successfully by Jacobsen et al. (2014), Baykal et al. (2015) and Baykal et al. (2017).

Generalized $k-\omega$ model

In the original $k-\omega$ model by Wilcox (1988) the specific turbulence dissipation rate, ω , is used as a quantity determining the length scale of the turbulence. The quantity represents the inverse of the timescale on which dissipation occurs (Andersson et al., 2012). An advantage of $k-\omega$ models, when compared to $k-\epsilon$ models, is the fact that $k-\omega$ models have exact equations for ω , which are measurable in a flow. Models with ϵ have complex equations that are not measurable by any degree. Other advantages of the $k-\omega$ model are the reduced mesh resolution demands near the wall and the robustness even for complex applications (Menter and Esch, 2001).

The Generalized $k-\omega$ model by Wilcox (2006) is an improvement of the original $k-\omega$ model. It performs better when predicting attached boundary layers, backward facing steps and mildly separated incompressible flows. It retains the strengths of the $k-\omega$ model from Wilcox (1988), while the free shear flow spreading rates correspond better with measurements. The differences in the equations between the original $k-\omega$ model and the Generalized model by Wilcox (2006) are the addition of the cross-diffusion term and the stress-limiter modification. The cross-diffusion term is used as a solution for the sensitivity to the freestream value of ω in the original model (Wilcox, 2006). It reduces the sensitivity of the model to the finite freestream boundary conditions on turbulence parameters (Wilcox, 2006). The stress-limiter modification introduces the dependence of the kinematic eddy viscosity (ν_T) upon the stress-limited specific turbulence dissipation rate ($\tilde{\omega}$) rather than strictly ω . It limits the magnitude of the eddy viscosity when the turbulence-energy production is larger than the dissipation. This modification of the turbulence model gives more accurate results when simulating shock-separated flows.

The equations of the Generalized $k-\omega$ model are given below. Equation (3.1) describes the kinematic eddy viscosity in the model, including the stress-limiter modification. The turbulence kinetic energy is included in Equation (3.2) and the specific dissipation rate in Equation (3.3). The different terms are specified in these equations. Finally, the closure coefficients and auxiliary relations are given in Equations (3.4) - (3.8).

Kinematic Eddy Viscosity

$$\nu_T = \frac{k}{\tilde{\omega}_T} \quad \tilde{\omega}_T = \max \left\{ \omega_T, C_{\text{lim}} \sqrt{\frac{2S_{ij}S_{ij}}{\beta_\star}} \right\} \quad C_{\text{lim}} = \frac{7}{8} \quad (3.1)$$

Where:	ν_T	[m ² /s]	Kinematic eddy viscosity
	k	[m ² /s ²]	Turbulence intensity
	ω_T	[s ⁻¹]	Specific turbulence dissipation rate
	$\tilde{\omega}_T$	[s ⁻¹]	Stress-limited specific turbulence dissipation rate
	C_{lim}	[m]	Stress-limiter strength
	S_{ij}	[s ⁻¹]	Mean strain-rate tensor
	β_\star	[-]	Closure coefficient in $k-\omega$ model

Turbulent kinetic energy

$$\underbrace{\frac{\partial k}{\partial t}}_{\text{local time derivative}} + \underbrace{u_j \frac{\partial k}{\partial x_j}}_{\text{advection}} = \underbrace{\tau_{ij} \frac{\partial u_i}{\partial x_j}}_{\text{production}} - \underbrace{\beta_* k \omega_T}_{\text{dissipation}} + \underbrace{\frac{\partial}{\partial x_j} \left[\left(\nu + \sigma^* \frac{k}{\omega_T} \right) \frac{\partial k}{\partial x_j} \right]}_{\text{diffusion}} \quad (3.2)$$

Where:	u_i	[m/s]	Flow velocity in i direction
	u_j	[m/s]	Flow velocity in j direction
	x_j	[m]	Coordinate in j direction
	τ_{ij}	[m ² /s ²]	Specific Reynolds stress tensor
	σ^*	[-]	Closure coefficient in k- ω model

Specific turbulence dissipation rate

$$\underbrace{\frac{\partial \omega_T}{\partial t}}_{\text{local time derivative}} + \underbrace{u_j \frac{\partial \omega_T}{\partial x_j}}_{\text{advection}} = \underbrace{\alpha_{k-\omega} \frac{\omega_T}{k} \tau_{ij} \frac{\partial u_i}{\partial x_j}}_{\text{production}} - \underbrace{\beta_{k-\omega} \omega_T^2}_{\text{dissipation}} + \underbrace{\frac{\sigma_d}{\omega_T} \frac{\partial k}{\partial x_j} \frac{\partial \omega_T}{\partial x_j}}_{\text{cross-diffusion}} + \underbrace{\frac{\partial}{\partial x_j} \left[\left(\nu + \sigma \frac{k}{\omega_T} \right) \frac{\partial \omega_T}{\partial x_j} \right]}_{\text{diffusion}} \quad (3.3)$$

Where:	$\alpha_{k-\omega}$	[-]	Closure coefficient in k- ω model
	$\beta_{k-\omega}$	[-]	Closure coefficient in k- ω model
	σ_d	[-]	Cross diffusion coefficient in k- ω model
	σ	[-]	Closure coefficient in k- ω model

Closure coefficients and auxiliary relations

$$\alpha_{k-\omega} = \frac{13}{25} \quad \beta_{k-\omega} = \beta_0 f_\beta \quad \beta_* = \frac{9}{100} \quad \sigma = \frac{1}{2} \quad \sigma^* = \frac{3}{5} \quad \sigma_{do} = \frac{1}{8} \quad (3.4)$$

$$\sigma_d = \begin{cases} 0, & \frac{\partial k}{\partial x_j} \frac{\partial \omega_T}{\partial x_j} \leq 0 \\ \sigma_{do} & \frac{\partial k}{\partial x_j} \frac{\partial \omega_T}{\partial x_j} > 0 \end{cases} \quad (3.5)$$

$$\beta_0 = 0.0708 \quad f_\beta = \frac{1 + 85\chi_\omega}{1 + 100\chi_\omega} \quad \chi_\omega \equiv \left| \frac{\Omega_{ij}\Omega_{jk}S_{ki}}{(\beta_*\omega_T)^3} \right| \quad (3.6)$$

$$\epsilon = \beta_* \omega_T k \quad \ell = \frac{k^{1/2}}{\omega_T} \quad (3.7)$$

$$S_{ij} = \frac{1}{2} \left(\frac{\partial u_i}{\partial x_j} + \frac{\partial u_j}{\partial x_i} \right) \quad \text{and} \quad \Omega_{ij} = \frac{1}{2} \left(\frac{\partial u_i}{\partial x_j} - \frac{\partial u_j}{\partial x_i} \right) \quad (3.8)$$

Where:	β_0	[-]	Closure coefficient in k- ω model
	f_β	[-]	Vortex-stretching function
	σ_{do}	[-]	Cross diffusion coefficient in k- ω model
	χ_ω	[-]	Cross diffusion coefficient in k- ω model
	Ω_{ij}	[s ⁻¹]	Mean rotation tensor
	ϵ	[m ² /s ³]	Turbulence dissipation
	ℓ	[m]	Turbulent length scale
	x_i	[m]	Coordinate in i direction

3.3. Near wall treatment

The necessity of near wall treatment in a numerical model is explained in Section A.1.6. In this section, both the bed and the free surface treatment in the numerical model are described.

3.3.1. Bed treatment

The treatment near the bed is performed using a wall function. The one that is used in the model is developed by [Fuhrman et al. \(2014\)](#). This wall function is based on the velocity profile by [Cebeci and Chang \(1978\)](#), who adapted the velocity profile by [Van Driest \(1956\)](#) in order to include roughness effects in the profile. The friction velocity u_* is determined from the values at the first cell center from the wall, see Equations (3.9), (3.10) and (3.11).

$$\frac{u}{u_\star} = 2 \int_0^{y_c^+} \frac{dy^+}{1 + (1 + 4\kappa^2(y^+ + \Delta y_{cc})^2 C_{cc})^{1/2}} \quad (3.9)$$

$$C_{cc} = \left(1 - \exp\left(-\frac{(y^+ + \Delta y_{cc}^2)}{25}\right) \right)^2 \quad (3.10)$$

$$\Delta y_{cc} = 0.9 \left(\sqrt{k_n^+} - k_n^+ \exp\left(-\frac{k_n^+}{6}\right) \right) \quad (3.11)$$

Where:	y_c^+	[-]	Dimensionless height of the first cell center (y_c/l_\star)
	y^+	[-]	Dimensionless coordinate in wall-normal direction (wall coordinate)
	y_c	[m]	Height of the first cell center ($\Delta y/2$)
	Δy	[m]	Near wall cell height
	κ	[-]	Von Kármán coefficient, $\kappa = 0.4$
	k_n^+	[m]	Dimensionless Nikuradse roughness height

The wall functions for k and ω_T are given by Equations (3.12) and (3.13).

$$\frac{k}{u_\star^2} = \min \left\{ A \Delta y^{+2}, \frac{1}{\sqrt{\beta_\star}} \right\} \quad \frac{\omega_T^v}{u_\star^2} = \max \left\{ \frac{B}{\Delta y^{+2}}, \frac{1}{\sqrt{\beta_\star} \kappa \Delta y^+} \right\} \quad (3.12)$$

$$A = \frac{1}{\delta^{+2} \sqrt{\beta_\star}} \quad B = \frac{\delta^+}{\sqrt{\beta_\star} \kappa} \quad (3.13)$$

Where:	Δy^+	[-]	Dimensionless height of the first cell
	δ^+	[-]	Dimensionless thickness of the boundary layer

During the first model validation study, the accuracy and mesh dependence of the wall function has been tested. This is described in Appendix F. From this study followed that the center of the first grid cell should at least reach up into the buffer layer. For a smooth case, this results in a y^+ value of at least 30. In case of a rough bed, the first cell center should be larger than 0.2 times the Nikuradse roughness height.

In the case of the scour hole from the experiment by Stenfert (2017), the bed roughness is equal to 0.6 mm. This results in a k^+ value of 10, which makes the flow condition in the intermediate rough regime. Therefore, it should meet both conditions mentioned above.

3.3.2. Free surface treatment

The rigid lid approximation is used to represent the free surface. This approximation assumes that the displacements of the free surface are small. In the case of a scour hole, free surface deformations will happen. In general, the rigid lid approximation is justified as long as the Froude number is low. According to Meselhe and Sotiropoulos (2000), the rigid lid approximation gives reasonable results when the Froude number in the simulation lies within the moderate region (Froude numbers below 0.6). The Froude number in the experiments by Stenfert (2017) lies between 0.3-0.4. Therefore, the rigid lid approximation can be used. In the model, the free surface is implemented as a slip boundary. The velocity in vertical direction is set to 0 m/s and in the other directions a zero gradient is induced. The other quantities (p , k and ω) have a zero gradient in all directions. This results in a wall shear stress of 0 N/m² at the free surface. The influence of the rigid lid approximation is discussed in Section 4.4.

3.4. Grid

In this section, the considerations regarding the representation of the bed level in the grid are described. The grids for the different models are based on measurements that are performed during the laboratory experiments. From the measurements, the bed levels are derived and the grid is generated with these bed levels. A description of the main aspects of grid generation is given below. More details can be found in Appendix E.

3.4.1. Coordinate system

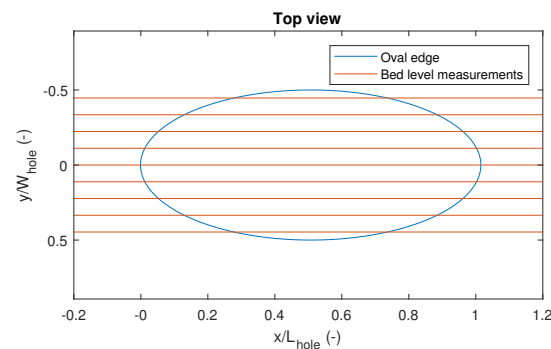
In this research both two-dimensional and three-dimensional simulations are performed. The coordinate systems for both types of simulations are consistent. The streamwise direction is aligned with the x -axis, the lateral direction is aligned with the y -axis and the z -axis describes the vertical direction. For two-dimensional simulations, the lateral direction is left out, as there are only two dimensions, see Figure 3.2a. The three-dimensional coordinate system is shown in Figure 3.2b.



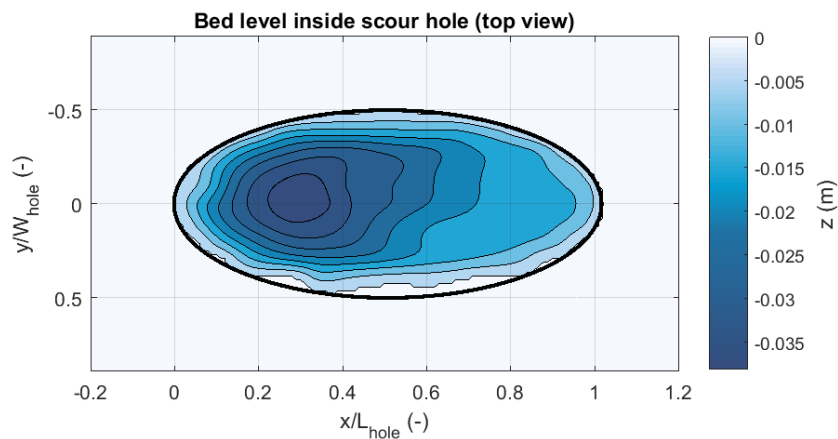
Figure 3.2: Coordinate systems for the two-dimensional and three-dimensional model simulations.

3.4.2. Bed topography

The measurements that are available for grid generation of the three-dimensional scour hole from the experiments by Stenfert (2017) are not covering the entire scour hole. Nine cross sections in streamwise direction are available (see Figure 3.3a), making interpolation and smoothening necessary. The resulting bed level inside the hole is shown in Figure 3.3b. This figure clearly shows a non-symmetrical scour hole and the presence of unrealistic ‘stacks’ of sand near the edge of the hole (the white areas around $y/W_{\text{hole}} = 0.45$ and $x/L_{\text{hole}} = 0.3$ and $0.4 - 0.8$). In the laboratory experiments these stacks are not observed. The non-symmetrical hole will induce non-symmetrical flow features in the hole, which will pollute the flow field and make it much harder to identify the flow structures that might be present. Therefore, generating the grid with inclusion of all measured cross sections is undesired.



(a) Available bed level measurements (Stenfert, 2017).



(b) Bed levels inside the scour hole after interpolation and smoothening.

Figure 3.3: Generation of the non-symmetrical bed.

In order to overcome the problems that arise with a non-symmetrical bed, a method to generate a symmetrical bed is used. Only the bed level measurements in the center axis in streamwise direction are used. Together with the oval-shaped edge of the hole, a symmetrical bed can be generated. A parabola is fitted through the three known points in each lateral cross section. An example of the three points that are used is shown in the front view in Figure 3.4. The symmetrical bed level that is generated using this method is shown in Figure 3.5.

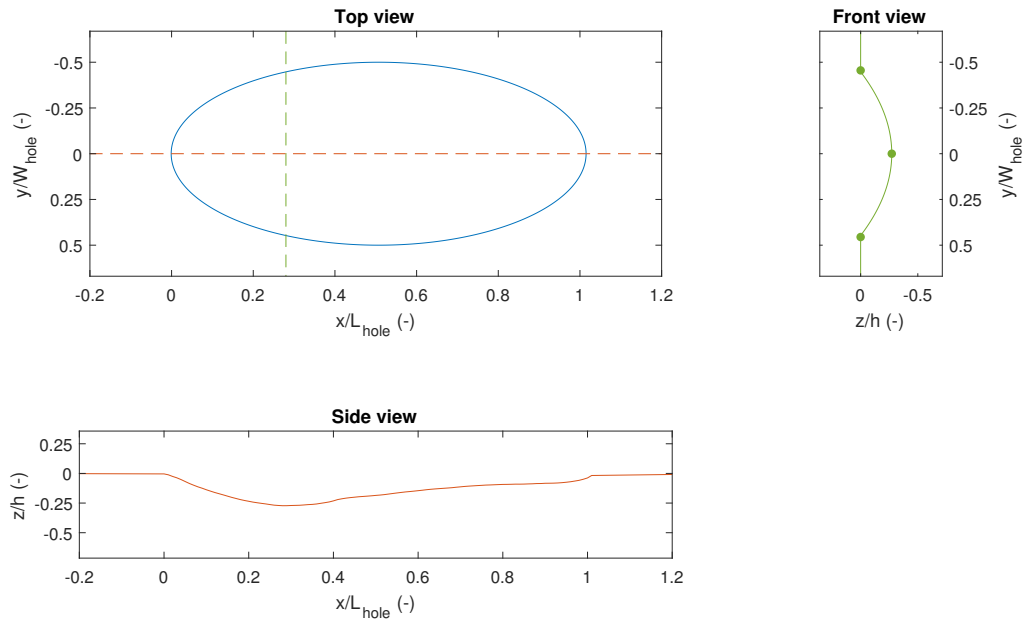


Figure 3.4: Plots showing the bed levels in the scour hole. The top view shows the oval edge and two dashed-lines representing the cross sections that are shown in the other two plots. The side view shows the cross section through the center axis in streamwise direction. The front view shows the cross section in lateral direction, with three points that are used to generate the symmetrical bed.

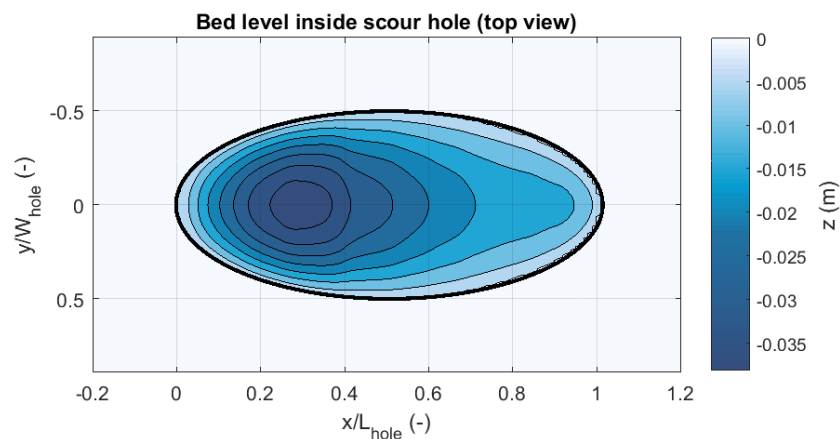


Figure 3.5: Symmetrical bed levels inside the scour hole.

When using the symmetrical bed for the model simulations, an error is made. The measured bed levels deviate from the values in the fitted parabola. Figure 3.6 visualizes the differences between the measured values and the fitted parabola. The figure includes cross sections at several locations in the scour hole. It is clearly observed that the non-symmetrical parts of the measured bed are removed. The error is given for each cross section. It shows the average error for all points in the cross section with reference to the maximum scour depth in the cross section. The maximum average error for a cross section is 20%. However, the maximum error for a single point is 63%. These are points with negative y/W_{hole} values at cross sections $x/L_{\text{hole}} = 0.5 - 0.9$. Generally speaking, the error that is made by using a symmetrical bed is acceptable. The influences of this choice are discussed in Chapter 5.3.4.

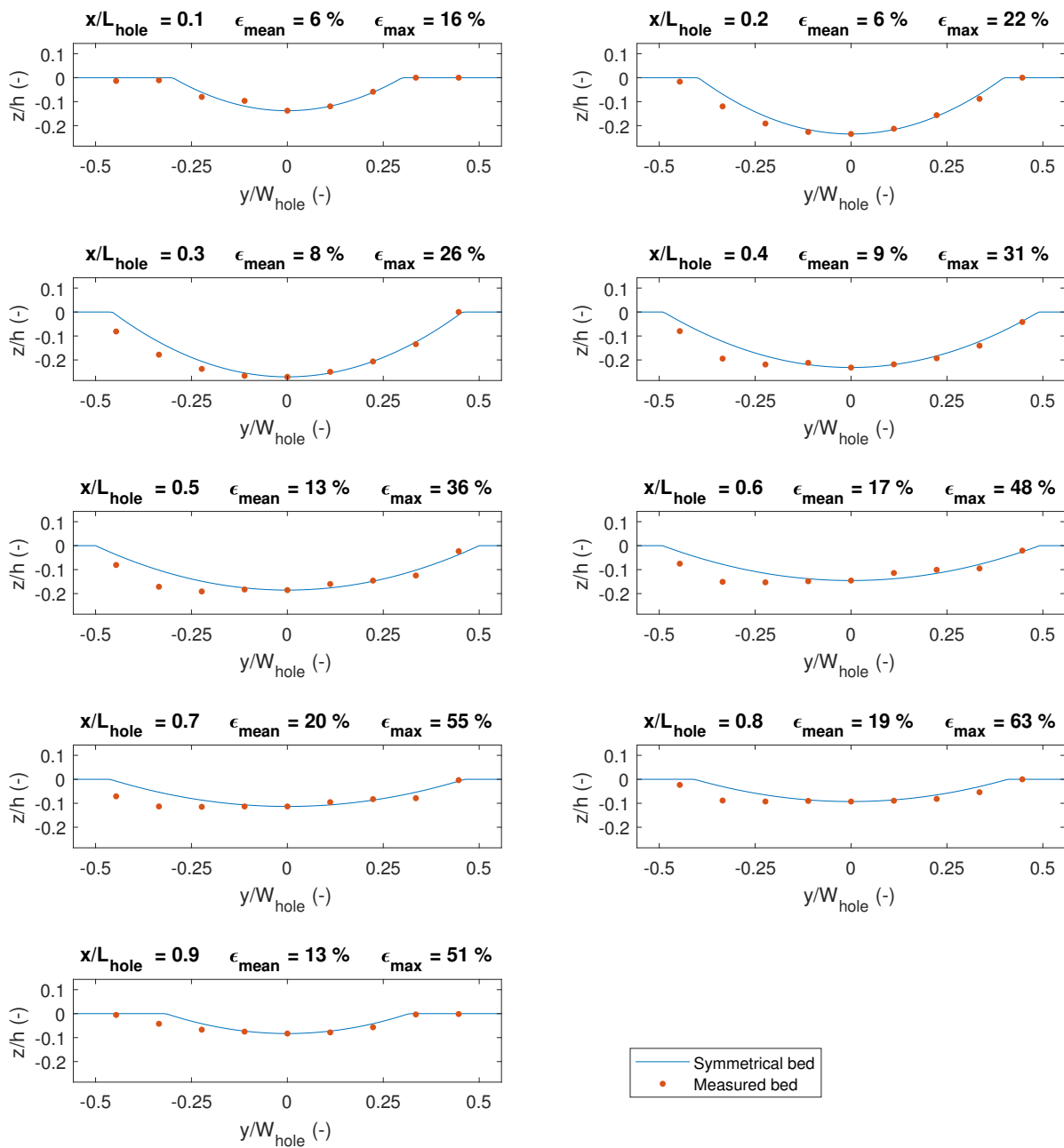


Figure 3.6: Comparison of the symmetrical bed and the bed level measurements from the laboratory experiments. 9 cross sections in lateral direction are given.

3.4.3. Grid generation

The calculated symmetrical bed level topography from the previous section is used as input for the process of grid generation. A detailed description of the grid generation is given in Appendix E. The number of cells and the cell sizes in the different directions are based on the following considerations:

- **Vertical grid requirement for the use of wall functions**

In Section 3.3.1 the requirements for the first grid cell near the bed are described. It turns out that the first cell center should reach up into the buffer layer. In case of an intermediate bed roughness, which is present in the experiments by Stenfert (2017), the y^+ value of the first cell center should be larger than 30 and should be larger than 0.2 times the Nikuradse roughness height.

- **Expansion factor and aspect ratio**

Grid cells that are located next to each other should not differ too much in size. An expansion factor can be applied to reduce the number of cells but keep the grid resolution high in the areas of interest. This expansion factor makes the size of the grid cells adapt gradually. In this way, the cell-to-cell ratio of the cells sizes is kept close to one. The cell-to-cell ratio in the model is equal to 1.01. From the grid study in Appendix F followed that the aspect ratio should be below 65. In the grid for this model, the maximum aspect ratio is 5, so this requirement is met.

- **Weighing between computational time and resolution of the results**

When a high resolution is needed in the domain, the required computational time becomes larger. A trade-off has to be made between the two. In the case of the scour hole from the experiments by Stenfert (2017), the cells inside the scour hole and in the surrounding area should be small. In that way, the bed topography in the hole can be captured nicely. The cells further upstream and downstream of the hole are larger, to save computational time.

Figure 3.7 shows the grid that is used in the model simulations. The parameters α and γ are smoothing parameters, which are explained in Appendix E. Table 3.2 shows the cell sizes and expansion ratios for the different directions. These values apply to the model of the scour hole from the experiments by Stenfert (2017).

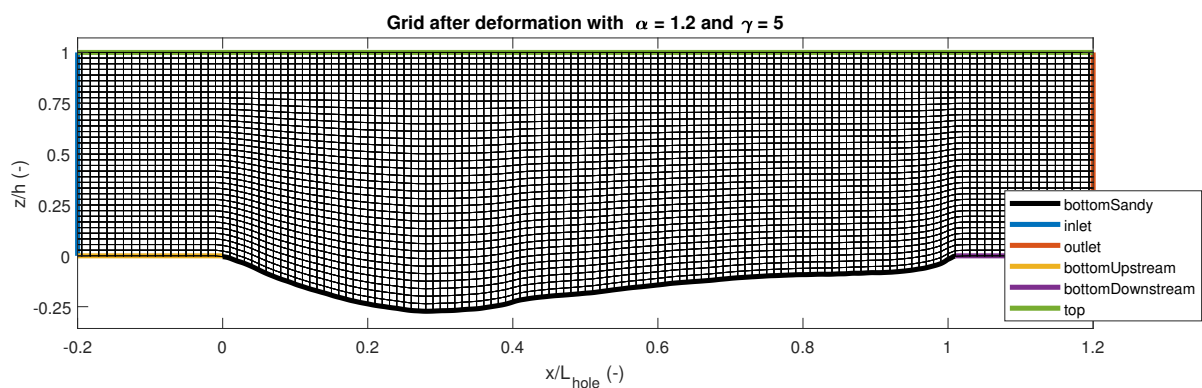


Figure 3.7: Cross section of the central axis in streamwise direction of the computational grid for the model of the scour hole from the experiments by Stenfert (2017). Parts of the upstream and downstream reach of the domain are left out for plotting purposes. The boundaries are indicated with colors.

Table 3.2: Cell sizes and expansion ratios in the different directions for the model of the scour hole from the experiments by Stenfert (2017).

Direction	Variable	Value
x	Domain size	1.5 m
	Smallest cell	10 mm
	Largest cell	5 mm
	Number of cells	240
	Maximum cell-to-cell expansion ratio	1.01
y	Domain size	0.6 m
	Smallest cell	2 mm
	Largest cell	2 mm
	Number of cells	300
	Maximum cell-to-cell expansion ratio	1
z	Domain size	0.14 m
	Smallest cell	3.9 mm
	Largest cell	3.9 mm
	Number of cells	36
	Maximum cell-to-cell expansion ratio	1

3.5. Boundary and initial conditions

In OpenFOAM, boundary conditions are specified at all boundaries surrounding the grid. The different boundary conditions that are used in this research are described in this section, together with the initial conditions.

Most of the boundaries that are present in the grid are shown in Figure 3.7. Two additional boundaries are not present in the figure: the `leftWall` and the `rightWall` boundary. The boundaries have different boundary types in OpenFOAM, which are described here. At the upstream boundary (`inlet`) an equilibrium velocity profile is implemented. This profile is generated using the cyclic modelling case, which is described in the next section.

Table 3.3 shows the boundary conditions and initial conditions for the different parameters in the domain. It can be seen that the pressure is set to a value of 0 at the outlet boundary. The velocity is set to `zeroGradient`, which simply means that there is no gradient in the velocity at this boundary. These boundary conditions at the outlet are chosen in order to generate a free outflow boundary. At the bed, the no-slip condition is applied (velocity of 0 m/s in all directions). The top boundary and side wall boundaries use the slip condition for the velocity. The slip boundary condition results in a wall shear stress equal to 0 N/m², see Section 3.3.2. Therefore, the top and side walls do not influence the flow field in the domain. All other boundary conditions are set to `zeroGradient`.

The initial conditions are also listed in Table 3.3. The velocity and pressure field are set to a value of 0. The flow field will slowly adapt to the upstream boundary condition, taking a simulation time of 100 seconds. k and ω have initial values that are close to the mean value of the parameters during a model simulation.

Table 3.3: Boundary conditions and initial conditions for the model of the scour hole from the experiments by Stenfert (2017).

Boundary	U	p	k	ω
inlet	cyclic profile (Figure 3.8)	zeroGradient	zeroGradient	zeroGradient
outlet	zeroGradient	0	zeroGradient	zeroGradient
bottomUpstream	(0,0,0)	zeroGradient	zeroGradient	zeroGradient
bottomSandy	(0,0,0)	zeroGradient	zeroGradient	zeroGradient
bottomDownstream	(0,0,0)	zeroGradient	zeroGradient	zeroGradient
top	slip	zeroGradient	zeroGradient	zeroGradient
leftWall	slip	zeroGradient	zeroGradient	zeroGradient
rightWall	slip	zeroGradient	zeroGradient	zeroGradient
Initial condition	(0,0,0)	0	1e-6	10

Upstream velocity profile

As discussed before, the velocity profile at the upstream boundary is generated using the cyclic model. The cyclic model is described in more detail in Appendix F. The result is shown in Figure 3.8. The profile is in fully developed equilibrium, which is generated using a pressure slope of 0.0020 m/s². The bed roughness is equal to the roughness of the main model: 0.0006 m.

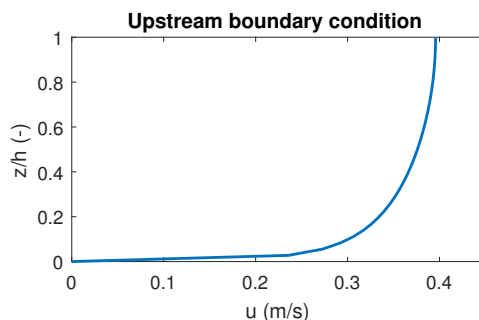


Figure 3.8: Velocity profile at the upstream boundary of the model, generated with the cyclic model (see Appendix F).

3.6. Numerical process

In OpenFOAM, a finite volume spatial discretization with a collocated variable arrangement is used, together with the PIMPLE algorithm. This algorithm solves for transient incompressible flows of Newtonian fluids (Baykal et al., 2017). An explanation of the PIMPLE algorithm can be found in Appendix D.

Specific solvers for each individual parameter in the model equations can be specified. The solvers are specified in the `fvSolution` dictionary, which is explained in Appendix D. In this model the GAMG solver is used for the pressure equation and the PBiCG solver is used for the momentum and the k - ω equations. These choices are made based on the previous successful studies with a similar flow situation by Jacobsen et al. (2014), Fuhrman et al. (2014), Baykal et al. (2015) and Baykal et al. (2017). In these studies the scouring around piles is modelled with the same settings and the results were satisfying.

Each term in the model equations is discretized with a numerical scheme. The schemes that are used are listed in Appendix D. The choices are made based on the same principle as the choices for the solvers.

Chapter 4

Model Validation

In this chapter, the validation of the model is described. This validation is done in several steps. The complexity of the model is increased with each step, making it easier to find errors in the model. The validation steps are described one by one. First, a model of a backward facing step (BFS) is described. After that, a two-dimensional scour hole from laboratory experiments by [Van Zuylen \(2015\)](#) is modelled. The last model validation is done using the three-dimensional scour hole by [Stenfert \(2017\)](#).

4.1. Backward facing step

A two-dimensional model of a backward facing step serves as the first model validation. From the analysis of the important processes in a scour hole in Section 2.2 follows that the area around the reattachment point is important. The highest attack on the bed takes place in this area and a high turbulent intensity is present. A reattachment point is only present when a flow separation is occurring. This is the case during the developed scouring stage. In the initial scouring stage of the scour hole development this is not present.

A widely investigated situation with many similarities to the flow separation in a scour hole is the backward facing step (BFS) case. A flow separation is occurring due to the bed step and the same flow zones, including the recirculation zone, the reattachment point and the mixing layer, are present. As extensive research and measurements have been carried out on the BFS case, this case is chosen as the first model validation step. For proper comparison, only cases with a free surface are relevant. As most experiments are without free surface, the available comparison cases were limited to three cases described by [Nakagawa and Nezu \(1987\)](#) and [Ampadu-Mintah and Tachie \(2015\)](#). Validation with the BFS case is used to verify whether the applied turbulence model and wall function are able to handle the adverse pressure gradients in a correct way. In this section, the results of the validation runs are presented. A more detailed description of the BFS model case is given in Appendix G.1.

4.1.1. Reference cases

For the validation of the model, two reference cases are used. [Nakagawa and Nezu \(1987\)](#) performed measurements of several BFS configurations. Two of them (ST1 and ST3) are elaborated on extensively in their study. The step height in the experiments is 2 cm. The Reynolds number is different for both cases. ST3 has a larger water depth and flow velocity, resulting in a higher Reynolds number. The parameters are given in Table 4.1.

The second reference case is a study by [Ampadu-Mintah and Tachie \(2015\)](#). In this experimental study, a BFS on a hydraulically smooth bed is measured. The upstream water depth is 7 cm and the step height is 9 mm. This is significantly smaller than the step height in the first two reference cases. The upstream flow velocity is larger and the Reynolds number is in the same order as the ST3 case.

Table 4.1: Hydraulic conditions for the experiments in the reference cases for the BFS model validation. The parameters are: downstream depth (h_d), step height (dh), maximum flow velocity (u_{\max}), downstream flow velocity (\bar{u}_d), Reynolds number (Re), Froude number (Fr) and relative reattachment point (x_R/dh).

Article	Case	h_d (cm)	dh (cm)	u_{\max} (cm/s)	\bar{u}_d (cm/s)	Re (-)	Fr (-)	x_R/dh (-)
Nakagawa and Nezu (1987)	ST1	5.8	2	24.3	14.2	8200	0.19	6.3
Nakagawa and Nezu (1987)	ST3	10.6	2	29.2	22.1	23400	0.22	5.2
Ampadu-Mintah and Tachie (2015)	-	7.9	0.9	35.9	-	25130	0.43	5.2

4.1.2. Validation results

The results of the numerical simulations are presented in this section and validated by comparing the flow velocity profiles and reattachment length with the measurements from the reference experiments.

Nakagawa and Nezu (1987)

In both cases by Nakagawa and Nezu (1987) the flow velocity is measured at multiple locations along the central channel axis. Figures 4.1 and 4.3 show the measurements and the model results. Velocity profiles at several locations along the channel are plotted. The profiles are normalized with the maximum velocity, which is the free stream velocity upstream of the step. The black solid line shows the recirculation zone. The point where the black solid line touches the bottom is called the reattachment point. The measured reattachment point is visualized using a black square. The main difference between the two cases is the relative step height compared to the water depth. The results of both runs are described in this section.

ST1

As can be seen in Figure 4.1, the velocity profile at the upstream boundary is well predicted by the model. The cyclic boundary condition results in a fully developed velocity profile, which is also present in the experiment.

When comparing the model results to the measurements, it can be concluded that the model reproduces the shape of the velocity profiles with an average relative error per profile of less than 4%, as indicated in the legend. This relative error is calculated by taking the average absolute error of all the measured points in a profile and dividing that by the maximum velocity in all measurements ($u_{\max} = 0.24$ m/s). Figure 4.2 visualizes the relative errors in the model results. The maximum relative error in all measured points is 10.2% at $x/dh = 6$. In the recirculation zone the model results deviate from the measurements (local relative errors are below 10%). The average relative error in the recirculation zone reduces from 5% at $x/dh = 1$ to below 3% further downstream. The profile at $x/dh = 5$ is very accurate, with a maximum relative error of only 1.4%. The modelled reattachment point deviates from the measured location. In the model results this location is more downstream.

The origin of the deviations is not known. Simulations with different mesh sizes are performed to check the mesh sensitivity of the model. It turned out that the simulation is converged for the mesh that is used, so this is not the reason for the deviations. A slightly different mixing or slight deviations in the chosen turbulence model could be responsible for the deviations. However, the deviations are small (maximum relative error < 10.2%, average relative error < 4%) so the model results are considered to be very accurate.

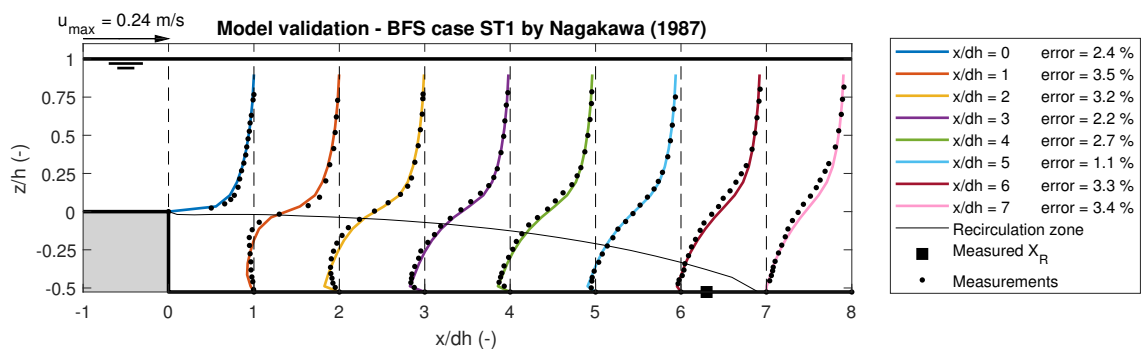


Figure 4.1: Model results and measurements of the ST1 case by Nakagawa and Nezu (1987). The plot includes velocity profiles at several locations in the model. The values are normalized with the maximum velocity, which is the streamwise velocity in the upstream region.

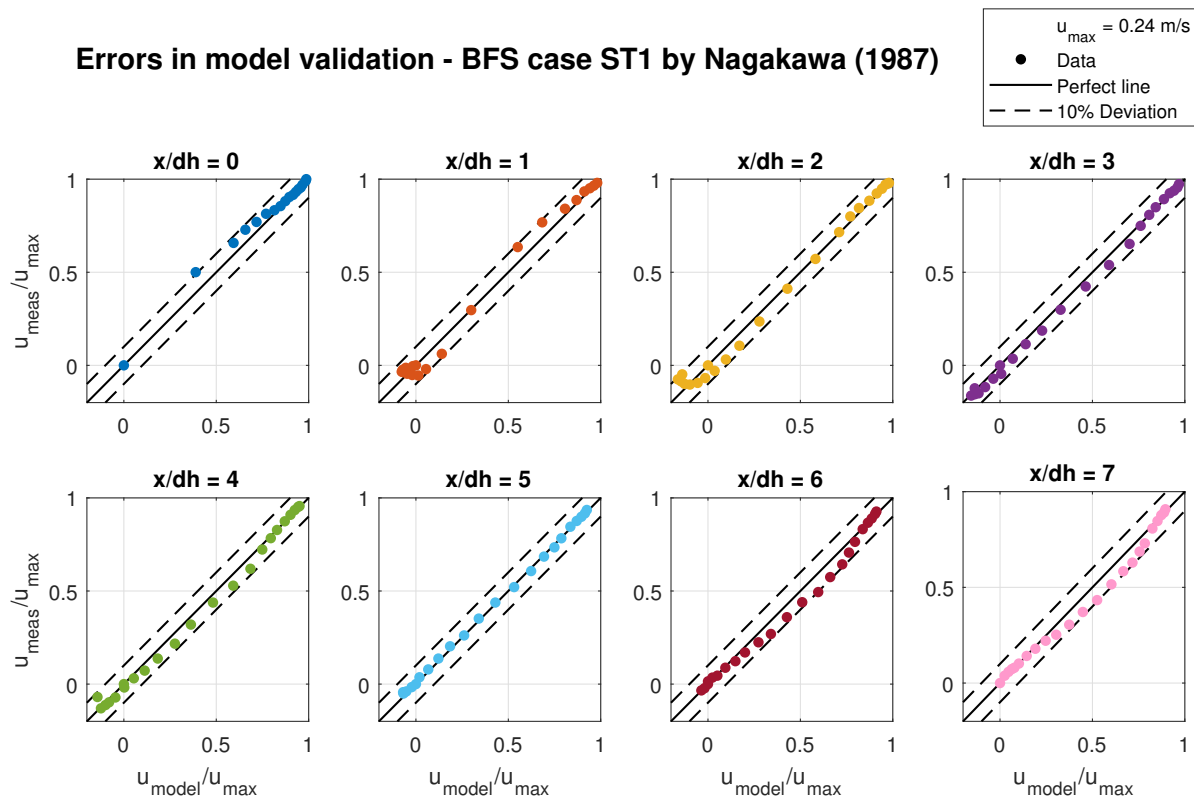


Figure 4.2: Visualization of the relative errors in the model validation using the BFS case ST1 by [Nagakawa and Nezu \(1987\)](#). For each location the normalized measured flow velocity is plotted against the normalized modelled flow velocity. Perfect agreement is indicated by the black solid line. All points that are between the dotted black lines have a difference of less than 10% between the model result and measurement.

ST3

In the ST3 case by [Nagakawa and Nezu \(1987\)](#), the step is relatively small. The larger depth results in a still developing velocity profile upstream of the step. This can be seen in the upstream profile in Figure 4.3. The upper part of the water column at that location has a constant flow velocity. In order to reproduce this profile in the model, the cyclic boundary condition is not used. Instead, a uniform velocity profile and a larger upstream reach are used in order to get a profile with an equal shape.

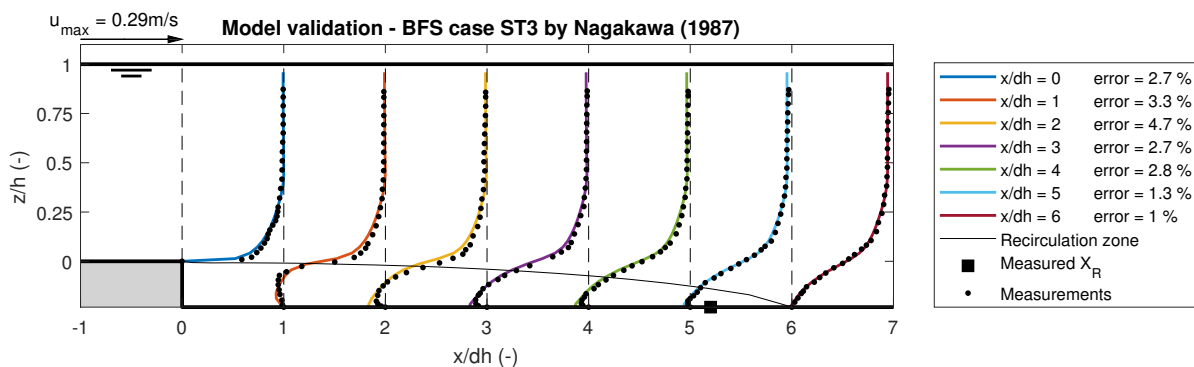


Figure 4.3: Model results and measurements of the ST3 case by [Nagakawa and Nezu \(1987\)](#). The plot includes velocity profiles at several locations in the model. The values are normalized with the maximum velocity, which is the streamwise velocity in the upstream region.

The results for this run are comparable to the results of the ST1 case. A figure showing the relative errors for this model validation is shown in Appendix H. The average relative errors indicated in the legend of Figure 4.3 have the same order of magnitude. The maximum local relative error is higher: 23%. This error is located in the cross section at $x/dh = 0$. The average relative errors in the recirculation zone are also a little higher: 5.6% at $x/dh = 1$ and 7.3% at $x/dh = 2$. Downstream of the reattachment point, the simulated profiles fit the

measurements very accurately again (average relative error of 1% and maximum relative error of 2.7%). The reattachment point in the model results is again further downstream, when compared to the experiment.

Ampadu-Mintah and Tachie (2015)

The second article that includes BFS measurements with a free surface is the one by Ampadu-Mintah and Tachie (2015). In this experiment, the relative step size is even smaller than in the ST3 case. Therefore, the recirculation zone behind the step is small, and will partially be modelled by the wall function. The measured upstream velocity profile is again not fully developed, therefore the same method is used as for the ST3 case to generate a non-uniform velocity profile at the step.

Figure 4.4 shows the velocity profiles along the channel. The measured profiles are again well predicted by the model. A visualization of the relative errors can be found in Appendix H. The average relative error at all locations is below 3%. The maximum relative error is located at $x/dh = 3$ and is 7.7%. The small step size has little influence, as the relative errors in the recirculation zone are comparable to the cases by Nakagawa and Nezu (1987). At $x/dh = 1$ and $x/dh = 3$ the average relative error in the recirculation zone is 4.0% and 4.9% respectively. The reattachment length is modelled correctly for this case. The measured reattachment point is some more downstream, but the effect of the relatively large first grid cell causes the model results to have an offset near the bottom.

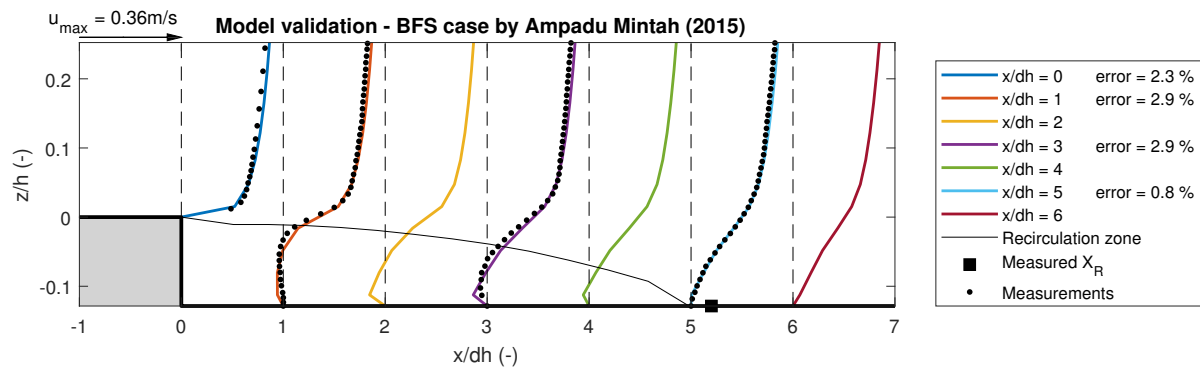


Figure 4.4: Model results and measurements of the BFS case by Ampadu-Mintah and Tachie (2015). The plot includes velocity profiles at several locations in the model. The values are normalized with the maximum velocity, which is the streamwise velocity in the upstream region.

4.1.3. Summary

From the BFS models can be concluded that the model is able to reproduce the flow field very accurately, with average relative errors ranging from 4.7% to 0.8% and a maximum local relative error of 23%. Even the small scale BFS from Ampadu-Mintah and Tachie (2015) is captured nicely. The errors in that simulation are the lowest, compared to the cases by Nakagawa and Nezu (1987). However, in the upstream part of the recirculation zone the model is overestimating the return flow in the simulations with an maximum local relative error of 16%. Besides, the reattachment length is overestimated by the model in the simulations of the cases by Nakagawa and Nezu (1987) with 13%. In the book by Wilcox (2006), a similar overestimation of the reattachment length is observed when using the $k-\omega$ Wilcox model, but larger deviations are found when using other turbulence models.

4.2. Scour hole by Van Zuylen (2015)

The second model validation is done using a scouring case of the laboratory experiments by Van Zuylen (2015). Measurements are done on several cases, all involving two-dimensional scouring, which means that the scour hole is uniform in lateral direction. The hydrodynamics of one of the experiments will be simulated and validated using the measurements. This model is functioning as a confirmation that the model is able to simulate the hydrodynamics in a scour hole in a correct way. First a two-dimensional model will be used. After that the model will be extended in lateral direction, and a three-dimensional simulation is done. The expectation is that the model results deviate a bit from the measurements, as laboratory measurements are never fully two-dimensional, but will always include a three-dimensional component. In this section, a brief elaboration of the model is given. In Appendix G.2.1 an extensive description of the model is present.

4.2.1. Reference case

As stated before, the situation that will be modelled is an experiment by Van Zuylen (2015). In his Master Thesis he performed many experiments where a scour hole could form in the sand between two steel plates. The experiment *Run 17* is selected for the model validation, as detailed velocity measurements are available for this experiment. A schematical representation of the experimental setup of Run 17 is shown in Figure 4.5. The experiment is uniform in lateral direction and has an opening between the steel plates of 50 cm. Small particles are glued on top of the plates, making them hydraulically rough. At the downstream edge a steel plate at an angle of 45° is placed. Therefore, the downstream slope of the hole will always have this angle. The hydraulic conditions of the experiment are shown in Table 4.2.

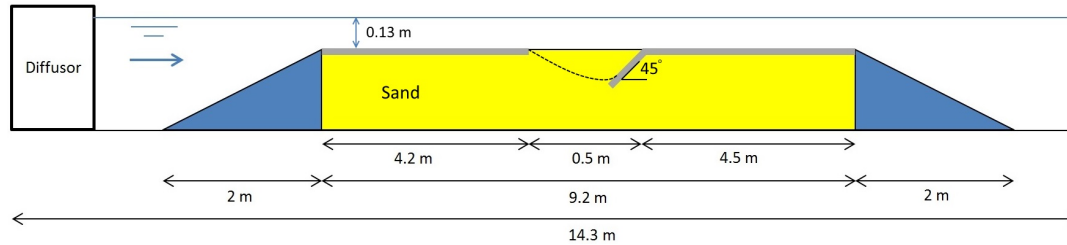


Figure 4.5: Schematical representation of the experiment *Run 17* by Van Zuylen (2015). The plate at the downstream edge of the hole has an angle of 45° and the length of the hole is 0.5 m. Image is based on Van Zuylen (2015).

Table 4.2: Hydraulic conditions for the experiments by Van Zuylen (2015). The parameters are: water depth (h), average flow velocity (\bar{u}), Reynolds number (Re), Froude number (Fr), bed shear velocity (u_{\star}), Nikuradse roughness of steel and sand ($k_{n, \text{steel}}$ and $k_{n, \text{sand}}$) and the length of the scour hole (L_{hole}).

Experiment	h (cm)	\bar{u} (m/s)	Re (-)	Fr (-)	u_{\star} (m/s)	$k_{n, \text{steel}}$ (mm)	$k_{n, \text{sand}}$ (mm)	L_{hole} (cm)
Run 17	13.0	0.60	$7.8 \cdot 10^4$	0.53	0.042	6.0	0.6	50

4.2.2. Validation results

The results of the two-dimensional simulation are presented in this section. The visualization of the results is done using profiles at several locations. The validation will be done using velocity profiles and turbulence intensity profiles. From the experiments by Van Zuylen (2015) the measured velocity profiles are available. Measurements are done at four locations inside the hole ($x/L_{\text{hole}} = 0.2, 0.4, 0.6$ and 0.8), at the upstream edge ($x/L_{\text{hole}} = 0.0$) and downstream of the hole ($x/L_{\text{hole}} = 1.2$). The resulting velocity profiles are shown in Figure 4.6. The turbulence intensity profiles are shown in Figure 4.8. The average relative error for each profile is shown in the legend. This error is calculated in the same way as in the BFS cases.

Flow velocity

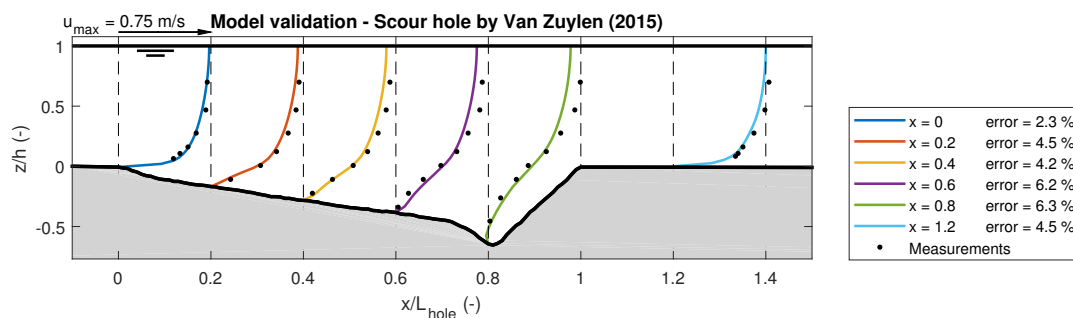


Figure 4.6: Model results of the two-dimensional simulation and measurements of the Run 17 experiment by Van Zuylen (2015). The plot includes velocity profiles at several locations in the model. The values are normalized with the maximum velocity, which is the streamwise velocity at the surface in the upstream region.

From Figure 4.6 can be concluded that the model results agree fairly well with the measurements. Visualizations of the relative errors are shown in Appendix H. Some remarkable points are listed below:

- The upstream and downstream velocity profiles correspond very well to the measurements. Especially the upstream profile has a low average relative error (2.3%) and a maximum local relative error of 4.1%.
- Near the bed inside the scour hole, the model shows accurate results. The average relative error near the bed is smaller than the average relative error for the full water column at all locations. $x/L_{\text{hole}} = 0.4$ and $x/L_{\text{hole}} = 0.8$ are outstanding, as the average relative error in the area close to the bed are only 2.2% and 3.6% respectively.
- Higher in the water column, the model results show lower values for the velocity than the measurements. At $x/L_{\text{hole}} = 0.8$ the model shows the largest relative error in this region (an average relative error of 9.1%). The maximum local relative error is 13.7%. The deviations in the upper part of the water column are expected to be a three-dimensional effect in the measurements, that is not present in the model simulation.
- Flow recirculation is present in the model results in two regions: around $x/L_{\text{hole}} = 0.1$ and around $x/L_{\text{hole}} = 0.8$. These regions are plotted with more detail in Figures 4.7a and 4.7b respectively. The measurements do not show these recirculation regions, because the recirculation zone is very small and the measuring device could not reach close enough to the bed. However, visual observations with coloured dye during the experiments confirmed that a recirculating flow is present in the scour hole. Therefore, the presence of the flow recirculation in the model results is desired.

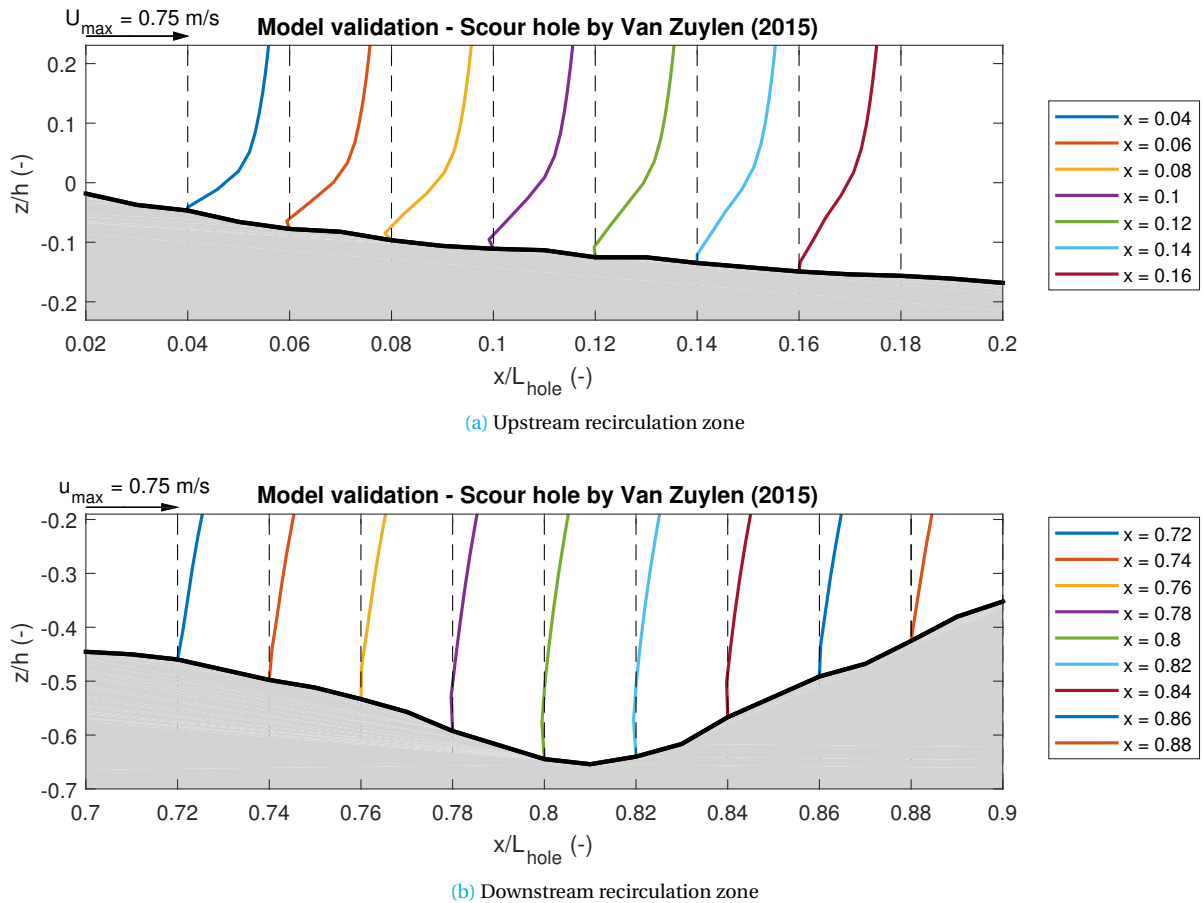


Figure 4.7: Zoomed model results of the Run 17 experiment by Van Zuylen (2015). The plot includes velocity profiles at several locations in the model. The values are normalized with the maximum velocity, which is the streamwise velocity at the surface in the upstream region.

Turbulence intensity

For the turbulence intensity the model results deviate more from the measurements, when compared to the flow velocity. The errors are calculated using the maximum value of the measurements at $x/L_{\text{hole}} = 0.8$: $k_{\text{max}} = 0.016 \text{ m}^2/\text{s}$. The maximum average relative error is located at $x/L_{\text{hole}} = 0.8$ (21.9%). The maximum local relative error is also present at this location and is 39.6%. In the upper part of the water column, the turbulence intensity is overestimated (average relative error of 10%). In the downstream half of the hole, the turbulence intensity is underestimated by the model in the lower part of the water column (average relative error of 25%). This underestimation can be caused by the error in the velocity profile. A smaller velocity gradient generates less turbulence, and therefore the turbulence intensity is smaller as well. Anisotropy in the turbulence can be present in the measurements, but not in the model results, because the k - ω model considers isotropic turbulence (i.e. uniform in all directions).

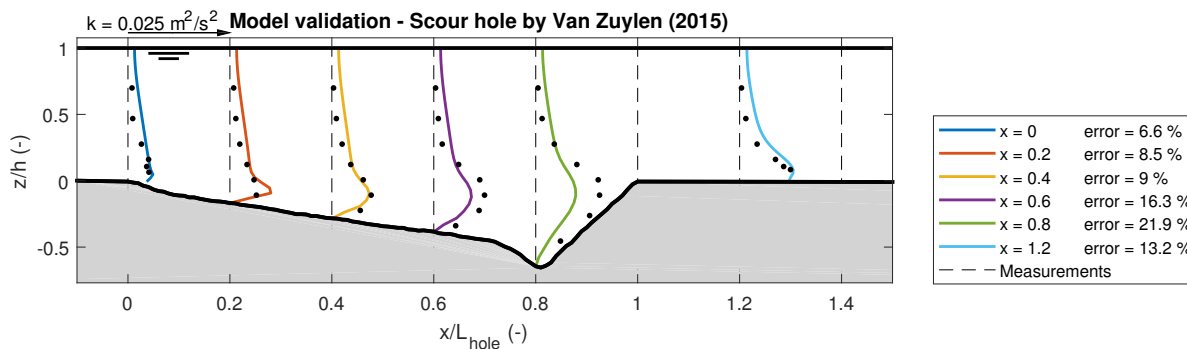


Figure 4.8: Model results of the three-dimensional simulation and measurements of the Run 17 experiment by Van Zuylen (2015). The plot includes turbulence intensity profiles at several locations in the model. The values are normalized with a value of $0.025 \text{ m}^2/\text{s}^2$.

Three-dimensional effects in the laboratory experiment could have influenced the measured flow field. Therefore, a three-dimensional model of the scour hole by Van Zuylen (2015) is modelled to check whether these effects are also present in a model simulation.

4.2.3. Three-dimensional model

The two-dimensional model is extended to a three-dimensional model by adding cells in the lateral direction. The bed is uniform in this direction. By simulating this case in a three-dimensional model, the influence of three-dimensional effects can be investigated. From the description of the two-dimensional model in the previous section follows that three-dimensional effects might be the cause of differences between the experiments and the model simulation.

Plots of the model results are not presented here, but in Appendix G.2.2, because at first sight there are no differences when compared to the results of the two-dimensional model. The differences between the two simulations are further examined. The mean difference in flow velocity is lower than the mean difference in turbulence intensity. In general, the differences between the simulations are small ($< 0.75\%$). However, the cross section at $x/L_{\text{hole}} = 0.2$ shows large differences, compared to the other locations ($\approx 1.5\%$). A possible cause for the differences between the two simulations are the three-dimensional effects. The magnitude of the three-dimensional effects is investigated by looking at motions in lateral direction. Figures showing these motions are presented in Appendix G.2.2. The motions are assumed to be so-called Görtler vortices.

4.2.4. Summary

From the model simulations of the scour hole by Van Zuylen (2015) can be concluded that the model is able to simulate the hydrodynamics inside a scour hole accurately. The velocity profiles show good agreement with the measurements. The maximum local relative error is 13.7% and the average relative error is 4.7%. In the upper part of the water column above the scour hole, the flow velocity is underestimated with an average relative error of 6.2%. When looking at the turbulence intensity, the model overestimates the measured values in the upper part of the water column by 10% on average. Underestimation of the turbulence intensity takes place in the downstream half of the scour hole (25%). This might be a result of the error in the velocity profiles.

The differences between the model results and the measurements can have different causes. First of all, the model simulates a purely two-dimensional case. In a laboratory experiment, two-dimensional conditions can be generated, but a real flow will never be purely two-dimensional. Therefore, three-dimensional effects will always play a role in experimental studies.

A second point that can cause differences is the evolving bed during the experiment. The measurements are performed in a period of three hours. During this period, the bed changed significantly. This may have had an effect on the measured velocity profiles. For completely reliable results, the bed topography should be fixed. In this way, a more or less steady state will be reached and the measurements are not dependent on the point in time that they are measured at.

Addition of cells in the third dimension does not make the measurements and model results correspond better. The differences between the two-dimensional and three-dimensional simulation are small (order 1%).

4.3. Scour hole by Stenfert (2017)

The final model validation is done using the three-dimensional scouring case measured by [Stenfert \(2017\)](#) and explained in Section 3.1. In this section, the velocity measurements are discussed and the model validation using the mentioned scour hole is described.

4.3.1. Data source

During the experiment the bed was evolving due to the ongoing erosion. In order to perform reliable velocity measurements, [Stenfert \(2017\)](#) fixed the bed topography after 30 hours of experiment. In this way, the problem of the evolving bed, which was present in the experiments by [Van Zuylen \(2015\)](#), is solved.

The velocity measurements are performed using a method with oxygen bubbles. An electronically loaded wire mesh is placed in the water and electrolysis is used to create the bubbles right upstream of the measuring location. This is shown in Figure 4.9. The bubbles are transported by the flow and measured by the Vectrino Profiler. This device needs the water to be seeded, which is done with the bubbles.

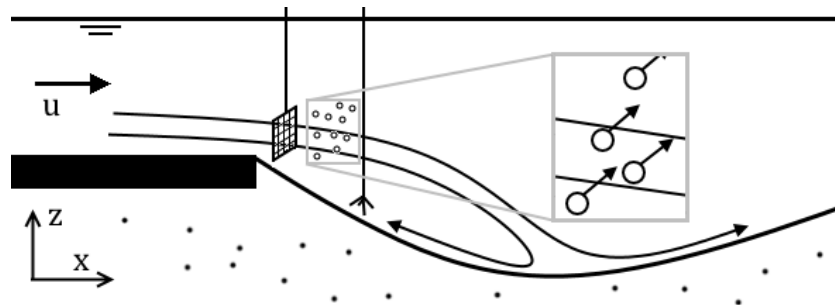


Figure 4.9: Schematization of the velocity measurements that were performed by [Stenfert \(2017\)](#). The oxygen bubbles are created using a wire mesh upstream of the measuring device. The bubbles tend to move upwards, as their density is much smaller than the density of water.

4.3.2. Validation results

Figure 4.10 shows the flow velocity profiles with the measurements by [Stenfert \(2017\)](#). The relative errors, which are indicated in the legend of the figure, are calculated by taking the average error of a velocity profile and dividing this by the maximum velocity ($U_{\max} = 0.398$ m/s). The major difference between the model results and the measurements is the recirculation of flow. In the upper part of the water column, the measurements are approximated to a large extent by the model results (average relative error of 3.1%). However, when the part of the profiles inside the scour hole is examined, the model shows a recirculation zone and the measurements do not. The average relative error in this zone is 21%. The velocity profiles at $x/L_{\text{hole}} = 0$, $x/L_{\text{hole}} = 0.8$ and $x/L_{\text{hole}} = 1.2$ show good agreement with an average relative error below 4.7%.

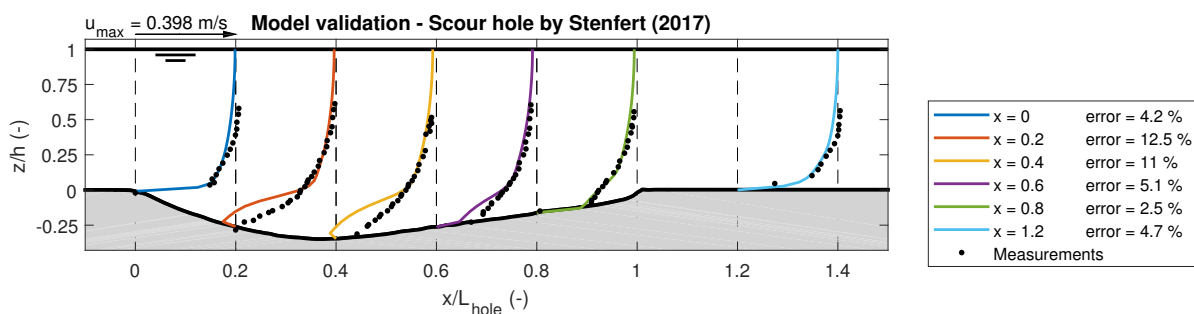
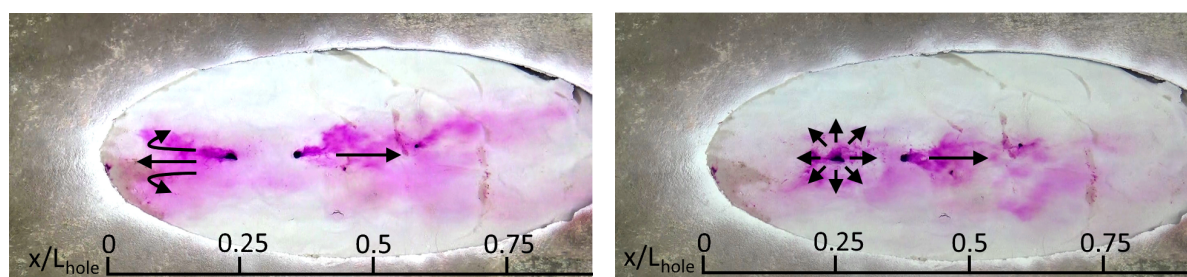


Figure 4.10: Model results of the simulation and measurements of the experiment by Stenfert (2017). The plot includes velocity profiles at several locations in the model. The values are normalized with the maximum velocity, which is the streamwise velocity at the surface in the upstream region.

During the laboratory experiments, a recirculation zone is clearly observed inside the hole. Figure 4.11 shows the visual observations using small dye particles on the bed. The flow in the recirculation zone is directed upstream, see the left particle in Figure 4.11a. Based on the dye visualization, the reattachment point is located around $x/L_{\text{hole}} = 0.25$, which can be seen in Figure 4.11b. This is not observed in the flow measurements. According to the model results, this location is at $x/L_{\text{hole}} = 0.44$.



(a) Distinction between upstream flow in the recirculation zone and downstream flow outside of the zone.

(b) The reattachment point is located around $x/L_{\text{hole}} = 0.25$.

Figure 4.11: Photos showing the visual observations during the scouring experiment. Small dye particles are placed on the bed, showing the local direction of flow. Figures based on (Stenfert, 2017).

The deficiency between the visual observations and the flow measurements may be explained by difficulties in measuring the recirculation zone. Near the reattachment point, the bubbles have to seed the recirculation zone by entering it. The density of oxygen bubbles is much lower than the density of water. Therefore, the oxygen bubbles tend to move upward in the water. As a consequence only few oxygen bubbles follow the downward motion at this location, resulting in too few bubbles entering the zone. In this way, the Vectrino is not able to provide measurements with a low uncertainty in the recirculation zone. The method with the oxygen bubbles works fine for the region behind the reattachment point, as the downward motion is much less important in that region.

Due to the uncertainty in the flow velocity measurements, it is not possible to verify whether the flow within the recirculation zone is modelled correctly. Additional measurements are required for a proper verification. An option could be to perform measurements with neutrally-buoyant particles instead of the air bubbles. The fact that the recirculation is included in the model results is not necessarily a deviation in the model.

In order to capture the recirculation zone in the flow measurements, a second set of detailed flow measurements is performed by Stenfert (2017) in a larger hole ($L_{\text{hole}} = 0.75$ m). The bed topography is fixed after 15 hours of experiment and includes dunes in the downstream half of the hole. Measurements are done in the upstream part of the hole (x/L_{hole} between 0 and 0.4). The method using the oxygen bubbles works better in the large hole, but still is not able to capture the recirculation zone perfectly. The model results for the large hole are shown in Figures 4.12 and 4.13. They show the flow velocity and the turbulence intensity respectively. The indicated average relative errors are calculated by taking the average difference of the model results and the measurements of a profile and dividing it by the maximum flow velocity ($u_{\text{max}} = 0.438$ m/s).

The measured flow velocity profiles correspond better with the model results when compared to Figure 4.10. The measured profiles in the upstream part of the hole include a flow in upstream direction near the bed, which is in agreement with the model results. However, the reattachment point in the measurements is still located around $x/L_{\text{hole}} = 0.25$, while the model has a reattachment point around $x/L_{\text{hole}} = 0.37$. The upstream profile shows deficiencies between the measurements and the model results (maximum local relative error is 14.3%, average relative error is 4.4%). The profile at $x/L_{\text{hole}} = 0.1$ shows good results, with an average relative error of only 2.1% and a maximum local relative error of 6.4%. In the profiles at $x/L_{\text{hole}} = 0.2, 0.3$ and 0.4 the model shows stronger effects of the recirculation zone and a stronger gradient in the flow velocity, resulting in larger errors in the lower part of the water column. The average relative error made in the lower part of the water column in this area is 17.7%, while in the upper part this value is 2.1%.

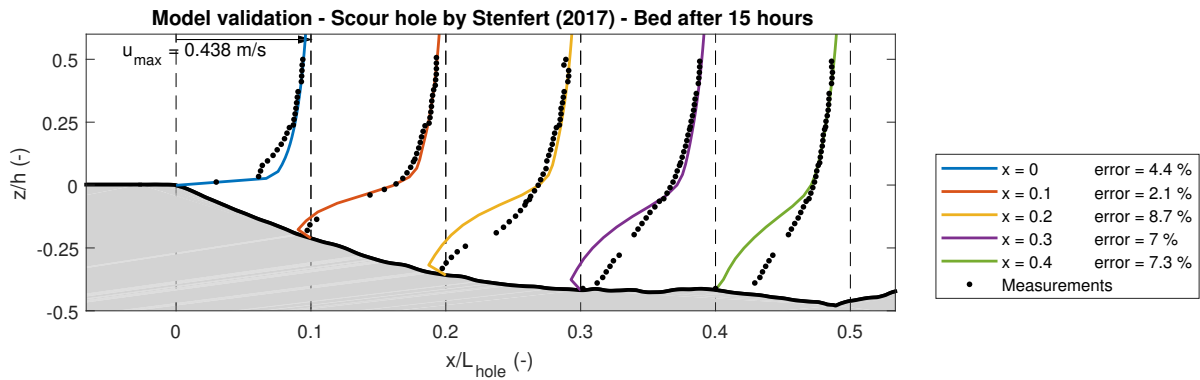


Figure 4.12: Model results of the simulation and measurements of the experiment by Stenfert (2017). The plot includes velocity profiles at several locations in the model. The values are normalized with the maximum velocity, which is the streamwise velocity at the surface in the upstream region.

The turbulence intensity profiles in Figure 4.13 show larger differences in the more upstream locations. The indicated average relative errors are calculated by taking the average difference of the model results and the measurements of a profile and dividing it by the maximum measured turbulence intensity at $x/L_{\text{hole}} = 0.2$ ($k_{\text{max}} = 0.013 \text{ m}^2/\text{s}^2$).

As can be seen in the figure, the profiles show good agreement in general. The largest deviations are found in the recirculation zone. Especially at $x/L_{\text{hole}} = 0.1$ and 0.2 the maximum relative errors are large (46% and 76% respectively). The upstream profile is very accurate, with an average relative error of 1.6%. The difference between the values inside the recirculation zone and higher in the column is large. Inside the recirculation zone, the average relative error is 13.3%, while higher in the water column this error is only 1.7%.

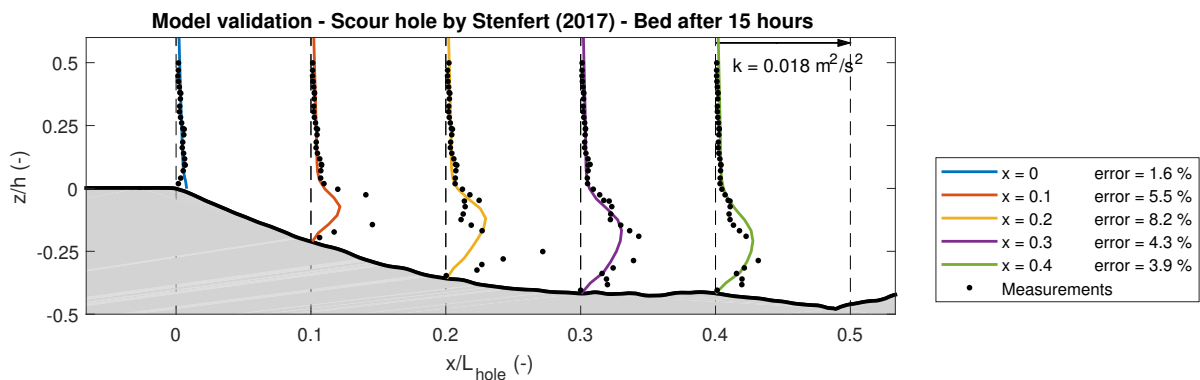


Figure 4.13: Model results of the simulation and measurements of the experiment by Stenfert (2017). The plot includes turbulence intensity profiles at several locations in the model. The values are normalized with a value of $k = 0.018 \text{ m}^2/\text{s}^2$.

4.4. Influence of the side walls and rigid lid approximation

The side walls in the numerical model are given the slip condition. In that way, the walls have limited influence on the flow field in the model domain. In the laboratory experiments, side walls have a more significant influence on the flow, as they decelerate the flow near the boundaries and induce more turbulence. In the model simulations of the scouring case by Van Zuylen (2015) this effect is clearly observed. The upstream flow velocity in the experiments is calculated using the discharge of the pump at the upstream boundary ($\bar{u} = 0.60$ m/s). However, the velocity profile that is measured upstream of the edge of the scour hole gives a different value for the average flow velocity ($\bar{u} = 0.65$ m/s). Based on continuity, the deceleration of flow near the side walls results in acceleration of flow in the center of the flume. In the model simulation this effect is included by using a value of $\bar{u} = 0.65$ m/s at the upstream boundary, as the model simulates a 2DV case in the central axis of the flume. A distance of 20 cm is left between the side walls and the area of interest in the numerical model, therefore the side walls will not have any further influence on this area.

The model simulations use the rigid lid approximation as representation of the free surface. As described in Section 3.3.2, the rigid lid approximation gives reasonable results for Froude numbers below 0.6. The Froude numbers in the model simulations are in the range between 0.3-0.4, so the rigid lid approximation is assumed to be a valid one. The free surface deformations are included in the model simulation by a pressure value at the top boundary of the domain. Figure 4.14 shows the pressure at the top boundary for the simulation of the scour hole by Stenfert (2017). The water level deformation can be calculated from the pressure by dividing it by the density and the gravitational acceleration. It can be seen that the difference in water surface between the area above the hole and downstream is 0.8 mm. This is 0.6% of the water depth. The error that is made in the volume of water in the domain is therefore acceptable.

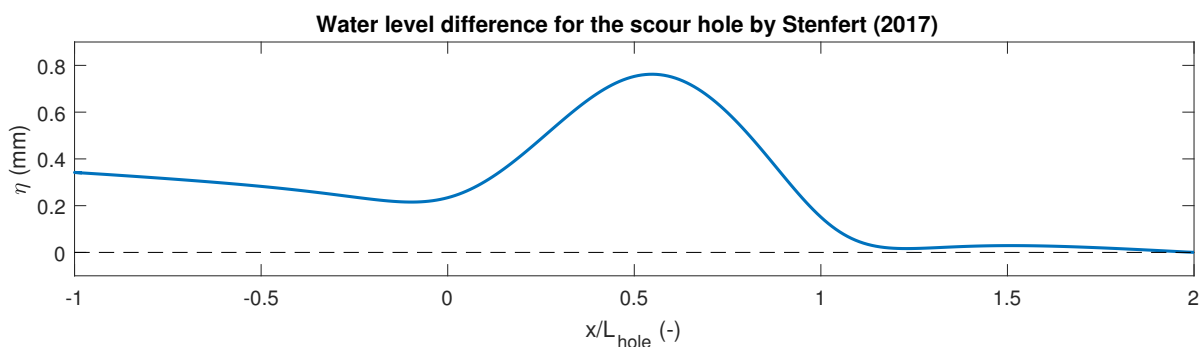


Figure 4.14: Plot showing the water level difference in the model simulation of the scour hole by Stenfert (2017). Above the hole ($x/L_{\text{hole}} = 0.0 - 1.0$) the water level increases.

4.5. Conclusion

All three parts of the model validation show that the model is performing well in the simulation of the hydrodynamics in a scour hole. From the backward facing step case is learned that the model captures the flow separation correctly. The velocity profiles are simulated with an maximum average relative error of 4.7% and the maximum local relative error is 23%.

The model of the scour hole from the experiments by Van Zuylen (2015) shows that a flow separation inside a scour hole with a gentle upstream slope is also simulated correctly, with an average relative error of 4.7% and a maximum local relative error of 13.7%. The turbulence intensity shows larger differences, with an underestimation by the model of 25% in the downstream half of the hole. This two-dimensional case shows some differences between the model results and the measurements. Three-dimensional effects in the experiments are probably the cause of these differences.

The model validation of the scour hole from the experiments by Stenfert (2017) shows a recirculation in both the model results and measurements. The recirculation in the measurements is less strong. The average relative error in the recirculation zone is 18.2%, while the other part of the water column only has an average relative error of 2.1%. In the research by Stenfert (2017) is stated that measurements in the recirculation zone are inaccurate, as the oxygen bubbles do not cover the entire zone (see Section 4.3.1). The simulated velo-

city profiles upstream and downstream of the hole are in good agreement with the measurements. Three-dimensional effects might also be a reason for the differences.

The major assumptions in the numerical model are discussed in Section 4.4 and the influence on the model results is considered to be acceptable. As the recirculation zone is captured by the model, enough confidence is gained to perform the parameter study with this model. The presence of the other hydrodynamical processes in the model results, that are described in Section 2.4, will be described and discussed in the parameter study in Chapter 5.

Chapter 5

Parameter study

This chapter describes the parameter study that is performed to check the influence of the flow velocity, water depth and the depth of the scour hole on the recirculation zone, flow structures, flow contraction, bed shear stress and erosion. Table 5.1 shows the values of the parameters that are used in the different simulations. The influence of changes in flow velocity, water depth and depth of the scour hole are examined. In addition, results of simulations with bed levels at two different points in time during the experiment with the small hole (after 10 hours and 30 hours) are examined. The two bed levels are shown in Figure 5.1. It shows the bed topography and the reattachment point in the central axis.

Table 5.1: Overview of the model simulations that are performed for the parameter study. The average flow velocity (\bar{u}), water depth (h), maximum scour hole depth (h_s), upstream slope (β), bed shear velocity (u_{\star}), Froude number (Fr) and Reynolds number (Re) are given.

Nr.	Name	Bed after	\bar{u} (m/s)	h (m)	h_s (cm)	β (-)	u_{\star} (m/s)	Fr (-)	Re (-)
1	base case	30 hours	0.360	0.14	4.9	0.456	0.0167	0.31	50400
2	$h_s \cdot 0.5$	30 hours	0.360	0.14	2.4	0.228	0.0167	0.31	50400
3	$h_s \cdot 0.75$	30 hours	0.360	0.14	3.7	0.342	0.0167	0.31	50400
4	$h_s \cdot 0.8$	30 hours	0.360	0.14	3.9	0.364	0.0167	0.31	50400
5	$h_s \cdot 0.85$	30 hours	0.360	0.14	4.2	0.387	0.0167	0.31	50400
6	$h_s \cdot 0.9$	30 hours	0.360	0.14	4.4	0.410	0.0167	0.31	50400
7	$h_s \cdot 0.95$	30 hours	0.360	0.14	4.6	0.433	0.0167	0.31	50400
8	$h_s \cdot 1.1$	30 hours	0.360	0.14	5.4	0.501	0.0167	0.31	50400
9	$h_s \cdot 1.25$	30 hours	0.360	0.14	6.1	0.570	0.0167	0.31	50400
10	$h_s \cdot 1.5$	30 hours	0.360	0.14	7.3	0.683	0.0167	0.31	50400
11	$u > u_0$	30 hours	0.442	0.14	4.9	0.456	0.0205	0.38	61880
12	$u < u_0$	30 hours	0.248	0.14	4.9	0.456	0.0118	0.21	34720
13	$h < h_0$	30 hours	0.360	0.10	4.9	0.456	0.0173	0.36	36000
14	$h > h_0$	30 hours	0.360	0.18	4.9	0.456	0.0162	0.27	64800
15	$u = 0.27$ m/s, $h = 0.10$ m	30 hours	0.268	0.10	4.9	0.456	0.0132	0.27	26800
16	$u = 0.29$ m/s, $h = 0.18$ m	30 hours	0.293	0.18	4.9	0.456	0.0132	0.22	52740
17	$u = 0.21$ m/s, $h = 0.10$ m	30 hours	0.217	0.10	4.9	0.456	0.0110	0.22	21700
18	base case	10 hours	0.360	0.14	3.8	0.431	0.0167	0.31	50400
19	$u > u_0$	10 hours	0.442	0.14	3.8	0.431	0.0205	0.38	61880
20	$u < u_0$	10 hours	0.248	0.14	3.8	0.431	0.0118	0.21	34720
21	$h < h_0$	10 hours	0.360	0.10	3.8	0.431	0.0173	0.36	36000
22	$h > h_0$	10 hours	0.360	0.18	3.8	0.431	0.0162	0.27	64800
23	$h_s \cdot 1.05$	10 hours	0.360	0.14	4.0	0.453	0.0167	0.31	50400

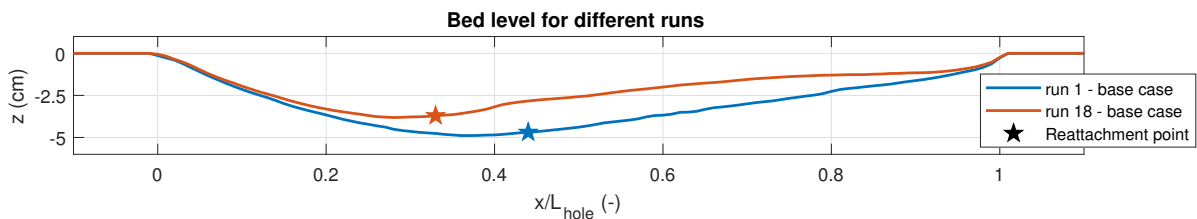


Figure 5.1: Bed levels at two different points in time during the experiment. The reattachment point is indicated with a star.

5.1. Recirculation zone

The first flow phenomenon in a scour hole that is examined is the recirculation zone. Figure 5.2 shows streamlines of the simulation with a bed topography after 30 hours. The recirculation zone is clearly observed. The reattachment point is located around $x/L_{\text{hole}} = 0.44$. In this section the influence of the water depth, flow velocity and depth of the scour hole are examined.

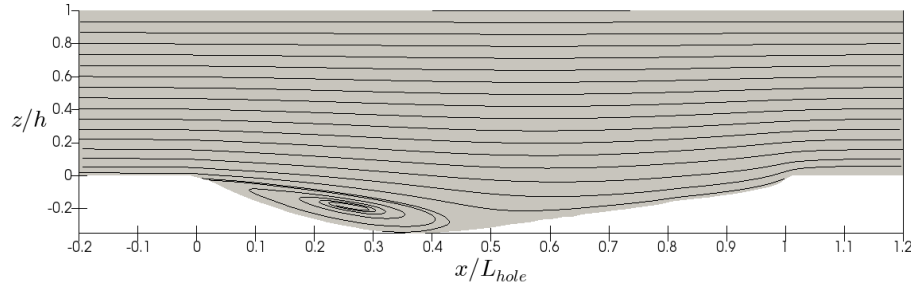


Figure 5.2: Model result for run 1, with a bed topography after 30 hours of scouring. Streamlines in the central axis in streamwise direction are shown.

5.1.1. Influence of the water depth

The runs that are performed to check the influence of the water depth are listed in Table 5.2. The table includes the recirculation velocity (magnitude and percentage of average upstream flow velocity) and the length of the recirculation zone (magnitude and recirculation length to depth of the scour hole ratio).

Table 5.2: Recirculation parameters in the scour hole for simulations with different water depths. Some of the parameters from Table 5.1 are given, together with the recirculation velocity magnitude (u_r), the percentage of the average upstream flow velocity (u_r/\bar{u}), the length of the recirculation zone (L_r) and the ratio of the recirculation length over the depth of the scour hole (L_r/h_s).

Nr.	Name	Bed after	h (m)	\bar{u} (m/s)	u_* (m/s)	u_r (m/s)	u_r/\bar{u} (%)	L_r (m)	L_r/h_s (-)
1	base case	30 hours	0.14	0.360	0.0167	0.0518	14.4%	0.220	4.5
13	$h < h_0$	30 hours	0.10	0.360	0.0173	0.0565	15.8%	0.230	4.7
14	$h > h_0$	30 hours	0.18	0.360	0.0162	0.0492	13.7%	0.220	4.5
18	base case	10 hours	0.14	0.360	0.0167	0.0365	10.2%	0.165	4.3
21	$h < h_0$	10 hours	0.10	0.360	0.0173	0.0392	11.0%	0.170	4.5
22	$h > h_0$	10 hours	0.18	0.360	0.0162	0.0352	9.8%	0.165	4.3

The table shows that for simulations with a larger water depth (run 14 and run 22) the recirculation velocity becomes smaller. This is the result of the difference in velocity profile of the runs. The average velocity is equal, but the velocity profile is different. This can be seen in Figure 5.3a, which shows the velocity profiles for the runs with a bed after 30 hours of scouring. The velocity near the bed at the upstream boundary is larger for a simulation with a smaller depth. The results for the bed after 10 hours of scouring show the same outcome. The length of the recirculation zone does not seem to be influenced by the water depth, as can be seen in the last column of Table 5.2.

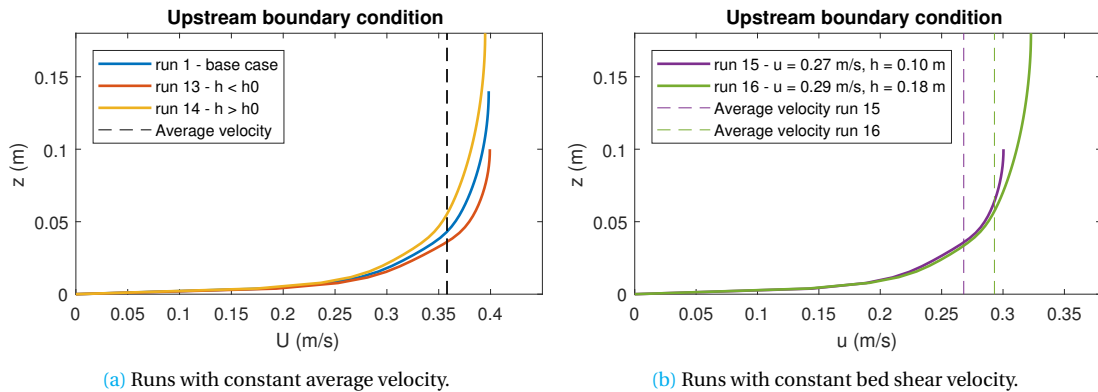


Figure 5.3: Plots showing the flow velocity profiles at the upstream boundary in the different model simulations.

The influence of the water depth is examined, but the differences in velocity profile close to the bed influence the results. These differences are resolved by using runs 15 and 16. The runs have different depths and different average velocities, but they have a similar velocity profile close to the bed and the value of the bed shear velocity is the same. The profiles are shown in Figure 5.3b. The values of the recirculation velocity, which can be found in Table 5.3, are close to each other for these runs ($u_r = 0.0432$ m/s and 0.0410 m/s). The recirculation regions also do not differ too much in size ($L_r/h_s = 4.7$ and 4.5). From this is concluded that the recirculation zone is approximately unaffected by the water depth.

Table 5.3: Recirculation parameters in the scour hole for simulations with different water depths. The definition of the parameters is given in Table 5.2.

Nr.	Name	Bed after	h (m)	\bar{u} (m/s)	u_* (m/s)	u_r (m/s)	u_r/\bar{u} (%)	L_r (m)	L_r/h_s (-)
15	$u = 0.27$ m/s, $h = 0.10$ m	30 hours	0.10	0.27	0.0132	0.0432	16.1%	0.230	4.7
16	$u = 0.29$ m/s, $h = 0.18$ m	30 hours	0.18	0.292	0.0132	0.0410	14.0%	0.220	4.5

5.1.2. Influence of the flow velocity

The influence of the flow velocity is investigated using the runs that are listed in Table 5.4. The table includes the recirculation velocity (magnitude and percentage of average upstream flow velocity) and the length of the recirculation zone (magnitude and recirculation length to depth of the scour hole ratio).

Table 5.4: Recirculation parameters in the scour hole for simulations with different flow velocities. The definition of the parameters is given in Table 5.2.

Nr.	Name	Bed after	h (m)	\bar{u} (m/s)	u_* (m/s)	u_r (m/s)	u_r/\bar{u} (%)	L_r (m)	L_r/h_s (-)
1	base case	30 hours	0.14	0.360	0.0167	0.0518	14.4%	0.220	4.5
11	$u > u_0$	30 hours	0.14	0.442	0.0205	0.0607	13.7%	0.220	4.5
12	$u < u_0$	30 hours	0.14	0.248	0.0118	0.0368	14.8%	0.225	4.6
18	base case	10 hours	0.14	0.360	0.0167	0.0365	10.2%	0.165	4.3
19	$u > u_0$	10 hours	0.14	0.442	0.0205	0.0441	10.0%	0.165	4.3
20	$u < u_0$	10 hours	0.14	0.248	0.0118	0.0260	10.5%	0.165	4.3

The values of the recirculation velocity are different for the model runs. However, the values of the relative recirculation velocity are close to each other. The runs with a bed after 30 hours of scouring all have values between 13.7% and 14.8%. The simulations with a bed after 10 hours of scouring even have a smaller range: 10.0%-10.5%. A higher average flow velocity gives a slightly lower relative recirculation velocity for both cases. The size of the recirculation zone is equal for all runs with a bed after 10 hours ($L_r/h_s = 4.3$). For the runs with a bed level after 30 hours the length of the recirculation zone lies inside a very small range ($L_r/h_s = 4.5 - 4.6$).

From this analysis can be concluded that a higher flow velocity results in a higher recirculation velocity, but the relative recirculation velocity is comparable for all the simulations.

5.1.3. Influence of the depth of the scour hole and upstream slope

The scour hole after 30 hours is used to investigate the influence of the depth of the scour hole and the upstream slope. For the runs in this part, the bed level values are multiplied by a certain factor. The runs and their recirculation parameters are shown in Table 5.5. Figure 5.4 shows the bed topography in the central axis of some of the runs. A selection is made for plotting purposes. The runs with a bed topography after 10 hours are used as an additional check on the conclusions.

The recirculation velocity for the different runs shows an interesting pattern. The values are rising with the depth of the scour hole. When the depth of the scour hole is increased, the upstream slope is getting steeper with the same factor. In Figure 5.5a, the upstream slope is plotted against the relative recirculation velocity. The upstream slope is defined as the tangent of the slope angle near the edge of the hole, see Figure 5.4. It can be seen in Figure 5.5a that the values are following a smooth line. For scour holes with smaller scour hole depths than the base case, the relation seems to be linear. The gradient of the line is getting smaller when the upstream slope increases, therefore an asymptote is expected to be present.

Table 5.5: Recirculation parameters in the scour hole for simulations with different depths of the scour hole. The definition of the parameters is given in Table 5.2, except for $\tan \beta$, which is the upstream slope. All runs have a water depth of $h = 0.14$ m and an average flow velocity of $\bar{u} = 0.360$ m/s.

Nr.	Name	Bed after	h_s (cm)	$\tan \beta$ (-)	u_r (m/s)	u_r/\bar{u} (%)	L_r (m)	L_r/h_s (-)
1	base case	30 hours	4.9	0.456	0.0518	14.4%	0.220	4.5
2	$h_s^*0.5$	30 hours	2.5	0.228	0.0000	0.0%	-	-
3	$h_s^*0.75$	30 hours	3.7	0.342	0.0000	0.0%	-	-
4	$h_s^*0.8$	30 hours	3.9	0.364	0.0000	0.0%	-	-
5	$h_s^*0.85$	30 hours	4.2	0.387	0.0121	3.4%	0.140	3.4
6	$h_s^*0.9$	30 hours	4.4	0.410	0.0245	6.8%	0.175	4.0
7	$h_s^*0.95$	30 hours	4.7	0.433	0.0388	10.8%	0.200	4.3
8	$h_s^*1.1$	30 hours	5.4	0.501	0.0753	20.9%	0.255	4.7
9	$h_s^*1.25$	30 hours	6.1	0.569	0.0929	25.8%	0.285	4.7
10	$h_s^*1.5$	30 hours	7.3	0.683	0.1075	29.9%	0.325	5.3
18	base case	10 hours	3.8	0.431	0.0365	10.2%	0.185	4.9
23	$h_s^*1.05$	10 hours	4.0	0.453	0.0507	14.1%	0.180	4.5

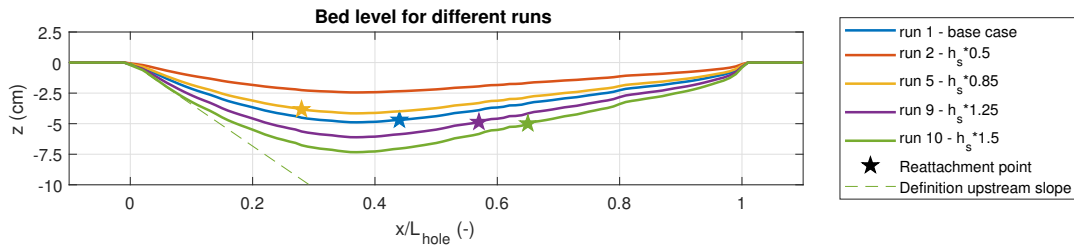


Figure 5.4: Plot showing some of the bed topographies used in the runs to investigate the influence of the depth of the scour hole and the upstream slope. The point of reattachment is indicated with a star. Run 2 does not have a flow separation, so there is no star for that simulation. The green dashed line shows the definition of the upstream slope ($\tan \alpha$).

From an ongoing experimental study at Delft University of Technology by Yorick Broekema follows that three-dimensional effects could influence the recirculation of flow. The effects, for example the flow contraction, suppress the flow separation, and the recirculation zone only forms for steeper upstream slopes, when compared to the values found in literature. In Section 2.2.2 is mentioned that flow separation is happening for slopes of at least 7° . However, Figure 5.5a shows flow separation at upstream slopes with an angle of 20° ($\tan \alpha = 0.36$) and higher only.

Two-dimensional simulations show different results for the recirculation zone, as can be seen in Figure 5.5b. The parameters and results for the two-dimensional simulations are given in Table 5.6. Flow separation is present for milder slopes, with an angle of 16.7° ($\tan \alpha = 0.30$), when compared to the three-dimensional simulations. However, the magnitude of the recirculation velocity is not larger for all two-dimensional simulations. For simulations with a scour hole depth larger than 0.95 times the base case depth, the recirculation velocity is higher in the three-dimensional simulations. The asymptote for the two-dimensional cases appears to be somewhere around $u_r/\bar{u} = 0.2$.

Another explanation for the difference in presence of the recirculation region is the deviation in definition of the angle. In the study of Chandavari and Palekar (2014), where the 7° value is found, the slope is constant and flow separation happens after many times the water depth in downstream direction. In this study, the defined angle is present behind the upstream edge. Further downstream, the angle flattens out. It is hypothesized that the flow separation happens only for steeper slopes than the mentioned 7° because of this.

In the backward facing step studies, the relative recirculation velocity ranges from 0.2 to 0.33 (Tani et al. (1961), Nakagawa and Nezu (1987) and Uijtewaal (2011)). The data points of the three-dimensional runs with a large depth of the scour hole are within this range.

Most of the data points in Figure 5.5a are points with a bed topography after 30 hours. However, two points have a bed topography after 10 hours (run 18 and run 23). These are added to this figure with a star marker,

in order to check whether the relation holds for a different bed topography. As can be seen, the data points for run 18 and 23 lie on the curve, so this relation is expected to hold in general for this scouring situation.

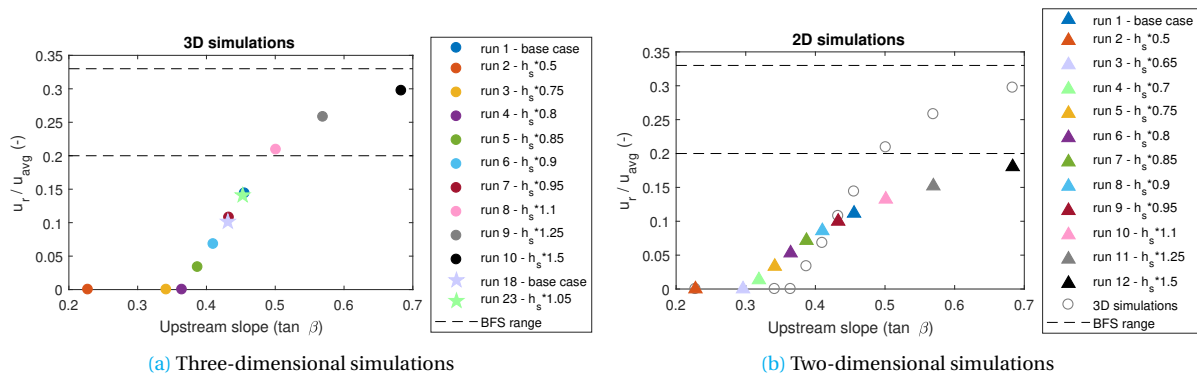


Figure 5.5: Visualization of the relation between the relative recirculation velocity and the upstream slope of the hole. The BFS range is based on Uijttewaai (2011), Tani et al. (1961) and Nakagawa and Nezu (1987).

Table 5.6: Recirculation parameters in the scour hole for the two-dimensional simulations with different depths of the scour hole. The definition of the parameters is given in Table 5.2, except for $\tan \beta$, which is the upstream slope. All runs have a water depth of $h = 0.14$ m and an average flow velocity of $\bar{u} = 0.360$ m/s.

Nr.	Name	Model type	h_s (cm)	$\tan \beta$ (-)	u_r (m/s)	u_r / \bar{u} (%)	L_r (m)	L_r / h_s (-)
1	base case	2D	4.9	0.456	0.0402	11.2%	0.255	5.2
2	$h_s * 0.5$	2D	2.5	0.228	0.0000	0.0%	-	-
3	$h_s * 0.65$	2D	3.2	0.296	0.0000	0.0%	-	-
4	$h_s * 0.7$	2D	3.4	0.319	0.0048	1.3%	0.115	3.4
5	$h_s * 0.75$	2D	3.7	0.342	0.0120	3.3%	0.160	4.4
6	$h_s * 0.8$	2D	3.9	0.364	0.0191	5.3%	0.190	4.8
7	$h_s * 0.85$	2D	4.2	0.387	0.0258	7.2%	0.210	5.0
8	$h_s * 0.9$	2D	4.4	0.410	0.0309	8.6%	0.225	5.1
9	$h_s * 0.95$	2D	4.7	0.433	0.0360	10.0%	0.240	5.2
10	$h_s * 1.1$	2D	5.4	0.501	0.0477	13.2%	0.275	5.1
11	$h_s * 1.25$	2D	6.1	0.569	0.0547	15.2%	0.305	5.0
12	$h_s * 1.5$	2D	7.3	0.683	0.0649	18.0%	0.340	4.6

The relative recirculation length varies between 3.4 and 5.3 in the simulations, see Table 5.5. As soon as a recirculation zone is present in the model simulation, the length of the recirculation zone immediately tends to move to the region between 4 and 5 times the depth of the scour hole. Only for a depth of the scour hole where the flow recirculation is very weak, the length of the recirculation is lower than 4 (run 5). The model simulation with the larger hole ($L_{\text{hole}} = 0.75$ m) from Section 4.3 also has a value of $L_r / h_s = 4.7$.

In this analysis, the relation between the upstream slope angle and the relative recirculation is obtained. However, the simulations have both a varying upstream slope angle and maximum depth of the scour hole. Therefore, it is a possibility that the relation is the result of the maximum scour hole depth, instead of the upstream slope angle. This could be checked by performing simulations with a similar upstream slope angle, but with a different scour hole depth. If the relation holds in that case, it is the result of the scour hole depth.

5.2. Flow contraction

Contraction of the flow lines is an expected phenomenon in the case of a scour hole, as described in Section 2.2.3. The flow will be dragged into the hole, resulting in flow velocities in lateral direction in the neighbouring areas. The model results show flow contraction. Figure 5.6 presents the velocities in lateral direction in a cross section at $z = 0.01$ m, accompanied by the flow lines. The flow is moving in the direction of the hole in the upstream region and in the opposite direction in the downstream region, as indicated by the arrows. As the streamwise component of the flow dominates the lateral component, the streamwise component is multiplied by a factor of 0.5 when plotting the flow lines, in order to make the flow contraction visible.

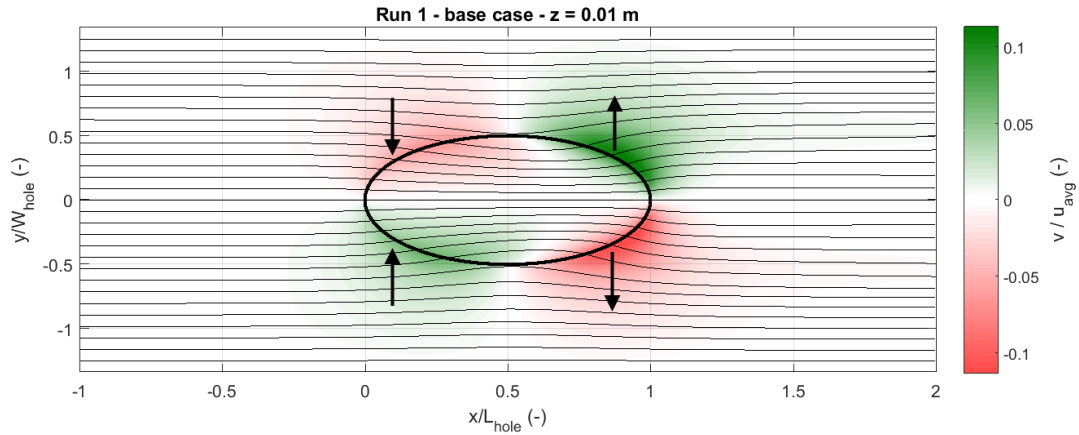


Figure 5.6: Plot showing the flow contraction in the model domain. The colors show the flow velocity in lateral direction and the lines represent the flow lines in the cross section. The cross section is located at a height of $z = 0.01$ m. The streamwise component of the flow velocity in the flow lines is multiplied with a factor 0.5.

Figure 5.7 includes the streamlines of two runs with different water depths in a cross section at $z = 0.05$ m. At this height, the flow contraction is weaker, so the streamwise component of the flow velocity is multiplied by a factor of 0.1 for plotting purposes. A lower water depth (run 13) results in a stronger flow contraction. The maximum offset of the streamlines in lateral direction in run 13 is 6.4 cm. For run 14, this value is 5.5 cm. The stronger contraction for a smaller water depth is expected, as the relative size of the scour hole is more significant. Therefore, a relatively larger part of the water column is dragged into the hole. However, the factor that is used for the streamwise component of the flow velocity makes the difference appear to be larger. Without the factor, the difference between the two runs is very small.

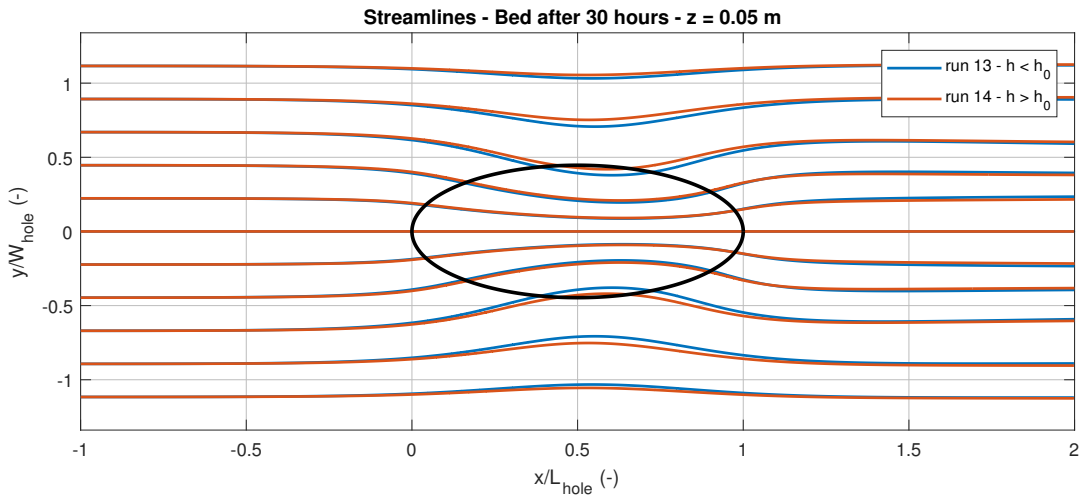


Figure 5.7: Plot showing the flow contraction in the model domain for runs with different depths. The lines represent the flow lines in the cross section at a height of $z = 0.05$ m. The streamwise component of the flow velocity is multiplied by a factor 0.1.

Figure 5.8a shows a graph that includes points of the maximum lateral flow velocity over the average flow velocity in streamwise direction versus the maximum depth of the scour hole over the upstream water depth for the runs with a varying depth of the scour hole. It shows that the magnitude of the flow contraction depends on the depth of the scour hole with a certain relation and has a maximum value around $h_s/h_0 = 0.3$. After this value, the graph has a negative slope.

The reason for the peak is found in the 'active' scour area. Active means the scour area that attracts flow, and is calculated by taking the total scouring area in the central axis of the hole and subtracting the recirculation zone area from it. Figure 5.8b shows a graph with the active scour area on the vertical axis. The peak is present around the same value for the depth of the scour hole. This could be expected, as the active scour area is responsible for the attraction of flow, and therefore also for the lateral flow velocity.

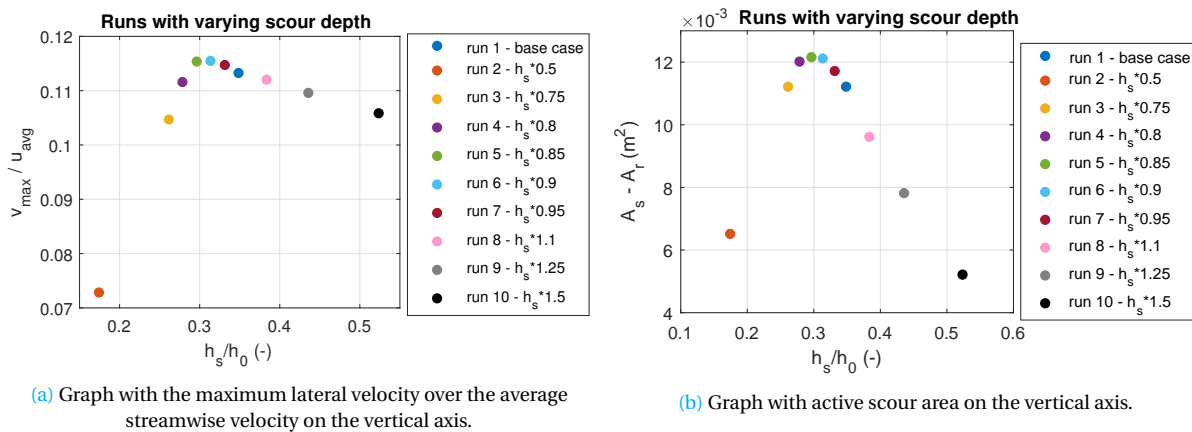


Figure 5.8: Graphs showing the relation between the relative maximum flow velocity in lateral direction at $z = 0.01$ m, the active scour area and the relative depth of the scour hole.

In Figure 5.9 the other simulations with a bed topography after 30 hours are plotted. Different markers are chosen to visualize the runs. The range of the values on the vertical axis in the figure is in the order of 10^{-3} , which is very small. Therefore, the differences between the runs are inside the uncertainty of the model, and conclusions should be drawn with caution.

The diamonds show runs with a varying flow velocity. It can be concluded that a larger upstream flow velocity results in a slightly stronger relative lateral flow velocity. The stars in the figure include runs with a varying water depth. The conclusions that are drawn from Figure 5.7 are confirmed by the star markers in Figure 5.9. A smaller water depth results in a larger lateral flow velocity and a stronger flow contraction. The triangles show runs with a constant Froude number. The markers can be used to identify what parameter has the largest influence, as both runs have a Froude number of 0.22. The simulation with the smaller water depth and smaller flow velocity has a stronger contraction, therefore the water depth is considered to be the more important parameter.

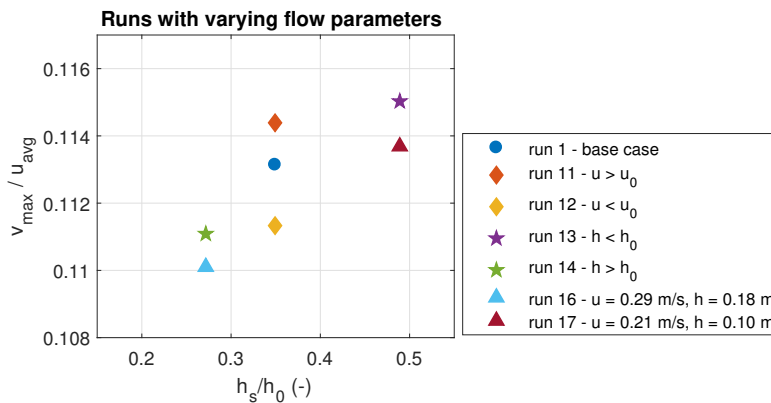


Figure 5.9: Graphs showing the relation between the relative maximum flow velocity in lateral direction at $z = 0.01$ and the relative depth of the scour hole. Runs with a varying flow velocity (run 11 and 12), water depth (run 13 and 14) and constant Froude number (run 16 and 17) are included.

As described in Section 2.2.3 the contraction of flow is expected to be the result of the distribution of the discharge at the hole. Relatively more discharge is present in the hole, when compared to the sections next to the hole. Figure 5.10 shows profiles of the specific discharge in a couple of lateral cross sections in the domain. It can be observed that the discharge inside the hole is higher and the discharge next to the hole is lower, when compared to the upstream value. Downstream of the hole the distribution of the discharge goes back to the upstream distribution, resulting in the divergence of the streamlines at this location.

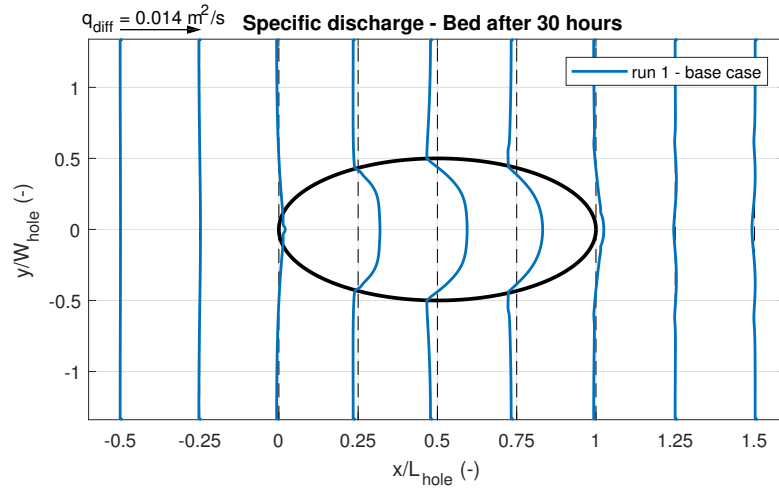


Figure 5.10: Plot showing the difference in specific discharge in several cross sections in the model results. The difference with the upstream value is plotted. The values are scaled with a value of $0.014 \text{ m}^2/\text{s}$.

Figure 5.11 shows the streamwise flow velocities in the cross section at a height of 1 cm above the upstream bed. As the streamlines are converging, the flow at this height will accelerate just upstream of the hole and above the hole. It can be observed that the highest flow velocities are present around $x/L_{\text{hole}} = 0.25$. However, when looking at the streamlines in Figure 5.6, the highest flow velocities are expected at the location where the streamlines are most converged, around $x/L_{\text{hole}} = 0.65$.

This deviation is expected to be the result of the absence of the vertical component in these visualizations. At the height of 1 cm above the upstream bed, the flow is moving into the hole, resulting in a relatively large vertical flow component. This vertical component changes the streamlines that are given in Figure 5.6 and results in the streamwise velocity values in Figure 5.11.

The flow velocity in the areas to the side of the hole is lower than the upstream value. This is the result of the diverging streamlines in these areas. Another phenomenon that can be observed in Figure 5.11 is the presence of areas with a low value of the streamwise flow velocity downstream of the hole. Two strips are starting from the sides of the hole and emerge in the downstream half of the hole. A third area is present in the center of the region downstream of the hole. These areas will be elaborated on in more detail in the next sections.

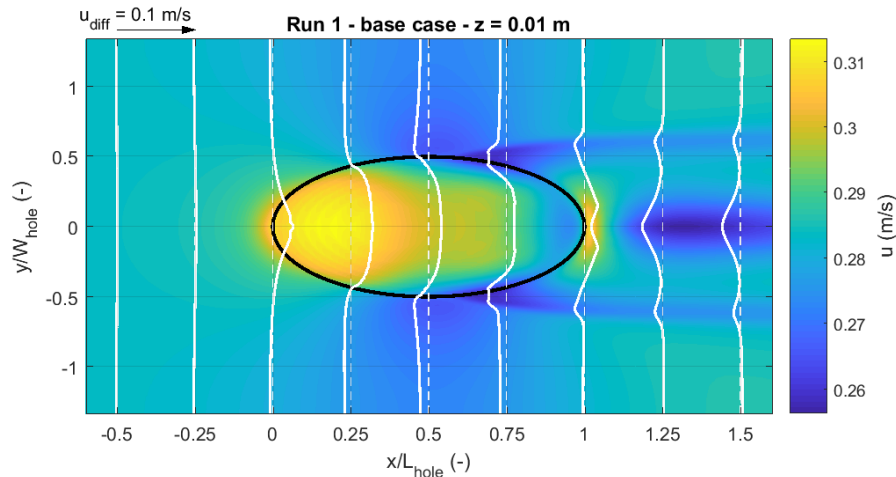


Figure 5.11: Plot showing the difference in flow velocity in streamwise direction in several cross sections. The difference in flow velocity with the average upstream value is plotted. The values are scaled with a value of 0.1 m/s .

5.3. Vortices and coherent structures

This section describes the vortices and coherent structures in the model simulations. In Appendix A.1.3 the definitions of these are given. Firstly an attempt is made to identify the horseshoe vortex, which is visually observed in the laboratory experiments. After that, the vortices that are found in the area downstream of the hole are described. Figure 5.12 presents a schematization of the vortices in the model domain. For visualization of flow structures, the vorticity is used. Besides, cross sections normal to the streamwise direction are used to visualize the velocity vectors with components in lateral and vertical direction. Last but not least, the scour hole is assumed to be symmetric, while in the flume experiment some asymmetry was observed (see Section 3.4.2). The last section evaluates the influence of the asymmetries on the calculated three-dimensional flow structures.

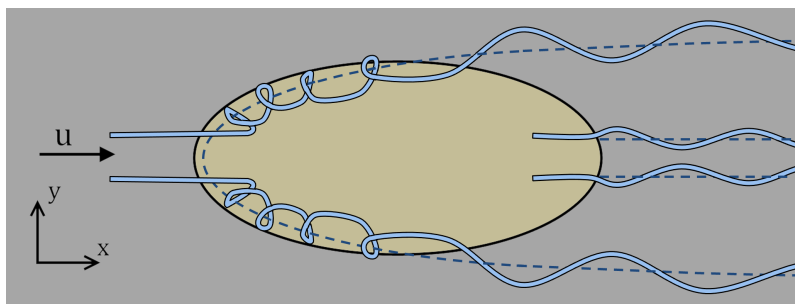


Figure 5.12: Schematic representation of the horseshoe vortex and the vortices downstream of the scour hole. The dotted lines represent the centers of the vortices.

5.3.1. Horseshoe vortex

As described in Section 2.2.3 the horseshoe vortex is observed by Uijttewaal et al. (2016) on the side slopes of the scour hole. The observations are purely visual, as no measurements of the vortex are available at this moment. The horseshoe vortex can be seen in the model results as well. Figure 5.13 shows a cross section at $x/L_{\text{hole}} = 0.5$ for the model simulation with a bed after 30 hours. The vectors indicate the flow velocity in lateral and vertical direction. The vectors show that the flow lines are directed downwards in the majority of the cross section. This is the case because the reattachment point is located around $x/L_{\text{hole}} = 0.44$. The flow lines are therefore still moving into the hole. On the side slopes a rotating structure can be distinguished. Both sides show outward directed flow velocities near the bed. The rotating structure is expected to be the horseshoe vortex mentioned by Uijttewaal et al. (2016).

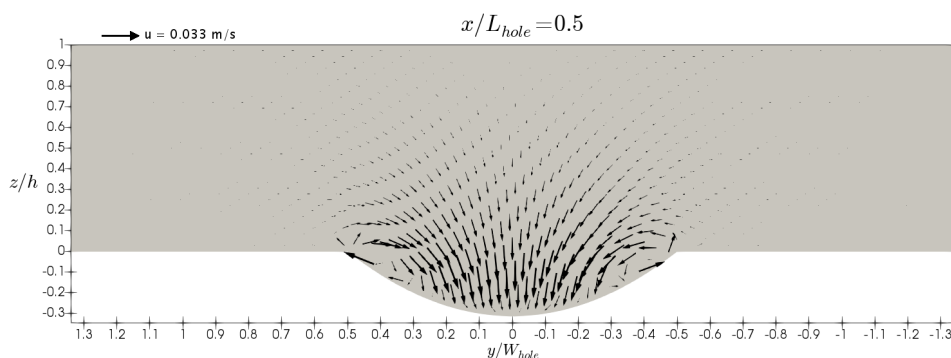


Figure 5.13: Cross section normal to the streamwise direction at $x/L_{\text{hole}} = 0.5$. The vectors are generated using the lateral and vertical flow velocity. The scale of the vectors is shown in the top left corner.

As described in Appendix A.1.3, the vorticity does not distinguish between swirling flows and shearing motions. Therefore, effects of the bed shear stress will be present in the results. As it is desired to visualize the swirling flows, the inclusion of shearing motions in the vorticity is undesired. When plotting surfaces of the vorticity in the domain, flow structures on the side slopes of the hole are present. Figure 5.14 shows vorticity surfaces with a value of $\omega_x = 2 \text{ s}^{-1}$ and $\omega_x = -2 \text{ s}^{-1}$. The vorticity areas are numbered in the figure. Areas 7 and 8 are the vortex structures on the side slopes. All other areas are located on the bed and visualize the vorticity influenced by the bed shear stress.

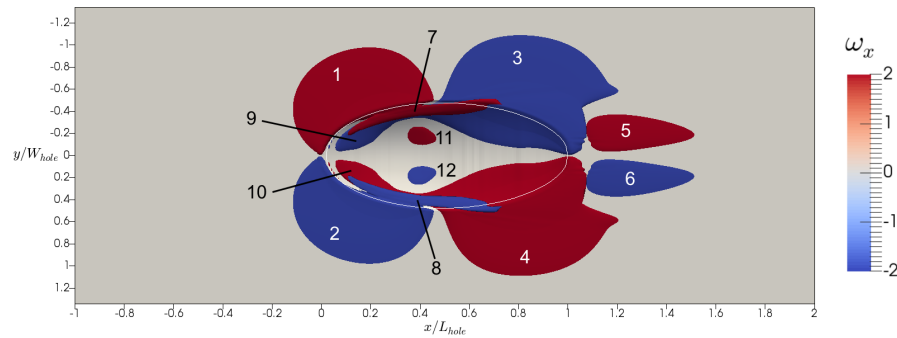


Figure 5.14: Top view of the domain showing surfaces of constant vorticity in streamwise direction. The surfaces are generated using values of $\omega_x = 2 \text{ s}^{-1}$ and $\omega_x = -2 \text{ s}^{-1}$. The areas that are indicated with a number are described in the text above the figure.

When plotting surfaces with a lower value ($\omega_x = 0.15 \text{ s}^{-1}$ and $\omega_x = -0.15 \text{ s}^{-1}$), vortex structures with a less strong rotational character are visible, see Figure 5.15. The horseshoe vortex is still visible (areas 7 and 8) and extends further outside the hole. Part of the rotational character of the horseshoe vortex forms new rotational cells downstream of the hole (areas 13 and 14). These structures lose strength when flowing further downstream. Most of the areas in the figure are induced by influences of the bed shear stress (areas 1-6 and 9-12). These areas are all located right on the bed. Areas 15 and 16 are rotating cells just above the bed. These cells emerge at the downstream edge of the scour hole. These downstream flow structures are described in the next subsection.

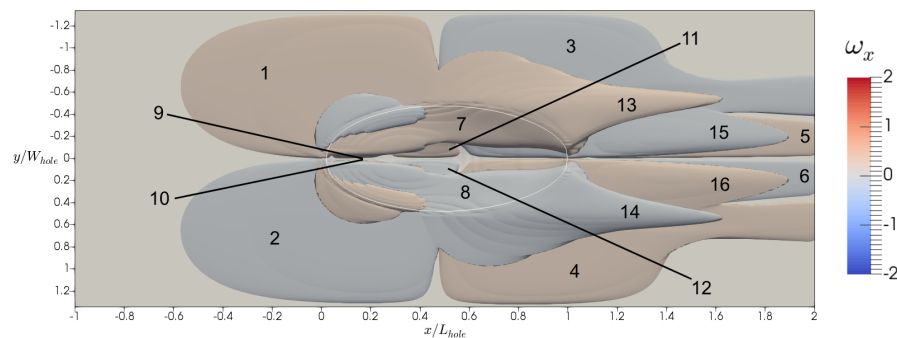


Figure 5.15: Top view of the domain showing surfaces of constant vorticity in streamwise direction. The surfaces are generated using values of $\omega_x = 0.15 \text{ s}^{-1}$ and $\omega_x = -0.15 \text{ s}^{-1}$. The areas that are indicated with a number are described in the text above the figure.

The horseshoe vortex is hypothesized to be a result of three driving mechanisms: the recirculation zone, the curved upstream edge of the hole and the flow contraction. The recirculation zone gives the horseshoe vortex its rotating character near the upstream edge. The curved upstream edge of the scour hole forces the vortex sideways, where it ends up at the side slopes. The attraction of flow lines into the hole adds momentum to the rotating motion and strengthens the vortex.

The horseshoe vortex has an influence on the erosion in the scour hole. The outward directed flow near the bed of the side slopes, which is particularly present in the downstream half of the hole, is expected to induce the undermining in this region. According to [Uijtewaal et al. \(2016\)](#), the horseshoe vortex is also dragging flow lines from upstream into the scour hole. The presence of this phenomenon could be confirmed nor rejected with the model.

5.3.2. Downstream flow structures

In the area downstream of the scour hole, flow structures are observed in the vorticity figures. In order to check the rotational character of the flow in this region, a cross section normal to the streamwise direction with flow velocity vectors is used, see Figure 5.16.

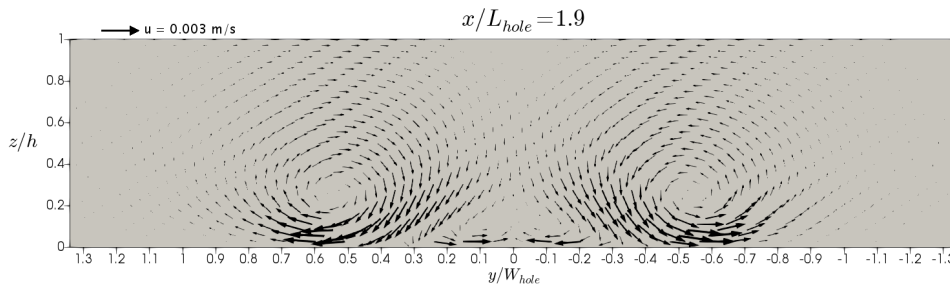


Figure 5.16: Cross section normal to the streamwise direction at $x/L_{hole} = 1.9$. The vectors are generated using the lateral and vertical flow velocity. The scale of the vectors is shown in the top left corner.

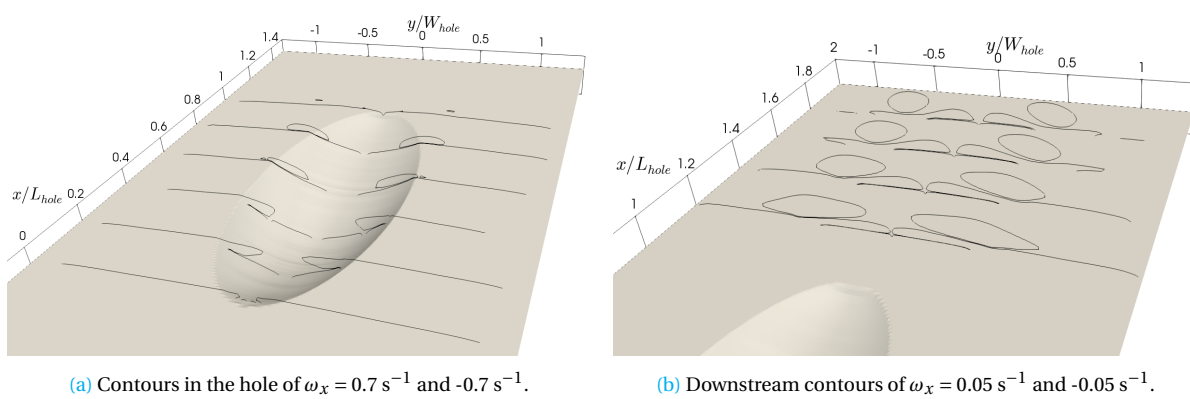
The rotational character of the flow is visible in the model results. Four rotating cells can be distinguished. Two outer cells, with their centers around $y/W_{hole} = 0.55$ and -0.55 and two inner cells with their centers around $y/W_{hole} = 0.1$ and -0.1 . The outer cells coincide with areas 13 and 14 in Figure 5.15, which extend further with a weaker rotation than visible in the figure. However, the velocity magnitude in the cross section in Figure 5.16 is only a fraction of the streamwise velocity ($v = 0.003$ m/s versus $\bar{u} = 0.360$ m/s). These structures are therefore very hard to measure in the flume experiments.

The downstream flow structures are the reason for the sediment ridges behind the scour hole in the experiments by Stenfert (2017), which are shown by the yellow ovals in Figure 5.17. The outer cells are sweeping the sediment to the sides, resulting in the two outer ridges. The inner cells are sweeping the sediment to the center of the flume, resulting in the central ridge.



Figure 5.17: Picture from the laboratory experiment by Stenfert (2017). The sediment ridges behind the scour hole are indicated with the yellow areas.

A three-dimensional visualization of the flow structures that are found in this section is shown in Figure 5.18.



(a) Contours in the hole of $\omega_x = 0.7$ s⁻¹ and -0.7 s⁻¹.

(b) Downstream contours of $\omega_x = 0.05$ s⁻¹ and -0.05 s⁻¹.

Figure 5.18: Three-dimensional visualizations of the flow structures inside the scour hole and in the downstream region. Contours of vorticity are shown for several cross sections.

5.3.3. Influence of water depth, flow velocity and depth of the scour hole

The flow structures in the model results are not constant for all runs. In this section the influence of the water depth, flow velocity and depth of the scour hole on the flow structures is examined. First, a definition of the phenomena that are used in this section is made. Four zones of the horseshoe vortex and the downstream structures are described. The horseshoe vortex in Figure 5.13 is divided in two parts: the outflow near the bed and the inflow higher in the water column. The downstream structures in Figure 5.16 are also divided in two: the outer vortices and the inner vortices.

The model simulations with a different value of the water depth show small differences when compared to the results shown above. When the water depth is increased, the outflow near the bed becomes slightly stronger and the inflow becomes slightly weaker. The outer vortices become stronger and the inner vortices become weaker. For a smaller water depth, the effects are the exact opposite. These effects are expected to be connected to the flow contraction. For a larger water depth, the flow contraction becomes weaker and therefore less water is flowing into the hole.

The influence of the flow velocity is very simple. For a higher upstream velocity, all vortices, both inside the hole and downstream of the hole, become stronger. For a lower flow velocity the opposite happens.

Figure 5.19 shows the results of the simulations with different depths of the scour hole. The magnitude of the inflow, outflow, inner vortex and outer vortex are plotted. From the figure can be concluded that the inflow of the horseshoe vortex and the inner vortex are correlated. The same holds for the outflow of the horseshoe vortex and the outer vortex. The inflow and the inner vortex get more distinct for deeper scour holes. If the values for the inflow or outflow are zero, no distinct horseshoe vortex was visible in the model results. When looking at the results for the outflow and the outer vortex, it can be seen that the most shallow hole deviates from the trend of all other holes. The trend of those holes follows: the deeper the hole, the weaker the outflow and the outer vortex.

From the analysis of the different depths of the scour hole can be concluded that the strength of the vortex is dependent on the presence of the recirculation zone. The runs that did not have a recirculation zone showed strong outflow and hardly any inflow, but as soon as the recirculation zone is present, the outflow gets weaker and the inflow gets stronger. Run 2, with the most shallow scour hole, forms an exception on this. The magnitude of the outflow and outer vortex for this simulation is average, instead of the expected stronger value. The peak that is found in the analysis of the flow contraction is not found in this analysis of the vortices and coherent structures. Therefore, the presence and strength of the vortices is not dependent on the flow contraction solely.

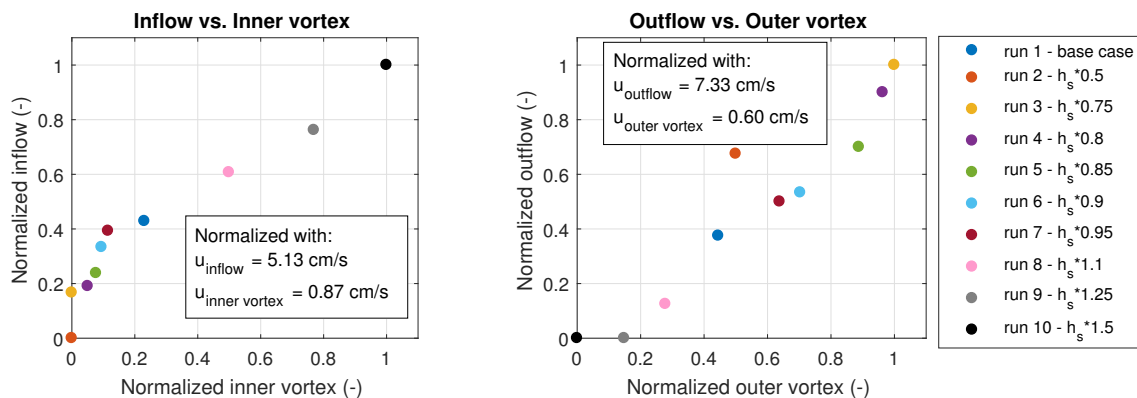


Figure 5.19: Graphs showing the magnitude of the flow structures. The values in the left plot are normalized with the values of run 10: inner vortex = 0.87 cm/s and inflow = 5.13 cm/s. The values in the right plot are normalized with the values of run 3: outer vortex = 0.60 m/s and outflow = 7.33 cm/s.

5.3.4. Influence of the symmetrical scour hole

During the setup of the model in Chapter 3, the scour hole measurements by Stenfert (2017) are found to be asymmetrical. The measurements consist of bed level values in nine longitudinal cross sections, see Figure 3.3a. Some of the flow structures that are examined in this research are expected to be the result of the hole geometry. Therefore, the geometry should be modelled with great care.

Simulations were performed with the asymmetrical bed to investigate its influence. The model results of this run show an asymmetrical flow contraction, as more water is attracted to the negative y side of the hole, which is the deeper side. The recirculation zone is asymmetrical as well, unlike the zone in the symmetrical model simulation. Additional flow structures are induced by the asymmetrical bed, as can be seen in Figure 5.20. The general flow structures are also present in this simulation.

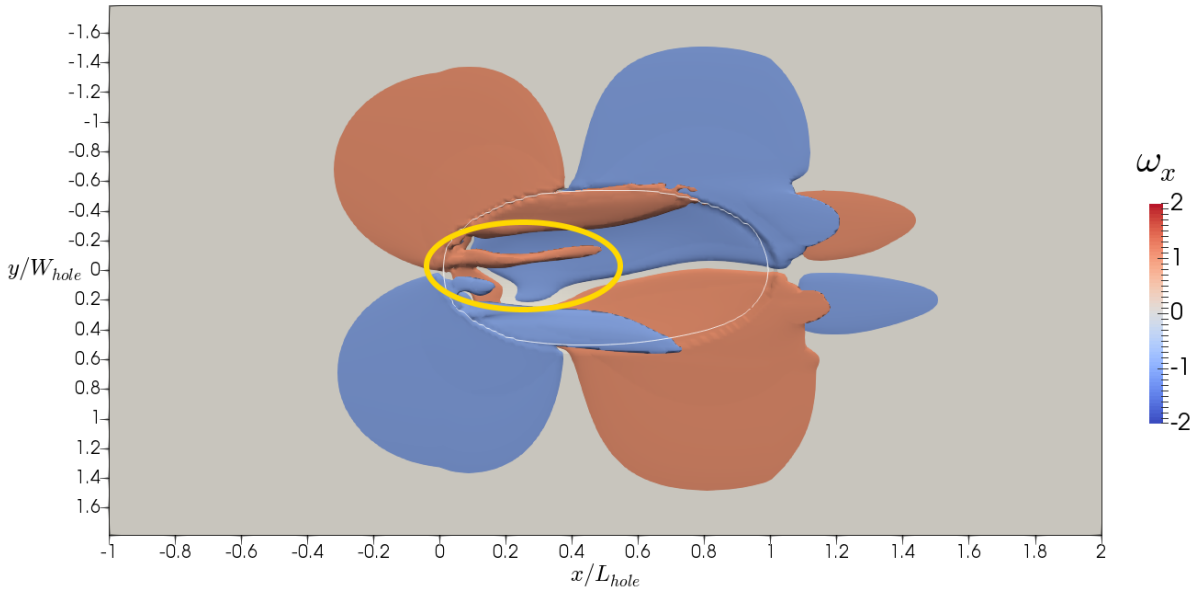


Figure 5.20: Top view of the domain showing surfaces of constant vorticity in streamwise direction for the model simulation with an asymmetrical bed. The surfaces are created using values of $\omega_x = 1 \text{ s}^{-1}$ and $\omega_x = -1 \text{ s}^{-1}$. The yellow circle highlights the asymmetrical flow structures that are found.

In order to eliminate the asymmetrical flow structures in the model results, it is chosen to create the symmetrical hole by using the oval shape edge and the cross section through the center of the hole. The error in bed level that is made by introducing the symmetrical hole is examined in Figure 3.6. The cross sections in the upstream part of the hole ($x/L_{\text{hole}} = 0.1 - 0.4$) have low errors. In the downstream part ($x/L_{\text{hole}} = 0.5 - 0.9$), the symmetrical hole deviates further from the measured bed levels. The left side (with negative values for y/W_{hole}) is deeper in the measurements. The measured bed shows asymmetrical features in the cross sections at $x/L_{\text{hole}} = 0.5 - 0.7$, as the bed values at the right side (positive y) are higher and at the left side (negative y) are lower than the symmetrical bed, as schematized in Figure 5.21.

The scouring situation in the laboratory experiments is never fully symmetrical. Deviations between flow measurements and model results due to this approximation are expected. Additional flow structures are observed in the model simulations with the asymmetrical bed. However, the general flow structures that are examined in this research are identical in both simulations, but more clear in the symmetrical simulation.



Figure 5.21: Schematic visualization of the asymmetrical features in a lateral cross section of the measured bed topography.

5.4. Bed shear stress and erosion

Assuming that bed load transport has an important contribution tot the total erosion, indication of the expected erosion can be derived from the bed shear stresses. The values that are presented in this section include the stress that is induced by the fluid and working on the bed. Figure 5.22 shows a top view of the domain including the bed shear stress in streamwise direction in the scour hole with a bed topography after 10 hours (run 18). The red colour indicates negative values of the bed shear stress. The zero value contour is shown in black, as well as the edge of the scour hole.

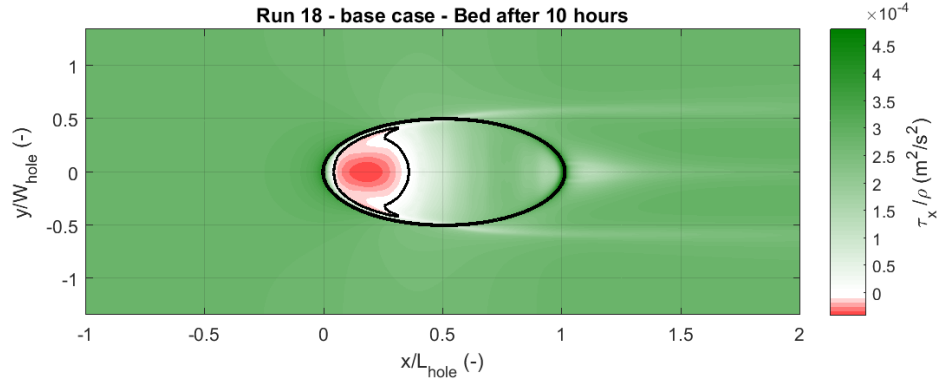


Figure 5.22: Top view of the bed shear stress in streamwise direction in the scour hole and the surrounding area. Negative values have red colour, positive values are coloured in green.

5.4.1. Coupling from bed shear stress to sediment transport and erosion

An important step in the investigation of the model results is the coupling from bed shear stress to erosion. This coupling is explained using the bed shear stress from the model results in the central axis in streamwise direction, see Figure 5.23a. As described in Section 2.3.2, the amount of erosion and sedimentation are calculated using Exner's equation. The rate of change of the bed is related to the slope in the sediment transport rate in streamwise direction. The sediment transport rate is derived using the relation by Meyer-Peter and Müller (1948), which is described in the same section. This relation uses the Shields parameter, which is proportional to the bed shear stress and is set to 0.04. The critical Shields parameter is corrected in case of a bed slope. Due to this correction, a graph showing the bed shear stress does not necessarily have the same shape as a graph showing the sediment transport. Also, at locations where the critical bed shear stress is not exceeded, no sediment transport is present. Figure 5.23b shows the sediment transport rate which is calculated using the bed shear stress from Figure 5.23a. The locations where sedimentation and erosion are expected, according to the sediment transport rate, are indicated in the figure.

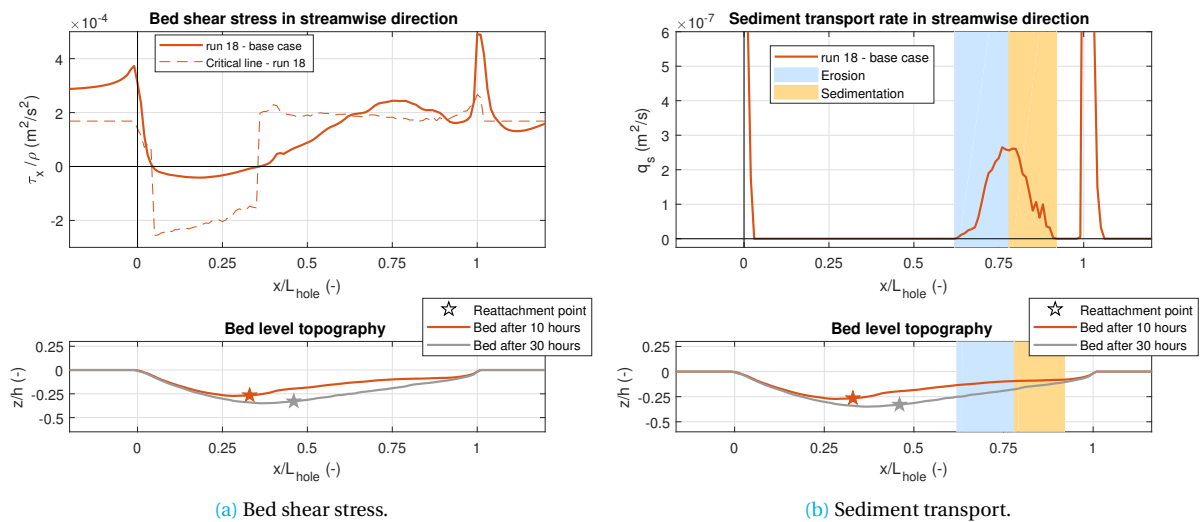


Figure 5.23: Plots showing the bed shear stress (left) and sediment transport (right) in the central axis in streamwise direction. The critical value of the bed shear stress is calculated using Equation 2.3 and the adaptations for a slope in Section 2.3.2.

The lines in Figure 5.23a have values that exceed the critical value in the region upstream of the hole. According to the calculations, these values result in sediment transport. However, due to the absence of transportable material upstream of the hole, no sediment transport takes place at that location. The negative slope in sediment transport around $x/L_{\text{hole}} = 0$ is therefore not causing sedimentation. The peak at the downstream edge of the hole ($x/L_{\text{hole}} = 1$) is considered to be the result of a singularity in the model due to the sharp corner that is present in the bed geometry. Therefore, it is neglected in the analysis of the sediment transport and erosion in the hole.

Figure 5.23 shows the model results for the base cases with a bed after 10 hours. The measured bed topography both after 10 hours and 30 hours are shown in the lower figures in Figure 5.23. At the upstream slope of the hole ($x/L_{\text{hole}} \approx 0 - 0.35$) the calculated bed shear stresses are far below the critical value. Therefore, no sedimentation and erosion are happening and the slope angle is constant, according to the model results. This is confirmed by the experiments, as the upstream slope after 10 hours and 30 hours show the same angle.

The bed shear stress at the reattachment point shows values close to zero. According to the model results no erosion or sedimentation happens at that location. However, the bed topography after 30 hours shows erosion around the reattachment point. This is the case due to the large impact on the bed in this area, as mentioned in Section 2.2.1.

The calculated values of the sediment transport rate in Figure 5.23b show a peak around $x/L_{\text{hole}} = 0.75$. At the location of the positive slope in the sediment transport rate the bed is eroding. Slightly further downstream, where the slope of the graph is negative, sedimentation is happening. The measured bed topography after 30 hours shows that no sedimentation takes place, and therefore contradicts the model results. An explanation for this can be found in the fact that the model simulates only one point in time, where locally some sedimentation occurs. Later, the sediment is transported further downstream and will slowly leave the hole.

The bed shear stress in the simulation with a bed topography after 30 hours of scouring does not reach the critical value inside the hole. Therefore, there will be no sediment transport as a result of the calculated bed shear stress (see Figure I.1 in Appendix I).

Other effects on erosion

The presence of erosion and sedimentation in the calculation in Figure 5.23 indicates that the hole is still evolving and getting deeper, which is observed in the experiments. However, the model only calculates the average bed shear stress, which results in structural erosion due to the flow field. In reality, erosion and sedimentation also happen due to local fluctuations in the flow, pressure and bed shear stress. The fluctuations are able to stir the sediment up in the water column, without a high value for the bed shear stress. This sediment can be transported with the flow and settle down somewhere else. This phenomenon is not included in the analysis of the bed shear stresses. Therefore, the erosion and sedimentation that are calculated from the model results are not giving the full picture.

5.4.2. Bed shear stresses in the base cases

The bed shear stresses in the base cases are examined in this section. The top view of the bed shear stresses in Figure 5.22 is showed again in Figure 5.25 including two yellow ovals. These ovals indicate areas with a strip of zero bed shear stress with an angle of 1:8. The same angle is found in the scour hole with a bed topography after 30 hours (run 1, see Figure 5.25). In the latter simulation, the strips are located outside the scour hole, whereas in the former simulation, the areas are located partially inside the scour hole. Koopmans (2017) found erosion with an identical angle of 1:8 during the laboratory experiment with a poorly erodible top layer. The initial scour hole eroded until undermining occurred at the sides of the hole. Then the top layer failed and the process started again. In this way, the hole extended in downstream direction with a 1:8 angle, as can be seen in Figure 5.26a. A bed shear stress with a value of zero does not necessarily result in zero erosion. If an area of zero bed shear stress is surrounded by areas with a higher or lower value, erosion or sedimentation will take place as there is a gradient in the bed shear stress, as described in Section 5.4.1.

During the laboratory experiments of Stenfert (2017), sediment ridges with the same angle are found. Figure 5.26b shows these ridges. The location of the sediment ridges is similar to the location of the 1:8 angle zero bed shear stress in Figure 5.25.

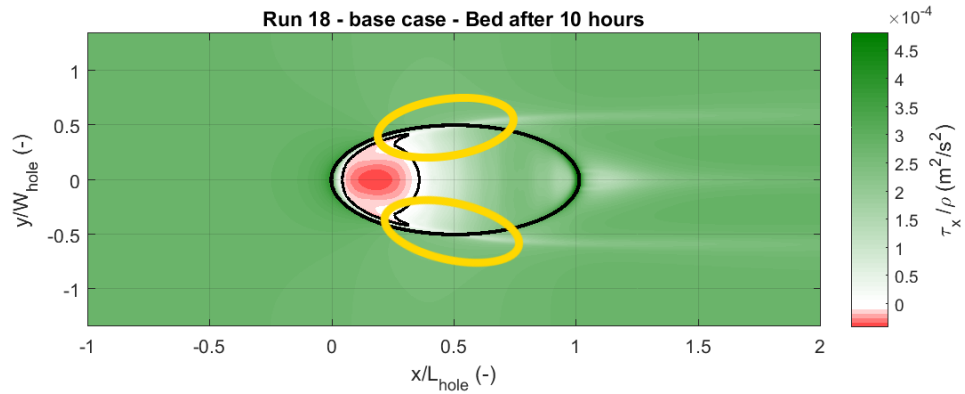


Figure 5.24: Top view of the bed shear stress in streamwise direction in the scour hole and the surrounding area. Negative values have red colour, positive values are coloured in green. The yellow ovals indicate the 1:8 slope in bed shear stress that is present inside the hole. The edge of the hole and the line with zero bed shear stress are indicated in black.

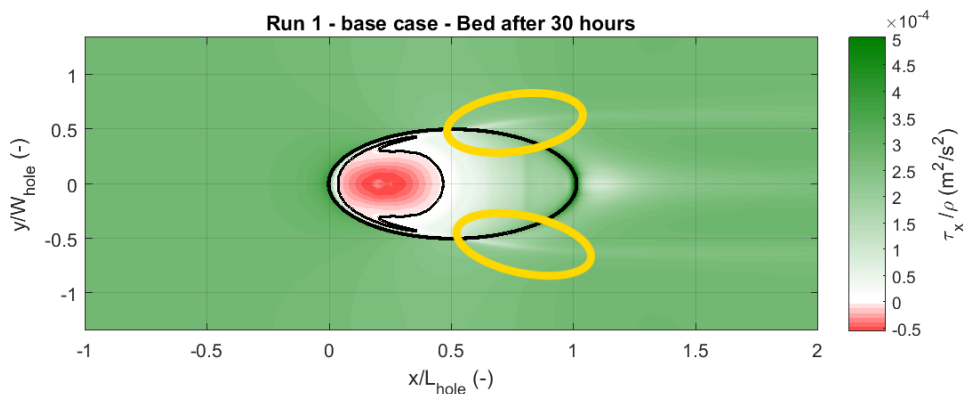
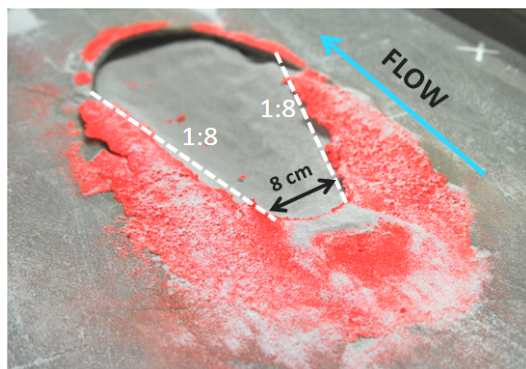
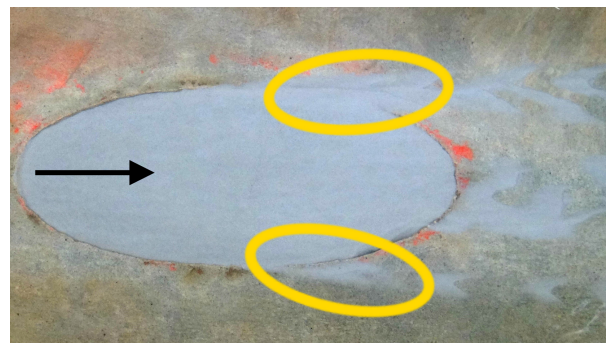


Figure 5.25: Top view of the bed shear stress in streamwise direction in the scour hole and the surrounding area. Negative values have red colour, positive values are coloured in green. The yellow ovals indicate the 1:8 slope in bed shear stress that is present outside the hole. The edge of the hole and the line with zero bed shear stress are indicated in black.



(a) Koopmans (2017)



(b) Stenfert (2017)

Figure 5.26: Pictures from the laboratory experiments by Koopmans (2017) and Stenfert (2017). The orange material in the left figure is used to mimic the poorly erodible top layer. The 1:8 slope is observed in the erosion of the poorly erodible layer. The right image shows the 1:8 slope in the sediment ridges that are formed at the edge of the hole.

Figures 5.27 and 5.28 are used to assess the bed shear stress in lateral direction. The figures show large areas with higher magnitudes in bed shear stress in lateral direction next to the upstream half of the hole. The bed shear stress in these regions is directed to the hole, and therefore these regions indicate that the flow near the bed is dragged to the hole (as indicated by the arrows in Figure 5.27). Outside the hole in the area downstream of the reattachment point, the bed shear stress has higher magnitude areas again, but directed away

from the hole. This is expected, as the flow is moving out of the hole. Downstream of the hole, four areas with alternately positive and negative bed shear stress are visible. These areas are indications of flow structures that are present in this region. The flow structures will be described in Section 5.3.

The magnitude of the bed shear stress in lateral direction is one order smaller than the bed shear stress in streamwise direction. Therefore, the main direction of transport of sediment will be in streamwise direction. However, at locations where the lateral component shows a large value, it can influence the transport significantly. This is observed in the area behind the scour hole in the experiments by Stenfert (2017). Three ridges of sediment behind the hole are present, which are indicated in Figure 5.17. The ridges are the result of the bed shear stress in lateral direction, which is induced by the downstream vortices. According to the model results, the ridges are located at $y/W_{\text{hole}} = 0, 0.65$ and -0.65 . The outer two ridges in Figure 5.17 are located more central around $y/W_{\text{hole}} = 0.5$ and -0.5 . Petersen et al. (2015) found a similar phenomenon in their laboratory experiments on scour around a circular pile. The counter rotating vortices (see Figure 2.14) behind the pile left a piled up sediment ridge.

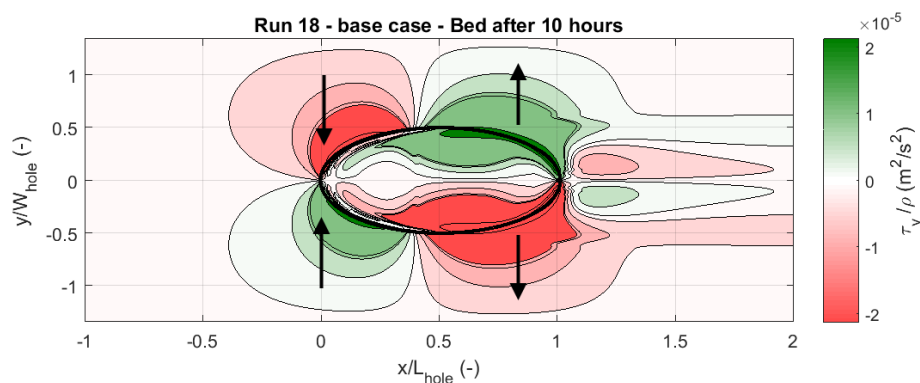


Figure 5.27: Top view of the bed shear stress in lateral direction in the scour hole and the surrounding area. Negative values have red colour, positive values are coloured in green. Contours of several values are shown.

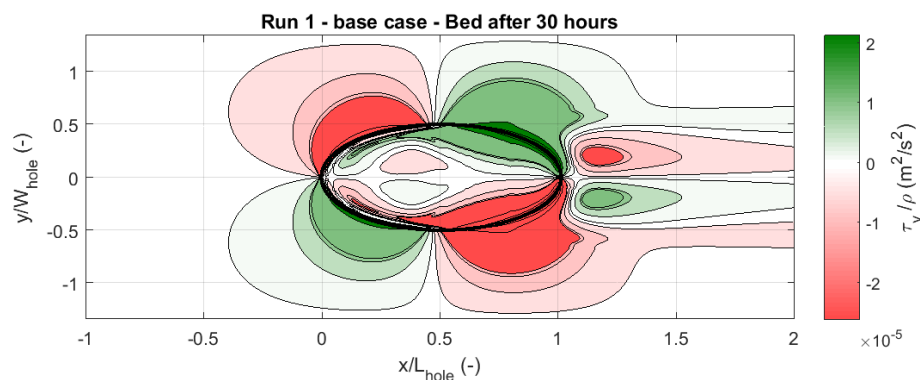


Figure 5.28: Top view of the bed shear stress in lateral direction in the scour hole and the surrounding area. Negative values have red colour, positive values are coloured in green. Contours of several values are shown.

5.4.3. Influence of the water depth, flow velocity and depth of the scour hole

Influence of the flow velocity and water depth

Model simulations with a higher upstream flow velocity (runs 11 and 19) result in larger bed shear stresses. In the downstream half of the hole, the critical value is reached much easier, resulting in more sediment transport in the hole (Figures I.2 and I.4). The influence of the water depth is only observed in the simulations with a bed topography after 10 hours of scouring. The bed shear stress in the model results for the bed topography after 30 hours does not reach the critical value for any of the runs with different water depths. The 10 hour runs show that more sediment transport occurs when the upstream depth is larger, see Figure I.5.

From this can be concluded that a larger upstream velocity results in more erosion, which is also observed in the experiments. A larger upstream water depth results in more erosion as well. However, this could be the result of the same effect as described in Section 5.1.1. The bed shear stress in the simulations with a similar velocity profile (runs 15 and 16) does not reach beyond the critical value. The graphs are very similar, as can be seen in Figure I.3a. Therefore, it is concluded that the water depth hardly influences the bed shear stress in the model results.

Influence of the depth of the scour hole

The effect of scour hole depth is based on a scaling of the 30 hour scour hole geometry. As mentioned above, for the base case the shear stresses did not reach beyond the critical value. Only for reduced depths of the scour hole, shear stresses reach beyond the critical value, resulting in sediment transport. This is illustrated in Figure 5.29.

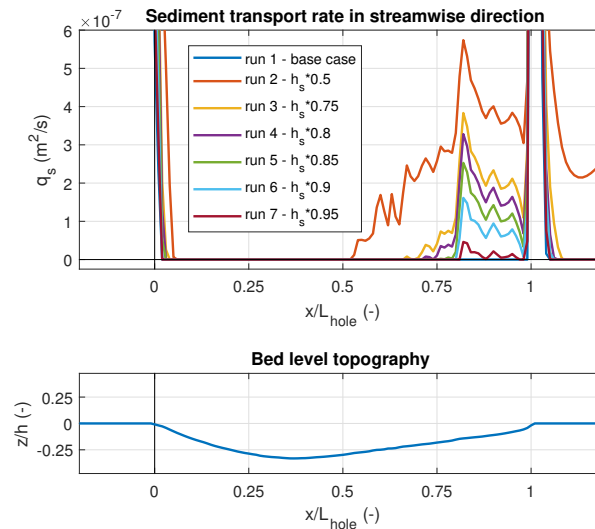


Figure 5.29: Plot showing the sediment transport in the central axis in streamwise direction. The model results of runs 1 - 7 are shown. The critical value of the bed shear stress is calculated using Equation 2.3 and the adaptations for a slope in Section 2.3.2.

The simulation with a depth of the scour hole of 0.5 times the base case depth (run 2) has sediment transport in a large part of the downstream half of the hole. This simulation represents an early moment in the scouring process, where the downstream half of the hole is eroded to a larger extent by the bed shear stress. The figure shows that a deeper scour hole has less sediment transport. This is expected, as a deeper scour hole is getting closer to the equilibrium state and therefore erodes slower.

5.5. Conclusion

All the hydrodynamical processes mentioned in Section 2.4 are reproduced by the model. In this section, an overview is given of the analysis in this chapter and the most important findings are listed.

Recirculation zone

The recirculation zone is clearly present in the model results, see Figure 5.2. The zone has a length of $L_r/L_{\text{hole}} = 0.44$, which could also be written as $L_r/h_s = 4.5$. The observations with dye showed that the recirculation in the laboratory experiments has a smaller recirculation zone of $L_r/L_{\text{hole}} \approx 0.25$. The magnitude of the recirculating flow is measured using ADV and is smaller as well, when compared to the model results.

The recirculation zone is hardly affected by changes in water depth, as long as the velocity profile close to the bed is similar. Differences in the upstream flow velocity do influence the recirculation zone, as the recirculation velocity is higher for a higher upstream flow velocity. However, the relative recirculation velocity stays approximately constant. The length of the recirculation zone and the location of the reattachment point are roughly equal for simulations with different water depths and flow velocities.

The flow recirculation is present for upstream slopes with an angle of 20° and higher. The magnitude of the relative recirculation velocity is dependent on the upstream slope angle or scour hole depth, see Figure 5.5a. Two-dimensional simulations show a flow separation for more gentle slopes. Therefore, it can be concluded that three-dimensional effects, like flow contraction, counteract the formation of a recirculation zone. However, for steeper slopes, the recirculation in three-dimensional simulations is stronger.

Flow contraction

A subtle flow contraction is observed in the model results, see Figure 5.6. The streamwise component of the flow velocity is much larger than the lateral component. At a height of 1 cm above the upstream bed, the streamwise component is a factor 10 larger than the lateral component. At a height of 5 cm above the bed, this factor is 40.

A larger upstream water depth will result in a weaker flow contraction, because the depth of the scour hole is relatively small compared to the water depth. For the same reason, a smaller water depth results in a stronger flow contraction. A larger upstream flow velocity results in a slightly stronger flow contraction. However, the differences are small and within the error margin of the model. A deeper scour hole does not necessarily result in a stronger flow contraction. The flow contraction depends on the active scour area. If the recirculation zone grows significantly, the active scour area could even decrease with increasing scour hole depth. This results in a weaker flow contraction for a deeper scour hole. The resulting dependency is showed in Figure 5.8.

The relation that is found between the flow contraction and the maximum scour depth contradicts the hypothesis by Uijttewaai et al. (2016), who expected deeper holes to contract more water and therefore become even deeper. According to the model results, a deeper scour hole does not contract more water and therefore does not become deeper.

Horseshoe vortex

The horseshoe vortex is observed when looking at the rotational character of the flow at the edge of the scour hole, see Figure 5.13. The rotation of this vortex is much weaker than the streamwise component of the flow velocity. Therefore, the vortex does not make a complete rotation inside the model domain. Observation of the vortex in a laboratory experiment with ADV is very hard, so other techniques are needed. The presence of the horseshoe vortex induces the formation of two rotational cells downstream of the hole around $y/W_{\text{hole}} = 0.55$ and -0.55 (see Figure 5.16). The stronger the outflow character of the horseshoe vortex, the more distinct the downstream cells.

A different water depth slightly influences the strength of the horseshoe vortex and the downstream flow structures. With a larger water depth the inflow of the horseshoe vortex is weaker and the outflow is stronger. The opposite holds for a smaller water depth. The influence of the flow velocity is straightforward. A higher upstream flow velocity results in a stronger horseshoe vortex. The influence of the depth of the scour hole is shown in Figure 5.19. For a deeper scour hole, the inflow of the horseshoe vortex gets stronger and the outflow gets weaker. One exception is present: the most shallow hole shows lower values for the outflow than the holes that are slightly deeper. The outward directed flow near the bed in the horseshoe vortex is expected to induce the undermining in the hole. This is particularly present in the downstream half of the hole.

Downstream vortices

Downstream of the hole four rotating cells are present, see Figure 5.16. These rotating cells are expected to be the result of the horseshoe vortex. If the inflow of the horseshoe vortex is strong, the inner vortices downstream of the hole are strong as well. The same holds for the outflow and the outer vortices. Therefore, the influence of the parameters is the same for the downstream vortices and the horseshoe vortex.

The downstream vortices are expected to be the cause for the presence of sediment ridges downstream of the hole. These ridges are observed in the laboratory experiments by Stenfert (2017).

Bed shear stress

From the simulated flow field, average values for the bed shear stress are calculated. These average values give a first rough indication of the erosion that would result from the flow field inside the scour hole. The results do not show any sediment transport in the upstream half of the scour hole, as the critical bed shear stress is reached only in the downstream half, see Figure 5.23. The constant upstream slope angle is confirmed by the measurements in the experiments. However, the area around the reattachment point is eroding in the experiments, whereas it remains unaffected in the model results. This is explained by the fact that the model simulation does not include fluctuations in flow, pressure and bed shear stress. These are present at the reattachment point and causing erosion at that location.

In the analysis of the model results, strips of zero bed shear stress with an angle of 1:8 are found at both sides of the hole, see Figure 5.24. This angle is identical to the angle of the downstream extension of a scour hole in experiments by [Koopmans \(2017\)](#). The influence of the water depth is very limited, as long as the velocity profile near the bed is kept constant. A larger flow velocity results in higher bed shear stress values. Scour holes with a small depth have a higher bed shear stress, which is expected because a scour hole in a shallow stage is evolving faster.

Chapter 6

Discussion

The objective of this research is to get a better understanding of the development of scour holes in heterogeneous subsoil. This is attempted to be achieved by simulating the hydrodynamics in a scouring situation on laboratory scale. The model validation in Chapter 4 gave confidence on the capability of the model to simulate the hydrodynamics in the scour hole correctly. A discussion on approximations in the model and the validation material can be found in the corresponding sections: the influence of the rigid lid approximation and side walls in Section 4.4, the influence of the symmetrical geometry of the hole in Section 5.3.4 and the validity of the validation data in Section 4.3.1. In this chapter, a discussion on the interpretation of the model results is given (Section 6.1), followed by a comparison of this study and the numerical part of the study by Van Zuylen (2015) (Section 6.2). Finally, the relevance for scour holes in the field is discussed in Section 6.3.

6.1. Interpretation of the results

In this section, the interpretation of the results is discussed. In the first place, the calculation of sediment transport and erosion is described. After that, the influence of the hydrodynamical processes on the morphodynamics is discussed, followed by a discussion on the interpretation of the estimated erosion.

6.1.1. Calculation of sediment transport and erosion

The calculation of sediment transport and erosion from the bed shear stress is performed in Section 5.4.1. Many approximations and simplifications are made in the calculation. In the first place, only bed load transport is included in the calculations. The critical value of the bed shear stress is obtained by using the Shields mobility parameter, in combination with an expression that includes the slope angle (see Equation 2.8). The critical Shields parameter was set to 0.04, which is proposed by Damgaard et al. (1997). The resulting critical line in Figure 5.23a has a large uncertainty, as the uncertainty in the critical Shields parameter and the inclusion of the slope effect is large. Besides, the relations by Shields are found based on uniform flow conditions, which are not present inside the scour hole. Changes in the critical line could lead to different results for sediment transport. If the critical line would become lower, more sediment transport would be present in the downstream half of the hole. However, the bed shear stresses in the upstream part of the hole are far below the critical value, so this part of the hole is assumed to certainly have a constant slope angle.

As mentioned before in Section 5.4.1, the bed shear stress values from the model results are average values, and fluctuations are not calculated by the model. At a location where the average bed shear stress does not reach beyond the critical value, fluctuations could be present that do reach beyond the critical value. In this way, a location that seems to be stable from the calculations could have erosion and sedimentation happening because of this phenomenon.

Another process that is important for sediment transport is turbulence. Sumer et al. (2003) found increased sediment transport rates for situations with increased turbulence. The calculation of sediment transport does not include the effects of turbulence. A method to include the effects is proposed by Pilarczyk (1998). He introduces the K_T parameter, which is used to include the effects of turbulence in the calculation of the stability parameter.

6.1.2. Influence of the hydrodynamical processes on the morphodynamics

The influence of the hydrodynamical processes, described in Section 5.5, on the morphodynamics is elaborated on in this section. This influence is obtained by coupling the observations on bed shear stress and erosion to the processes.

Recirculation zone

Before the recirculation of flow is present, the upstream slope is eroding. As soon as the slope becomes steep enough, flow separation happens and the bed shear stress at the upstream slope is directed in upstream direction. The average recirculating flow never exceeds the critical value that is needed to structurally transport sediment uphill. From this can be concluded that the recirculation of flow is keeping the upstream slope constant. However, fluctuations in the recirculating flow and turbulence inside the recirculation zone might be able to stir up sediment. The upstream directed flow could transport this sediment uphill. If the slope becomes steeper than the angle of repose of the sediment ($\phi \approx 35^\circ$ (Hoffmans and Verheij, 1997)), avalanching can happen, which will make the slope more gentle. Although, this is not observed during the experiments. This could be the result of scaling effects, as the slope stretches over a small distance. This is expected to reduce the avalanching effects. In the field, the slopes are much longer, therefore avalanching is expected to happen for more easily.

Around the reattachment point, the flow has the highest impact on the bed (Bradshaw and Wong, 1972). The flow lines are impinging on the bed, creating large pressure differences. These pressure differences will stir up sediment, resulting in more sediment being in suspension. The flow is able to transport this sediment, resulting in erosion at this location. As stated before, this phenomenon is not included in the erosion and sedimentation values calculated from the model results. The expected evolution of the bed is schematized in Figure 6.1. The downstream half of the hole (inside the grey square) evolves due to the calculated bed shear stress, while the area upstream from that erodes due to the impact of the reattachment of the flow.



Figure 6.1: Schematization of the evolution of the bed, derived from the bed shear stress in the model results and the expected erosion near the reattachment point. The grey square indicates the area that is influenced by the bed shear stress.

Flow contraction

The flow contraction drags the flow lines into the hole. Along with these flow lines, extra momentum enters the hole, which can be deduced from the higher streamwise flow velocity just above the hole (see Figure 5.11). Because of this, more turbulence will be present and more erosion will take place in the downstream half of the hole. However, a deeper hole does not always result in a stronger flow contraction. In Section 5.2 is shown that the magnitude of the flow contraction is dependent on the active scour area. This area does not always grow when the scour hole gets deeper. Therefore, the hypothesis from Uijttewaal et al. (2016) (a deeper hole attracts more flow and therefore gets even deeper) is not necessarily true. Although, other effects could also play a role in the deepening of the scour hole. For example, the influence of turbulence on suspended sediment could be important but cannot be seen in the model results.

Horseshoe vortex

The most important effect of the horseshoe vortex on the scouring process is the outward directed flow near the bed at the side slopes of the hole. This flow is particularly present in the downstream half and is hypothesized to induce the undermining of the poorly erodible edge. The outward directed component is expected to be able to transport sediment out of the hole. This is confirmed by the presence of sediment next to the downstream half of the hole (see Figure 5.26b). The component of the horseshoe vortex directed into the scour hole has the same effect as the contraction of flow. More momentum will be dragged into the hole, resulting in more turbulence inside the hole, which could lead to more erosion.

Downstream vortices

The downstream vortices have an effect on the downstream deposition of sediment. Sediment is deposited in three ridges behind the hole. This could be of importance when a tidal situation is investigated, as the sediment would flow back into the hole after flow reversal and the clear-water scour approximation would not be completely valid anymore.

6.1.3. Interpretation of the estimated erosion

The estimated erosion, occurring as a result of the calculated bed shear stress, only gives an image of one moment in time. The bed development that is sketched in Figure 6.1 could be updated in the model, and a new simulation of the hydrodynamics could be done.

According to the erosion due to the calculated bed shear stress only, the hole would not become any deeper after 30 hours of experiment, as no sediment transport is happening. However, in the laboratory experiments by Stenfert (2017) is found that the hole is still slightly evolving at that time. This is the result of the processes that are not included in the model and the approximations in the calculation of sediment transport, as discussed in Section 6.1.1. Therefore, if an update of the bed level based on the calculated sediment transport is preferred, an expression of additional sediment transport should be included, based on the turbulence levels inside the hole.

In the analysis of the bed shear stress, a strip with zero bed shear stress with an angle of 1:8 is found at the sides of the hole. The gradient in bed shear stress is large at these locations, therefore the sediment transport capacity will be large as well. Koopmans (2017) found that a scour hole with a poorly erodible top layer expanded in downstream direction with a widening angle of 1:8. This may be related to the zero bed shear stress strip.

6.2. Comparison with numerical simulations by Van Zuylen (2015)

Numerical modelling of a scour hole in heterogeneous subsoil is performed by one researcher in the past. Van Zuylen (2015) set up a 2DV model in FINEL to simulate the hydrodynamics in a two-dimensional scouring situation as a first attempt. In his study, he compared simulations with different turbulence models to check the influence of these models. He found that the $k-\epsilon$ turbulence model is too diffusive for the simulation of flow in a scour hole. The numerical simulations cover only a small part of his research, so no other analyses are performed. Therefore, no insight in the influence of the hydrodynamical processes is gained.

In the current research, the focus is on the analysis of the numerical results. The used turbulence model ($k-\omega$) was not included in the study by Van Zuylen (2015). The results give insight in the presence and dependencies of the hydrodynamical processes, and give a rough estimate of the expected erosion based on the flow field.

6.3. Relevance for scour holes in the field

In this section the relevance of the model simulations for the understanding of scour holes in the field is discussed. First, the simplifications that are made in the model are described. After that the coupling between the calculated erosion process and the actual process in the field is discussed.

6.3.1. Simplifications

In the first place, some simplifications of the scour holes in the field are made for the numerical model. These simplifications are used in order to be able to study the processes that are present inside a scour hole and to be able to validate the model results with the measurements from laboratory experiments, without too many factors influencing this.

Upstream flow conditions

The first simplification is the uniformity of the upstream flow conditions. In the numerical model, the upstream velocity profile is a uniform equilibrium profile. In the field, many factors can be present that disturb the upstream flow conditions in a river, like structures, bed level features, geometrical features (e.g. river bends, confluences) or vegetation. Different upstream flow conditions have an influence on the hydrodynamical processes that take place in a scour hole. For example, helical motion due to a river bend results in higher lateral velocities near the bed. As a result, the recirculation zone will be asymmetrical and the deepest

point of the scour hole is expected to be located outside the central axis, as schematized in Figure 6.2. However, it is expected that the horseshoe vortex will still be present in these conditions, as the assumed driving mechanisms (a combination of the recirculation zone, flow contraction and upstream edge) are still present. These hypotheses could be verified by running a model simulation where the upstream flow conditions are disturbed by for example an object or a bend.

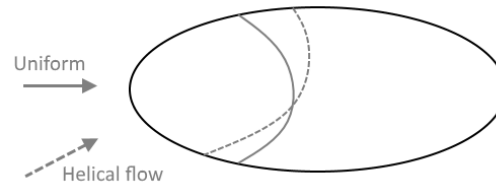


Figure 6.2: Schematic representation of the effect of helical flow on the recirculation zone inside the scour hole. The grey lines in the hole indicate the edge of the recirculation zone for uniform flow conditions (solid line) and flow conditions behind a river bend (helical flow, dashed line).

Influence of the tide

The river branches in the Rhine-Meuse Delta are influenced by the tide. Variations in flow velocity are present over time. The recirculation zone, which is assumed to play a role in the presence of the constant upstream slope angle, changes direction during every tidal cycle. It is expected that the hydrodynamical processes will adapt quickly to the changes in hydrodynamics. The bed level topography will take much longer to adapt, as this is a slower process. Van Zuylem (2015) found in his experiments that the bed topography will reshape to a mirrored version of the geometry that was present before the flow reversal.

Roughness of the bed

In the model simulations, the upstream and downstream bed are modelled as intermediately rough. In river branches in the Rhine-Meuse Delta the roughness of the bed can be influenced by many factors. Influences of vegetation, ripples, dunes and human interferences like bed protections can change the roughness of the bed. A different roughness can change the amount of turbulence in the flow and the gradient near the bed in the flow velocity profile.

Geometry of the hole

Another simplification in the model is the geometry of the scour hole. In the laboratory experiments by Koopmans (2017), the edge of the scour hole is modelled as an oval shape. This oval shape is used to represent a discontinuity in the subsoil, exposing an underlying sand layer to the flow. In the field this is the process that initiates the scour hole formation, but the shape will never be a perfect oval. However, to investigate the processes that are taking place, the choice for this shape is justified. The following question rises: *to what extent are the observed flow patterns present in a scour hole without the idealized shape?*

The flow recirculation is observed in many situations with a sudden transition in bed slope, so this is expected to happen in a non-idealized scour hole as well, as long as the transition is steep enough ($\beta > 20^\circ$). Flow contraction will also be present in such a hole, as the shape of the hole only influences this to a small extent. Continuity will always need the flow lines to contract just upstream of a scour hole. The horseshoe vortex, on the other hand, is expected to be less distinct in a non-idealized scour hole. This flow structure forms at the upstream edge of the scour hole and can be influenced by small perturbations in the geometry of the hole. The oval shaped hole has a smoothly curved edge, which gives rise to the formation of the horseshoe vortex. If this edge is straight or curved with many perturbations, the existence of the horseshoe vortex is not assured. Other vortices might be induced in a hole with a non-idealized geometry.

From the discussion on the simplifications described above, can be concluded that the hydrodynamics in the scour holes with a non-idealized geometry are much more complex and dependent on the circumstances than in the scour hole that is simulated with the model. However, the choice for the oval shaped hole is based on the investigation of the general processes that play a role in the development of the scour hole. These processes are present in the model results and are simulated according to the experimental results and observations. The idealized hole gives confidence that it may be possible to simulate a scour hole geometry

from the field on small scale with the model and identify the hydrodynamic processes in the scour holes. This model should be created to check the influence of the different scour hole geometry on the processes.

Prototype scale

The scour hole that is included in the model simulations has the dimensions of the scour hole in the research by [Stenfert \(2017\)](#). The dimensions of the laboratory flume are roughly an order 10^2 smaller than the dimensions of a prototype scale river. The Froude number is not scaled with this factor, as the flow velocity is only a factor three higher in a prototype situation. In the experiments no Froude similarity was used because the mobility parameter would become too low. If the flow velocity were to be decreased by a factor ten (for Froude similarity), no sediment transport would be present. The Froude number in the simulation is a factor three higher than in the field. The Reynolds number in the field is an order 10^2 larger. The influence of this scale effect is hard to be quantified, as all parameters of importance should be investigated first.

A difference between the laboratory scale and the prototype scale is the velocity profile. In a fully developed velocity profile in a laboratory flume, the boundary layer is spread over a large part of the water depth. In a prototype situation, the velocity profile has a shape that has a larger gradient close to the bed, when compared to the laboratory scale situation, which can be seen in [Figure 6.3](#). When looking at the area close to the bed, the profiles have a different value for the shear velocity. The shear velocity in the prototype scale profile is equal to $u_* = 0.040$ m/s, whereas the model simulations have a u_* -value of 0.0167 m/s. The scouring in the laboratory scale situation will be less severe due to this effect.

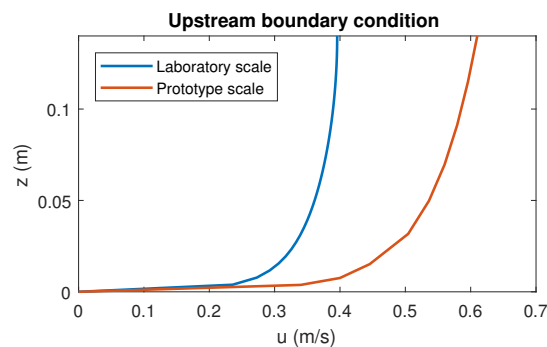


[Figure 6.3](#): Schematization showing the difference in velocity profile between the laboratory scale and the prototype scale.

The hydrodynamical processes observed in the model simulations have not been measured prototype situations yet. Though, from the research by [Koopmans \(2017\)](#) follows that approximately one-third of the scour holes in the Oude Maas and Dordtsche Kil have an upstream slope of more than 20° . These scour holes are expected to have a recirculation of flow, as this value was found to be the lower boundary in the parameter study. About two-third of the scour holes in this region have an upstream slope of more than 7° . This is the value where flow separation starts to occur, as discussed by [Chandavari and Palekar \(2014\)](#). However, some space was needed for the flow separation to happen in this study. This space was not available in the laboratory scale model simulations, but might be available in prototype scale scour holes. Therefore, scour holes in prototype scale might have a recirculation zone with less steep slopes.

Flow contraction will not be greatly influenced by changing the scale of the simulation. As followed from the parameter study, the strength of the flow contraction is a result of ratio between the 'active' size of the hole and the water depth. This ratio does not change significantly when moving from a laboratory scale to a prototype scale.

If both the flow contraction and the recirculation zone are present, it is hypothesized that the only thing that is needed to form a horseshoe vortex is a smoothly curved upstream edge. The presence of this edge depends on the chosen geometry, and does not depend on the scaling to a prototype situation. Therefore, the horseshoe vortex is assumed to be present in a prototype scale simulation, as long as the edge of the hole is smoothly curved.

In order to check the influence of the prototype scale, some model simulations on prototype scale are performed. The dimensions of the scour hole are multiplied with a factor 100 and the average flow velocity is 0.92 m/s, which is approximately 2.5 times the value from the laboratory scale simulations. The two upstream velocity profiles can be seen in Figure 6.3. The results of the simulations are presented in Appendix J. The results show no recirculation zone for the base case simulation, whereas the horseshoe vortex is clearly present. A simulation with a deeper scour hole ($1.25 \cdot h_s$) still does not include a recirculation zone, whereas for a scour hole with a depth of $1.5 \cdot h_s$, a recirculation zone is present. The horseshoe vortex is present in all simulations and is much more clear than the one in the laboratory scale simulation. The relative size of the horseshoe vortex is smaller, when compared to the present laboratory scale simulations.

The contraction of flow is getting stronger for deeper scour holes, which is expected due to the absence of a recirculation zone. The absence of the recirculation zone can be the result of the difference in velocity profile. Besides that, it should be noted that no extensive mesh dependency study is performed for the simulations with the prototype scale scour hole. The mesh near the bed meets the requirements on cell size described in Section 3.3.1, but the aspect ratio of the cells is different. This might affect the model results. If hard conclusions are to be drawn from this analysis, more research should be performed.

6.3.2. Erosion process

The erosion patterns that are calculated from the model simulations are very limited. As only a part of the processes is included in the calculation, no hard conclusions can be drawn. However, the model simulations for the bed topography after 10 hours show results that correspond with the observations during the laboratory experiments. The bed in the downstream part of the hole is evolving, while no transport is present at the upstream slope. This gives rise to the conclusion that the calculation of the erosion and sedimentation patterns from the model results give a reliable rough estimation. It is expected that if a bed topography of a scour hole in the field were to be modelled, a rough estimation of the erosion and sedimentation patterns could be made. For a more detailed assessment of the erosion, the missing processes should be incorporated in the calculation.

The erosion in a non-idealized scour hole is expected to be different from the case of an idealized hole. Perturbations in the geometry will influence the recirculation zone and the level of turbulence inside the hole. This could result in more erosion at some places, and more sedimentation at others. The actual effect is greatly dependent on the details in the geometry and therefore hard to predict. Besides, the model uses uniform sediment, whereas in practice, many different sediment sizes are present, which have differences in erodibility. Although, the general erosion process is expected to be similar for different hole geometries. Flow separation and a recirculation zone are expected to be present near the upstream edge, together with a reattachment point inside the scour hole. The erosion around this point and a constant upstream slope during the development of the hole will be present too. The presence of the horseshoe is less certain, as the oval shape of the hole is expected to be an important factor in the formation of the vortex. In order to confirm this, a simulation with a bed level topography from a scour hole in the field on laboratory scale could be performed.

Generally, the scour holes in the field are expected to have the same erosion principle as the hole in the model results. However, the peak flow velocities in the field are much higher, so the critical bed shear stress will be reached more often. The hole is therefore expected to have more structural erosion and the erosion process will be less dependent on the turbulence and pressure fluctuations in the hole. The geometry of the hole could induce additional flow structures and reduce the strength of the flow structures that are observed.

The tidal influence in the river branches in the Rhine-Meuse Delta will influence the scour hole growth. The scour hole will expand in two directions, as the flow is coming from two sides. The upstream and downstream slope are expected to have a similar angle. In case of an asymmetrical tide, the scour hole development will be asymmetrical as well. It is unknown whether the influence of the higher peak velocities or the longest duration is dominant.

Chapter 7

Conclusions and recommendations

In this chapter the conclusions and recommendations of this research are described. Section 7.1 includes the conclusions, followed by the recommendations in Section 7.2.

7.1. Conclusions

The conclusions will be based on evaluating the research objective and answering the research questions.

7.1.1. Research objective

The research objective was formulated in Chapter 1 as follows:

Understanding of the formation and development of scour holes in heterogeneous subsoil by creating a three dimensional numerical model that is able to simulate the hydrodynamics in the scour hole.

The numerical model that is set up in OpenFOAM during this research is able to reproduce the most important flow processes in a scour hole in heterogeneous subsoil. The accuracy of the magnitude of the processes in the model results could not be verified, as the quality of the available flow measurements was not sufficient. However, the numerical model gave insight into the dependence of the flow processes on flow velocity, water depth and scour hole depth and into the influence of the processes on the morphodynamics in the scour hole.

7.1.2. Subquestions

1. *What are the important hydrodynamical processes that play a role in the development of a scour hole in heterogeneous subsoil?*
 - The following important flow structures related to the scour hole are found in previous experimental research and in the numerical model results: a flow separation and recirculation zone, a horseshoe vortex, contraction of flow and downstream vortices.
 - The horseshoe vortex, contraction of flow and downstream vortices are present because of the three-dimensionality of the scour hole.
2. *For each identified process: is it reproduced by the numerical model and how does it contribute to the morphodynamics inside the scour hole?*
 - All processes mentioned at Subquestion 1 are present in the model results. The horseshoe vortex is expected to be the result of a combination of the recirculation zone, the curved upstream edge of the hole and the attraction of flow lines into the hole. The recirculation zone gives the horseshoe vortex its rotating character. The curved upstream edge of the scour hole forces the vortex sideways, where it ends up at the side slopes. The attraction of flow lines into the hole adds momentum to the rotating motion and strengthens the vortex.
 - Due to the recirculation zone, no sediment transport occurs at the upstream slope of the hole. The impinging flow around the reattachment point is expected to have a large impact on the bed,

resulting in erosion. In the downstream half of the hole, erosion occurs due to the gradients in flow velocity, reaching beyond the critical value. Flow contraction strengthens the erosion due to the extra momentum that is brought into the hole. The edges in the downstream half of the hole are undermined due to the outwards directed flow near the bed, as a result of the horseshoe vortex.

3. *What is the effect of the water depth, flow velocity and the depth of the scour hole on the processes?*

- A higher upstream flow velocity results in a higher recirculation velocity, but the relative recirculation velocity stays approximately constant. The location of the reattachment point does not change significantly for changes in flow velocity and water depth. Deeper scour holes result in a stronger recirculation velocity, having an asymptote in the range of backward facing step studies. The flow separation for mild upstream slopes is found to be suppressed by three-dimensional effects. When the upstream slope gets larger, three-dimensional effects strengthen the flow recirculation.
- The magnitude of the flow contraction is not directly related to the depth of the scour hole. The flow contraction magnitude shows a peak in the mid-range of the examined depths of the scour hole, and is lower for both deeper and shallower holes. The contraction of flow is found to be a result of the 'active' area of the scour hole. This active area is equal to the total scour hole area minus the area of the recirculation zone. For deeper scour holes, the area of the recirculation zone grows significantly, making the active area of such a hole smaller when compared to shallower holes.
- A deeper hole results in stronger inflow in the horseshoe vortex and stronger inner vortices downstream. The opposite holds for the outflow and the outer vortices. This process is not directly related to the changes in flow contraction.

7.1.3. Main question

Which processes are the most important for the erosion in scour holes in heterogeneous subsoil and where is the erosion most severe?

- The important hydrodynamical processes are: a flow separation and recirculation zone, a horseshoe vortex, contraction of flow and downstream vortices.
- Calculations using the bed shear stress showed that no sediment transport is present at the upstream slope of the hole, because the bed shear stress is not reaching beyond the critical value. Therefore, the upstream slope angle will be constant, which is also observed in the experiments.
- The downstream slope of the hole shows values of the bed shear stress that exceed the critical value. The calculated sediment transport rate results in erosion and sedimentation on this slope. The experiment verifies this, as the downstream slope was still developing at this stage. However, no sedimentation occurs in the experiments by [Stenfert \(2017\)](#).
- Impinging of the flow on the bed in the area around the reattachment point results in erosion. This phenomenon is not included in the model results, but is important for the evolution of the scour holes.
- At the side edges of the hole in the downstream half, the outwards directed flow near the bed results in undermining. In the field, this undermining will result in failure of the poorly erodible top layer. Preliminary scale model tests show an expansion in downstream direction with an angle of 1:8. Numerical simulations show this 1:8 angle as a strip of zero bed shear stress.
- The model results are expected to be useful for the estimation of the development of scour holes in the field. The recirculation zone and the flow contraction are expected to be present in a field situation. The existence of the horseshoe vortex in the field is unknown. The expected driving mechanisms (the recirculation zone and flow contraction) are present, but in the case of an upstream edge with a less smoothly curved geometry, the presence of the horseshoe vortex is unknown.
- The model can function as a first rough estimation of the expected erosion in the scour hole. The processes that are not included in the model simulation should be taken into account in a qualitative manner. Besides that, the model can function as a first step in the direction of a model that simulates both hydrodynamics and morphology.

- The erosion process in the development of scour holes in the field is expected to be similar to the process in this research. More structural erosion could be present, as the flow velocities in the field are larger and reach beyond the critical value more often. The erosion in the field is influenced by many factors, for example by the composition of the subsoil. The influence of the tide is another factor that will have a large effect on the development of the scour hole, as the flow will come from two sides. Therefore, the hole will grow in two directions and the angle of the upstream and downstream slope is expected to be determined by the dominance of the asymmetrical tide.

7.2. Recommendations

- Perform additional flow velocity measurements in the laboratory experiments, as measurements with a vectrino profiler and oxygen bubbles lead to inaccurate measurements in the recirculation zone. Particle Image Velocimetry (PIV) or Laser Doppler Anemometry (LDA) are proposed measuring techniques. Another option is the usage of a vectrino profiler with neutrally buoyant seeding material.
- Perform detailed flow measurements in a scour hole in the field, in order to gain validation data for a model of a scour hole in the field in prototype scale. Many uncertainties are present in such a model, so without validation data, the results would not be reliable.
- Include sediment transport and morphology in the numerical model. A module for both the transport by bed shear stress and by stirred up sediment should be included. For the stirring up of sediment it is advised to use the turbulence intensity. With a model that includes sediment transport and morphology the influence of the different parameters on the erosion patterns in the hole can be checked in more detail. [Dixen et al. \(2013\)](#), for example, modelled the scour around a sphere using a RANS-model including a sediment transport module with turbulence effects and morphology.
- Undermining of the non-erodible top layer is an important phenomenon, which happened in the laboratory experiments, but is not included in the numerical model simulations. In the field, undermining is not observed, as either the top clay layer fails as a result of undermining, or the layer is too thick to allow for undermining. Therefore, addition of a method that represents the failure mechanism of the top layer, both in the numerical model and in the experiments, would add value to the research. By doing this, knowledge can be gained on the evolution of a scour hole and the essential scouring locations in the hole that should be protected can be found.
- Inclusion of the fluctuating parts of the flow velocity and bed shear stress can be achieved by modelling a Large Eddy Simulation (LES), which solves the large scale motions of the turbulence. By including these features in the determination of sediment transport and erosion, a better approximation of the development of a scour hole is obtained. However, one should keep in mind that a LES is computationally much more expensive than a RANS-model.
- Modelling of the scour hole from the laboratory experiment in prototype scale helps in the determination of the validity of the model results for scour holes in the field. Preliminary model simulations with prototype scale are performed in this study. However, many uncertainties are present in these simulations. An extensive study with a prototype scale model will give more reliable information on the scaling of the processes. The existence of the horseshoe vortex in the larger scale geometry can be studied and the magnitude of the recirculation zone and flow contraction can be verified. This model will give information on whether or not the simulation on laboratory scale is accurate enough and how to interpret the results from the laboratory case. If this is known, numerical studies on scouring in laboratory scale can be translated to prototype scale much easier. In this study, a first attempt to model the prototype is made, but some uncertainties should be studied in more detail to draw hard conclusions from it.
- A model of a scour hole as it appears in the field creates knowledge on the differences between the idealized scour hole and a real scour hole. When these differences are known, the processes that are present in an idealized case and that are relevant for the real scouring case can be identified. The geometry of a scour hole in the field can be downscaled to laboratory scale to perform this simulation.

Bibliography

- [1] Aguerrea, H. J., Damiána, S. M., Gimenez, J. M., and Nigroa, N. M. Modeling of compressible fluid problems with openfoam using dynamic mesh technology. *Mecánica Computacional*, 32:995–1011, 2013.
- [2] Ampadu-Mintah, A. and Tachie, M. Surface roughness effects on separated and reattached turbulent flow in open channel. *Journal of Hydraulic Research*, 53(3):302–316, 2015.
- [3] Andersson, B., Andersson, R., Håkansson, L., Mortensen, M., Sudiyo, R., and van Wachem, B. *Computational Fluid Dynamics for Engineers*. Cambridge University Press, Cambridge, 2012.
- [4] Baykal, C., Sumer, B. M., Fuhrman, D. R., Jacobsen, N. G., and Fredsøe, J. Numerical investigation of flow and scour around a vertical circular cylinder. *Philosophical Transactions Royal Society Publishing*, 373(2033), 2015.
- [5] Baykal, C., Sumer, B. M., Fuhrman, D. R., Jacobsen, N. G., and Fredsøe, J. Numerical simulation of scour and backfilling processes around a circular pile in waves. *Coastal Engineering*, 122:87–107, 2017.
- [6] Bradshaw, P. and Wong, F. Y. F. The reattachment and relaxation of a turbulent shear layer. *Journal of Fluid Mechanics*, 52(1):113–135, 1972.
- [7] Breusers, H. N. C. Conformity and time scale in two-dimensional local scour. Report, Hydraulic Research Laboratory, Poona, India, 1966.
- [8] Cebeci, T. and Chang, K. C. Calculation of incompressible rough-wall boundary-layer flows. *AIAA Journal*, 16:730–735, 1978.
- [9] Chandavari, V. and Palekar, S. Diffuser angle control to avoid flow separation. *International Journal of Technical Research and Applications*, 2(5):16–21, 2014.
- [10] Crosato, A. *River Morphodynamics. Morphological response at the reach scale*. Lecture notes LN381. UNESCO-IHE, Delft, the Netherlands, 2015.
- [11] Damgaard, J., Whitehouse, R., and Soulsby, R. Bed-load sediment transport on steep longitudinal slopes. *Journal of Hydraulic Engineering*, 123(12):1130–1138, 1997.
- [12] Dargahi, B. The turbulent flow field around a circular cylinder. *Experiments in Fluids*, 8:1–12, 1989.
- [13] De Graauw, A. and Pilarczyk, K. Model-prototype conformity of local scour in non-cohesive sediments beneath overflow-dam. *19th IAHR-congress, New Delhi, India*, 1981.
- [14] De Souza, L. F., de Mendonça, M. T., de Medeiros, M. A. F., and Kloker, M. Seeding of görtler vortices through a suction and blowing strip. *Journal of the Brazilian Society of Mechanical Sciences and Engineering*, 26(3), 2004.
- [15] Deltares. *Delft3D-FLOW User Manual*. Deltares, Delft, 2014.
- [16] Deltares. *D-FLOW Flexible Mesh User Manual, draft version*. Deltares, Delft, 2017.
- [17] Dietz, J. and Wittke, W. *Kolkbildung in feinen oder leichten Sohlmaterialien bei strömendem Abfluß*. PhD thesis, Universität Fridericiana Karlsruhe, 1969.
- [18] Diken, M., Sumer, B. M., and Fredsøe, J. Numerical and experimental investigation of flow and scour around a half-buried sphere. *Coastal Engineering*, 73:84–105, 2013.
- [19] Escarameia, M. and May, R. W. P. Scour around structures in tidal flows. Report, HR Wallingford, 1999.
- [20] Fuhrman, D. R., Diken, M., and Jacobsen, N. G. Physically-consistent wall boundary conditions for the $k-\omega$ turbulence model. *Journal of Hydraulic Research*, 48(6):793–800, 2010.

- [21] Fuhrman, D. R., Baykal, C., Sumer, B. M., Jacobsen, N. G., and Fredsøe, J. Numerical simulation of wave-induced scour and backfilling processes beneath submarine pipelines. *Coastal Engineering*, 94:10–22, 2014.
- [22] Hoffmans, G. J. C. M. *Two dimensional mathematical modelling of local-scour holes*. Doctor thesis, University of Technology Delft, 1992.
- [23] Hoffmans, G. J. C. M. A hydraulic and morphological criterion for upstream slopes in local-scour holes. Report, Ministry of Transport, Public Works and Watermanagement, 1993.
- [24] Hoffmans, G. J. C. M. and Booij, R. Two-dimensional mathematical modelling of local-scour holes. *Journal of Hydraulic Research*, 31(5):615–634, 1993a.
- [25] Hoffmans, G. J. C. M. and Booij, R. The influence of upstream turbulence on local-scour holes. *25th IAHR-congress, Tokyo, Japan*, 1993b.
- [26] Hoffmans, G. J. C. M. and Pilarczyk, K. W. Local scour downstream of hydraulic structures. *Journal of Hydraulic Engineering*, 121(4):326–340, 1995.
- [27] Hoffmans, G. J. C. M. and Verheij, H. J. *Scour Manual*. A.A. Balkema, Rotterdam, 1997.
- [28] Holmén, V. *Methods for Vortex Identification*. MSc thesis, 2012.
- [29] Huismans, Y., van Velzen, G., Mahoney, T. S. D. O., Hoffmans, G. J. C. M., and Wiersma, A. P. *Scour hole development in river beds with mixed sand-clay-peat stratigraphy*. Deltares, 2016.
- [30] Jacobsen, N. G., van Velzen, G., and Fredsøe, J. Analysis of pile scour and associated hydrodynamic forces using proper orthogonal decomposition. *Proceedings 7th International Conference on Scour and Erosion, Perth, Australia*, 2014.
- [31] Jansen, P. P., van Bendegom, L., van den Berg, J., de Vries, M., and Zanen, A. *Principles of River Engineering. The non-tidal alluvial river*. Delftse Uitgevers Maatschappij, Delft, 1994.
- [32] Jorissen, R. and Vrijling, J. Local scour downstream of hydraulic constructions. *Proceedings 23rd IAHR-congress, Ottawa, Canada: B433-B440*, 1989.
- [33] Khosronejad, A., Kang, S., and Sotiropoulos, F. Experimental and computational investigation of local scour around bridge piers. *Advances in Water Resources*, 2012:73–85, 2012.
- [34] Kim, H. S., Nabi, M., Kimura, I., and Shimizu, Y. Numerical investigation of local scour at two adjacent cylinders. *Advances in Water Resources*, 70:131–147, 2014.
- [35] Kim, H. S., Nabi, M., Kimura, I., and Shimizu, Y. Computational modeling of flow and morphodynamics through rigid-emergent vegetation. *Advances in Water Resources*, 84:64 – 86, 2015.
- [36] Koopmans, H. *Scour holes in tidal rivers with heterogeneous subsoil under anthropogenic influence*. Master thesis, Delft University of Technology, 2017.
- [37] Liu, X. and García, M. H. Three-dimensional numerical model with free water surface and mesh deformation for local sediment scour. *Journal of Waterway, Port, Coastal and Ocean Engineering*, 134(4): 203–217, 2008.
- [38] McGovern, D. J., Ilic, S., Folkard, A. M., McLelland, S. J., and Murphy, B. J. Time development of scour around a cylinder in simulated tidal currents. *Journal of Hydraulic Engineering*, 140(6), 2014.
- [39] Menter, F. and Esch, T. Elements of industrial heat transfer predictions. *16th Brazilian Congress of Mechanical Engineering (COBEM), Uberlandia, Brazil*, pages 26–30, 2001.
- [40] Meselhe, E. A. and Sotiropoulos, F. Three-dimensional numerical model for open channel with free surface variations. *Journal of Hydraulic Research*, 38(2):115–121, 2000.
- [41] Meyer-Peter, E. and Müller, R. Formulas for bed-load transport. *Rep. 2nd Meet. Int. Assoc. Hydraul. Struct. Res.*, pages 39 – 64, 1948.

- [42] Mirskhoulava, T. Y. *Basic physics and mechanics of channel erosion*. Gidrometeoizdat, Leningrad, 1988.
- [43] Mirskhoulava, T. Y. Scouring by flowing water of cohesive and noncohesive beds. *Journal of Hydraulic Research*, 29(3), 1991.
- [44] Mosonyi, E. and Schoppmann, B. *Ein Beitrag zur Erforschung von örtlichen Auskolkungen hinter geneigten Befestigungsstrecken in Abhängigkeit der Zeit*. Universität Fridericiana Karlsruhe, 1968.
- [45] Muzzammil, M. and Gangadhariah, T. The mean characteristics of horseshoe vortex at a cylindrical pier. *Journal of Hydraulic Research*, 41(3):285–297, 2003.
- [46] Nabi, M., de Vriend, H. J., Mosselman, E., Sloff, C. J., and Shimizu, Y. Detailed simulation of morphodynamics: 1. hydrodynamic model. *Water Resources Research*, 48, 2012.
- [47] Nakagawa, H. and Nezu, I. Experimental investigation on turbulent structure of backward-facing step flow in an open channel. *Journal of Hydraulic Research*, 25(1):67–88, 1987.
- [48] Nichols, R. H. and Nelson, C. C. Wall function boundary conditions including heat transfer and compressibility. *AIAA Journal*, 42(6):1107–1114, 2004.
- [49] Nieuwstadt, F. T. M., Boersma, B. J., and Westerweel, J. *Turbulence - Introduction to Theory and Applications of Turbulent Flows*. Springer, Delft, 2016.
- [50] OpenFOAM Foundation Ltd. *OpenFOAM User Guide version 4.0*. OpenFOAM Foundation Ltd., 2016.
- [51] Petersen, T. U., Sumer, B. M., Fredsøe, J., Raaijmakers, T. C., and Schouten, J. J. Edge scour at scour protections around piles in the marine environment — laboratory and field investigation. *Coastal Engineering*, 106:42–72, 2015.
- [52] Pietrzak, J. *An Introduction to Oceanography for Civil and Offshore Engineers - Lecture Notes CIE5317*. TU Delft, 2015.
- [53] Pilarczyk, K. *Dikes and Revetments*. A.A. Balkema, 1998.
- [54] Roulund, A., Sumer, B. M., Fredsøe, J., and Michelsen, J. Numerical and experimental investigation of flow and scour around a circular pile. *Journal of Fluid Mechanics*, 534:351–401, 2005.
- [55] Schiereck, G. J. *Introduction to Bed, bank and shore protection, update by Verhagen, H.J.* VSSD, Delft, 2012.
- [56] Sloff, C. J., van Spijk, A., Stouthamer, E., and Sieben, A. Understanding and managing the morphology of branches incising into sand-clay deposits in the dutch rhine delta. *International Journal of Sediment Research*, 28(2):127–138, 2013.
- [57] Stenfert, J. *Scour holes in heterogeneous subsoil*. Master thesis, Delft University of Technology, 2017.
- [58] Sumer, B. M. Mathematical modelling of scour: A review. *Journal of Hydraulic Research*, 45(6):723 – 735, 2007.
- [59] Sumer, B. M., Chua, L. H. C., Cheng, N.-S., and Fredsøe, J. Influence of turbulence on bed load sediment transport. *Journal of Hydraulic Engineering*, 129(8):585 – 596, 2003.
- [60] Tani, I., Iuchi, M., and Komoda, H. Experimental investigation of flow separation associated with a step or a groove. Report, University of Tokyo, 1961.
- [61] Uijtewaal, W. S. J. *Lecture Notes Turbulence in Hydraulics, CT5312*. TU Delft, 2011.
- [62] Uijtewaal, W. S. J., Huismans, Y., and Koopmans, H. A scaled experimental pilot-study on deep scour holes in river beds of heterogeneous composition. Report, 2016.
- [63] Van der Meulen, T. and Vinjé, J. Three-dimensional local scour in non-cohesive sediments. *16th IAHR-congress*, 1975.

- [64] Van Driest, E. R. On turbulent flow near a wall. *Journal of the Aeronautical Sciences*, 23(11):1007 – 1011, 1956.
- [65] Van Zuylen, J. *Development of scour in non-cohesive sediment under a poorly erodible top layer*. Master thesis, Delft University of Technology, 2015.
- [66] Van Zuylen, J. and Sloff, C. Development of scour in non-cohesive sediments under a poorly erodible top layer. *RCEM 2015: 9th Symposium on River, Coastal and Estuarine Morphodynamics, Iquitos, Peru*, 2015.
- [67] Wilcox, D. C. Reassessment of the scale-determining equation for advanced turbulence models. *AIAA Journal*, 26(11):1299 – 1310, 1988.
- [68] Wilcox, D. C. *Turbulence modeling for CFD*. DCW Industries, Inc., La Canada, California, 2006.
- [69] Zanke, U. *Zusammenhänge zwischen Strömung und Sedimenttransport, Teil 2: Berechnung des Sedimenttransportes hinter befestigten Sohlenstrecken-Sonderfall zweidimensionaler Kolk*. PhD thesis, 1978.

Appendix A

Additional literature

A.1. Flow

In this section, some basic aspects of turbulent open channel flow are explained. First, the types of flow are described and the principles of turbulence and the turbulent boundary layer are explained. Finally vortices and coherent structures are described. Appendix A.1 gives additional information on flows, including the basic equations that describe a flow and aspects of modelling of flows, like turbulence closure models and near wall modelling.

First, two dimensionless numbers that play a role in the behaviour of fluids are given. The ratio between the inertia and gravitational forces of a fluid is called the Froude number, see Equation (A.1). The Froude number determines whether the flow is sub-critical ($Fr < 1$), super-critical ($Fr > 1$) or critical ($Fr = 1$).

$$Fr = \frac{U}{\sqrt{gL}} \quad (\text{A.1})$$

Where: Fr [-] Froude number
 U [m/s] Velocity scale
 L [m] Length scale

The ratio between the inertia and viscous forces is called the Reynolds number, see Equation (A.2). From the Reynolds number can be determined whether a flow is laminar or turbulent. Laminar flows have Reynolds numbers smaller than 1000 (Uijttewaai, 2011). When the Reynolds number is much larger, the flow is turbulent.

$$Re = \frac{UL}{\nu} \quad (\text{A.2})$$

Where: Re [-] Reynolds number

A.1.1. Types of flow

Uniform flow

Uniform flow is the an elementary type of flow. In uniform flow conditions, an equilibrium between the bed shear stress and the pressure component in the direction of the slope is present. The average flow velocity of the water is constant in a uniform flow and the boundary layer is fully developed. Figure A.1 shows the forces in a uniform flow, together with the velocity, horizontal velocity fluctuations and a measure of the turbulence in a uniform flow. Equation (A.3) describes the equilibrium that is present in uniform flow conditions. From this follows Equation (A.4).

$$\tau_b = \rho_w \nu \left. \frac{\partial u}{\partial z} \right|_{z=0} = \rho_w u_*^2 = \rho_w g h i_b \quad (\text{A.3})$$

$$u_*^2 = g h i_b \quad (\text{A.4})$$

Where:	τ_b	[N/m ²]	Bed shear stress
	z	[m]	Coordinate in vertical direction
	u_*	[m/s]	Bed shear velocity
	i_b	[-]	Bed slope

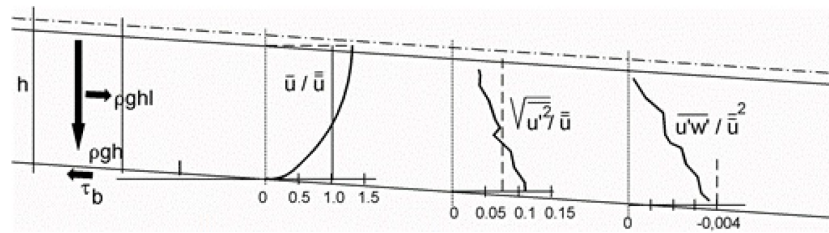


Figure A.1: Uniform flow in a sloping channel (Schiereck, 2012).

The boundary layer is the part of the water column that is influenced by the presence of the wall. In a uniform flow this layer reaches up to the water surface. This leads to a logarithmic velocity profile, which is described in Section A.1.6. When water starts to flow along a wall, the boundary layer will slowly develop. After a distance of 30 to 50 times the water depth, the flow will reach uniform conditions (Schiereck, 2012).

Non-uniform flow

In reality, flows are hardly ever uniform. The boundary layer is influenced by accelerations and decelerations of the flow. When the flow accelerates, the boundary layer shrinks. If a deceleration is present the opposite happens.

$$\frac{d\delta}{dx} = \frac{-(4 \text{ to } 5)\delta}{u_0} \frac{du_0}{dx} \quad (\text{A.5})$$

Where:	δ	[m]	Thickness of the boundary layer
	u_0	[m/s]	Upstream flow velocity in streamwise direction

When the flow accelerates ($\frac{du_0}{dx} > 0$), the boundary layer shrinks. If a deceleration is present ($\frac{du_0}{dx} < 0$) the opposite happens. Figure A.2 shows the influence of a velocity gradient on the velocity profile in the channel (Schiereck, 2012).

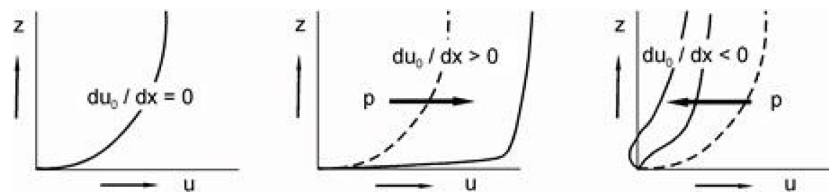


Figure A.2: Influence of the pressure gradient on the velocity profile (Schiereck, 2012).

A.1.2. Turbulence

A turbulent flow is characterized by random fluctuations in flow velocity and pressure. Turbulent flows typically have large Reynolds numbers. An important characteristic of turbulence is the diffusivity. Turbulent flows allow much faster mixing rates of momentum and energy than the molecular diffusion would allow by itself. Because of the three-dimensional character of the turbulence, the quantities are transported in all directions. Fluid elements can be transported in a direction perpendicular to the mean flow velocity, even though the mean flow velocity component in that direction is zero (Andersson et al., 2012).

Kinetic energy from the mean flow is extracted by the largest turbulent eddies. The energy is not lost in this transfer. All turbulent flows show a flux of energy from the large- to the small scales. This is called the energy cascade. Inviscid processes transfer the kinetic energy to smaller and smaller scales. At some point, the Kolmogorov scales (see Equation (A.7)) are reached and the energy is dissipated into heat by the molecular viscosity.

From a single point velocity measurement, information about the turbulence in the flow can be deduced. Passage of small eddies can be seen as velocity fluctuations with small amplitudes and high frequencies. Large eddies are observed by large amplitudes and low frequencies. The frequency of the fluctuations ranges from 1 Hz to 10000 Hz in air and water flows (Andersson et al., 2012). The velocity signal can be divided in a mean and fluctuating part. The fluctuating part represents the turbulent motion. The intensities of the velocity fluctuations are usually measured in terms of turbulent kinetic energy per unit mass, see Equation (A.6).

$$k = \frac{1}{2} (\overline{u'^2} + \overline{v'^2} + \overline{w'^2}) \quad (\text{A.6})$$

Where: u' [m/s] Velocity fluctuations in streamwise direction
 v' [m/s] Velocity fluctuations in lateral direction
 w' [m/s] Velocity fluctuations in vertical direction

Scales of turbulence

Eddies in a turbulent flow have a wide range of length scales, time scales and velocity scales. The larger scales are determined by the geometry of the domain. The smallest scales are the Kolmogorov scales, see Equation (A.7) (Uijttewaai, 2011).

$$\eta = \left(\frac{\nu^3}{\epsilon} \right)^{1/4} \quad \tau_\eta = \left(\frac{\nu}{\epsilon} \right)^{1/2} \quad v_\eta = (\nu\epsilon)^{1/4} \quad (\text{A.7})$$

Where: η [m] Kolmogorov length scale
 τ_η [s] Kolmogorov time scale
 v_η [m/s] Kolmogorov velocity scale

The Kolmogorov scales are decreasing for an increasing Reynolds number, and therefore the range of scales increases with the Reynolds number.

A.1.3. Vortices and coherent structures

No strict definition is available for both vortices and coherent structures. Generally, vortices can be referred to as “existence of some form of common particle rotation” (Holmén, 2012). A coherent structure can be “any form of pattern arising in the flow that has an effect on transport” (Holmén, 2012). The difficulty in identifying vortices is the radius of the motion. Identifying how far a vortex stretches from the center of rotation is hard, especially when several structures are interacting with each other. Coherent structures are identified as sections of the fluid that stay roughly together while moving in the fluid. These sections can be areas with less mixing than one would expect from the velocity field.

Vorticity

Vorticity is defined as the tendency of a fluid to rotate. It is calculated with the curl of the velocity, see Equation (A.8) (Pietrzak, 2015).

$$\omega = \nabla \times u \quad (\text{A.8})$$

Where: ∇ [m^{-1}] Nabla operator (vector of partial derivatives)

The three components of the vorticity vector are expressed in Equation (A.9).

$$\omega_x = \left(\frac{\partial w}{\partial y} - \frac{\partial v}{\partial z} \right) \quad \omega_y = \left(\frac{\partial u}{\partial z} - \frac{\partial w}{\partial x} \right) \quad \omega_z = \left(\frac{\partial v}{\partial x} - \frac{\partial u}{\partial y} \right) \quad (\text{A.9})$$

Where: ω_x [s^{-1}] Vorticity in streamwise direction
 ω_y [s^{-1}] Vorticity in lateral direction
 ω_z [s^{-1}] Vorticity in vertical direction
 y [m] Coordinate in lateral direction
 v [m/s] Flow velocity in lateral direction
 w [m/s] Flow velocity in vertical direction

The vorticity can be used a method to identify vortices in a flow. However, vorticity does not distinguish between swirling flows and shearing motions, making it less useful for this application (Holmén, 2012).

A.1.4. Basic equations

The equations that describe a flow are based on the conservation of mass and energy and Newton's second law (force is equal to mass times acceleration). The combination of these three properties, combined with some assumptions, results in the Navier-Stokes equations. The derivation of the Navier-Stokes equations is described in detail by Pietrzak (2015) and many other textbooks. Therefore, only a short summary of the equations and the assumptions is given here.

The derivation of the Navier-Stokes equations is based on the volume of a fluid element. The equations describe the motion of the element. Because of the fact that the flow velocities in a flow are much smaller than the speed of sound, a flow can be called incompressible (Nieuwstadt et al., 2016). This is an important assumption in the derivation of the Navier-Stokes equations.

Mass conservation

The first quantity that is conserved is mass. The combination of mass conservation and the incompressible flow assumption leads to the continuity equation for incompressible flow, see Equation (A.10).

$$\frac{\partial u}{\partial x} + \frac{\partial v}{\partial y} + \frac{\partial w}{\partial z} = \nabla_i(u_i) = 0 \quad (\text{A.10})$$

Where: ∇_i [m⁻¹] Nabla operator in i direction (vector of partial derivatives)

Momentum conservation

The conservation of momentum is derived using Newton's second law. According to Pietrzak (2015), the forces that act on a fluid element are: pressure forces, viscous forces and the gravity force. Using the second law of Newton, the Navier-Stokes equations for incompressible flow are derived, see Equations (A.11), (A.12) and (A.13).

$$\rho \left(\frac{\partial u}{\partial t} + \nabla_i(u_i u) \right) = -\nabla_x(p) + \rho \nu \nabla_i^2(u) \quad (\text{A.11})$$

$$\rho \left(\frac{\partial v}{\partial t} + \nabla_i(u_i v) \right) = -\nabla_y(p) + \rho \nu \nabla_i^2(v) \quad (\text{A.12})$$

$$\rho \left(\underbrace{\frac{\partial w}{\partial t}}_{\text{local acceleration}} + \underbrace{\nabla_i(u_i w)}_{\text{convective}} \right) = \underbrace{-\nabla_z(p) + \rho \nu \nabla_i^2(w)}_{\text{diffusive}} - \underbrace{\rho g}_{\text{source}} \quad (\text{A.13})$$

Where: p [Pa] Pressure

Equation (A.13) shows the different terms in all the equations. The left hand side contains the local acceleration and convection (or: advection) terms. The diffusive terms on the right hand side contain the pressure and the viscous shear stresses, which act on the fluid element (Uijtewaal, 2011). The only source that is present is gravity. The Coriolis effect is neglected in the equations above. This is valid, because the length scales that are used in this research are much smaller than the length scales that are influenced by the Coriolis effect (Pietrzak, 2015).

In theory, the Navier-Stokes equations together with the continuity equation describe the complete flow. In practice, even with proper boundary conditions, it is hard to find analytical solutions for the equations, due to the non-linear terms. Poiseuille and Couette flows, in which viscosity plays a dominant role, can be solved, but as soon as the other terms are of importance as well, the solutions are much harder to be found. This is the case in flows at moderate and high Reynolds numbers (Uijtewaal, 2011).

In order to mitigate this problem the equations can be solved using a numerical method in which all time and length scales have to be taken into account. The smallest length scales are in the order of 10^{-4} m, which are the Kolmogorov length scales, see Section A.1.2. Solving for these length scales is not a practical way to obtain a solution, as brutal computational force is required. The number of grid points is proportional to the Reynolds number to the power 9/4, which results in several million grid points for $Re = 1000$. Computations with this amount of grid points will not be feasible in the next decades (Uijttewaal, 2011).

A second option is the simplification of the Navier-Stokes equations. This is less accurate because the smallest scales are unresolved, but in many cases solving these scales is not necessary. The required computational power is reduced as a result of the simplification, resulting in shorter simulation times. Simplification of the equations is done by Reynolds averaging and is described in the next section.

Reynolds averaging

For the averaging of the Navier-Stokes equations, Reynolds decomposition is used. The flow is decomposed into a mean and a fluctuating component. For the velocity in streamwise direction this decomposition is: $u_1 = \bar{u}_1 + u'_1$. Decomposed descriptions for the velocity in all directions and the pressure are substituted in the Navier-Stokes equations. The averaging of these equations gives the Reynolds Averaged Navier-Stokes equations (RANS), which can be seen in Equations (A.14), (A.15) and (A.16).

$$\rho \left(\frac{\partial \bar{u}}{\partial t} + \nabla_i (\bar{u}_i \bar{u}) + \nabla_i (\overline{u'_i u'}) \right) = -\nabla_x(\bar{p}) + \rho \nu \nabla_i^2(\bar{u}) \quad (\text{A.14})$$

$$\rho \left(\frac{\partial \bar{v}}{\partial t} + \nabla_i (\bar{u}_i \bar{v}) + \nabla_i (\overline{u'_i v'}) \right) = -\nabla_y(\bar{p}) + \rho \nu \nabla_i^2(\bar{v}) \quad (\text{A.15})$$

$$\rho \left(\underbrace{\frac{\partial \bar{w}}{\partial t}}_{\text{local acceleration}} + \underbrace{\nabla_i (\bar{u}_i \bar{w})}_{\text{convective}} + \underbrace{\nabla_i (\overline{u'_i w'})}_{\text{Reynolds stresses}} \right) = \underbrace{-\nabla_z(\bar{p}) + \rho \nu \nabla_i^2(\bar{w})}_{\text{diffusive}} - \underbrace{\rho g}_{\text{source}} \quad (\text{A.16})$$

The additional term that can be distinguished represents the Reynolds stresses. This term originates from the non-linear convective term. These stresses include the effects of the velocity fluctuations. Because the Reynolds averaging adds extra unknowns to the set of equations, additional equations are needed to obtain analytical solutions. In literature, this is referred to as the turbulence closure problem (Uijttewaal, 2011).

A.1.5. Turbulence closure

To overcome the turbulence closure problem, a turbulence model is used. Turbulence models range from very simple to very complex. Generally, all models represent the Reynolds stresses either in the form of an eddy viscosity or as a transport equation for the Reynolds stresses (Uijttewaal, 2011). The most common models are shown in Table A.1, accompanied by their advantages and disadvantages. For a detailed description of the models, see Andersson et al. (2012).

Table A.1: Different turbulence models with their advantages and disadvantages, based on [Andersson et al. \(2012\)](#).

Turbulence model	Advantages	Disadvantages
Direct Numerical Simulation (DNS)	<ul style="list-style-type: none"> No turbulence model Useful for low Re-numbers 	<ul style="list-style-type: none"> Extreme computational costs Huge amount of data
Large Eddy Simulation (LES)	<ul style="list-style-type: none"> Applicable for complex flows Information on structures in turbulent flows 	<ul style="list-style-type: none"> High computational costs Large amount of data Difficult to identify time convergence Requires additional treatment at no-slip walls
Reynolds stress models (RSMs)	<ul style="list-style-type: none"> Applicable for complex flows: swirl, flow separation, plane jets Accounts for anisotropy 	<ul style="list-style-type: none"> Computationally expensive (11 equations) Sometimes poor performance due to closures
Two equation models	<ul style="list-style-type: none"> Velocity and length scales are predicted with transport equations Good results for engineering applications Robust, economical and easy to apply 	<ul style="list-style-type: none"> Limited to an eddy viscosity assumption Isotropic turbulent viscosity Convection and diffusion of shear stresses are neglected
<ul style="list-style-type: none"> Standard k-ϵ model 	<ul style="list-style-type: none"> Most widely used and validated 	<ul style="list-style-type: none"> Not applicable for: round jets, flows with significant curvature, swirl, sudden acceleration, flow separation, low Re-regions
<ul style="list-style-type: none"> RNG k-ϵ model 	<ul style="list-style-type: none"> Improved simulations for swirling flows and flow separations 	<ul style="list-style-type: none"> Less stable than standard k-ϵ model No round jets
<ul style="list-style-type: none"> Realizable k-ϵ model 	<ul style="list-style-type: none"> Improved simulations for swirling flows, flow separations and round jets 	<ul style="list-style-type: none"> Less stable than standard k-ϵ model
<ul style="list-style-type: none"> k-ω model 	<ul style="list-style-type: none"> Works well at low Re-numbers No wall functions needed Works well with adverse pressure gradients and separating flows 	<ul style="list-style-type: none"> Needs a fine grid close to the wall (if no wall function is used)
<ul style="list-style-type: none"> k-ω SST model 	<ul style="list-style-type: none"> Combination of k-ϵ with k-ω in wall-bounded region. Often recommended to replace the k-ϵ model 	<ul style="list-style-type: none"> Needs a fine grid close to the wall Overpredicts turbulence in stagnation regions and strong accelerating regions
One equation models	<ul style="list-style-type: none"> Cost effective solution for some situations 	<ul style="list-style-type: none"> Algebraic equation for the length scale is too restrictive Transport of the length scale is not included
Zero equation models	<ul style="list-style-type: none"> Cost effective solution for some situations 	<ul style="list-style-type: none"> No lateral gradient in streamwise velocity means no turbulence Lack of transport of turbulent scales Cannot be used as general turbulence model

A.1.6. Near wall modelling

In flow near a solid boundary, such as a wall, viscous effects are the dominant factor in transport processes ([Andersson et al., 2012](#)). Steep gradients of flow variables in the near-wall region require a very fine computational mesh. Some of the turbulence models (for example the k- ϵ model) are not applicable in the near-wall region. The problems with the near-wall modelling can be overcome in two ways. First, the turbulence models can be modified in order to be able to resolve the viscosity-affected region. The second option involves wall functions. Boundary conditions for the mean flow velocity components and turbulence quantities at the

first grid point are calculated with the wall function. The detailed near-wall processes are not resolved when using wall functions. Wall functions are described later in this chapter.

Turbulent boundary layer

In the near-wall region the no-slip condition holds. This condition states that the relative velocity between the wall and the flow is zero. Due to the presence of the wall, the flow in the surrounding area is slowed down. The affected flow area is called the 'boundary layer'. The velocity increases from zero at the wall to the free flow velocity at the upper edge of the layer. In a flow with a large Reynolds number, the boundary layer is turbulent. This means that the transfer of different quantities is higher, compared to smaller Re-number flows, and the wall shear stress is larger (Andersson et al., 2012).

A turbulent boundary layer, with thickness δ , can be divided into several regions. Figure A.3a shows the division in the inner- and outer region. The inner region approximately reaches up to one fifth of the layer ($0 < y < 0.2\delta$) and the outer region covers the other part of the boundary layer ($0.2\delta < y < \delta$).

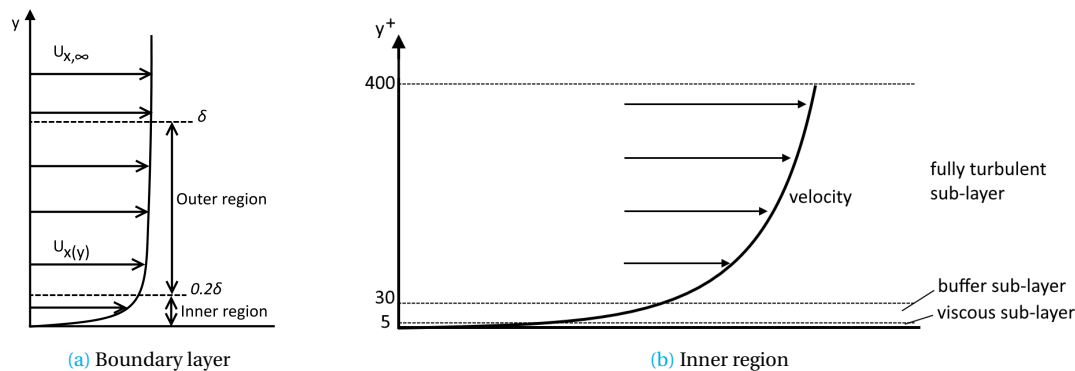


Figure A.3: Velocity profiles in the boundary layer and inner region, based on Andersson et al. (2012).

The inner region can be subdivided in three layers. The division is based on the relative importance of the viscous forces and the turbulent forces. The layer closest to the bed is called the viscous sub-layer. In this layer the molecular viscosity dominates the turbulent forces. At the wall, the shear stress is completely covered by viscous shear, which is shown in Equation (A.17) (Andersson et al., 2012).

$$\tau_b = \rho_w \nu \left. \frac{d\bar{u}}{dz} \right|_{z=0} \quad (\text{A.17})$$

Where: \bar{u} [m/s] Average flow velocity in streamwise direction

Further away from the wall, the viscous forces and turbulent forces are of equal importance. This transition region is called the buffer layer. In the region above the buffer layer the turbulent forces dominate. Viscous forces are negligible in this region, which is called the fully turbulent sub-layer. All the sub-layers can be seen in Figure A.3b.

In the literature the physical extend of the sub-layers is usually expressed in wall variables. The characteristic velocity in the boundary layer is the friction velocity, defined in Equation (A.18).

$$u_* = \sqrt{\frac{\tau_b}{\rho_w}} \quad (\text{A.18})$$

The characteristic length scale is derived by using the kinematic viscosity and the friction velocity, see Equation (A.19).

$$l_* = \frac{\nu}{u_*} \quad (\text{A.19})$$

Where: l_* [m] Characteristic length scale

Another common practice in the literature is the usage of dimensionless wall-coordinates, which are based on the characteristic velocity and length scales, see Equations (A.20) and (A.21).

$$u^+ = \frac{\bar{u}}{u_*} \quad (\text{A.20})$$

$$y^+ = \frac{y}{l_*} = \frac{y u_*}{\nu} \quad (\text{A.21})$$

Where: u^+ [-] Dimensionless flow velocity in streamwise direction (wall coordinate)

Andersson et al. (2012) proposes a classification of the different layers as in Table A.2. The values for the different regions are based on empirical studies.

Table A.2: Overview of the different sub-layers in the turbulent boundary layer (Andersson et al., 2012). For clarification of the velocity expressions see Section A.1.6.

Region	Layer	Velocity
$0 < y^+ < 5$	Viscous sub-layer	$u^+ = y^+$
$5 < y^+ < 30$	Buffer layer	
$30 < y^+ < 400$	Fully turbulent layer	$u^+ = \frac{1}{\kappa} \ln(y^+) + B$
$y^+ > 400$	Outer region	$\frac{u_0 - \bar{u}}{u_*} = \frac{1}{\kappa} \ln(\gamma) + B + h(\gamma)$

Figure A.4 shows the shear stresses in the inner region. It can be seen that the sum of the stresses is approximately constant over the inner region. The value is equal to the wall shear stress (τ_w). The inner region is often referred to as the constant-stress layer.

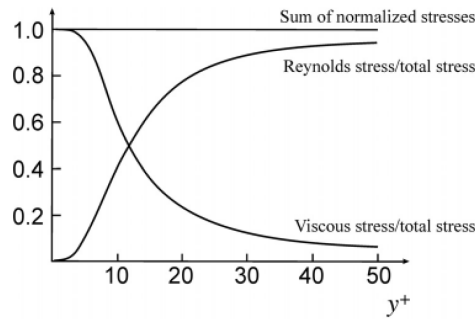


Figure A.4: Near-wall stresses in the inner region of the boundary layer (Andersson et al., 2012).

Wall functions

A wall function is an empirically-determined relationship for the streamwise velocity and the turbulence characteristics close to a wall. A wall function is used to avoid the need for very fine computational meshes near the wall. The most common wall function is the ‘law of the wall’. This law states that the streamwise velocity varies logarithmically when getting further away from the wall (Wilcox, 2006).

In the viscous sub-layer, the shear stress is assumed to be equal to the wall shear stress (Equation (A.17)). When integrating with respect to y and applying the no-slip condition, Equation (A.22) is the result.

$$\bar{u} = \frac{\tau_b z}{\rho_w \nu} = \frac{u_*^2 z}{\nu} \quad \text{or} \quad u^+ = y^+ \quad (\text{A.22})$$

In the fully turbulent layer the velocity profile is determined using Prandtl’s mixing-length model. The derivation can be found in multiple textbooks: Wilcox (2006), Andersson et al. (2012) and Nieuwstadt et al. (2016). The result is the well known logarithmic velocity profile, see Equation (A.23).

$$u^+ = \frac{1}{\kappa} \ln(y^+) + B \quad (\text{A.23})$$

Where: B [-] Coefficient in the logarithmic velocity profile ($B = 5.5$)

Figure A.5 shows the wall functions for both the viscous sub-layer and the fully turbulent layer. It can be seen that the buffer layer functions as a transition region between the two wall functions. As stated before, in this layer both the viscous forces and turbulent forces are important.

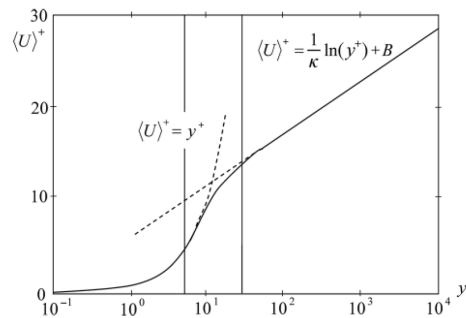


Figure A.5: Wall functions in the inner region of the boundary layer (Andersson et al., 2012).

The use of wall functions in hydrodynamic modelling comes with requirements for the grid size. The first grid point adjacent to the wall should be inside the fully turbulent layer ($y^+ > 30$), where the logarithmic velocity profile is present. Placing the first grid point as close to the lower boundary of the layer as possible is desired, because more grid cells will be present in this layer in that way. This results in a higher resolution of the model results near the bed.

In many modelling cases, wall functions performed well, which has been verified by experimental studies (Andersson et al., 2012). However, the validity of the standard wall functions for more complicated flows can be questioned. For flows with strong adverse pressure gradients, such as separating flows and impinging flows, the wall functions are likely to predict the flow in an incorrect way. For these flows, non-equilibrium wall functions have to be used.

Wall functions for non-equilibrium boundary layers

For certain cases the assumptions that are used for deriving the standard wall functions are not valid. The two most important assumptions are the assumption of constant shear in the inner layer and the assumption of a local equilibrium between dissipation and production of turbulence quantities. Adverse pressure gradients influence the wall shear stress, the mean velocity profile and the turbulence in the boundary layer. Therefore, in flows with strong adverse pressure gradients, the standard wall function is not valid (Andersson et al., 2012).

Wall functions that are capable of including pressure gradients have been developed. Using these wall functions for non-equilibrium boundary layers usually results in improved predictions. The non-equilibrium wall function consists of a logarithmic profile for the mean velocity, which is sensitized to effects of the pressure gradients (Andersson et al., 2012).

Nichols and Nelson (2004), for example, have developed non-equilibrium wall functions. Their functions are especially effective for both attached and separated flows, by including effects of both pressure gradients and surface heat transfer. They provide grid independent solutions when using the $k - \omega$ model.

Outer region

According to Uijtewaal (2011), the turbulent shear stress is still dominant in the outer region, but cannot be considered as a constant. It is a function of the vertical coordinate, which is scaled with the dimensions of the flow geometry. The velocity profile in the outer layer is based on empirical approximations, because it is not possible to define a characteristic mixing length scale. The velocity profile is considered relative to a characteristic velocity, which is usually taken as the free surface velocity. The so-called velocity defect law is shown in Equation (A.24).

$$\frac{u - \bar{u}}{u_*} = -\frac{1}{\kappa} \ln(\gamma_z) + B + h(\gamma_z) \quad (\text{A.24})$$

Where: γ_z [-] Normalized vertical coordinate ($\gamma_z = z/R$)
 $h(\gamma_z)$ [-] Correction factor in velocity profile of the outer layer

The integration constant B in Equation (A.23) can be used to match the inner and outer layer. The correction factor $h(\gamma)$ is needed to take deviations near the free surface into account. Coles proposed the ‘law of the wake’, which can be seen in Equation (A.25).

$$h(\gamma_z) = \frac{\Pi}{\kappa} \left(1 + \sin \left(\frac{(2\gamma_z - 1)\pi}{2} \right) \right) \quad (\text{A.25})$$

Where: Π [-] Coles parameter ($\Pi = 0.2$)

The Coles parameter Π includes the strength of the wake and is related to the mean pressure gradient. Adverse pressure gradients generally require a larger value of the parameter (Uijtewaal, 2011).

Bed roughness

In the derivation of the law of the wall, no attention is paid to the influence of the bed roughness. The integration constant can be used to include the roughness in the equation. A different definition of the logarithmic velocity profile is given in Equation (A.26).

$$u^+ = \frac{1}{\kappa} \ln \left(\frac{y}{y_0} \right) \quad (\text{A.26})$$

Where: y_0 [m] Integration constant in the logarithmic velocity profile

For a smooth wall, y_0 is given by $0.11 \frac{\nu}{|u_*|}$, which results in the same expression as Equation (A.23). A wall is assumed to be smooth when the dimensionless roughness height k_n^+ is smaller than five. The dimensionless roughness height is calculated with Equation (A.27).

$$k_n^+ = \frac{k_n u_*}{\nu} \quad (\text{A.27})$$

Where: k_n [m] Nikuradse roughness height

A wall is defined as a rough wall when the k_n^+ value is larger than 70. The y_0 value for a rough wall is given by $\frac{k_n}{30}$. Walls with a dimensionless roughness height between 5 and 70 are in the intermediate range. For this range y_0 is calculated with a combination of a smooth and rough wall: $y_0 = 0.11 \frac{\nu}{|u_*|} + \frac{k_n}{30}$.

A.2. Erosion and sediment transport

Izbash approach

Izbash considered the forces on an individual grain in a bed, see Figure A.6. The second law of Newton is applied to the forces, to check the stability of the grain. The different forces on a grain consist of (Schierck, 2012):

- Gravity force ($W_s \propto (\rho_s - \rho_w)gd^3$);
- Lift force due to the turbulent fluctuations and pressure differences around the grain ($F_L \propto \rho_w u^2 d^2$);
- Shear force due to the flow ($F_S \propto \rho_w u^2 d^2$);
- Drag force due to the flow ($F_D \propto \rho_w u^2 d^2$);
- Friction force due to surrounding grains ($F_F \propto fW$).

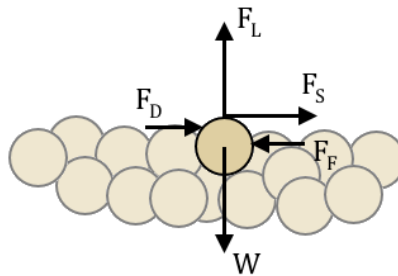


Figure A.6: The forces on a grain in a flow, adapted from Schierck (2012).

From the parameterisations of the different forces the important parameters for the stability of a grain can be deduced. The square of the flow velocity and the grain diameter are the most important parameters for the stability of grains. The local flow velocity consists of the mean flow velocity and fluctuations due to turbulence. The critical velocity for the stability of grains according to Izbash is given in Equation (A.28) (Schierreck, 2012).

$$u_c = 1.2\sqrt{2\Delta g d} \quad (\text{A.28})$$

Where: u_c [m/s] Critical velocity acting on the grain

Shields approach

The steps in Equation (2.3) are done using Equations (A.29)-(A.31) (Schierreck, 2012).

$$\tau_c = \rho_w \cdot u_{\star,c}^2 \quad (\text{A.29})$$

$$\Delta = \frac{\rho_s - \rho_w}{\rho_w} \quad (\text{A.30})$$

$$\bar{u}_c = \frac{u_{\star,c} \cdot C}{\sqrt{g}} \quad (\text{A.31})$$

The Chézy roughness coefficient is given by Equation (A.32) (Hoffmans and Verheij, 1997).

$$C = \frac{\sqrt{g}}{\kappa} \log\left(\frac{12h_0}{k_n}\right) = 18 \log\left(\frac{12h_0}{k_n}\right) \quad (\text{A.32})$$

Where: h_0 [m] Initial water depth

Using Equations (2.3) and (A.32), an expression for the critical velocity can be derived. This expression is shown in Equation (A.33).

$$\bar{u}_c = 2.5\sqrt{\Psi_c \Delta g d} \cdot \log\left(\frac{12h_0}{k_n}\right) \quad (\text{A.33})$$

The empirical relations between the Shields parameter and D_\star are shown in Table A.3.

Table A.3: Empirical relations for Ψ_c as a function of D_\star (Hoffmans and Verheij, 1997).

Ψ_c		D_\star
$\Psi_c = 0.24D_\star^{-1}$	for	$D_\star \leq 4$
$\Psi_c = 0.14D_\star^{-0.64}$	for	$4 < D_\star \leq 10$
$\Psi_c = 0.04D_\star^{-0.10}$	for	$10 < D_\star \leq 20$
$\Psi_c = 0.013D_\star^{0.29}$	for	$20 < D_\star \leq 150$
$\Psi_c = 0.055$	for	$D_\star > 150$

In the equations of the Shields approach, the grain diameter is given as d and is an important parameter in the calculation of the stability of grains. It can be defined in multiple ways. The most common way is to use the nominal stone diameter, d_n . This is the value equal to the side of a cube with the same volume as the grain, see Equation (A.34) (Schierreck, 2012). The median value, d_{n50} , is the value where 50% of weight of the stones in the bed is larger or smaller than that value.

$$d_n = \sqrt[3]{V_s} = \sqrt[3]{\frac{M_s}{\rho_s}} \quad (\text{A.34})$$

Where: d_n [m] Nominal grain diameter
 V_s [m³] Volume of the grain
 M_s [kg] Mass of the grain

Cohesive material

The erosion of cohesive material, like clay, is more complex, when compared to the erosion of non-cohesive material. In general, relatively large forces are needed to erode the cohesive particles from the bed and relatively small forces are needed to transport the loose particles (Hoffmans and Verheij, 1997). According to Sloff et al. (2013), the erosion of clay has two possible mechanisms:

- **Abrasive erosion**

In the case of abrasive erosion, the flow scrapes the sediment particles from the bed. Hoffmans and Verheij (1997) describe experiments of Mirtskhoulava (1988) and Mirtskhoulava (1991) from which followed that the scour of clay happens in several stages. Initially, the loosened particles in the bed are washed away by the flow. After that, the surface of the bed is rougher, which causes higher forces on resulting protruding particles. This destroys the bonds between the particles and suddenly the particles will be pulled out of the bed. This type of erosion will happen when the flow velocity exceeds the critical flow velocity of the clay. This critical flow velocity depends on many factors. Hoffmans and Verheij (1997) state that as a first estimate, $\bar{u}_c = 0.80$ m/s can be taken for fairly compacted clay and $\bar{u}_c = 1.50$ m/s for stiff clay. Based on the work by Mirtskhoulava (1988) and Mirtskhoulava (1991), Equation (A.35) is found for the critical flow velocity for cohesive sediments.

$$\bar{u}_c = \log\left(\frac{8.8h_0}{d_a}\right) \sqrt{\frac{0.4}{\rho_w} ((\rho_s - \rho_w)gd_a + 0.6C_f)} \quad , \text{ where } C_f = 0.035C_c \quad (\text{A.35})$$

Where: d_a [m] Size of the detaching aggregates ($d_a = 0.004$ m)
 C_f [Pa] Fatigue rupture strength of clay
 C_c [Pa] Cohesion

- **Pulling-off of fragments**

The pulling-off of fragments of clay happens in an undrained situation. For this mechanism, the critical shear strength can be derived from the undrained shear strength. This undrained shear strength can be obtained using the cone resistance and the bearing capacity of the clay (Sloff et al., 2013).

A.2.1. Types of scour

When the local sediment transport is larger than the sediment supply from upstream, the erosion process is called scour. Schiereck (2012) describes two possible types of scour:

- When there is no sediment supply from upstream, but there is sediment transport downstream, the case is known as **clear-water scour**. This might be the case due to low flow velocities upstream (no sediment can be transported) or a non-erodible bed upstream (there is no sediment to be transported). Clear water scour reaches its equilibrium scour depth when a value is reached that makes the flow velocity drop below the critical value.
- When there is sediment supply from upstream, but the sediment transport downstream is larger, the case is known as **live-bed scour**. This is the most common in river branches. In this situation the equilibrium scour depth is reached when the transport capacity downstream equals the transport capacity upstream. The actual scour hole depth will be fluctuating around the equilibrium value, as can be seen in Figure A.7. This equilibrium value is smaller than the one in case of clear-water scour.

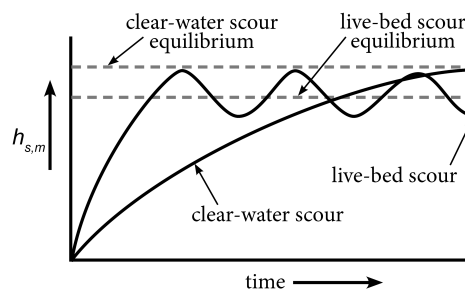


Figure A.7: Scour depth as a function of time, based on (Hoffmans and Verheij, 1997).

A.3. Scour hole development

In the past, many experiments have been performed in an attempt to predict the development of local scour holes. Hoffmans and Verheij (1997) described the most important studies, including the formulas and parameters that are used. The local scour in heterogeneous subsoil is not described, and can best be approximated by the scour behind a bed protection and a sill. Figure A.8 shows a schematization of the reference situation, including some of the parameters used in the equations. In this section, the formulas and parameters that are found for this scour situation are presented, together with some additional information on the development of local scour holes.

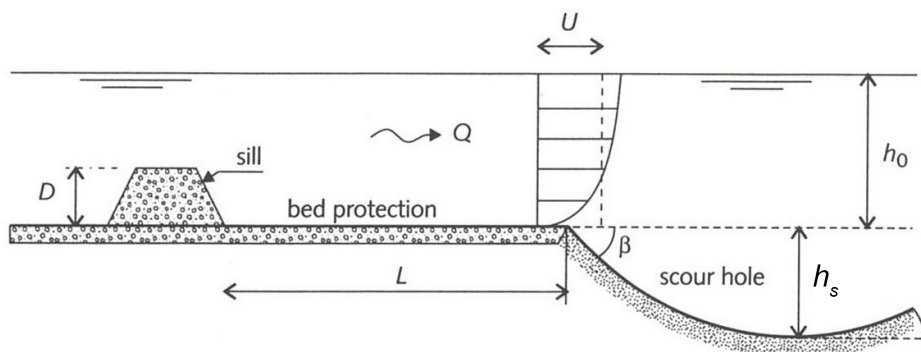


Figure A.8: Schematization of a local scour hole behind a bed protection and a sill, based on (Hoffmans and Verheij, 1997).

A.3.1. Scour development in time

The formation of a scour hole takes time. Many researchers performed experimental tests to be able to describe the development of a scour hole in time. In this section, these studies are described.

Phases in scour hole development

According to Zanke (1978), the evolution of a scour hole in time can be divided into four phases. He based the different phases on the results of clear-water scour experiments by Breusers (1966) and Dietz and Wittke (1969). The four phases are shown in Figure A.10.

- **Initiation**

During the initial phase, the main scouring process is governed by the stability of the grains, which is described earlier. The flow regime is nearly uniform over the approximately horizontal initial bed. Some sediment near the upstream slope is going into suspension, but also bed load transport is occurring in this phase.

- **Development**

The development phase is characterized by a more or less constant ratio between the maximum scour depth and the distance from the end of the bed protection to the point of maximum scour depth. The scour depth increases substantially, but the shape of the scour hole stays approximately the same. There is a decrease in flow velocity, but an increase in turbulence energy, due to the flow separation that starts to occur (see Figure A.9). This results in less suspended sediment near the bed. The upstream part of the scour hole is in equilibrium, while the downstream part is still developing.

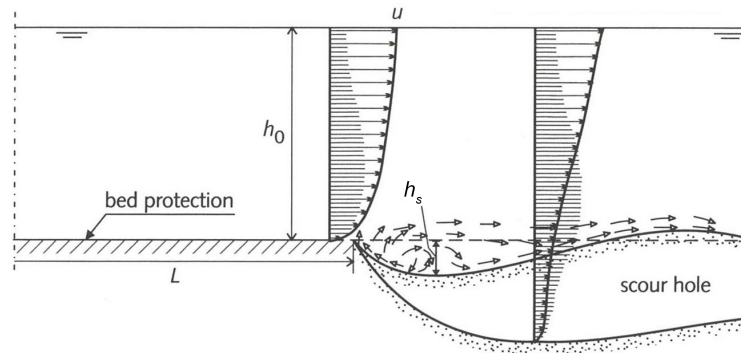


Figure A.9: Schematization of a local scour hole behind a bed protection, showing the flow separation and recirculation in the scour hole, based on (Hoffmans and Verheij, 1997).

- **Stabilization**

The development of the maximum scour depth decreases in this phase. The shape of the scour hole changes more in horizontal direction than in vertical direction. Due to the erosion capacity behind the point of reattachment, the downstream slope will be eroded, until the equilibrium situation is almost reached.

- **Equilibrium**

The last phase is the equilibrium phase. The dimensions of the scour hole are not changing much in this phase.

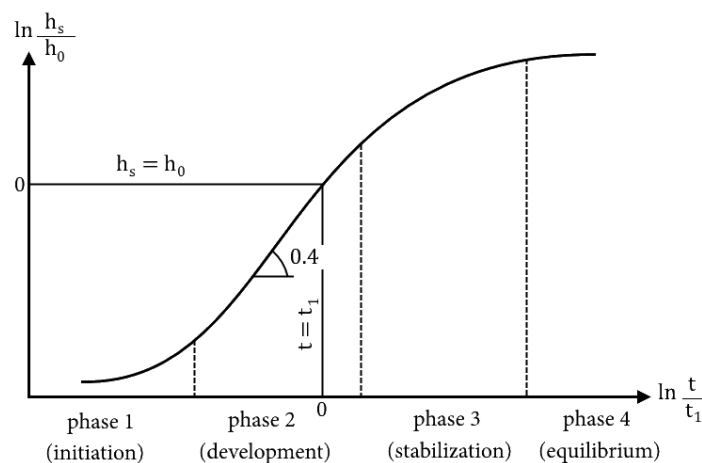


Figure A.10: Four phases in the evolution of a scour hole by clear-water scour, based on (Hoffmans and Verheij, 1997).

Description

From several hundreds of experiments with clear-water scour, an empirical relation is derived for the scour hole development in time (Hoffmans and Verheij, 1997). This relation can be seen in Equation (A.36). For cases where the equilibrium scour depth is larger than the initial flow depth, the relation gives reasonable accurate results (Hoffmans and Verheij, 1997).

$$\frac{h_s}{h_{s,e}} = 1 - e^{\ln\left(1 - \frac{\lambda}{h_{s,e}}\right)\left(\frac{t}{t_1}\right)^\gamma} \quad (\text{A.36})$$

Where:	h_s	[m]	Maximum scour depth
	$h_{s,e}$	[m]	Equilibrium scour depth
	λ	[m]	Characteristic length scale
	t_1	[s]	Characteristic time scale
	γ	[-]	Breusers' coefficient

In the development phase of a scour hole, where $t < t_1$, Equation (A.36) reduces to Equation (A.37), which was first proposed by Breusers (1966).

$$\frac{h_s}{\lambda} = \left(\frac{t}{t_1} \right)^\gamma \quad (\text{A.37})$$

Breusers (1966) determined a value of 0.38 for the γ -coefficient. According to Hoffmans and Verheij (1997) other researchers have also determined the value of γ . The results are summarized in Table A.4. From the table can be deduced that for a three-dimensional flow condition, a higher value for γ should be used. The value by Breusers (1966) seems to be confirmed by the other two-dimensional studies, as it lies in between the values of the two others.

Table A.4: Results of different researches on the value of γ in Equation (A.36) (Hoffmans and Verheij, 1997).

Research	γ	Flow condition
Breusers (1966)	0.38	Two-dimensional
Mosonyi and Schoppmann (1968)	0.27 - 0.35	Two-dimensional
Dietz and Wittke (1969)	0.34 - 0.40	Two-dimensional
Van der Meulen and Vinjé (1975)	0.40 - 0.80	Three-dimensional

According to Hoffmans and Verheij (1997), the characteristic length scale λ is widely described in literature. Values are found ranging from the Kolmogorov length scale to the size of hydraulic structures. Because of the fact that the largest eddies are an important part of turbulent flows, the characteristic length scale is usually taken as the upstream water depth h_0 .

Characteristic time scale

The characteristic time scale in Equation (A.37) is described by Van der Meulen and Vinjé (1975). The value is equal to the time at which the scour depth is equal to the characteristic length scale (usually the upstream water depth). Equation (A.38) shows the calculation of the characteristic time scale.

$$t_1 = \frac{K h_0^2 \Delta^{1.7}}{(\alpha u_0 - \bar{u}_c)^{4.3}} \quad (\text{A.38})$$

Where: K [hours $\text{m}^{2.3}/\text{s}^{4.3}$] Coefficient
 α [-] Amplification factor for the flow velocity

Multiple studies have been performed to assess the value of K . Van der Meulen and Vinjé (1975) proposed a value of 250, which they based on more than a hundred tests in three-dimensional situations. According to De Graauw and Pilarczyk (1981), K should have a value of 330. They based their value on tests with a rough bed. The value of 330 is the generally applied (Hoffmans and Verheij, 1997). Hoffmans (1992) showed that the value is not constant, but weakly dependent on sedimentary characteristics. As can be seen, the units of t_1 and K include hours. If the units are rewritten to seconds, the unit of K becomes $[\text{m}^{2.3}/\text{s}^{3.3}]$. The generally applied value then becomes $1.19 \cdot 10^6$.

The amplification factor for the flow velocity is used to take into account the turbulence. Jorissen and Vrijling (1989) came with an expression for the amplification factor for hydraulically rough conditions in a three-dimensional situation, see Equation (A.39).

$$\alpha = 1.5 + 5r_0 \quad (\text{A.39})$$

Where: r_0 [-] Relative turbulence intensity, see next section

Hoffmans and Booij (1993b) included the roughness in the determination of α , see Equation (A.40).

$$\alpha = 1.5 + 4.4r_0 f_c \quad (\text{A.40})$$

Where: f_c [-] Roughness function

The roughness function is related to the roughness of the bed protection and calculated by Equation (A.41).

$$f_c = \frac{C}{C_0}, \quad \text{if } C < C_0 \text{ then } f_c = 1 \quad (\text{A.41})$$

Where: C_0 [m^{1/2}/s] Maximum Chézy coefficient in f_c ($C_0 = 40$ m^{1/2}/s)

Equation (A.40) is applicable for two-dimensional situations (Hoffmans and Verheij, 1997). According to De Graauw and Pilarczyk (1981), the amplification factor in three dimensional flow depends strongly on the geometry upstream of the scour hole. They generated design curves for a specific flow situation, where the value for α can be found. The two-dimensional α -values are between 2.0 and 3.2, while the three-dimensional case has α -values between 3.7 and 8.9. In general can be said that a three-dimensional situation has a higher amplification factor than a two-dimensional situation.

Relative turbulence intensity

An expression for the relative turbulence intensity is deduced by Hoffmans and Booij (1993b) (see Equation (A.42)). This expression described the relative turbulence intensity at the transition between the non-erodible and erodible bed. This transition is assumed to be located in the relaxation zone, behind the reattachment point.

$$r_0 = \sqrt{0.0255 \left(1 - \frac{D}{h_0}\right)^{-2} \left(\frac{L_p - 6D}{6.67h_0} + 1\right)^{-1.08} + 1.45 \frac{g}{C^2}} \quad \text{for } L_p > 6D \quad (\text{A.42})$$

Where: D [m] Height of the sill
 L_p [m] Length of the bed protection

The reference case (see Figure A.9) includes a sill with sill height D and a bed protection with length L . In the real case, there is no sill and bed protection. Therefore, a value of 0 m is taken for D and L is assumed to be infinitely long to exclude them from the formulas. The result can be seen in Equation (A.43).

$$r_0 = 1.2 \sqrt{\frac{g}{C^2}} \quad (\text{A.43})$$

A.3.2. Equilibrium depth

For most engineering situations, the equilibrium depth of a scour hole is the most important parameter to calculate, because it determines whether a scour hole will be a threat for a certain structure or dike. Hoffmans and Verheij (1997) state that a long period of time is needed to reach the equilibrium scour depth, especially in case of low Froude numbers and clear-water scour. Dietz and Wittke (1969) found Equation (A.44) for calculating the equilibrium scour depth.

$$\frac{h_{s,e}}{h_0} = \frac{\omega_s u_0 - \bar{u}_c}{\bar{u}_c} \quad (\text{A.44})$$

Where: ω_s [-] Turbulence coefficient, $\omega_s = 1 + 3r_0$ according to Dietz and Wittke (1969)

Schiereck (2012) proposed another formula (Equation (A.45)), which is using the amplification factor α , which is described above.

$$\frac{h_{s,e}}{h_0} = \frac{0.5\alpha u_0 - \bar{u}_c}{\bar{u}_c} \quad (\text{A.45})$$

A.3.3. Upstream slope

During the scouring process, the upstream slope of the scour hole will be eroded by the water flow. Hoffmans (1993) found a semi-empirical expression for the upstream slope angle. This expression represents the equilibrium of bed load transport due to the downward sloping bed shear stress and the upward sloping bed shear stress. It can be seen in Equation (A.46).

$$\beta = \arcsin \left(2.9 \cdot 10^{-4} \frac{\bar{u}^2}{\Delta g d_{50}} + (0.11 + 0.75r_0) f_c \right) \quad (\text{A.46})$$

Where: d_{50} [m] Median grain diameter

The equation has a shear stress factor and a turbulence factor, which represents the skewness of the bed shear stress due to sweeps and ejections (Hoffmans and Pilarczyk, 1995). It follows that more turbulence (higher r_0 -value) induces a steeper slope. Generally, if the flow velocity is smaller than 1 m/s, the influence of the shear stress factor is negligible. However, in deltaic regions, where the flow velocities are higher than 1 m/s and the sediment is relatively fine, the shear stress factor dominates (Hoffmans and Verheij, 1997).

The stability of the upstream slope is dependent on the fluid motion and the material properties. When the slope angle exceeds the angle of repose of the soil ϕ , failure will occur. Soil particles will roll into the scour hole, resulting in a less steep slope (Schierreck, 2012). The angles of repose for different soil types can be seen in Table A.5.

Table A.5: The angle of repose for different soil types (Hoffmans and Verheij, 1997).

	Soil type	Angle of repose ϕ
Coarse sand, sand and gravel	Compact	45°
	Firm	38°
	Loose	32°
Medium sand	Compact	40°
	Firm	34°
	Loose	30°
Fine sand, silty sand, sandy silt	Compact	30-34°
	Firm	28-30°
	Loose	26-28°
Clay (saturated)	Medium	10-20°
	Soft	0-20°

Failure

According to Hoffmans and Verheij (1997), the two most important types of slope failure are shear failure and flow slides. Shear failure is simply the failure due to high flow velocities of the water. This process is already described in Section 2.3.1. The only difference compared to the shear failure method by Shields, is the presence of a sloping bed. Schierreck (2012) proposes a method to correct the stability criterion. Figure A.11 shows the possible situations. Situation *a* is described in Section 2.3.1. The upstream slope of the scour hole is best approximated by situation *b*, where the flow is in the direction of the slope. For this situation, a reduction factor for the strength can be calculated, see Equation (A.47).

$$K_{\alpha_s//} = \frac{W_s \cos(\alpha_s) \tan(\phi) - W_s \sin(\alpha_s)}{W_s \tan(\phi)} = \frac{\sin(\phi) \cos(\alpha_s) - \cos(\phi) \sin(\alpha_s)}{\sin(\phi)} = \frac{\sin(\phi - \alpha_s)}{\sin(\phi)} \tag{A.47}$$

Where: $K_{\alpha_s//}$ [-] Reduction factor for slope strength
 α_s [°] Slope angle

Situation *c* is representing the side slopes of the scour hole, where the flow is not in the direction of the slope. Graph *d* in Figure A.11 shows the reduction factor versus the slope angle for both situation *b* and *c*, assuming an angle of repose $\phi = 40^\circ$. It can be seen that the upstream slope is clearly less stable than the side slopes of the scour hole.

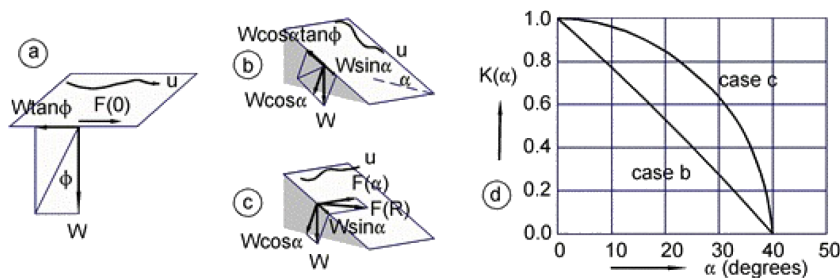


Figure A.11: Influence of the slope on stability (Schierreck, 2012).

In the case of slope failure by flow slides, the porosity of the sand plays an important role. In the Netherlands, sand is loosely packed if the porosity exceeds a value of 40% (Hoffmans and Verheij, 1997). If shear stresses are working on loosely packed sand, the sand particles will get a denser packing. Over-pressure will be induced, as the pores are filled with water. In some cases this might result in the soil particles having no contact with each other. In that case, the frictional resistance is lost and liquefaction will occur. The soil acts like a thick fluid, and will slide down into the scour hole. Hoffmans and Verheij (1997) determined the critical slope angle and failure mechanism for different packings of sand. This can be seen in Table A.6.

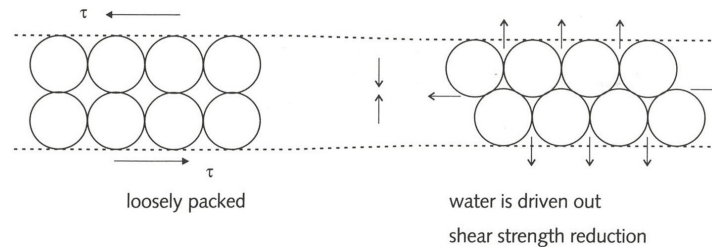


Figure A.12: Effect of shear on loose sand (Hoffmans and Verheij, 1997).

Table A.6: Angle of repose, critical slope angle and failure mechanism for different sand densities (Hoffmans and Verheij, 1997).

Bulk density of fine sand	Angle of repose ϕ	Critical slope angle $\alpha_{s,c}$	Phenomenon
Very loose	30° (1V:1.7H)	24° (1V:2.25H)	Flow slide
Loose	33° (1V:1.5H)	27° (1V:2.00H)	Flow slide
Dense	37° (1V:1.3H)	30° (1V:1.75H)	Shear failure
Very dense	40° (1V:1.2H)	34° (1V:1.50H)	Shear failure

Undermining

When the slope fails, the soil particles roll down, resulting in a milder slope. Due to this process the sand layer will undermine the clay layer at the upstream edge of the scour hole. According to Van Zuylen and Sloff (2015) the undermining of the clay layer would result in failure and crumbling of the clay layer, like the observed block-failure at the edges in the field. Deformation of the clay layer might stabilize the slopes, when it acts like a falling apron.

A.3.4. Influence of the tide

All the equations that are described above are valid for scour hole formation and development in uniform flow conditions. Rivers in the Rhine-Meuse delta are influenced by the tide from the North Sea. This tidal influence makes the flow velocity fluctuate. Besides that, the flow direction changes during a tidal cycle. This all makes the situation more complex, when comparing to uniform flow conditions.

Equation (A.37), which describes the scour depth in the development stage, can be rewritten for a case with unsteady flow. This is done by Hoffmans and Verheij (1997) and shown in Equation (A.48).

$$\frac{h_s(t)}{h_0(0)} = \left(\frac{t}{t_{1,u}} \right)^{\gamma} \quad (\text{A.48})$$

Where: $t_{1,u}$ [s] Characteristic time scale in unsteady flow

The characteristic time scale K is different for unsteady flow. Hoffmans and Verheij (1997) adapt Equation (A.38) by including a succession of infite short-lasting steady situations. For cyclic flow, the characteristic time scale is derived by Equation (A.49).

$$t_{1,u} = \frac{K h_0(0) \Delta^{1.7}}{\frac{1}{T} \int_{t_{2,tide}}^{t_{1,tide}} \frac{(\alpha \bar{u}(t) - \bar{u}_c)^{4.3}}{h_0(t)} dt} \quad (\text{A.49})$$

Where: T [s] Part of the tidal period where $\alpha \bar{u}_0 > \bar{u}_c$ ($T = t_2 - t_1$)
 $t_{1,tide}$ [s] Time at which $\alpha \bar{u}_0$ first exceeds \bar{u}_c during flood tide
 $t_{2,tide}$ [s] Time at which $\alpha \bar{u}_0$ drops below \bar{u}_c during ebb tide

The mean velocity and flow depth are the only parameters that are time-dependent. When these parameters are known as a function of time, the characteristic time scale can be determined by numerical integration. Ebb flow is left out of Equation (A.49), because it was based on a case at the Brouwersdam with a dominating flood flow.

[McGovern et al. \(2014\)](#) studied the development of scour under variable reversing currents with lab experiments. They concluded that the influence of the reversing tide resulted in a lower equilibrium scour depth, when comparing to the scour depth predicted by existing equations for unidirectional conditions. The shape of the scour hole in longitudinal direction was more symmetric. During the experiments, four half-cycles of the tide were tested.

[Escarameia and May \(1999\)](#) performed laboratory experiments for both unidirectional conditions and tidal conditions. Their study was carried out to investigate the influence of the following parameters on scour development around large obstructions under tidal conditions: reversal of the flow direction, tidal cycle duration, water depth, shape of the obstruction and sediment size. From the test results is concluded that the equilibrium scour depth after one half-cycle is a little larger for tidal conditions, when comparing to unidirectional conditions. The scour depth stabilizes after 4-5 half cycles at an equilibrium value that is significantly less than the value for unidirectional flow. Besides this effect, the study showed that the water depth of the flow influenced both the maximum- and the equilibrium scour depth.

Appendix B

Numerical modelling of scour holes

The numerical modelling of scour holes can be done using a method based on Computational Fluid Dynamics (CFD). Over the last 25 years many researchers have tried to model the formation of scour holes using a CFD-based numerical model. The majority of these models simulate scour around an object at the bed or due to a jet. Obviously, a situation like that is not the same as local scour in heterogeneous subsoil, but similarities in the flow structures are present. Therefore, investigating the studies with an object is beneficial for this research. In the following part, a sum-up is given on the studies that are modelling scour in several situations.

Circular object

Most of the scour studies that are done, involve scour around a circular object, like a bridge pier. [Sumer \(2007\)](#) summed up the main developments in numerical modelling of scour around circular objects. The more recent and relevant studies are described here.

[Roulund et al. \(2005\)](#) achieved to gain steady state solutions for the live-bed scour regime. They solved the unsteady RANS (URANS) equations numerically, combined with a $k-\omega$ turbulence closure model. The motion of particles in the surface layer of the bed and sliding of the bed are taken into account in the morphological model. This model couples the flow solution with a sediment transport description to update the computational mesh. The results are compared to experimental data and it was found that the equilibrium depth of the simulations agrees reasonably well with the measured values. Upstream of the pile, the computed scour depth is 15% smaller than the scour depth from the experiment. Downstream, this value is 30% smaller. This is ascribed to the fact that the model solves for the steady state solution, while unsteady effects (like fluctuating components of the horseshoe- and lee-wake vortex) are of importance in the formation of the scour hole. These effects are not taken into account by the model.

The studies by [Kim et al. \(2014 and 2015\)](#) simulated the local scouring around two adjacent cylinders. Large Eddy Simulations (LES) are done using the incompressible, filtered URANS equations. The subgrid-scale stresses (the stresses that result from eddies that are unresolved by the grid) are modelled using the Smagorinsky subgrid model. The numerical scheme that is used includes a ghost-cell immersed boundary method. This method imposes a force, which is space- and time dependent on the flow at the boundaries. The force is not located at a grid point, so a so-called ghost-cell is needed for inter- and extrapolation to the grid. The sediment motion is modelled in a Lagrangian framework by solving the motion stages for spherical particles. The model validation is done using experimental data. The results show good agreement between the model and the measurements. The model is able to predict the evolution of the scour, as well as the maximum scour depth and the equilibrium scour depth in a correct way. This can be seen in [Figure B.1](#).

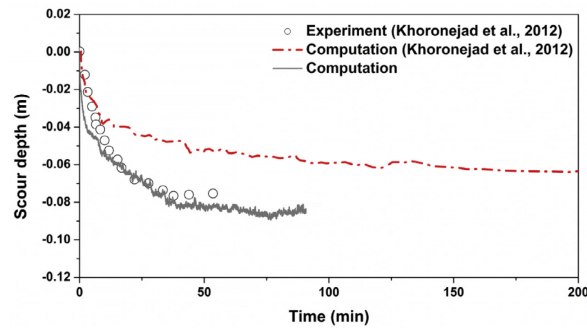


Figure B.1: Time evolution of the maximum scour depth. The gray line is computed in Kim et al. (2014). The experimental data are retrieved from Khosronejad et al. (2012).

Finally, the study by Baykal et al. (2015) is described. They used OpenFOAM to model a three-dimensional numerical model based on the incompressible RANS equations to investigate the flow and scour around a vertical cylinder, which is exposed to a current. The model uses the $k-\omega$ turbulence closure model and includes vortex shedding processes, sediment transport (both bed load and suspended load) and bed morphology. The focus lies on the influence of the vortex shedding and suspended load transport. Especially the influence of the suspended load transport is significant. When the suspended sediment transport is not accounted for, the equilibrium scour depth is decreased by 50%. The influence of the vortex shedding is limited to the initial stage of the scour process. The vortex structures are visualised by plotting the phase-averaged velocity streamlines, as can be seen in Figure B.2.

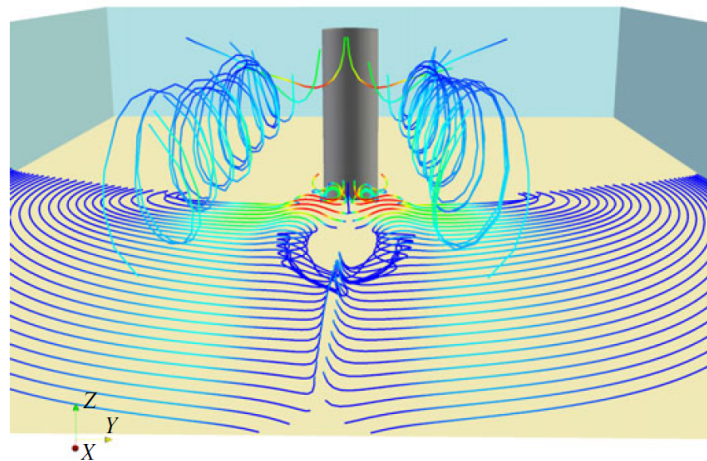


Figure B.2: Visualisation of the streamwise phase-averaged velocity streamlines Baykal et al. (2015).

Jet scour

Jet scour is another type of scour. Jets can be found in different forms, like wall jets, or jets due to propellers of ships. In this part, two studies on jet scour are described.

In the paper by Liu and García (2008) a turbulent wall jet scour problem is modelled numerically, using two different methods for the interfaces. The air-water interface is modelled with the volume of fluid (VOF) method, which is an Eulerian method. The water-sediment interface is modelled with the moving-mesh method, which is a Lagrangian method. The RANS equations are used, combined with the conventional $k-\epsilon$ turbulence closure model. The bed elevation update is done using the Exner equation. The bed load transport is simulated using a transport formula, taking into account the bed shear stress, slope of the bed and grain size. The chosen equation for suspended load is the standard convection diffusion equation. The mesh deformation is done by a Laplacian smooth operator. The code that is used to solve the equations is OpenFOAM. This open source software is adapted by addition of the sediment transport equation and the bed deformation to a new solver called *FOAMSCOUR*. Measurements from experiments are used to validate the model. The resulting velocity fields and other flow characteristics compare very well with these measurements.

Flow over dunes

In [Nabi et al. \(2012\)](#), a model is made to simulate the hydrodynamics of flow over an artificial dune. First a two-dimensional dune geometry is used and after that a three-dimensional geometry is modelled. The model uses LES for turbulence closure and the governing equations are discretized using a finite-volume method on a staggered grid. The Cartesian grid is locally refined and a ghost-cell immersed boundary technique is applied.

Results of the simulations can be seen in [Figure B.3](#). According to the comparison between model and measurements, the model is simulating reality fairly well. The fluctuation in vertical direction $\overline{w'}$ is underestimated by the model, resulting in lower nondimensional time-averaged Reynolds stresses $\overline{u'w'}$. For the three-dimensional dune, the model showed qualitatively good agreement with the measurements as well. The model is able to simulate the recirculation and the current of turbulence in a physics based way.

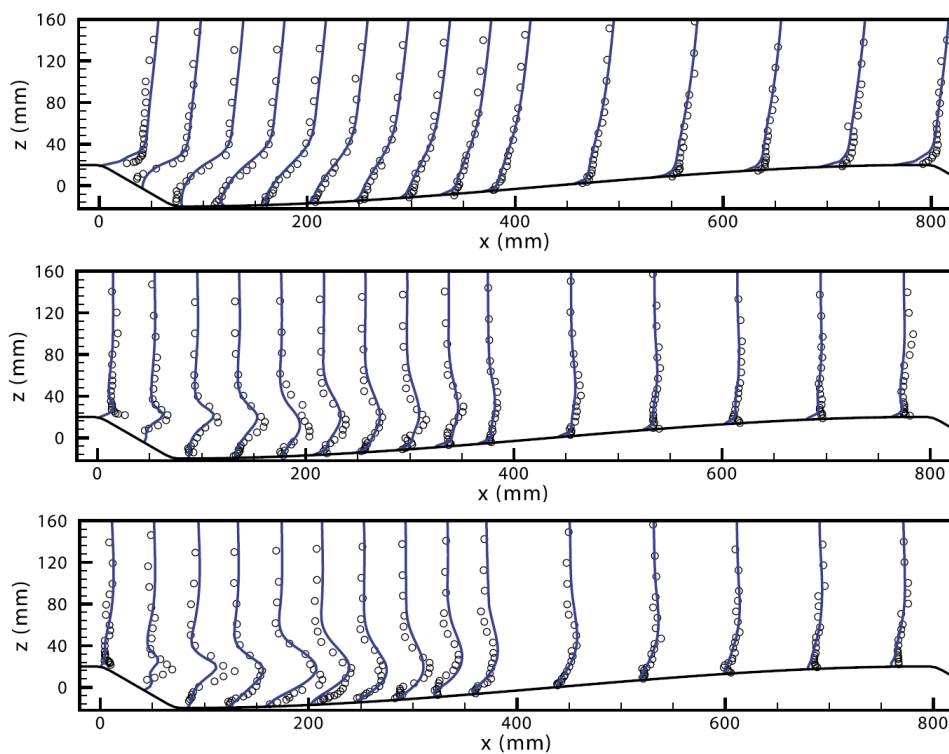


[Figure B.3](#): Comparison of different flow parameters, circles are measurements and solid lines are simulated profiles. Upper: time averaged streamwise flow velocity, Middle: nondimensional time-averaged Reynolds stress profiles of $-\overline{u'u'}$, Lower: nondimensional time-averaged Reynolds stress profiles of $-\overline{u'w'}$ ([Nabi et al., 2012](#)).

Appendix C

Modelling software choice

In this appendix the choice of modelling software is described. This choice is an important one and should therefore be made based on a thorough analysis of the different models that are available. In order to be able to compare the models, meetings were organized with different people from Deltares and the TU Delft. During these meetings the aspects and possibilities of the models were discussed. A short overview of the different models is given below.

C.1. Delft3D

Delft3D is the in-house developed hydrodynamic and morphological model of Deltares. The model can be used for 1D, 2D and 3D computations for coastal, river and estuarine areas. Both non-steady flow and transport phenomena can be calculated. The grid in Delft3D Flexible Mesh is unstructured. Morphological calculations are not yet included in the latest version of Delft3D Flexible Mesh. They will be added in a future release. Non-hydrostatic calculations are not yet available in Delft3D Flexible Mesh (Deltares, 2017). Therefore, this model can not be used for this research.

Delft3D-FLOW does have a non-hydrostatic solver. A drawback of this solver is the fact that it can only be used with Z-layers (Deltares, 2014). Figure C.1 shows the differences between Z-layers and σ -layers. In order to model the scour holes correctly, a smooth bed is preferred. Therefore, σ -layers would have been used if possible.

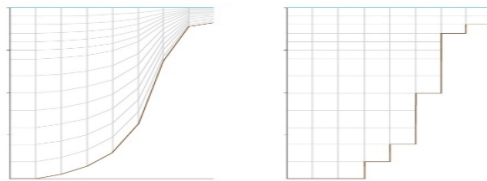


Figure C.1: Difference between σ - (left) and Z-layers (right) (Deltares, 2014).

Advantages of Delft3D are the user-friendliness of the model, which is induced by the Graphical User Interface (GUI), and the experience from previous projects that involved modelling with Delft3D. Another asset of Delft3D are the User Manuals. Most of the problems that a user of the software might encounter are described in these manuals. When a solution is not described, help is available from many employees of Deltares.

C.2. FINEL3D

FINEL3D is a non-hydrostatic flow solver, which implicitly solves the three-dimensional Navier-Stokes equations. For this, an unstructured computational grid of triangles (in 2DV mode) or tetrahedrons (in 3D mode) is used. FINEL is an acronym of FINite ELEments, which is referring to the finite element method, used to solve the equations. The model is created at Svašek Hydraulics and new features are still being added to the model by this company.

The most important assets of FINEL3D are the non-hydrostatic solver, the fact that the bed can be modelled in a smooth way and the user experience from previous projects that involved modelling with FINEL during an internship at Svašek Hydraulics. Besides that, the model has a straightforward user manual and personal help from experts is available at the company.

A morphology module is not included in FINEL3D at the start of this research. When the modelling software choice was made, this research aimed on modelling the development of a scour hole, including morphology. Therefore, FINEL was not considered as an option.

C.3. OpenFOAM

OpenFOAM is a free and open source Computational Fluid Dynamics (CFD) software package and is short for Open Field Operation And Manipulation. The software is written in the C++ language and includes many solver applications. These applications are used in most of the branches within science and engineering. Besides the solver applications, OpenFOAM also includes pre-processing and post-processing utilities. However, the OpenFOAM user is able to use its own post-processing software.

Users of OpenFOAM can create new solver applications, resulting in solvers for a wide range of problems. Together with the solvers, many tutorials are available for new users. Modelling with the OpenFOAM software as a beginner is difficult, as the model does not have a Graphical User Interface (GUI). However, at Deltares there are employees who have experience in modelling in OpenFOAM and who are willing to provide personal assistance.

As described in Appendix B multiple researchers used OpenFOAM in the past to model a scour situation. These studies proved that the model is able to include the necessary flow features and that it is able to model the formation and development of a scour hole.

C.4. Model of Mohamed Nabi

The final model that is examined is the model created by Mohamed Nabi. Nabi works at Deltares and created a Large Eddy Simulation (LES) model for simulating scour situations. Nabi's model was used during the study by Kim et al. (2014). The results of that study are promising and proved that the model is able to simulate scour in a correct way.

However, there are some drawbacks to the model. In the first place, the code is written by Nabi himself and not documented at all. According to Nabi, even he is sometimes lost in the code, which makes it very hard to implement the model as a 'stranger'. Besides, a single run with the model takes up to one month of computation time. This is too long for this research.

C.5. Conclusion

The model choice is made based on the possibilities and the practical advantages and disadvantages. The processes that are important for a correct representation of the scour situation are mostly the result of the bed forms. Delft3D will not be an option, because it models the bed using Z-layers, resulting in a stepwise approximation of bed slopes. Errors would rise in the modelling of a scour hole because of this effect. FINEL3D is not an option, because it does not have a morphology module. The formation of a scour hole cannot be simulated using that model.

The modelling Toolbox OpenFOAM will be used in this research, since it meets the requirements best. Many applications and extensions can be added to the model. Different discretizations, advection schemes and transport modules are available. In the past, the OpenFOAM Toolbox is used in multiple successful researches ((Liu and García, 2008), (Jacobsen et al., 2014), (Baykal et al., 2015), (Baykal et al., 2017)), which include comparable processes: horseshoe vortices, recirculation zones and wall boundary layers. The model by Niels Jacobsen is available for this research, as he will be assisting in the execution of this project.

Appendix D

OpenFOAM

In this appendix the set up and execution of an OpenFOAM case is explained. First, the structure of directories of an OpenFOAM case is discussed. The function of all important files is described, and examples of the files are given. At last, details are given on the post-processing tool, Paraview. The main source for the content in this appendix is the OpenFOAM User Manual by [OpenFOAM Foundation Ltd. \(2016\)](#).

D.1. Structure of an OpenFOAM case

A case in OpenFOAM consists of a case-directory with a set of files and directories that define the case. The structure of directories and files that are needed for every OpenFOAM case is shown in Figure D.1. In this section, the different directories and the files within them are described, starting with the time directories at the bottom in the figure and working up. The files inside the folders are called dictionaries.

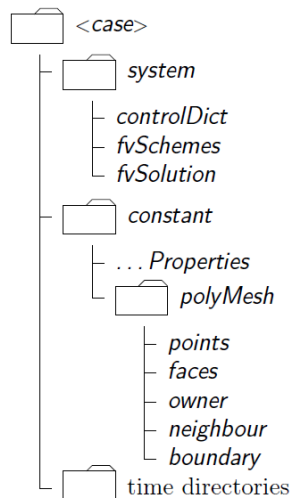


Figure D.1: Directory structure of an OpenFOAM case ([OpenFOAM Foundation Ltd., 2016](#)).

D.1.1. The time directories

The time directories consist of files for the different variables (U , k , ω , p). In the files the values of the variables at all grid points are defined. All time directories are generated during the execution of a case, except for the 0 directory. The name of the time directories is the time value that the files in the directory represent.

The 0 directory

The 0 directory contains the same files as the time directories. The contents of the files in this directory describe the initial and boundary conditions and are specified by the user. An example of a variable-file is shown in Figure D.2. This is a file for U in the 0 directory.


```

20     nPostSweeps      2;
21     nFinestSweeps   2;
22
23     cacheAgglomeration true;
24     nCellsInCoarsestLevel 10;
25     agglomerator     faceAreaPair;
26     mergeLevels      1;
27 };
28
29 pFinal GAMG
30 {
31     tolerance         1e-9;
32     relTol            0.0;
33
34     smoother          DIC;
35     nPreSweeps        0;
36     nPostSweeps       2;
37     nFinestSweeps     2;
38
39     cacheAgglomeration true;
40     nCellsInCoarsestLevel 10;
41     agglomerator      faceAreaPair;
42     mergeLevels       1;
43 };
44
45 "(U|k|omega)"
46 {
47     solver             PBiCG;
48     preconditioner     DILU;
49     tolerance          1e-08;
50     relTol             0;
51 }
52
53 "(U|k|omega)Final"
54 {
55     solver             PBiCG;
56     preconditioner     DILU;
57     tolerance          1e-08;
58     relTol             0;
59 }
60 }
61
62 PIMPLE
63 {
64     momentumPredictor  yes;
65     nCorrectors         3;
66     nNonOrthogonalCorrectors 0;
67     nOuterCorrectors    3;
68
69     pRefCell            0;
70     pRefValue           0;
71 }
72
73 relaxationFactors
74 {
75     p                   0.7;
76     U                   0.85;
77 }
78
79 // ***** //

```

Figure D.4: Example of a `fvsolution` file in the `system` folder of an OpenFOAM case. The header of the file is left out.

The `fvschemes` file

The last file that is elaborated on is the `fvschemes` file. In this file the numerical schemes for different terms in the equations are set. An example of the `fvschemes` file that is used in the cases in this research is shown in Figure D.5. The different sub-dictionaries in this file are described below.

the Gauss integration and use different schemes for interpolation. The `linear` scheme is second order and unbounded. When `linearUpwind` is chosen, a discretisation of the velocity gradient is needed, which is set after this keyword.

- `laplacianSchemes`
This sub-dictionary sets the numerical scheme for the Laplacian terms (∇^2) in the equations. A typical Laplacian term is the diffusion term in the momentum equations. The only possibility for a discretisation scheme is the Gauss scheme. Two additional keywords are given. The first defines the selection of the interpolation scheme for the diffusion coefficient (`linear`) and the second defines the scheme for surface normal gradients (`corrected`, see also `snGradSchemes`).
- `interpolationSchemes`
This sub-dictionary sets the numerical scheme for the interpolation of values from grid points to cell faces. The `linear` scheme is chosen for this research. This option is used in almost all tutorial cases as well, except for the Direct Numerical Simulation (DNS) cases.
- `snGradSchemes`
This sub-dictionary sets the numerical scheme for the component of a gradient normal to a cell face (surface-normal schemes). The `corrected` scheme is used to maintain second order accuracy. It adds an explicit non-orthogonal correction to the orthogonal component of a variable.
- `fluxRequired`
This sub-dictionary sets the fields which require the generation of a flux.

D.2. PIMPLE algorithm

In this research the PIMPLE algorithm is used to solve the system of equations. As stated before, the PIMPLE algorithm is a combination of the SIMPLE and PISO algorithms. [Aguerrea et al. \(2013\)](#) described the PIMPLE algorithm, including a schematization of the solving loop of the algorithm, see [Figure D.6](#).

The SIMPLE (semi-implicit method for pressure-linked equations) algorithm solves steady-states problems. The treatment of the non-linear effects of the velocity is more important than the exact determination of the pressure. Each iteration of the SIMPLE algorithm is equivalent to a pseudo time step, so the properties are under-relaxed to stabilize the method and improve convergence.

The PISO (pressure-implicit split-operator) algorithm is used for performing transient simulations where the velocity-pressure coupling is fully solved for each time step. Small time steps, characterized by Courant numbers smaller than one, are used to reduce the non-linear effects of the velocity field.

The PIMPLE algorithm consists of an inner loop and an outer loop. For each time step, the PIMPLE algorithm goes through the following processes:

1. The outer loop is started.
2. Solve the continuity equation is solved and a solution for the momentum equation is predicted. A first estimate of the velocity field is calculated.
3. The total energy equation is solved. (optional)
4. The inner loop is started.
5. The pressure is solved and a correction is done on the momentum equation. The velocity field is recalculated.
6. The total energy equation is solved. (optional)
7. End of the inner loop. The inner loop is cycled a predefined number of times (`nCorrectors` in `fvSolution`).
8. End of the outer loop. The outer loop is also cycled a predefined number of times (`nOuterCorrectors` in `fvSolution`).
9. If the last time step is not reached yet, the next time step is started (start again at 1).

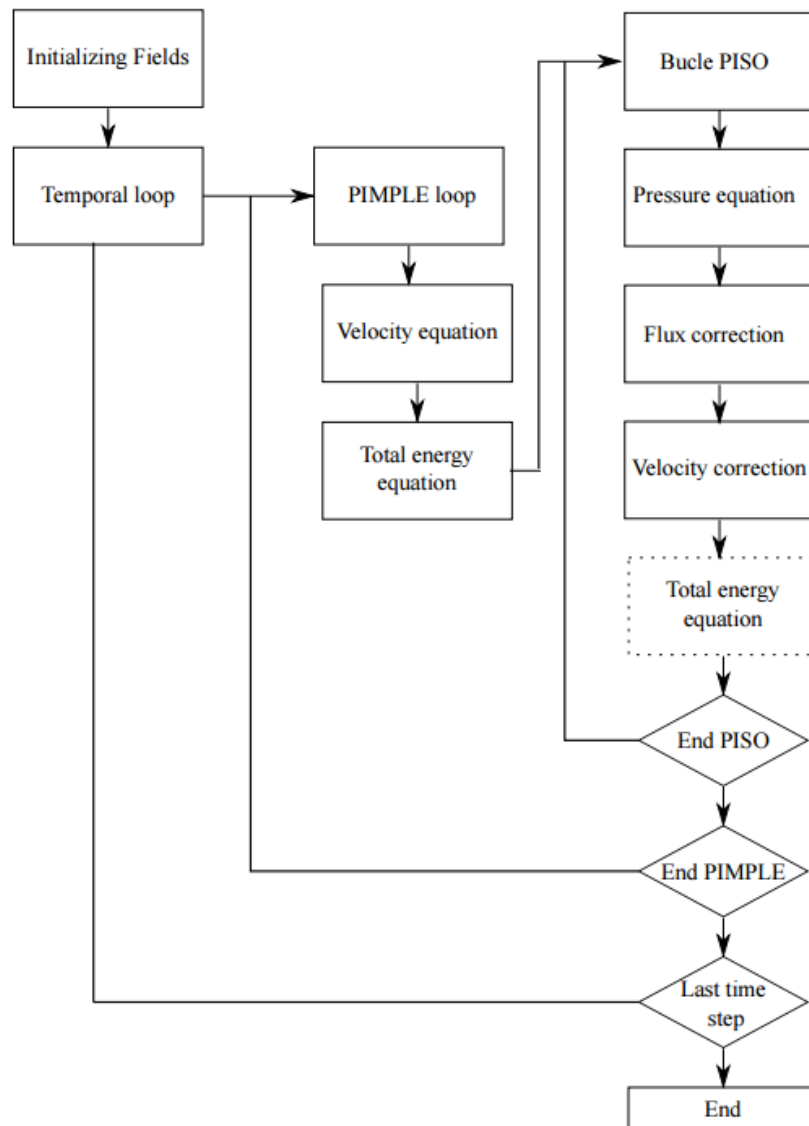


Figure D.6: Schematization of a loop of the PIMPLE algorithm in solving the equations (Aguerre et al., 2013).

Appendix E

Grid generation

In this appendix, the process of grid generation is explained. As an example, the grid of the two-dimensional model runs of the scour hole by [Van Zuylen \(2015\)](#) is used. The grid that is shown in the figures is not the actual grid that is used for the simulations, but a more coarse grid. This is done for plotting purposes.

E.1. blockMesh

Multiple meshing utilities are implemented in OpenFOAM. The most basic one is `blockMesh`, which is used to make the 'skeleton' of the grid. In `blockMesh` the domain is divided into different hexahedral blocks. The edges of the blocks can be shaped as straight lines, arcs and splines. The number of cells in all three directions is set, together with the grading. This is all specified in the dictionary `blockMeshDict`, which is located in the folder `constant/polyMesh/`, see [Appendix D](#). An example of a `blockMeshDict` file is shown in [Figure E.1](#). The different keywords in the `blockMeshDict` are explained here:

- `convertToMeters`
Factor to scale the vertex coordinates. In the `blockMeshDict` below the vertex coordinates are defined in meters.
- `vertices`
All vertices that the blocks in the mesh are composed of are specified here. Each block consists of 8 vertices, so at least 8 vertices have to be defined. The order of the vertices is not important.
- `blocks`
The blocks are defined in this section. First the vertices that are part of the block are named. After that the number of cells in x-, y- and z-direction are specified. The last three numbers are the grading of the cells in the different directions. When the grading is, for example, set to two, the first cell is twice as small as the last cell in that block.
- `edges`
By default the edges of the blocks are straight lines. In this case, the basic grid only needs straight lines, so therefore the edges section does not include anything.
- `patches`
In this section, the different boundaries are defined. Each boundary is defined separately. The four vertices that are inside the face of the block are listed. If a boundary consists of multiple blocks, all the faces have to be listed. The top patch in the `blockMeshDict` in [Figure E.1](#) is an example of this.
- `mergePatchPairs`
When using multiple blocks, some of the faces of different blocks have to be connected. When the blocks are defined by a set of vertices that is used in both blocks, the blocks are connected automatically. This section can therefore be left blank.

The `blockMeshDict` in Figure E.1 generates a grid similar to the one in Figure E.2. The only difference is the coarseness of the grid. The grid in the figure is made more coarse for plotting purposes. The different boundaries are added to the figure. It can be seen that the bottom consists of three different boundaries, while the top only has one single boundary. This is done because the sandy part of the bed has a different roughness than the surrounding plates.

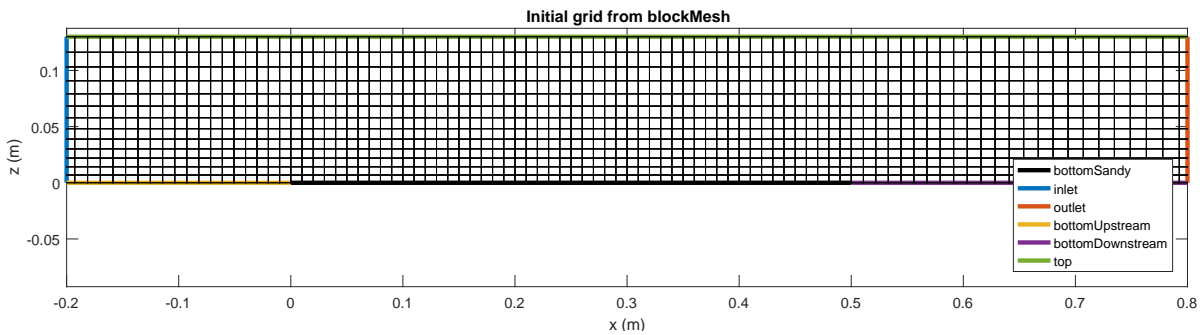


Figure E.2: Initial grid after using the `blockMesh` utility. The boundaries are added to the figure.

E.2. Deformation in Matlab

The next step in the grid generation process is the deformation of the grid in Matlab. At the location of the hole the grid is stretched, in order to include the scour hole in the model. Many methods exist to perform the grid stretching. For example, the cells can be stretched proportionally to the difference in height between the actual bed and the bottom in the initial grid. This is a simple process, but it invokes sudden changes in the orientation of the grid cells. This may lead to numerical instabilities. In order to prevent this, the grid is smoothed. The smoothing process is described below.

Smoothing of the grid

The process of the deforming and smoothing the grid is described with use of an example. Figure E.3 is a schematic representation of a part of the grid. The column of cells at location x_0 is deformed. The actual bed at this location is Δy_0 lower than the lowest cell of the grid. For the smoothing of the grid, the deformation of the neighboring cells (Δy^- and Δy^+) is also needed.

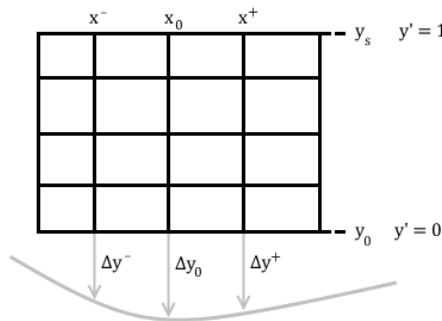


Figure E.3: Schematic representation of a part of the grid. The gray line is the actual bed level.

The first step is the scaling of the coordinates to values between 0 and 1, according to Equation (E.1). For the definition of the parameters, see Figure E.3.

$$y' = \frac{y - y_0}{y_s - y_0} \tag{E.1}$$

With the scaled values, the wait function and alpha function are calculated for each cell in the column of cells at x_0 . The functions are respectively shown in Equation (E.2) and E.3.

$$w = \min(1, \gamma \cdot y') \quad , \text{ where } \gamma > 0 \tag{E.2}$$

$$y_\alpha = \min(1, \alpha \cdot y') \quad , \text{ where } \alpha \geq 1 \tag{E.3}$$

The wait function determines to which extend the neighboring cells are taken into account. The alpha function determines from which height the cells should be deformed. The final deformation of each cell in the column is calculated with Equation (E.4).

$$\Delta y = (0.25w(\Delta y^- + \Delta y^+) + (1 - 0.5w)\Delta y_0)(1 - y_\alpha) \quad (\text{E.4})$$

When a three-dimensional grid is generated, all neighboring cells have to be taken into account. A slight adjustment of Equation (E.4) is needed, to include the columns in all four directions. This adjusted expression is shown in Equation (E.5).

$$\Delta y = (0.125w(\Delta y_{\text{left}} + \Delta y_{\text{right}} + \Delta y_{\text{upstream}} + \Delta y_{\text{downstream}}) + (1 - 0.5w)\Delta y_0)(1 - y_\alpha) \quad (\text{E.5})$$

E.3. Resulting grids

In this section, the resulting grids after the deformation and smoothing are presented. Also, the influence of the α and γ parameters is pointed out. Figure E.4 shows the grid with $\alpha = 1$ and $\gamma = 0$. In fact, this is the proportional stretching of the grid that is mentioned earlier. The effect of the two parameters is zero in this grid. No smoothing is performed, because of the 0 value for γ and all cells are deformed because $\alpha = 1$.

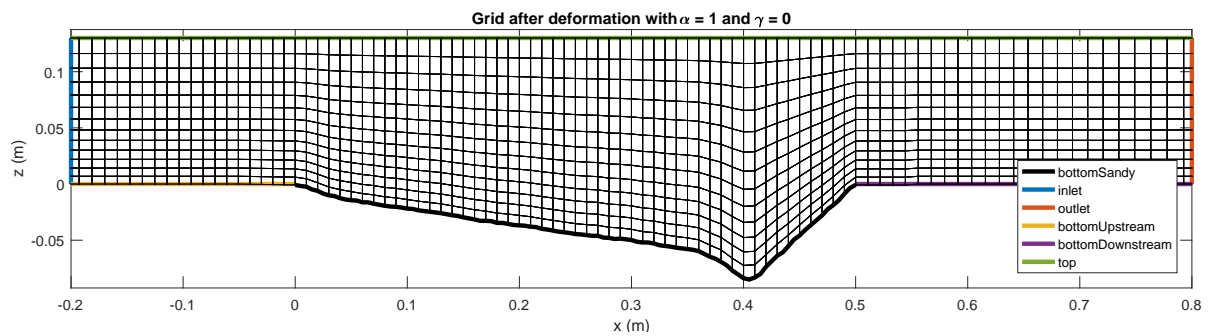


Figure E.4: Deformed grid with $\alpha = 1$ and $\gamma = 0$. The boundaries are added in the figure.

The grid in Figure E.5 is generated using $\alpha = 4$ and $\gamma = 0$. When comparing this grid to the one in Figure E.4, the effect of the α parameter can clearly be observed. For a value of 4 only the lowest quarter of the cells is deformed. The higher cells are kept at their positions. This results in more deformation for the lower cells when α is increased.

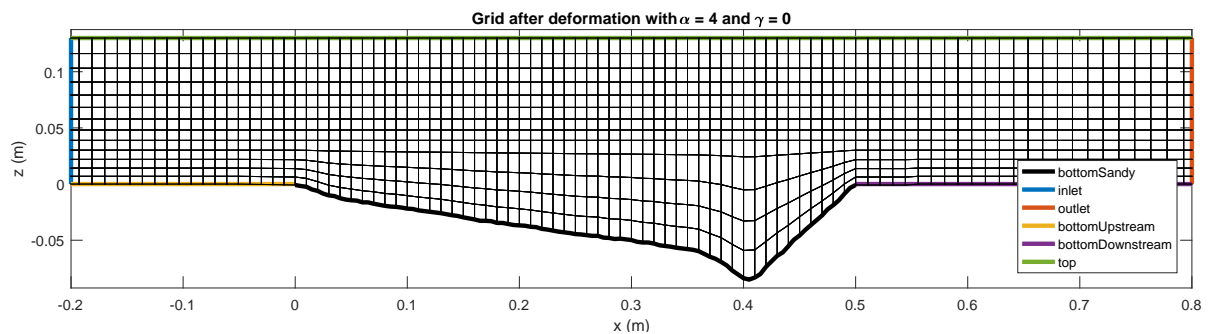


Figure E.5: Deformed grid with $\alpha = 4$ and $\gamma = 0$. The boundaries are added in the figure.

Figure E.6 shows a grid with $\alpha = 1$ and $\gamma = 5$. The effect of the smoothing can be seen when comparing this figure to Figure E.4. The differences are subtle, but especially near the edges of the scour hole and in the deepest part, the cells are smoothed

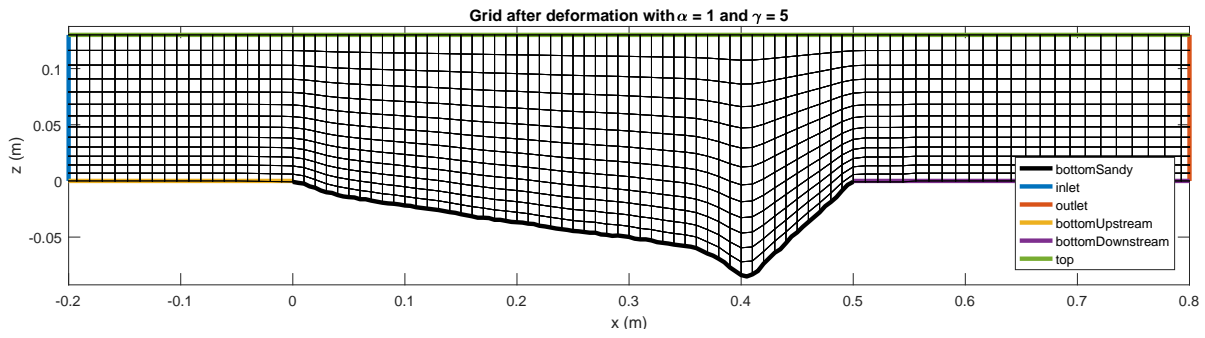


Figure E.6: Deformed grid with $\alpha = 1$ and $\gamma = 5$. The boundaries are added in the figure.

The last grid that is shown, is the grid that is used for the two-dimensional model simulations of the scour hole by Van Zuylen (2015) (as mentioned before, it is a coarser version of the grid for plotting purposes). Figure E.7 shows this grid. After some tweaking, the optimal values for the parameters are $\alpha = 1.2$ and $\gamma = 5$. The value for α results in only the upper row of cells staying at the same location (in the actual grid this is the upper few rows of cells). The smoothing parameter is kept to a value of 5, in order to have a sufficient level of smoothness in the grid. Making the value even larger does not influence the grid too much.

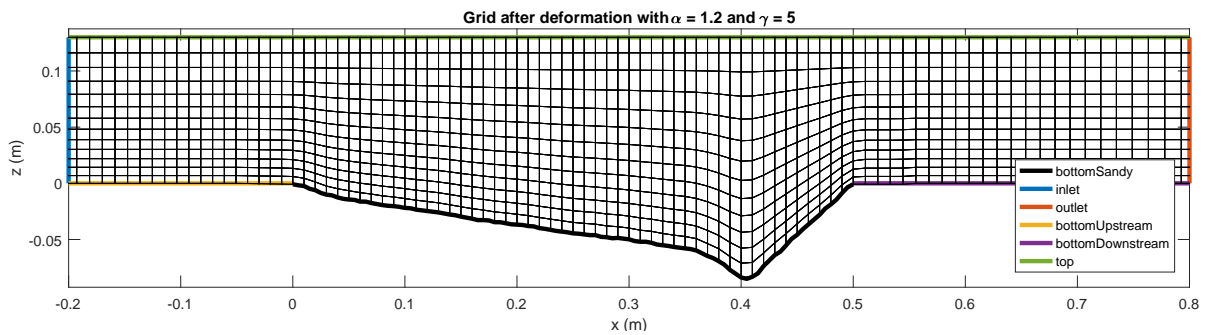


Figure E.7: Deformed grid with $\alpha = 1.2$ and $\gamma = 5$. The boundaries are added in the figure.

Appendix F

Cyclic modelling

This appendix describes the model setup and results of the cyclic case. The cyclic model is generated as a first OpenFoam model in this research. It is a very simple model of a flat bed, where only hydrodynamics are simulated. The simplicity makes the cyclic model a suitable model for the first acquaintance with OpenFoam. It is used to check the working of the turbulence model and the wall functions. A generalised wall function is available which should not have a grid size restriction. This function is not tested widely yet, so therefore it will be tested with the cyclic model. A convenience is the fact that this model can later be used as upstream boundary condition for other simulations, as the output of this model will be a fully developed velocity profile.

F.1. Model setup

In this section the model setup of the cyclic case is described.

F.1.1. Reference cases

For the validation of the model, two reference cases are used from the article by [Fuhrman et al. \(2010\)](#).

Table E1: Hydraulic conditions for the experiments in the reference cases of the cyclic case.

Article	Case	h (cm)	\bar{u} (cm/s)	Re (-)	Fr (-)	u_{\star} (m/s)	k_n (mm)	k_n^+ (-)
Fuhrman et al. (2010)	smooth	6.0	31.0	$1.9 \cdot 10^4$	0.40	0.016	-	-
Fuhrman et al. (2010)	rough	6.2	22.0	$1.4 \cdot 10^4$	0.28	0.021	9.9	208

F.1.2. Grid and boundary conditions

The model consists of a simple flat bed with a rectangular grid with a width of 25 cm and a height of 6 cm (see Figure E1). In this stage, the cyclic model will be used to get a feeling for the mesh sensitivity of the model. Therefore, the cell sizes varied for different runs. The flow in the model is directed from left to right.

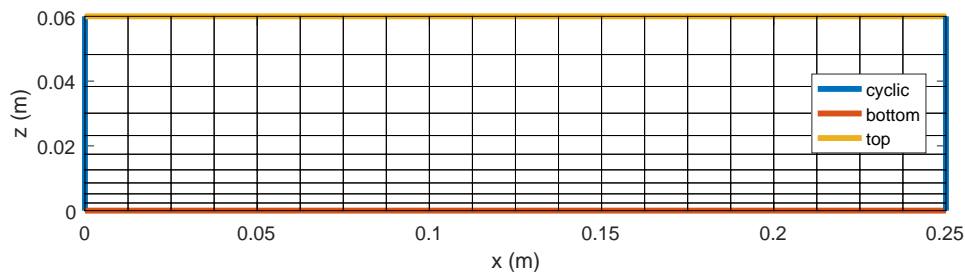


Figure E1: Example grid of the cyclic simulation with the different boundaries.

The principle of the cyclic case lies within the boundary conditions. A pressure difference between the left boundary and the right boundary is implemented. This difference is the driving force that induces a flow. The velocity profile that flows out at the downstream boundary is used as inflow at the upstream boundary in the next timestep. In that way, the model will reach an equilibrium state after a certain amount of timesteps. The principle is shown schematically in Figure E2. The pressure difference is implemented as a slope in pressure over the reach of the river, see Equation (E1). With the pressure difference, uniform flow conditions are reached after a certain amount of time.

$$i_p = \frac{\Delta p}{\lambda} \quad (\text{E1})$$

Where: i_p [m/s²] Pressure slope between inflow and outflow boundary of the cyclic model
 Δp [m²/s²] Pressure difference

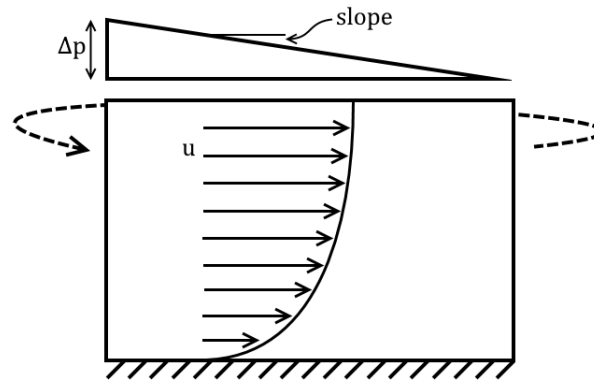


Figure E2: Principle of the cyclic case.

The pressure slope can be implemented in Equation (A.4) by substitution of the bed slope and the gravitational acceleration. The result is shown in Equation (E2). Using the equation, the cyclic boundary condition can be coupled to a certain value of the friction velocity.

$$i_p = \frac{u_*^2}{h} \quad (\text{E2})$$

The boundary conditions for the different boundaries of the model (see Figure F.1) are shown in Table E2. At the bottom, U is given a value of 0 m/s in all directions, which is the so called no-slip condition. At the surface the velocity has a slip boundary condition, in order to get a free surface. The slip boundary condition results in a wall shear stress equal to 0 N/m². A two-dimensional model is obtained by setting the front and back boundaries to empty. In this way they do influence on the flow in the domain.

Table E2: Boundary conditions cyclic model

Boundary	U	p	k	ω
cycl	cyclic	cyclicWaveBoundary slope = 0.0043	cyclic	cyclic
bottom	(0,0,0)	zeroGradient	zeroGradient	zeroGradient
top	slip	zeroGradient	zeroGradient	zeroGradient
back	empty	empty	empty	empty
front	empty	empty	empty	empty
Initial condition	(0,0,0)	0	1e-6	10

E.1.3. Turbulence model and wall functions

The turbulence model that is used in the model is the Generalised k - ω model by Wilcox (2006). This model is described in Section 3.2. The logarithmic wall function is used in the model. This wall function is described in Section A.1.6. Another available wall function, which is being developed by Niels Jacobsen from Deltares, has been looked into, but this function turned out to give unwanted results. Therefore, it is not further described in this research.

F.1.4. Bed roughness

Two types of bed roughness are modelled: a hydraulically smooth case and a hydraulically rough case. The smooth case has a k_n^+ value of 0 and the rough case has a k_n^+ value of approximately 208, see Equation (A.27).

F.2. Results

Runs are done with different sizes of the grid cells. Because of this, the runs have different y^+ -values for the first grid cell, see Equation (A.21). The values range from the viscous sub-layer to the fully turbulent layer. In this section, the results for both the smooth and the rough case are presented.

F.2.1. Smooth

Figure E3 compares the velocity profile from the different model runs with the theoretical velocity profile (see section A.1.6) and measurements by Fuhrman et al. (2010). The errors are calculated by taking the difference between the model result and the measurements and dividing it by the value of the measurement. The errors indicated in the legend are the mean values of all errors in one profile.

It can be seen that when the first cell is located in the viscous sub-layer or the buffer layer ($y^+ < 30$), the model is not performing well. The flow velocity is underestimated by these predictions. When the first cell reaches to the fully turbulent layer ($y^+ > 30$), the model is doing better. The measured values are predicted very accurately for these simulations, with a maximum error of 1.7%.

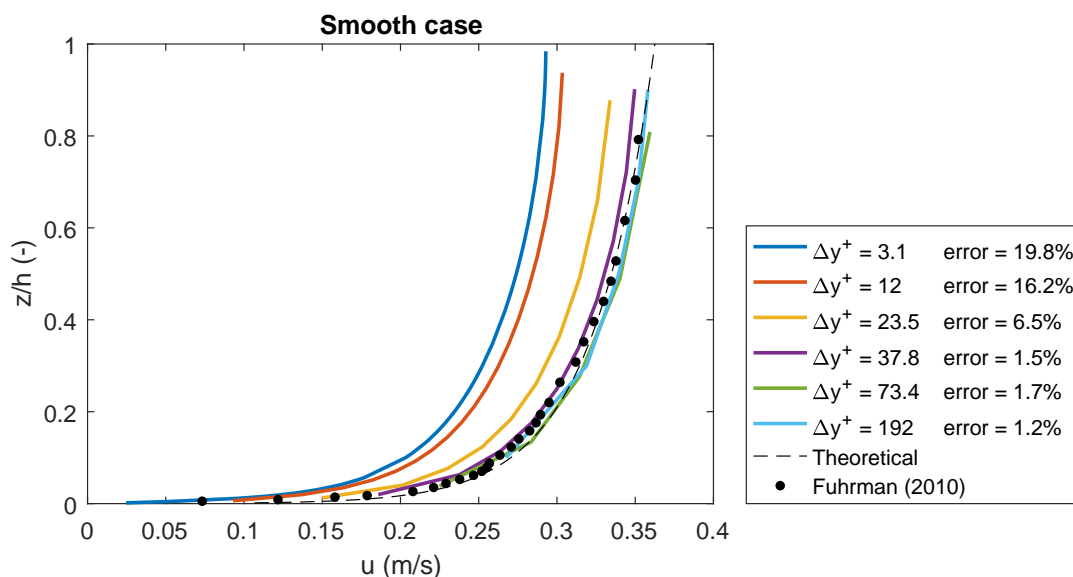


Figure E3: Comparison of measurements from Fuhrman et al. (2010) and model results for the smooth case. The error is calculated for each simulation with reference to the measurements.

F.2.2. Rough

The results in the case of a rough bed can be seen in Figure E4. The theoretical line deviates from the model results and measurements by Fuhrman et al. (2010). The model results for grids with the a value of $y/k_n > 0.2$ are predicting the velocity profile well. Even the simulation with a value of 0.10 has results with an error under 10%.

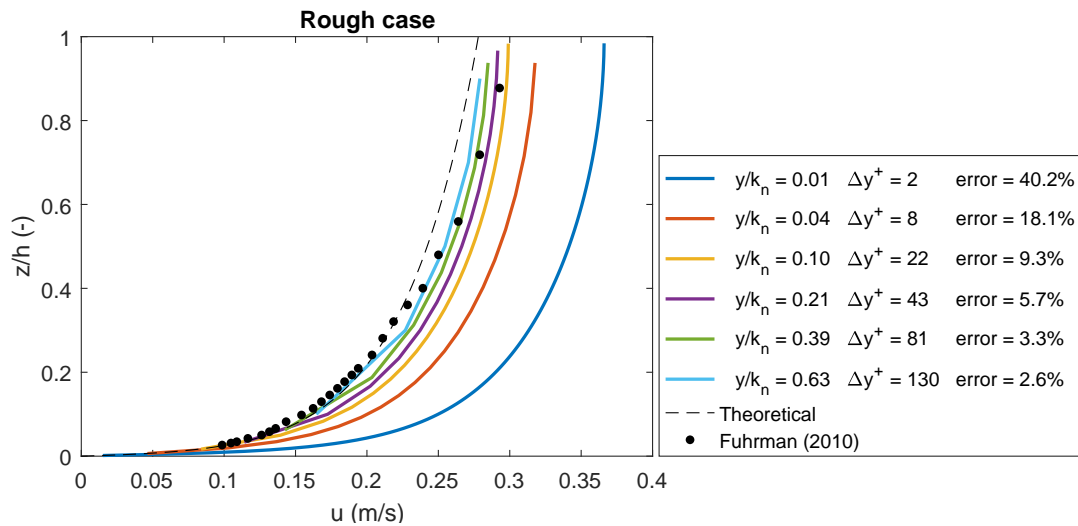


Figure E4: Comparison of measurements from Fuhrman et al. (2010) and model results for the rough case. The error is calculated for each simulation with reference to the measurements.

F2.3. Aspect ratio

During the modelling of the cyclic case, the aspect ratio between the horizontal and vertical cell size is investigated. Aspect ratios up to 65 at the first grid cell are used. All the simulations showed the same results, so it can be concluded that up to 65, the aspect ratio does not play a role.

F.3. Conclusion

The results of the investigation on grid sensitivity of the cyclic model confirmed the guidelines found in literature. Especially the smooth model shows accurate results when the first grid cell at the bottom reaches into the fully turbulent layer ($y^+ > 30$). When smaller grid cell heights are used, the model results deviate significantly from the measured values, with errors exceeding 6.5%.

In the article by Fuhrman et al. (2010), the error is also investigated. According to this research, the results of the model simulations are satisfying when the error is in the order of single percentages. When following this approach, the results of the smooth case are satisfying.

The results of the rough case are deviating further from the measured values. Clearly, a (very) rough bed brings extra difficulties in modelling the situation. The velocity profiles of the model simulations have a different shape, when compared to the measurements and the theoretical profile. The model results are approaching the measurements when the first cell center of the grid is larger than 0.2 times the roughness height, with a maximum error of 5.7%.

The influence of the aspect ratio of the cells is also investigated. Up to values of 65, this parameter does not influence the model results.

In the next stages of the modelling process, the cyclic model is used to generate an equilibrium velocity profile that can be implemented at the upstream boundary. This reduces the computational time of a model significantly, as a large region between the upstream boundary and the area of interest is not needed. Normally, this area would be necessary in order to get an equilibrium velocity profile at the upstream end of the area of interest.

Appendix G

Additional information for Chapter 4

Chapter 4 includes a concise description of the model validation. This appendix gives complementary information to support this chapter. It is not a self-contained story.

G.1. Backward Facing Step Model

G.1.1. Grid and boundary conditions

From the cyclic case in Appendix F is concluded that the first grid cell should reach up into the fully turbulent layer, in order to get correct results. This condition holds specifically for equilibrium situations. Upstream of the BFS, the flow is in equilibrium. After the point of reattachment, the velocity profile slowly forms an equilibrium profile again. In the recirculation zone, the flow is far from equilibrium. Adverse pressure gradients are present and the flow is directed in negative streamwise direction. Model runs with the inclusion of the pressure gradients are performed, but the results did not change. Therefore, it is chosen to use the equilibrium wall function.

Simulations are done with different grid sizes in horizontal direction. In order to get a higher resolution in the recirculation zone, the grid resolution is increased in that region. Figure G.1 shows the grid for a simulation of the Nagakawa ST1 case. According to the model simulations with the cyclic model, the y^+ value should be kept above 30, in order to assure a good performance of the wall function. A value close to 30 is chosen, because this gives the highest possible resolution in the recirculation zone.

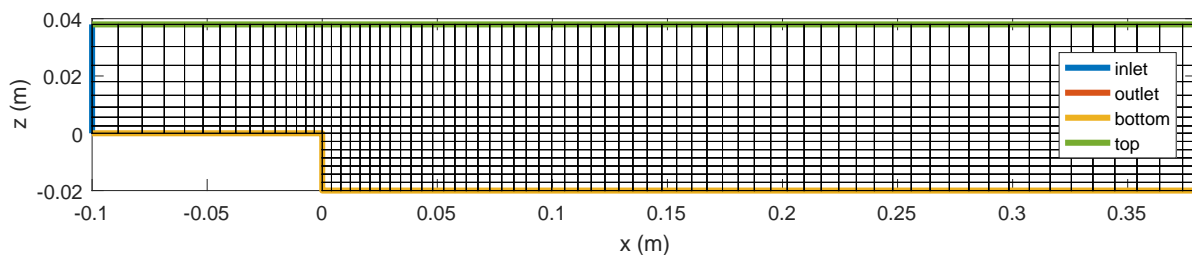


Figure G.1: Example grid of the BFS simulation with the different boundaries.

For each simulation an equilibrium velocity profile is generated, depending on the upstream conditions of the reference experiments. The profile is generated using the cyclic modelling case. This velocity profile is mapped onto the upstream boundary of the domain. The other boundary conditions that are used for the different cases are the same. Table G.1 shows the boundary conditions for the different parameters. It can be seen that the pressure is set to a value of 0 at the outlet boundary. The velocity is set to `zeroGradient`, which simply means that there is no gradient in the velocity in downstream direction. These boundary conditions at the outlet are chosen in order to get a free outflow boundary.

Table G.1: Boundary conditions of the BFS models.

Boundary	U	p	k	ω
inlet	cyclic profile	zeroGradient	zeroGradient	zeroGradient
outlet	zeroGradient	0	zeroGradient	zeroGradient
bottom	(0,0,0)	zeroGradient	zeroGradient	zeroGradient
top	slip	zeroGradient	zeroGradient	zeroGradient
back	empty	empty	empty	empty
front	empty	empty	empty	empty
Initial condition	(0,0,0)	0	1e-6	10

G.1.2. Model results

Definition of the recirculation zone

The recirculation zone in a BFS situation is bounded by the flow separation line. The line represents the height below which the net flow velocity is zero. Figure G.2 is a schematization of a BFS case. The velocity profiles (in grey) are included in the figure. The net flow velocity below the flow separation line is zero, because the green and red areas below line are equal. The figures in Chapter 4.1 include the flow separation line that is calculated with the model results.

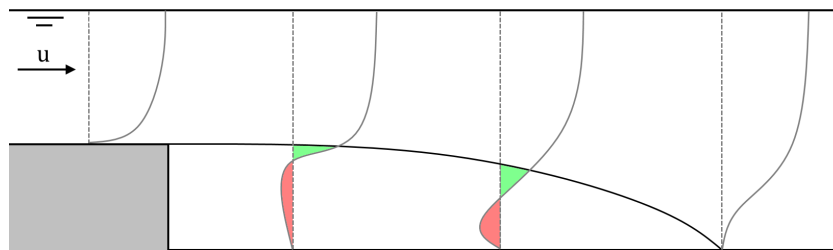


Figure G.2: Schematization of the flow separation line and the recirculation zone in a BFS case. The gray lines are flow velocity profiles in streamwise direction.

Presence of a corner eddy

Figure G.3 shows a zoom of the streamlines in the model results of the ST1 case. Close to the corner of the BFS a secondary eddy is formed. This eddy rotates in counter-clockwise direction, which is opposite to the clockwise rotation of the large eddy in the recirculation zone. Bradshaw and Wong (1972) included this eddy in their schematical representation of the behaviour of a BFS case, see Figure 2.3. The size of the corner eddy corresponds to the article, where the eddy size is between one third and half of the step size.

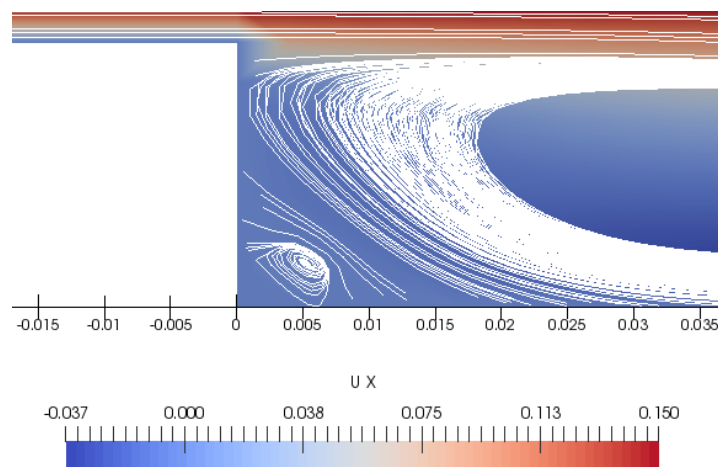


Figure G.3: Streamlines close to the step in the ST1 case, with a corner eddy clearly visible. The background colors indicate the streamwise component of the flow velocity.

G.1.3. Additional validation: analytical model

Besides the validation of the model results using measurements from experiments in other articles, the model can also be validated using an analytical model. By setting up a simple momentum balance between two cross sections in the flume, the accuracy of the model results can be checked. The left cross section is chosen at a very small distance downstream from the step. The right cross section is chosen further downstream from the step, where the water level is adapted to a new equilibrium. A schematization of the analytical model can be seen in Figure G.4a.

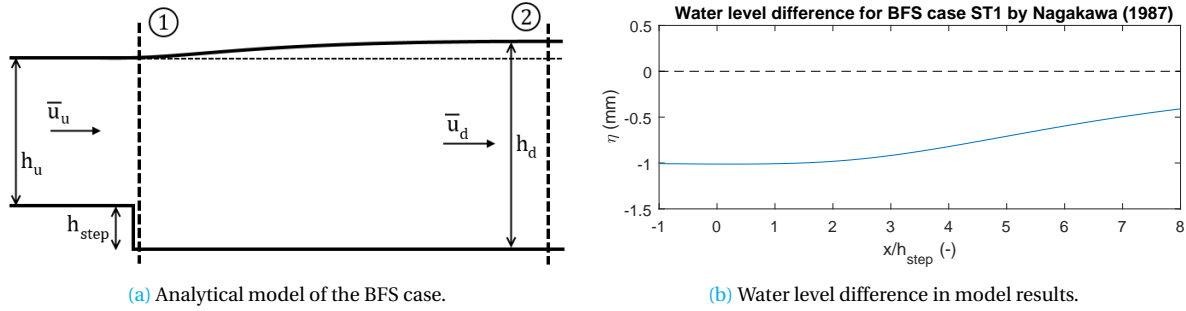


Figure G.4: Supporting images for the analytical model of the BFS cases.

The momentum in a cross section is calculated with Equation (G.1). For the two cross sections in Figure G.4a, this results in Equation (G.2).

$$F = \bar{u}^2 h + \frac{1}{2} g h^2 \quad (\text{G.1})$$

$$F_1 + F_2 = 0 \quad \rightarrow \quad \bar{u}_u^2 h_u + \frac{1}{2} g (h_u + d h)^2 = \bar{u}_d^2 h_d + \frac{1}{2} g h_d^2 \quad (\text{G.2})$$

Where:

F	$[\text{m}^3/\text{s}^2]$	Momentum
F_1	$[\text{m}^3/\text{s}^2]$	Momentum in cross section 1
F_2	$[\text{m}^3/\text{s}^2]$	Momentum in cross section 2
\bar{u}_u	$[\text{m}/\text{s}]$	Upstream mean flow velocity
h_u	$[\text{m}]$	Upstream water depth

In the model, the water surface is fixed. Using the pressure value in the highest cell, an adaptation of the water level can be made, which represents the free surface water level. This is shown in Figure G.4b for the ST1 case by Nagakawa and Nezu (1987). The values of the downstream average flow velocity and the downstream water depth are used to calculate the water level difference between the two cross sections, according to Equation (G.2). This is compared to the water level difference that the model results include. The error is calculated by taking the difference between the analytical value and the model result and dividing this by the analytical value. This error can be seen in Table G.2.

Table G.2: Analytical validation of the different BFS cases.

Article	Case	Analytical Δh (mm)	Model Δh (mm)	Error (%)
Nagakawa and Nezu (1987)	ST1	1.1961	1.0194	14.8
Nagakawa and Nezu (1987)	ST3	1.2562	1.0314	17.9
Ampadu-Mintah and Tachie (2015)	-	1.0434	0.7766	25.6

In general, the model is simulating the water level difference in a correct way. However, the difference in the simulations is always slightly smaller than the analytical value. The error lies between 14.8% and 25.6%. The approximation of the rigid lid at the top boundary of the model is partly responsible for this, as the approximation always introduces an error. The errors are acceptable, as the absolute difference between the analytical values and the model is in the order of 10^{-4} m.

G.2. Scour hole by Van Zuylen (2015)

G.2.1. Two-dimensional simulation

Grid and boundary conditions

The generation of the grid is based on the bed level measurements after 6 hours. This bed configuration was still evolving at this point, but unfortunately no more measurements were done after this time. In the process of generating the grid, the grid requirement with reference to the wall functions is taken into account. Because of the roughness elements on the steel plates, the conditions in the experiment are hydraulically rough. Therefore, the center of the first grid cell has a y/k_n -value of 0.28, which fulfils the requirement ($y/k_n > 0.2$). The grid cells are constant in width in the sandy part of the grid. In the vertical the grid cell size expands with a factor 2 between the bottom and the top cell. The total grid consists of 216 cells in streamwise direction, 26 cells in vertical direction and one cell in lateral direction. Therefore, the total amount of cells is 5616. The process of grid generation is described in Appendix E. The result can be seen in Figure G.5.

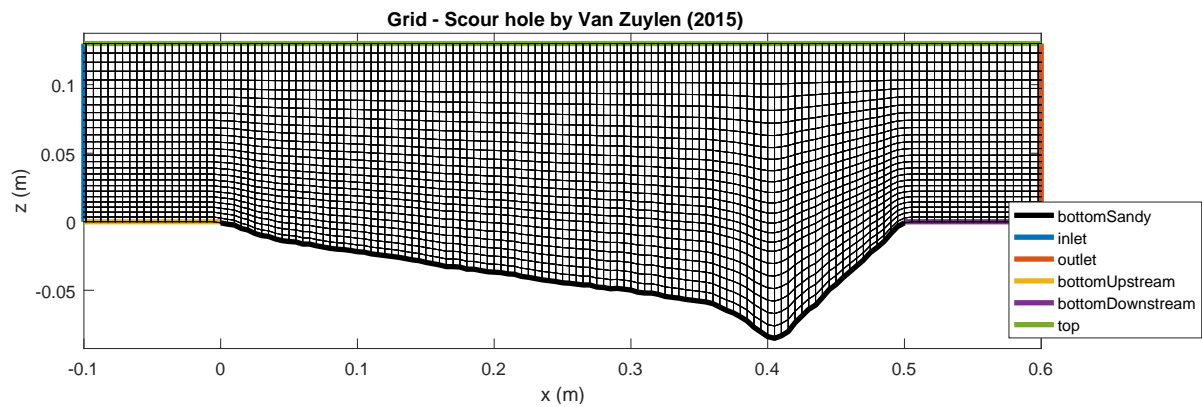


Figure G.5: Part of the grid for the simulation of run 17 by Van Zuylen (2015) with the different boundaries. In reality, the inlet and outlet boundaries are located further upstream and downstream.

For the simulation an equilibrium velocity profile is generated, using the cyclic modelling case. This velocity profile is mapped onto the upstream boundary of the domain. Table G.3 shows the boundary conditions and initial conditions for the different parameters in the simulation. It can be seen that the pressure is set to a value of 0 at the outlet boundary. The velocity is set to `zeroGradient`, which simply means that there is no gradient in the velocity at this boundary. The boundary conditions at the outlet are chosen in order to make a free outflow boundary. At the bed, the no-slip condition is applied (velocity of 0 m/s in all directions). The top boundary uses the slip condition for the velocity, in order to make a free surface. The slip boundary condition results in a wall shear stress equal to 0 N/m². All parameters of the back and the front boundaries are set to empty, resulting in a purely two-dimensional simulation.

Table G.3: Boundary conditions of the BFS model.

Boundary	U	p	k	ω
inlet	cyclic profile	zeroGradient	zeroGradient	zeroGradient
outlet	zeroGradient	0	zeroGradient	zeroGradient
bottomUpstream	(0,0,0)	zeroGradient	zeroGradient	zeroGradient
bottomSandy	(0,0,0)	zeroGradient	zeroGradient	zeroGradient
bottomDownstream	(0,0,0)	zeroGradient	zeroGradient	zeroGradient
top	slip	zeroGradient	zeroGradient	zeroGradient
back	empty	empty	empty	empty
front	empty	empty	empty	empty
Initial condition	(0,0,0)	0	1e-6	10

G.2.2. Three-dimensional simulation

The two-dimensional model is extended to a three-dimensional model by adding cells in the lateral direction. The bed is uniform in this direction. By simulating this case in a three-dimensional model, the influence of three-dimensional effects can be investigated. From the description of the two-dimensional model in Section 4.2 follows that three-dimensional effects might be the cause of differences between the experiments and the model simulation.

Grid and boundary conditions

The grid and boundary conditions of this simulation are the same as in the two-dimensional simulation in Section 4.2. In order to perform a three-dimensional simulation, the grid is extended in lateral direction. In the two-dimensional case, the grid consisted of only one cell in this direction. For the three-dimensional case 80 cells are chosen in the lateral direction. This makes the total amount of grid cells 449280.

The boundary conditions are exactly the same as the boundary conditions for the two-dimensional case (see Table G.3), except for the front and back boundaries. In order to get a two-dimensional simulation those boundary were set to empty. To make the simulation three-dimensional, the front and back boundaries are set to slip for the flow velocity and zeroGradient for the others.

Results

The results of the simulation are presented in this section. The velocity and turbulence intensity profiles are plotted in the same way as in Section 4.2. The plots are shown in Figure G.6a and G.6b.

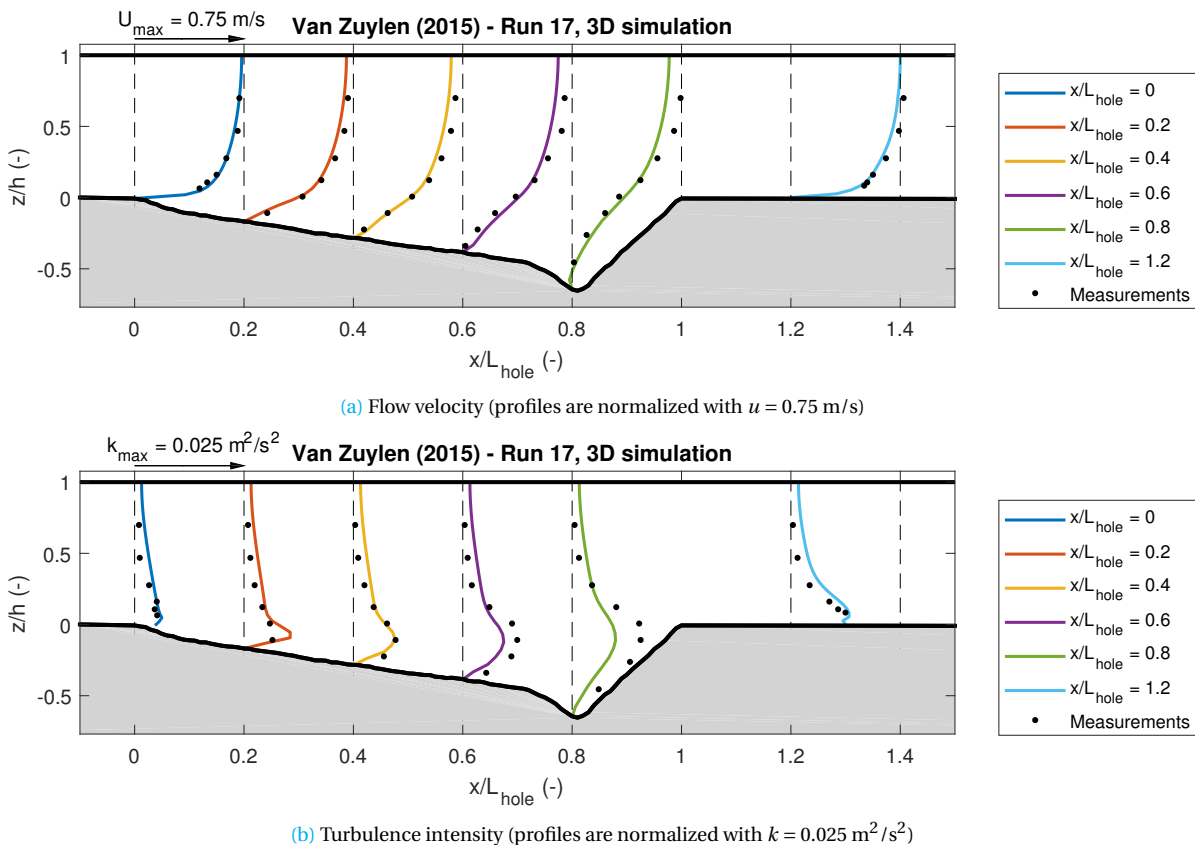


Figure G.6: Model results of the three-dimensional simulation and measurements of the Run 17 experiment by Van Zuylen (2015).

When visually observed, no differences can be seen when comparing the profiles to the two-dimensional simulation (Figures 4.6 and 4.8). The differences between the two simulations are further examined. Figure G.7 shows the difference between the two cases over depth, divided by the local value in the three dimensional simulation.

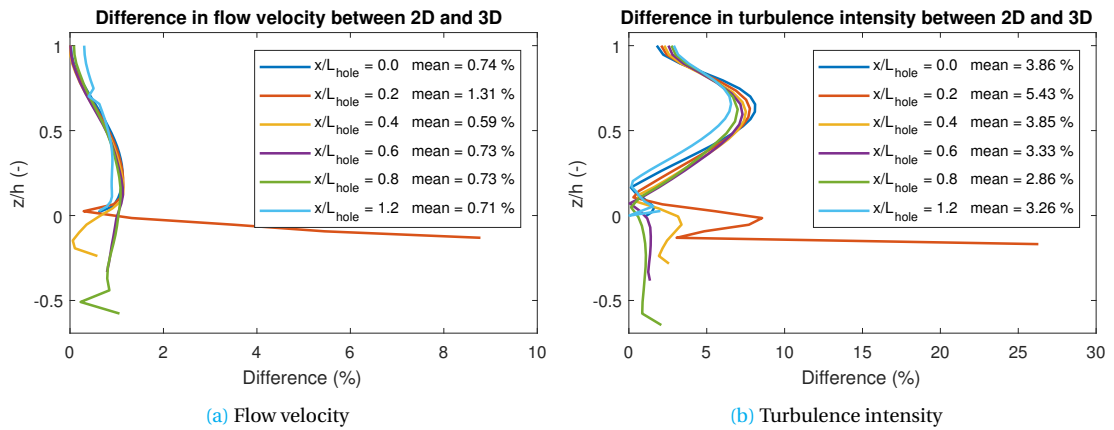


Figure G.7: Plots showing the difference between the two-dimensional and three-dimensional model simulations at different locations over depth. The difference between the simulations is divided by the local value of the three-dimensional simulation.

From the figures can be deduced that the mean difference in flow velocity is lower than the mean difference in turbulence intensity. In general, the differences between the simulations are small ($< 1\%$). However, the cross section at $x/L_{\text{hole}} = 0.2$ shows large differences, compared to the other locations. A possible cause for the differences between the two simulations are the three-dimensional effects. The magnitude of the three-dimensional effects is investigated by looking at motions in lateral direction.

Figures G.8 and G.9 show two plots of a cross section in the domain, one lateral and one vertical. Both plots include the three-dimensional effects in the area just downstream of the upstream edge of the hole (x/L_{hole} between 0 and 0.3). The three-dimensional effects in the model only influence this part of the domain. The velocity and turbulence intensity profiles at other locations are in good agreement with the two-dimensional case.

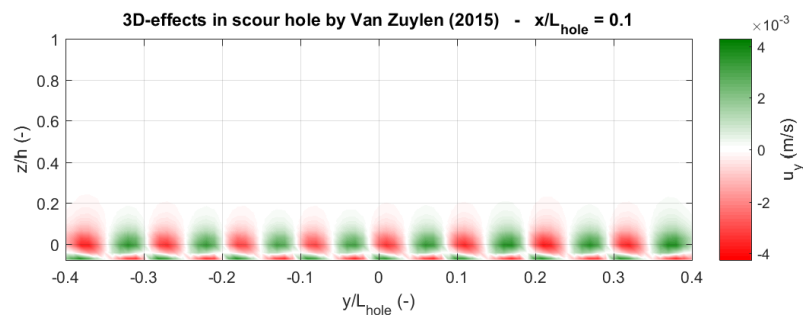


Figure G.8: Plot showing the three-dimensional effects in the model simulations. The flow velocity in lateral direction in a cross section at $x/L_{\text{hole}} = 0.1$ is shown.

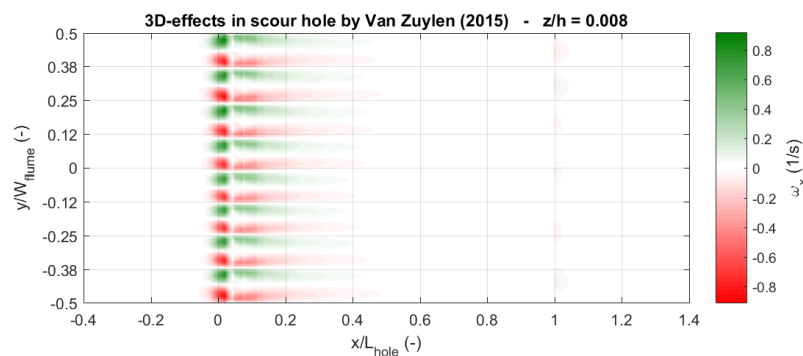


Figure G.9: Plot showing the three-dimensional effects in the model simulations. The vorticity in streamwise direction in a cross section at $z/h = 0.008$ is shown.

Figure G.8 shows the flow velocity in lateral direction. Several cells are found with flow velocity magnitudes of 0.003 m/s in lateral direction. Figure G.9 shows the vorticity in streamwise direction. This is a measure for the curl of the flow velocity, which is described in Section A.1.3.

The flow structures that are observed in the three-dimensional model are assumed to be so-called Görtler vortices, see Figure G.10. These vortices occur in boundary layers over concave surfaces. The surface in the model at the upstream side of the scour hole is concave-shaped and the vortices show large similarities to the Görtler vortices (De Souza et al., 2004).

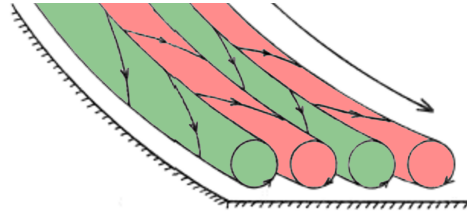


Figure G.10: Schematization of Görtler vortices (De Souza et al., 2004).

Appendix H

Errors in model validation

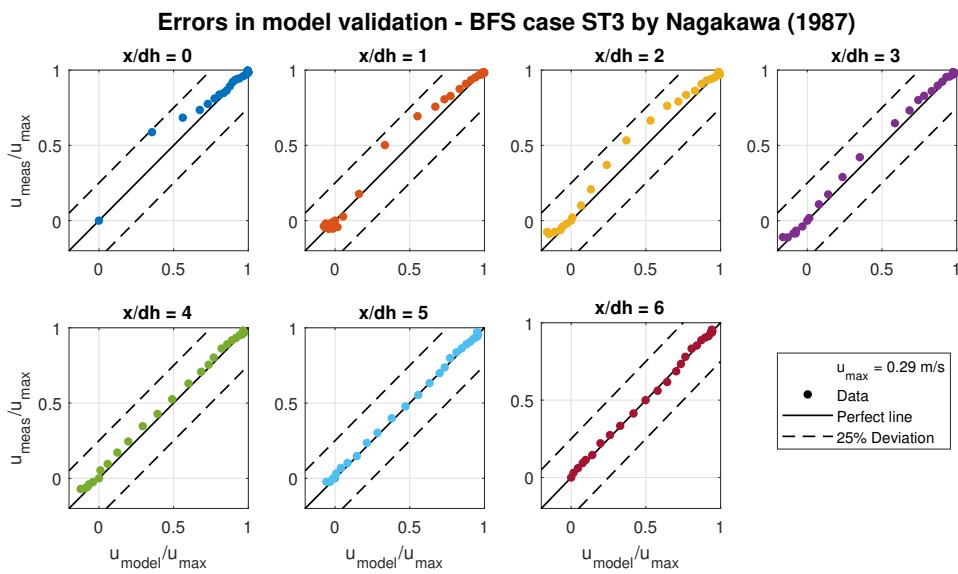


Figure H.1: Visualization of the relative errors in the model validation using the BFS case ST3 by [Nagakawa and Nezu \(1987\)](#). For each location the normalized measured flow velocity is plotted against the normalized modelled flow velocity. Perfect agreement is indicated by the black solid line. All points that are between the dotted black lines have a difference of less than 25% between the model result and measurement.

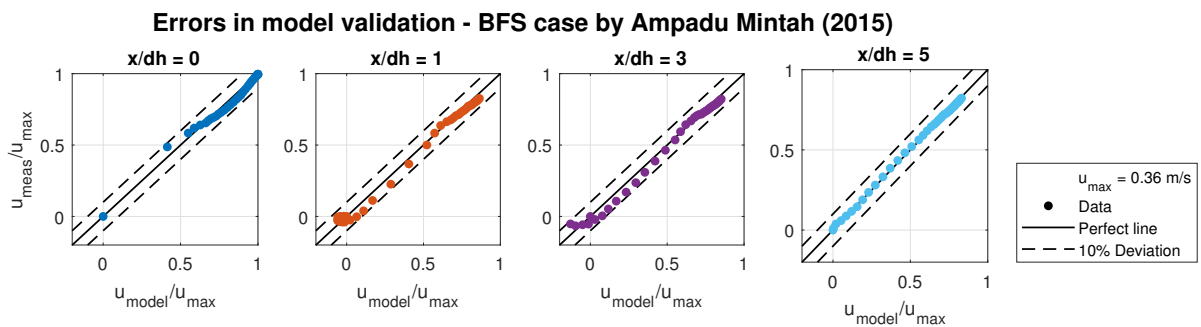


Figure H.2: Visualization of the relative errors in the model validation using the BFS case by [Ampadu-Mintah and Tachie \(2015\)](#). For each location the normalized measured flow velocity is plotted against the normalized modelled flow velocity. Perfect agreement is indicated by the black solid line. All points that are between the dotted black lines have a difference of less than 10% between the model result and measurement.

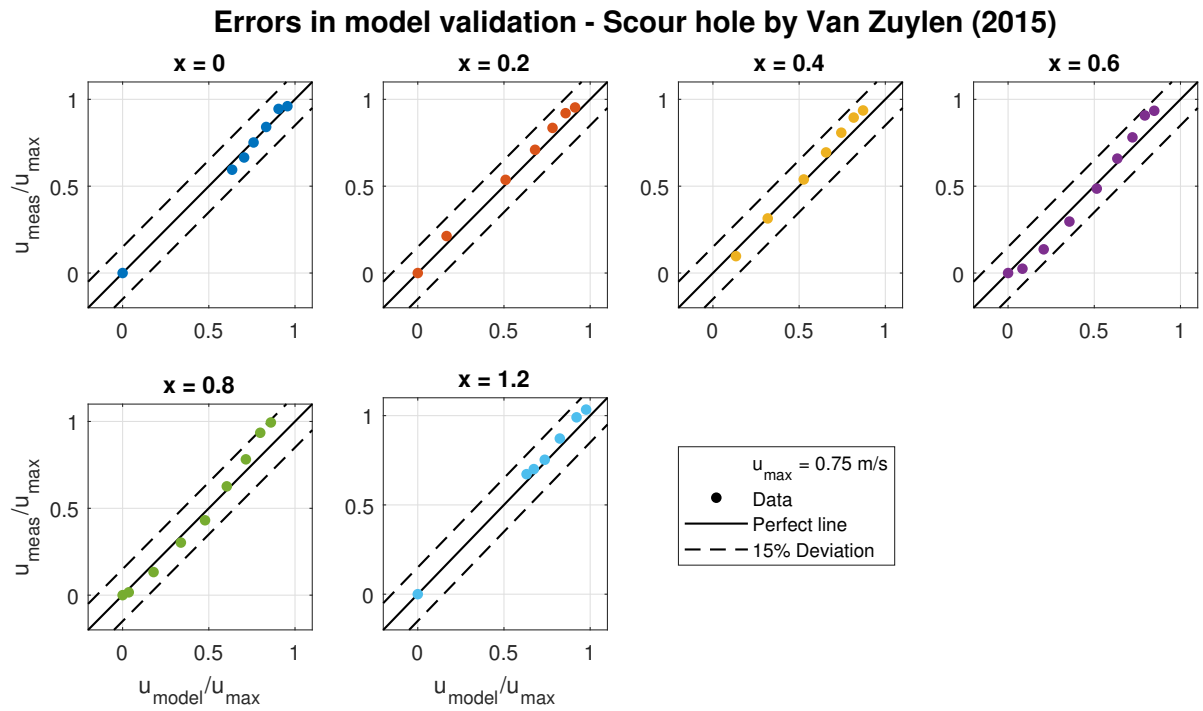


Figure H.3: Visualization of the relative errors in the model validation using the scouring case by Van Zuylen (2015). For each location the normalized measured flow velocity is plotted against the normalized modelled flow velocity. Perfect agreement is indicated by the black solid line. All points that are between the dotted black lines have a difference of less than 15% between the model result and measurement.

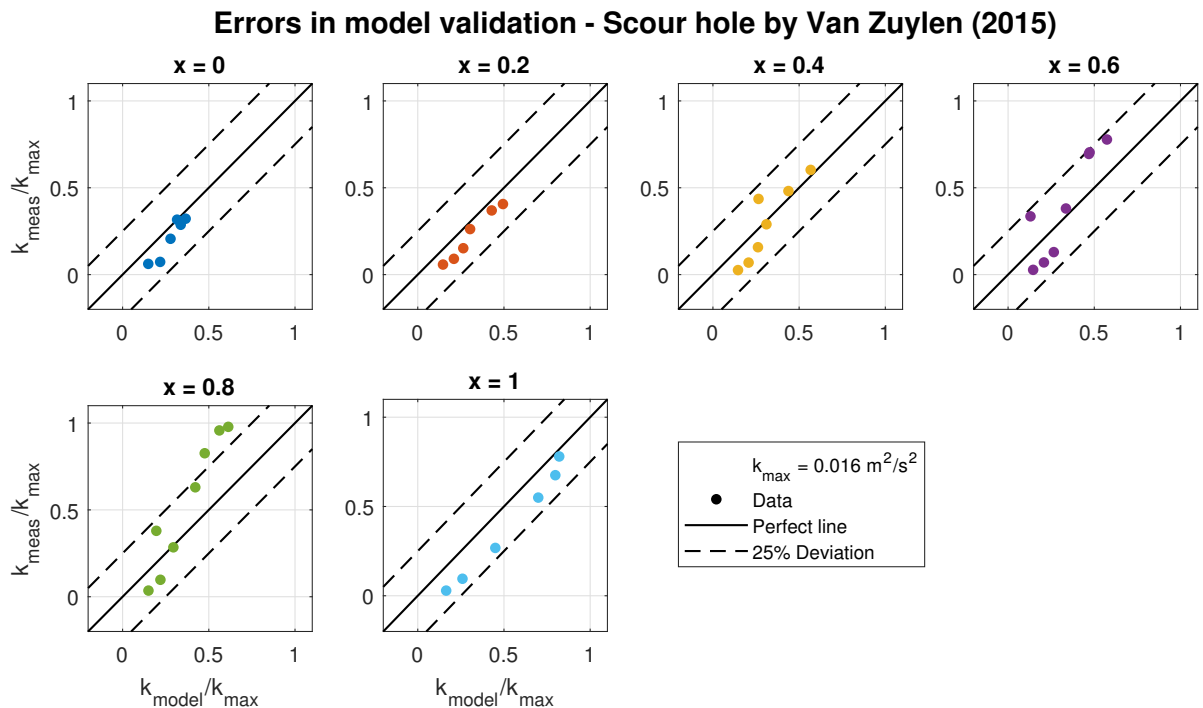


Figure H.4: Visualization of the relative errors in the model validation using the scouring case by Van Zuylen (2015). For each location the normalized measured turbulence intensity is plotted against the normalized modelled turbulence intensity. Perfect agreement is indicated by the black solid line. All points that are between the dotted black lines have a difference of less than 25% between the model result and measurement.

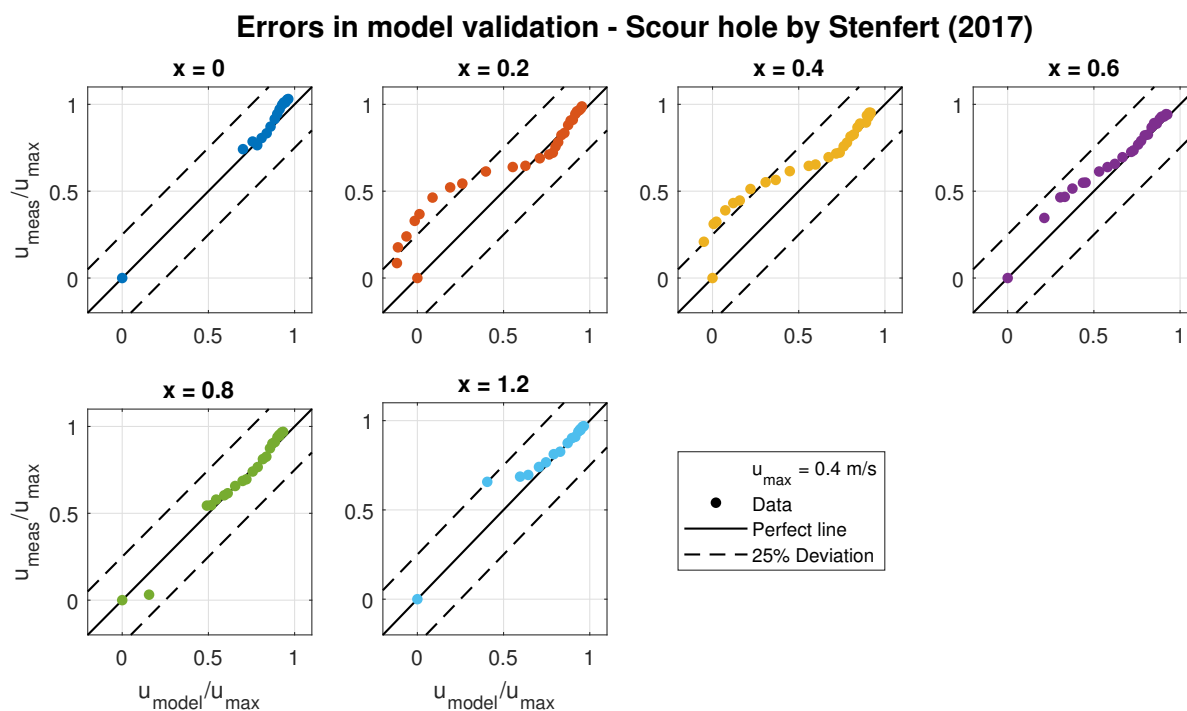


Figure H.5: Visualization of the relative errors in the model validation using the scouring case by Stenfert (2017). For each location the normalized measured flow velocity is plotted against the normalized modelled flow velocity. Perfect agreement is indicated by the black solid line. All points that are between the dotted black lines have a difference of less than 25% between the model result and measurement.

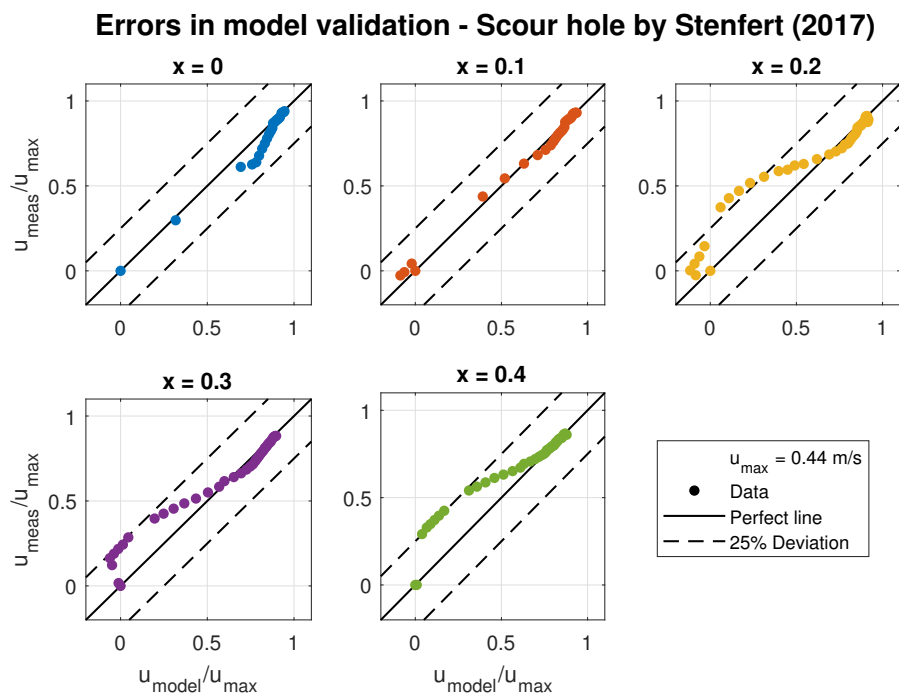


Figure H.6: Visualization of the relative errors in the model validation using the scouring case of the larger hole by Stenfert (2017). For each location the normalized measured flow velocity is plotted against the normalized modelled flow velocity. Perfect agreement is indicated by the black solid line. All points that are between the dotted black lines have a difference of less than 25% between the model result and measurement.

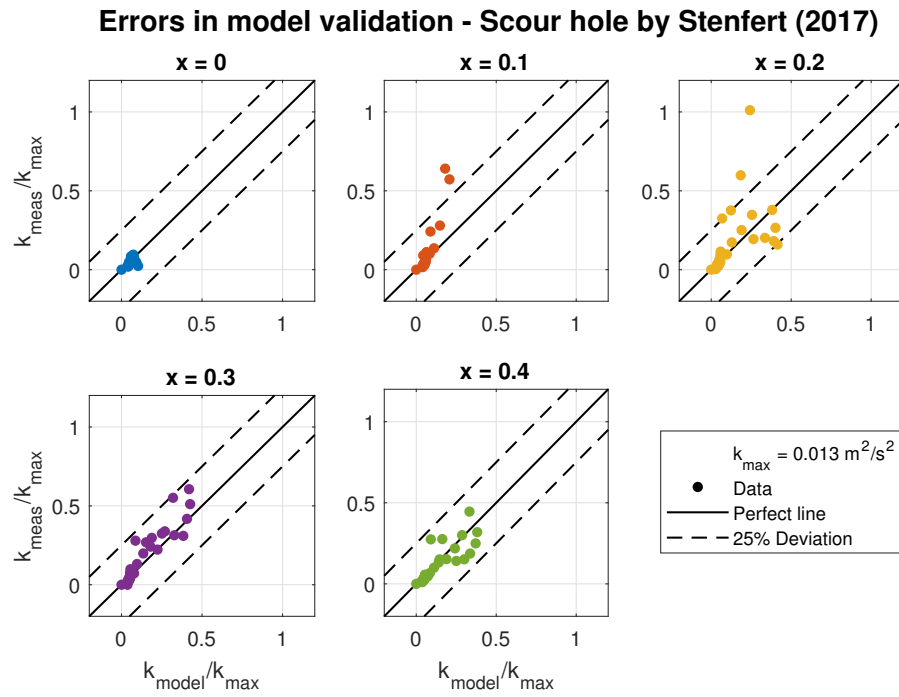


Figure H.7: Visualization of the relative errors in the model validation using the scouring case of the larger hole by Stenfert (2017). For each location the normalized measured turbulence intensity is plotted against the normalized modelled turbulence intensity. Perfect agreement is indicated by the black solid line. All points that are between the dotted black lines have a difference of less than 25% between the model result and measurement.

Appendix I

Additional figures for Chapter 5

I.1. Bed shear stress and sediment transport

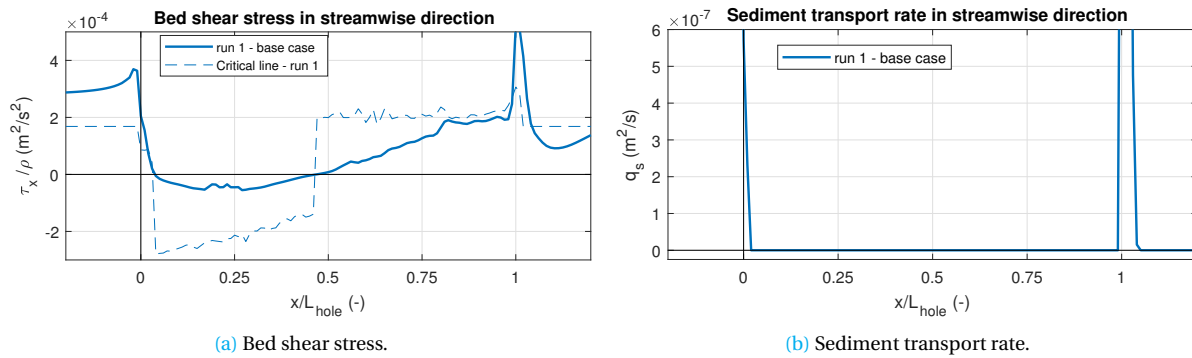


Figure I.1: Plots showing the bed shear stress and sediment transport rate in the central axis in streamwise direction. The critical value of the bed shear stress is calculated using Equation (2.3) and the adaptations for a slope in Section 2.3.2.

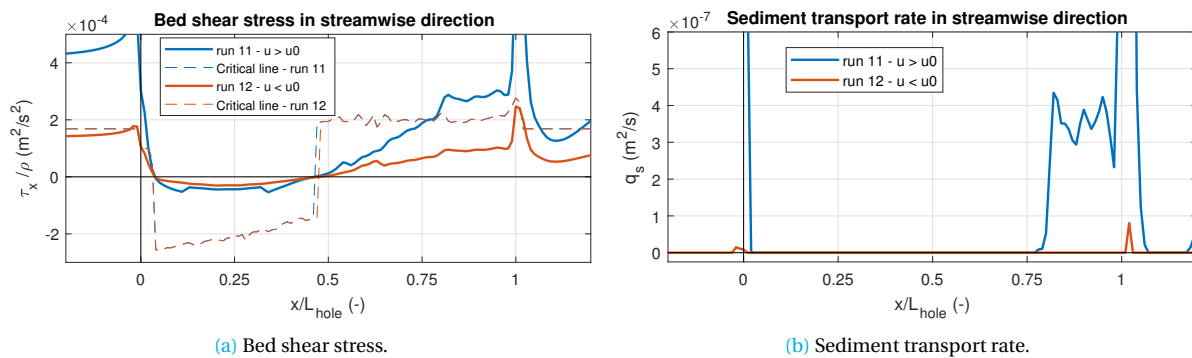


Figure I.2: Plots showing the bed shear stress and sediment transport rate in the central axis in streamwise direction. The critical value of the bed shear stress is calculated using Equation (2.3) and the adaptations for a slope in Section 2.3.2.

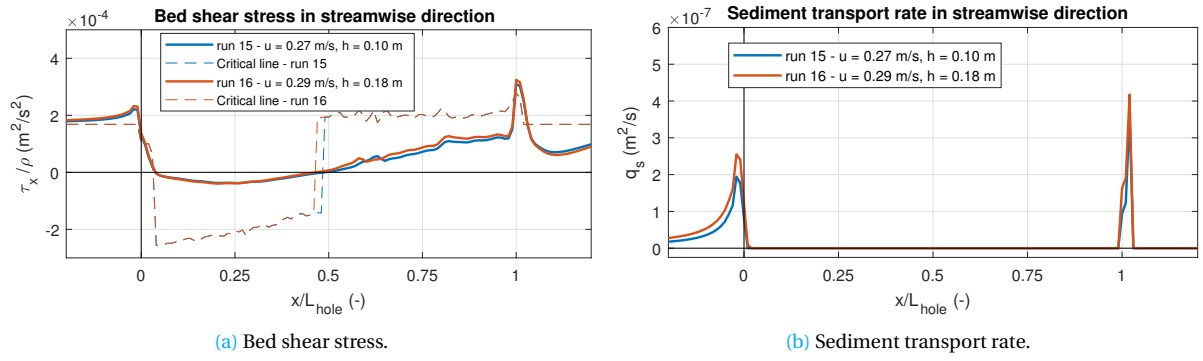


Figure I.3: Plots showing the bed shear stress and sediment transport rate in the central axis in streamwise direction. The critical value of the bed shear stress is calculated using Equation (2.3) and the adaptations for a slope in Section 2.3.2.

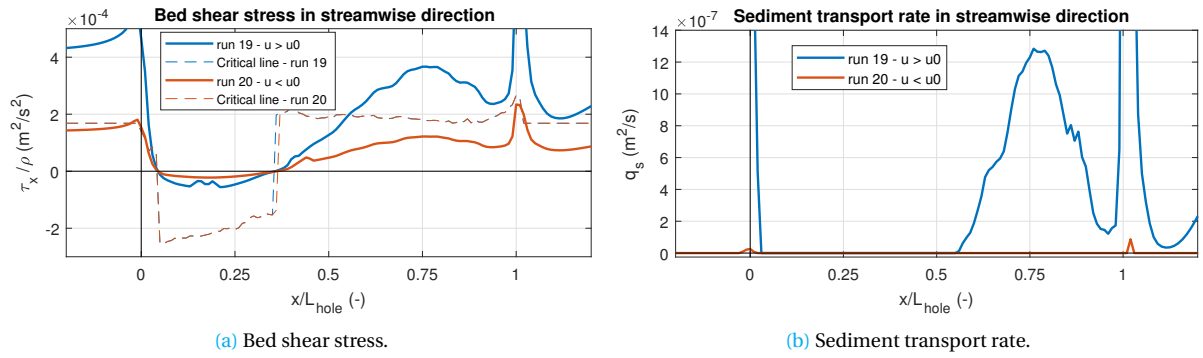


Figure I.4: Plots showing the bed shear stress and sediment transport rate in the central axis in streamwise direction. The critical value of the bed shear stress is calculated using Equation (2.3) and the adaptations for a slope in Section 2.3.2.

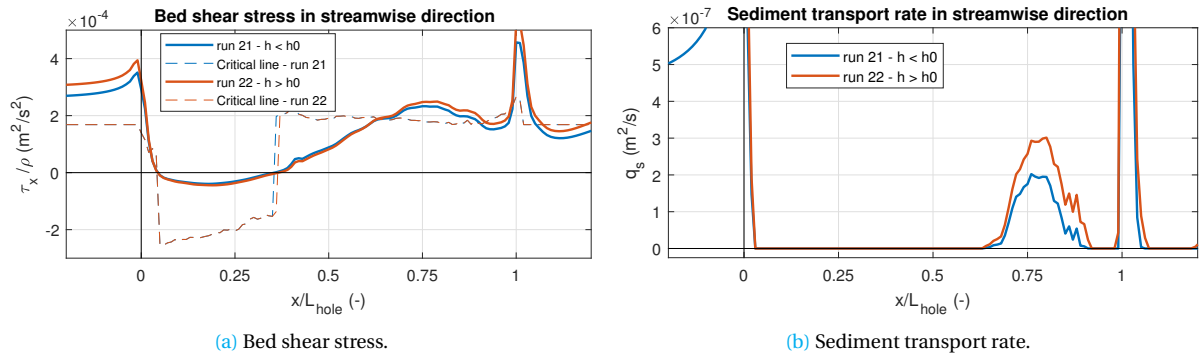


Figure I.5: Plots showing the bed shear stress and sediment transport rate in the central axis in streamwise direction. The critical value of the bed shear stress is calculated using Equation (2.3) and the adaptations for a slope in Section 2.3.2.

I.2. Flow structures

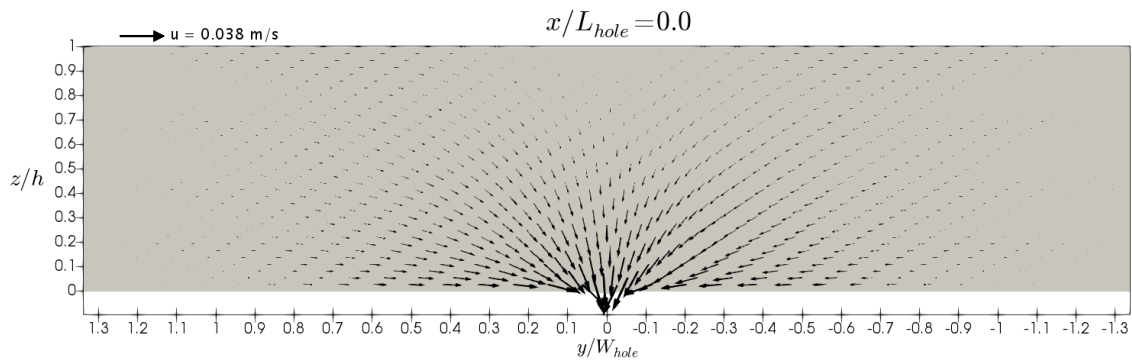


Figure 1.6: Cross section normal to the streamwise direction at $x/L_{hole} = 0.0$. The vectors are generated using the lateral and vertical flow velocity. The scale of the vectors is shown in the top left corner.

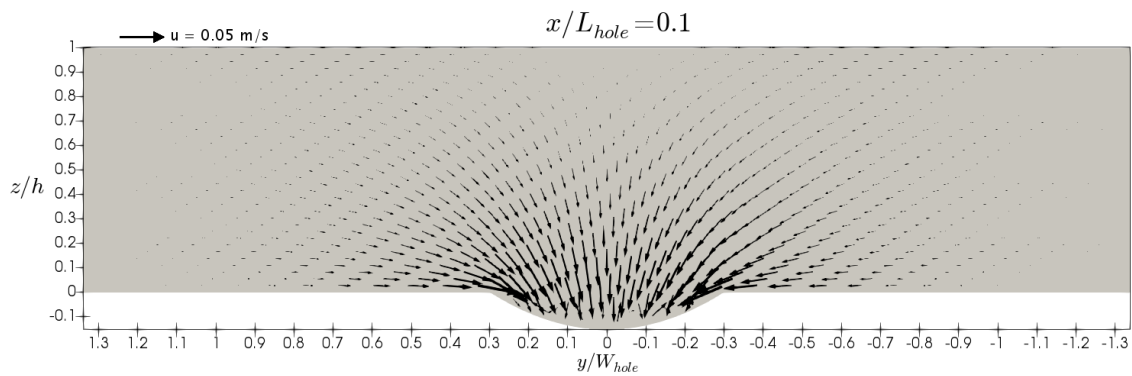


Figure 1.7: Cross section normal to the streamwise direction at $x/L_{hole} = 0.1$. The vectors are generated using the lateral and vertical flow velocity. The scale of the vectors is shown in the top left corner.

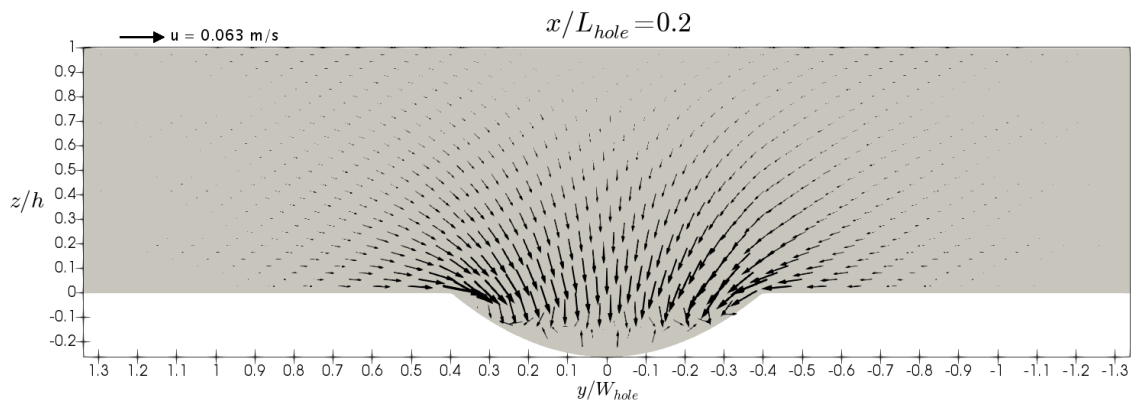


Figure 1.8: Cross section normal to the streamwise direction at $x/L_{hole} = 0.2$. The vectors are generated using the lateral and vertical flow velocity. The scale of the vectors is shown in the top left corner.

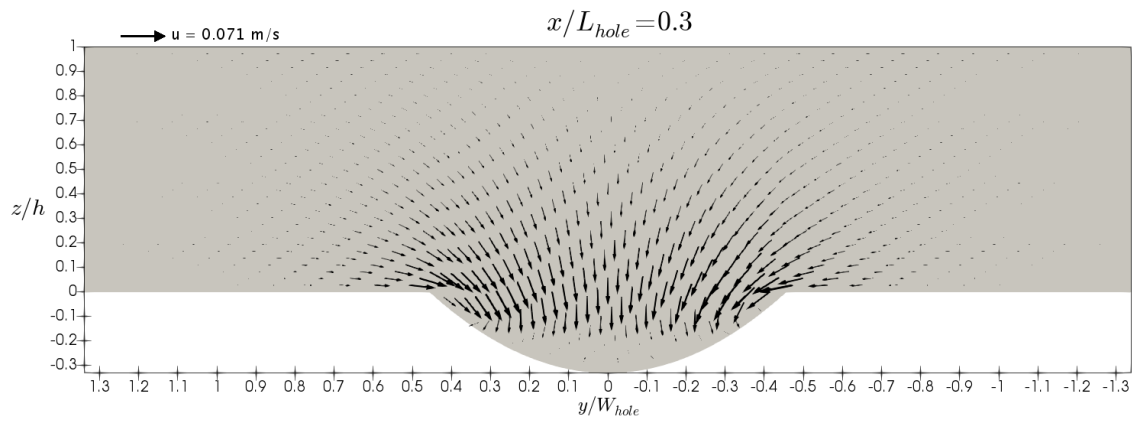


Figure 1.9: Cross section normal to the streamwise direction at $x/L_{hole} = 0.3$. The vectors are generated using the lateral and vertical flow velocity. The scale of the vectors is shown in the top left corner.

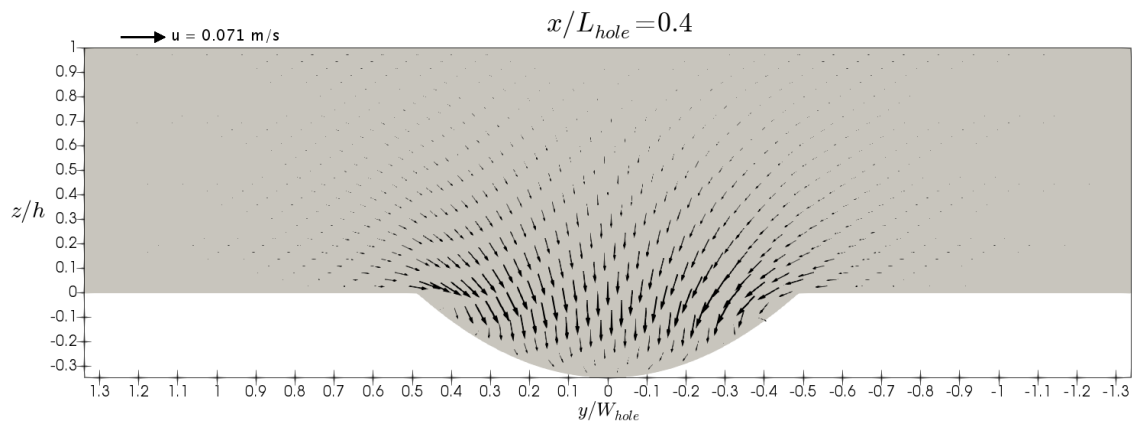


Figure 1.10: Cross section normal to the streamwise direction at $x/L_{hole} = 0.4$. The vectors are generated using the lateral and vertical flow velocity. The scale of the vectors is shown in the top left corner.

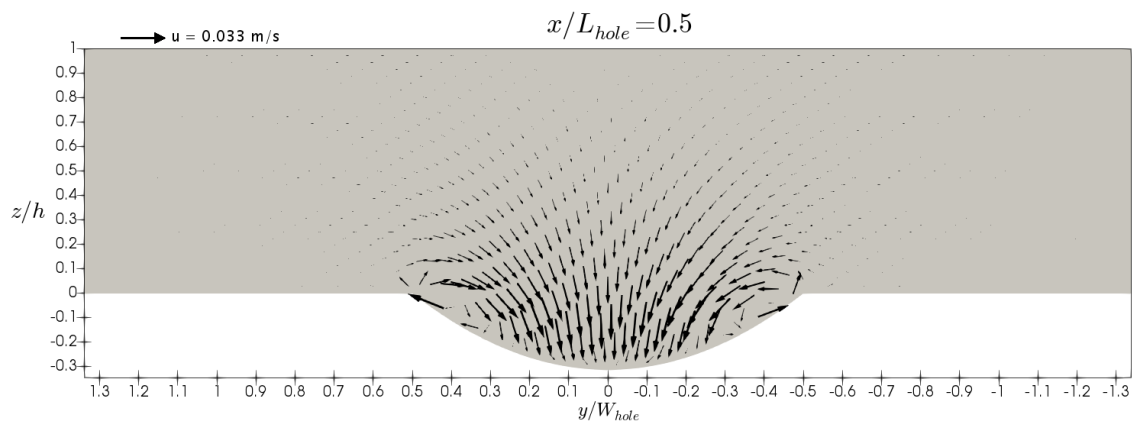


Figure 1.11: Cross section normal to the streamwise direction at $x/L_{hole} = 0.5$. The vectors are generated using the lateral and vertical flow velocity. The scale of the vectors is shown in the top left corner.

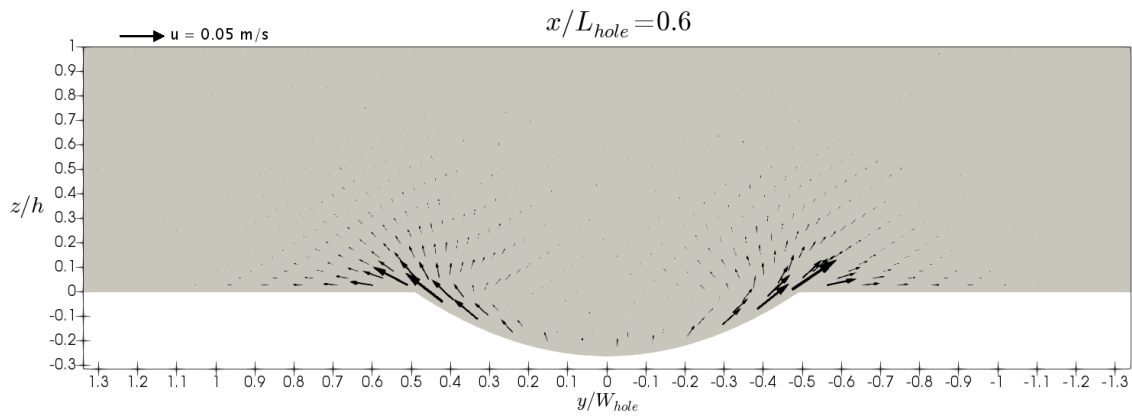


Figure I.12: Cross section normal to the streamwise direction at $x/L_{hole} = 0.6$. The vectors are generated using the lateral and vertical flow velocity. The scale of the vectors is shown in the top left corner.

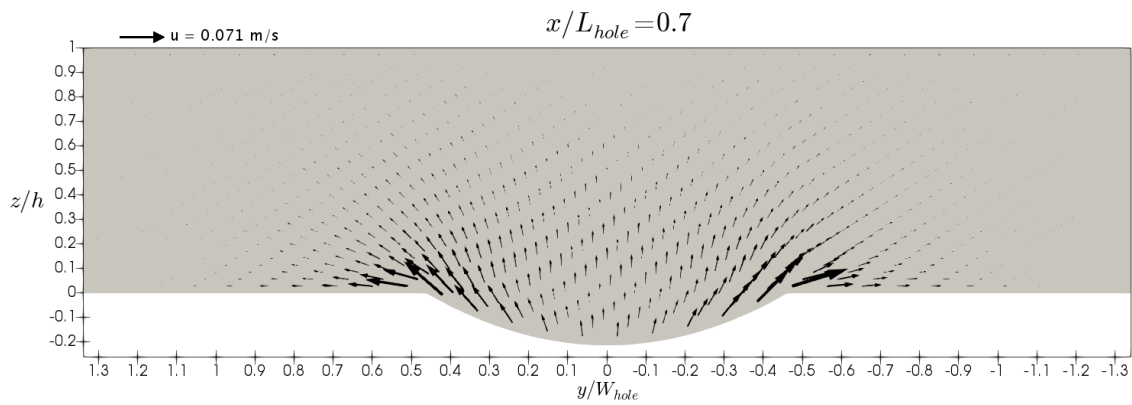


Figure I.13: Cross section normal to the streamwise direction at $x/L_{hole} = 0.7$. The vectors are generated using the lateral and vertical flow velocity. The scale of the vectors is shown in the top left corner.

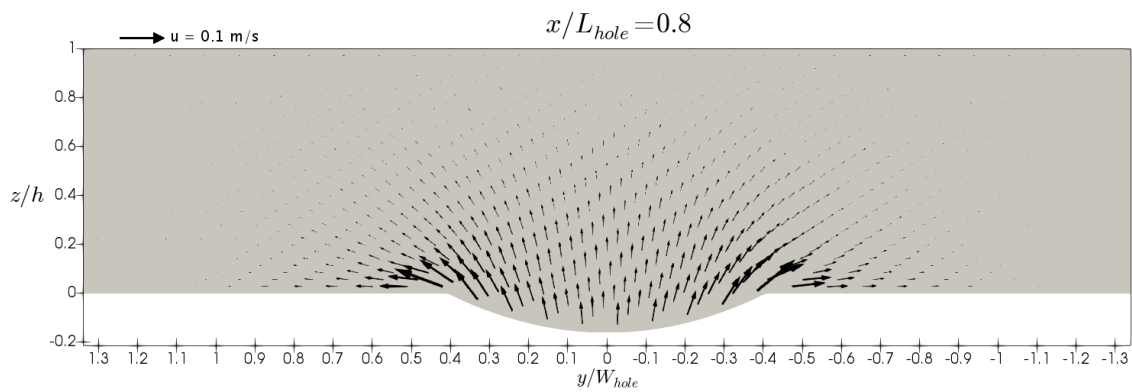


Figure I.14: Cross section normal to the streamwise direction at $x/L_{hole} = 0.8$. The vectors are generated using the lateral and vertical flow velocity. The scale of the vectors is shown in the top left corner.

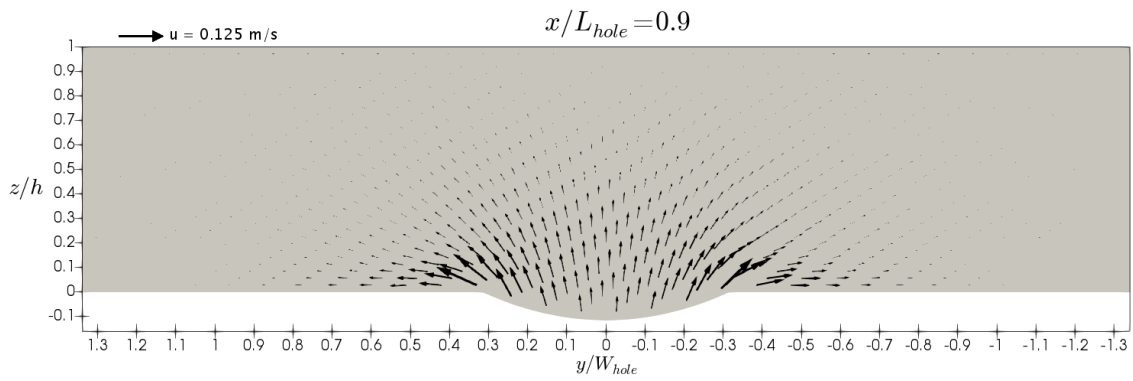


Figure 1.15: Cross section normal to the streamwise direction at $x/L_{hole} = 0.9$. The vectors are generated using the lateral and vertical flow velocity. The scale of the vectors is shown in the top left corner.

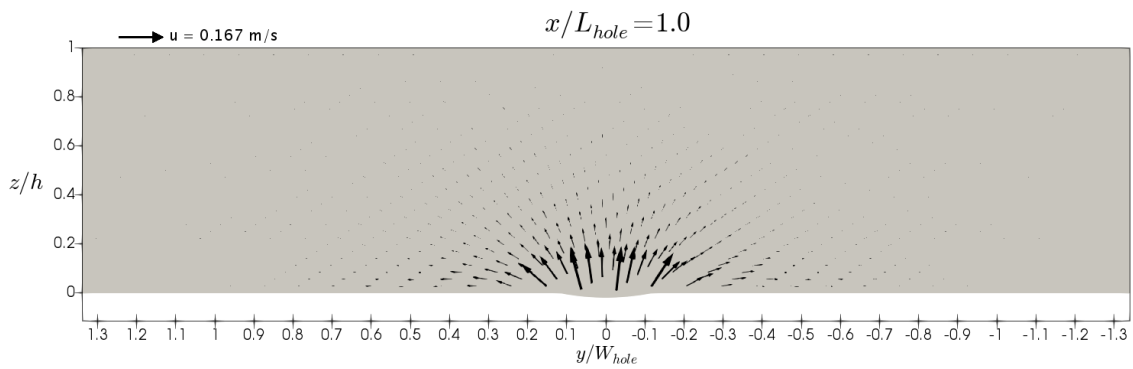


Figure 1.16: Cross section normal to the streamwise direction at $x/L_{hole} = 1.0$. The vectors are generated using the lateral and vertical flow velocity. The scale of the vectors is shown in the top left corner.

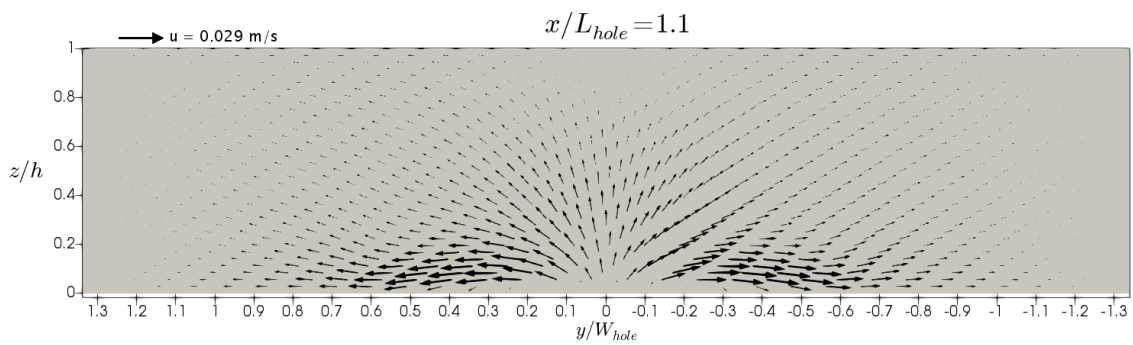


Figure 1.17: Cross section normal to the streamwise direction at $x/L_{hole} = 1.1$. The vectors are generated using the lateral and vertical flow velocity. The scale of the vectors is shown in the top left corner.

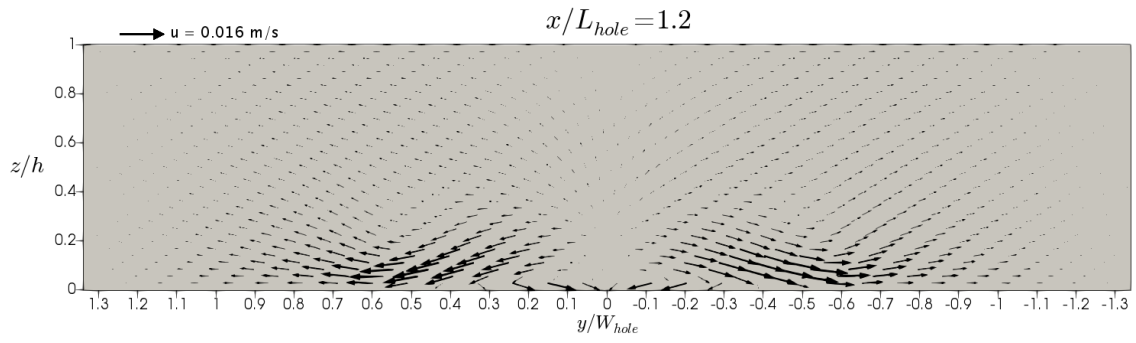


Figure I.18: Cross section normal to the streamwise direction at $x/L_{hole} = 1.2$. The vectors are generated using the lateral and vertical flow velocity. The scale of the vectors is shown in the top left corner.

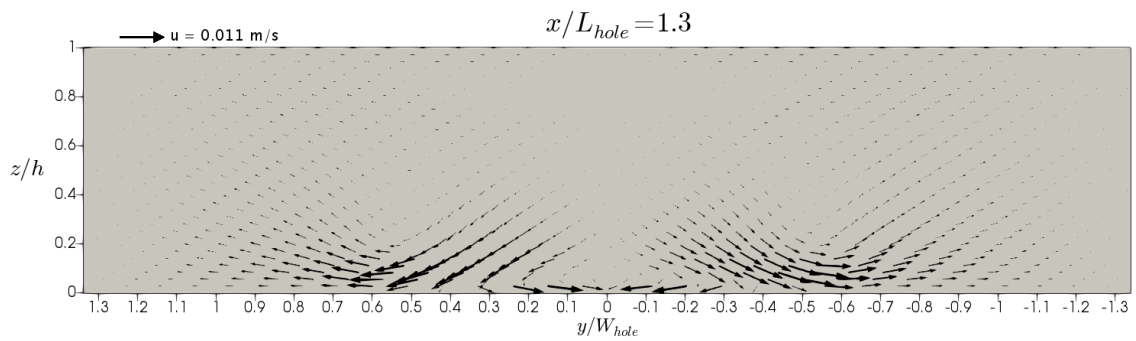


Figure I.19: Cross section normal to the streamwise direction at $x/L_{hole} = 1.3$. The vectors are generated using the lateral and vertical flow velocity. The scale of the vectors is shown in the top left corner.

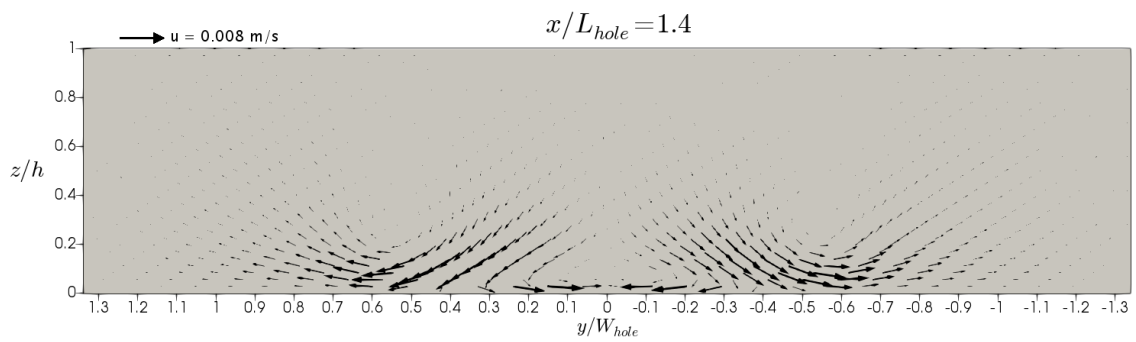


Figure I.20: Cross section normal to the streamwise direction at $x/L_{hole} = 1.4$. The vectors are generated using the lateral and vertical flow velocity. The scale of the vectors is shown in the top left corner.

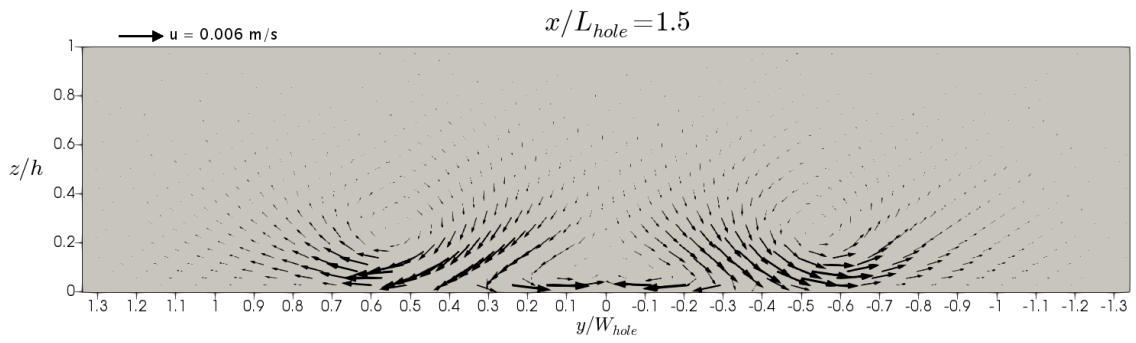


Figure 1.21: Cross section normal to the streamwise direction at $x/L_{hole} = 1.5$. The vectors are generated using the lateral and vertical flow velocity. The scale of the vectors is shown in the top left corner.

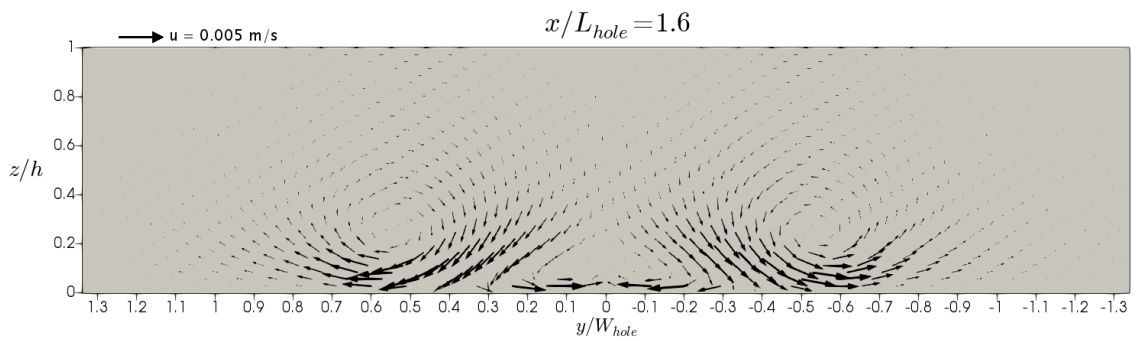


Figure 1.22: Cross section normal to the streamwise direction at $x/L_{hole} = 1.6$. The vectors are generated using the lateral and vertical flow velocity. The scale of the vectors is shown in the top left corner.

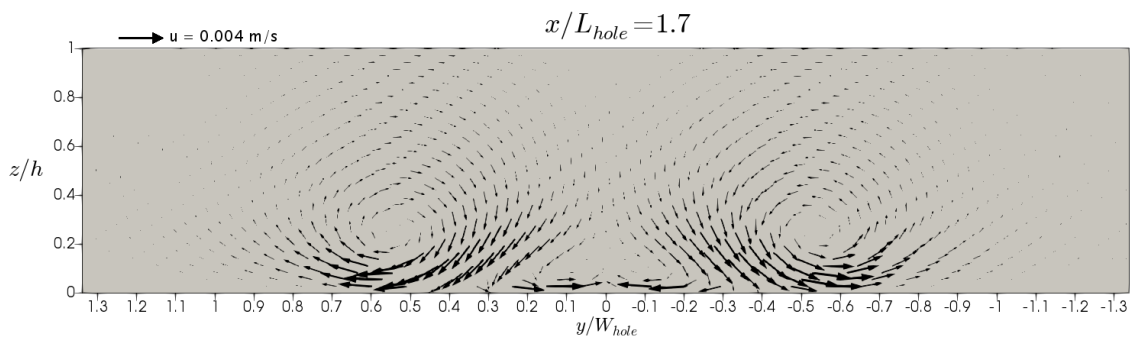


Figure 1.23: Cross section normal to the streamwise direction at $x/L_{hole} = 1.7$. The vectors are generated using the lateral and vertical flow velocity. The scale of the vectors is shown in the top left corner.

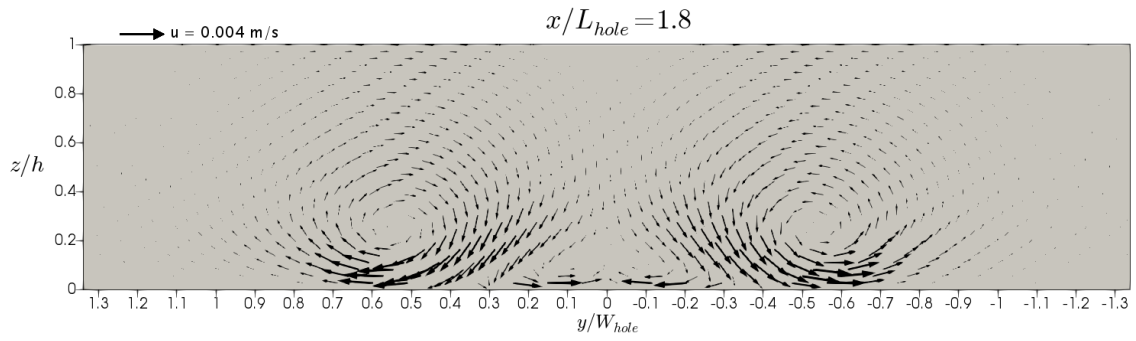


Figure I.24: Cross section normal to the streamwise direction at $x/L_{hole} = 1.8$. The vectors are generated using the lateral and vertical flow velocity. The scale of the vectors is shown in the top left corner.

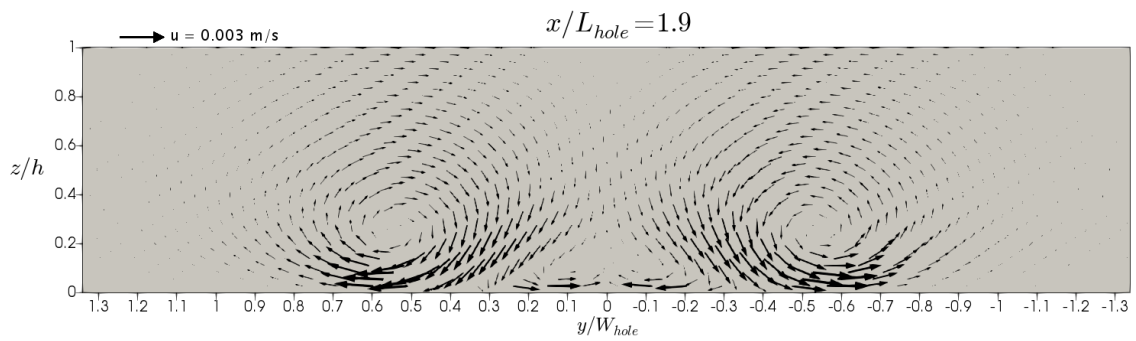


Figure I.25: Cross section normal to the streamwise direction at $x/L_{hole} = 1.9$. The vectors are generated using the lateral and vertical flow velocity. The scale of the vectors is shown in the top left corner.

Appendix J

Figures of the prototype scale simulations

Table J.1: Overview of the model simulations that are performed with a prototype scale scour hole. The average flow velocity (\bar{u}), water depth (h), maximum scour hole depth (h_s), upstream slope (β), bed shear velocity (u_*), Froude number (Fr) and Reynolds number (Re) are given.

Nr.	Name	Bed after	\bar{u} (m/s)	h (m)	h_s (m)	β (-)	u_* (m/s)	Fr (-)	Re (-)
1	base case	30 hours	0.924	14	4.9	0.456	0.040	0.08	$1.29 \cdot 10^7$
2	$h_s * 1.25$	30 hours	0.924	14	6.1	0.228	0.0140	0.08	$1.29 \cdot 10^7$
3	$h_s * 1.5$	30 hours	0.924	14	7.3	0.342	0.0140	0.08	$1.29 \cdot 10^7$

J.1. Run 1 - base case

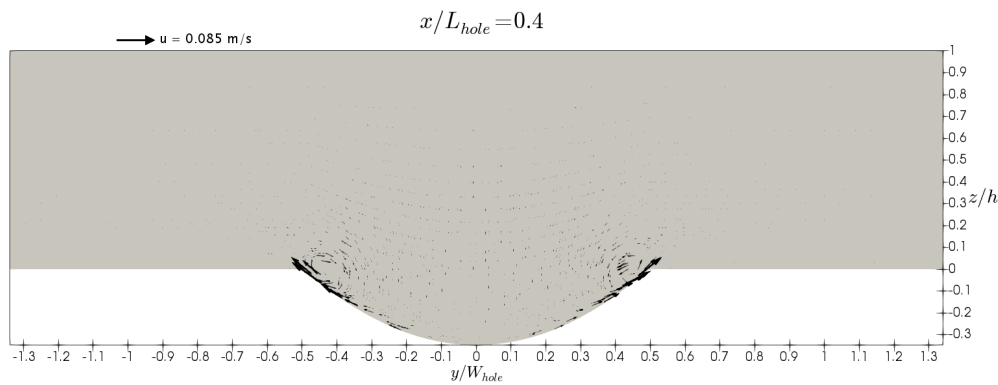


Figure J.1: Cross section normal to the streamwise direction at $x/L_{hole} = 0.4$ in the base case prototype scale simulation. The vectors are generated using the lateral and vertical flow velocity. The scale of the vectors is shown in the top left corner.

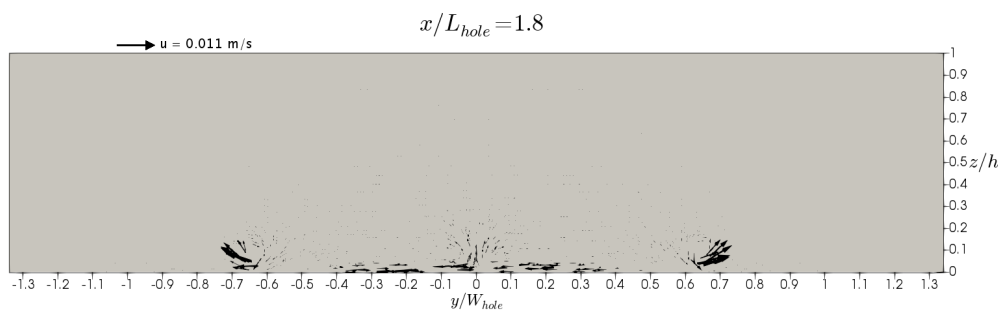


Figure J.2: Cross section normal to the streamwise direction at $x/L_{hole} = 1.8$ in the base case prototype scale simulation. The vectors are generated using the lateral and vertical flow velocity. The scale of the vectors is shown in the top left corner.

J.2. Run 2 - $1.25 \cdot h_s$

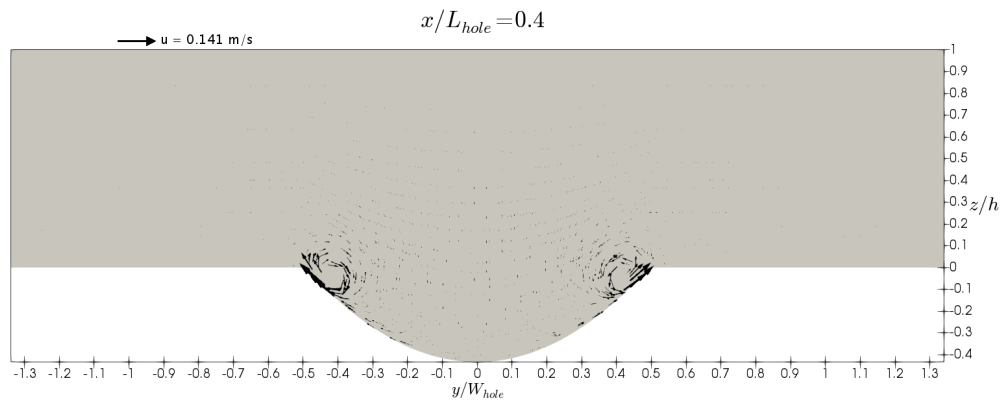


Figure J.3: Cross section normal to the streamwise direction at $x/L_{hole} = 0.4$ in the prototype scale simulation with a scour depth of $1.25 \cdot h_s$. The vectors are generated using the lateral and vertical flow velocity. The scale of the vectors is shown in the top left corner.

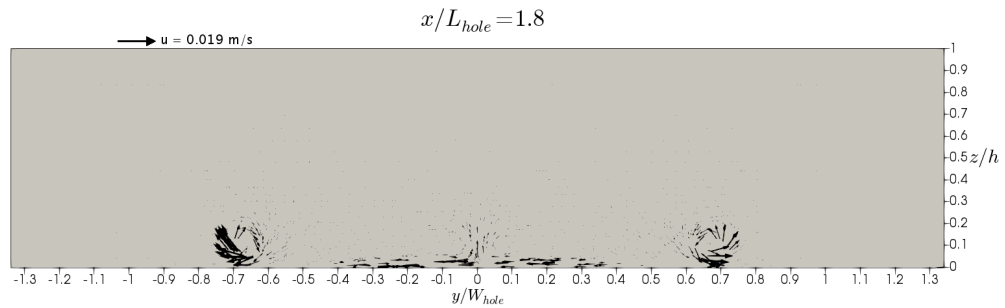


Figure J.4: Cross section normal to the streamwise direction at $x/L_{hole} = 1.8$ in the prototype scale simulation with a scour depth of $1.25 \cdot h_s$. The vectors are generated using the lateral and vertical flow velocity. The scale of the vectors is shown in the top left corner.

J.3. Run 3 - $1.5 \cdot h_s$

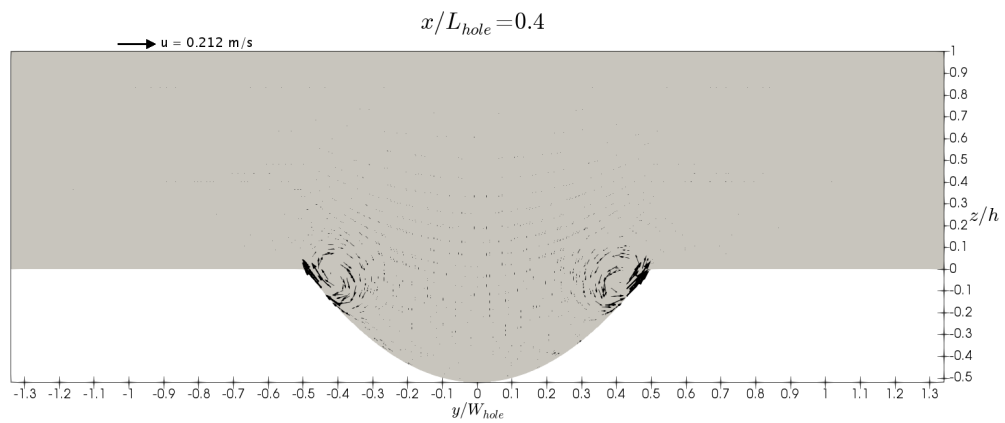


Figure J.5: Cross section normal to the streamwise direction at $x/L_{hole} = 0.4$ in the prototype scale simulation with a scour depth of $1.5 \cdot h_s$. The vectors are generated using the lateral and vertical flow velocity. The scale of the vectors is shown in the top left corner.

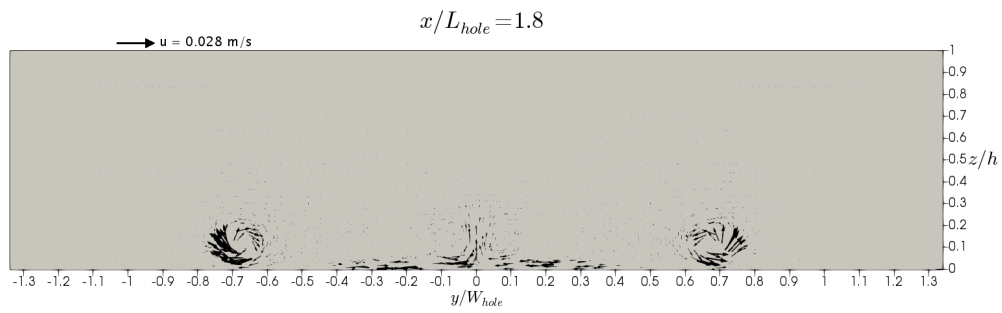


Figure J.6: Cross section normal to the streamwise direction at $x/L_{hole} = 1.8$ in the prototype scale simulation with a scour depth of $1.5 \cdot h_s$. The vectors are generated using the lateral and vertical flow velocity. The scale of the vectors is shown in the top left corner.